Laser Irradiation Effects in Polymers, Lithium Niobate Crystal and Applications in Photonics

A Thesis Submitted for the Degree of

DOCTOR OF PHILOSOPHY

By

K. L. N. DEEPAK

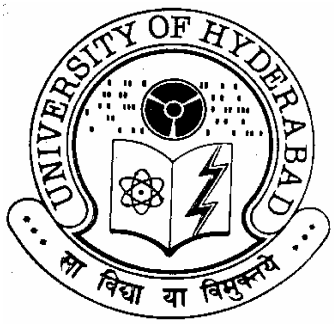

School of Physics
University of Hyderabad
Hyderabad 500 046
India

November 2011

To my parents, grandma, and brother

DECLARATION

I hereby declare that the matter embodied in the thesis entitled "**Laser Irradiation Effects in Polymers, Lithium Niobate Crystal and Applications in Photonics"** is the result of investigation carried out by me in the School of Physics, University of Hyderabad, India, under direct supervision of Prof. D. Narayana Rao.

Place: Hyderabad

Date: (K. L. N. Deepak)

CERTIFICATE

This is to certify that the work described in this thesis entitled "**Laser Irradiation Effects in Polymers, Lithium Niobate Crystal and Applications in Photonics"** has been carried out by **K. L. N. Deepak**, under my direct supervision and this has not been submitted for any degree or diploma at this or any other University.

Place: Hyderabad

Date: **(Prof. D. Narayana Rao)**

Dean

School of Physics

Table of Contents

ACKNOWLEDGEMENTS

I express my gratitude and profound thanks to my thesis supervisor, Prof. D. Narayana Rao, for his inspiring guidance and constant encouragement throughout the course of this research work. I have been able to learn a great deal in this fascinating field of research through his inspiring and thought provoking discussions, and I consider my association with him a rewarding experience.

I thank Prof. Bansal, Dean, School of Physics, former Dean Prof. Vipin Srivastava, and faculty for their co-operation in providing facilities in the School. I should also express my sincere thanks to Dr. Ashoka for his constant support in the development of my research work during the course of my dissertation work. The encouragement and support provided by the Non-teaching staff in the school is highly appreciable.

My association with Dr. S. Venugopal Rao, ACRHEM has been rewarding and sincere thanks to him. I have learnt the art of literature search from him. Also my thanks to Dr. Manoj, Dr. Prem Kiran who helped me during different discussions. My special word of thanks and appreciation to all my lab seniors, Dr. N. Venkat Ram, Dr. Krishna Chaitanya, Dr. Shiva Kiran Bhakta, Dr. Sai Santosh, Dr. Manoj for constantly encouraging and supporting me throughout my time here and directly helping me in getting into suitable research problems. Thanks to my present lab members Ali, Balamurali, Sreeram, Sree Ramulu, Shekhar, Kuladeep, Praveen, Ashok for creating friendly and pleasant lab atmosphere. Without the support of these guys this thesis work wouldn't have been successful. I am also thankful to Dr. T. P. S. Nathan.

My stay on this campus has been pleasant with the association of many other students whose list cannot be mentioned due to lack of space. I would like to thank my SSSU classmates in Hyderabad. Special thanks to Sarat and Sampy for constantly supporting and encouraging me.

The unconditional love of my mother, father, and my dear brother made me what I am today and I owe everything to them. As a final note, I would like to express my love and gratitude to Bhagawan Sri Sathya Sai Baba, who is my source of inspiration and my guru, and who taught me the basic principles of life. I thank him for giving me patience and perseverance to endure challenges in my life. I dedicate this thesis at his lotus feet.

K. L. N. Deepak

Chapter 1

Abstract

In this chapter, the advent of femtosecond (fs) laser direct writing (LDW) technique is introduced which is a nascent and recently developed technology based on nonlinear optics field. The birth of fs LDW and preliminary works carried out are introduced. Different materials such as absorptive and transparent which are of interest for fs LDW applications are described in the context of modifications of linear and nonlinear absorption schemes. Different ionization schemes such as tunneling, multi-photon and avalanche ionization are explained for transparent materials. Optical damage of the materials due to high laser fluencies and the role of pulse duration are summarized. Free electron generation in transparent dielectrics in the conduction band is explained through simple and multiple rate equations. Keldysh parameter which is used to estimate the dominant ionization scheme in case of transparent materials is described. The usage of fs laser pulses compared with continuous and long pulses for micromachining is elucidated in the context of thermal diffusion length for ns, ps, and fs laser pulse regimes. Different kinds of structural modifications that occur with fs laser micromachining are explained. The role of focusing, aberrations; pulse duration and dispersion which influence micromachining process are explored.

1.1 Introduction

Maxwell's equations describe the interaction of light with matter theoretically. Depending on the interaction of light, matter can be dielectrics that transmit light, metals which reflect, and opaque surfaces that absorb. The interaction of light with matter can be either linear or nonlinear; if the interaction is linear, then two electromagnetic waves do not interact with each other and the system response to the signals is the sum of individual signal's response. Also, there will not be any change in frequency when passing through the system and the intensity is not sufficient to change the material's properties. In this linear regime, one can write the induced polarization ($\vec{P}$) which depends on electric field ($\vec{E}$) as

$$\vec{P} = \varepsilon_0 \chi^{(1)} . \vec{E} \tag{1.1}$$

where ε_0 = 8.85×10^{-12} As/Vm is the vacuum permeability. $\chi^{(1)}$ is the linear susceptibility. However, if the interaction is nonlinear then the occurrence of interaction between two light fields which lead to change in the frequency of light while propagating through the media and dependence of material's properties on the intensity of light take place. The second (lowest) order of nonlinear polarization can arise from $\chi^{(2)}$ nonlinearity. The nonlinear polarization then has a component which depends quadratically on the electric field of an incident light wave. More precisely, the tensor nature of the nonlinear susceptibility needs to be considered. If P_i is the *i*-th Cartesian coordinate of the polarization, $\chi^{(2)}$ is the nonlinear susceptibility, and E (t) is the optical electric field, then i^{th} component of the polarization in general can be written in form of equation (1.2).

$$P_i(t) = \sum_j \chi_{ij}^{(1)} E_j(t) + \sum_{j,k} \chi_{ijk}^{(2)} E_j(t) E_k(t) \tag{1.2}$$

If the incident field is much smaller than the binding field, the electron motion is induced by external field is perturbed to small displacements around the equilibrium position. In case of stronger external fields, electron is perturbed more and is driven further away from its equilibrium position setting up anharmonicity. In this case, the induced polarization can be explained by only equation (1.2) for lowest order of nonlinearity. Such strong incident electric

field ionizes the electron which oscillates driven by the electric field. After the invention of the laser in 1960, nonlinear optical phenomena in the optical range became easily accessible [1]. Second harmonic generation was first demonstrated in 1961 [2]. Generation of optical pulses using Q switching and mode locking techniques almost occurred simultaneously which resulted in the increase in the peak output power by several orders of magnitude.

Ultrafast lasers with extremely short pulse duration (and extremely wide spectral bandwidth) resulted in the fabrication of integrated photonic communications and signal processing systems inside transparent materials. A new approach for local modification of transparent materials through nonlinear optical processes has been investigated due to the extraordinarily high peak powers of short-duration optical pulses. Recent demonstrations of three dimensional (3D) micromachining of glass and polymers using ultrafast laser pulses include the fabrication of waveguides, couplers, gratings, binary data storage devices, lenses, and channels. (give references) The most important feature of this micro fabrication technique is its ability to integrate 3D optical or photonic devices inside transparent materials by sequential direct-writing of individual devices. Although such a sequential approach is slow in comparison with conventional lithography, the new capability for 3D integration is priceless, in that it is quite difficult to achieve by other methods.

Through nonlinear field ionization, the intensity in the focal volume can become high to initiate absorption, when an intense femtosecond laser pulse is tightly focused inside the bulk of a transparent material. This nonlinear absorption results in the creation of electron-ion plasma that is localized to the focal volume. As the plasma recombines and its energy is dissipated, permanent structural changes can be induced in the material. Because the nonlinear absorption allows energy to be deposited into the bulk of a transparent material, these structural changes can be produced inside the sample without affecting the surface, allowing 3D structures to be fabricated by translating the laser focus through the sample. Figure 1 shows various mechanisms that occur when an intense femtosecond (fs) laser pulse interacts with a transparent dielectric [3]. Figure 1 (a) shows the interaction of an fs pulse inside a transparent dielectric. As the fs laser pulse is focused we have nonlinear absorption of laser energy playing a major role. There are two types of interactions that take place as shown in figure 1 (b). First one is field ionization

which can be either tunneling ionization or multiphoton ionization where seed electrons are produced in the conduction band which undergo avalanche ionization. Thus, the generated hot electron-ion plasma transfers the energy to the lattice as shown in figure 1 (c). There are three major phenomena reported in the literature when focused intense fs pulses interact with transparent dielectrics which are summarized in figure 1 (d). When the energy of fs laser pulses is low, it results in refractive index change of the material which is called isotropic refractive index change (Δn) mechanism. At moderate energies, it leads to formation of a nanograting, called birefringent refractive index change mechanism. Still at higher energies, it results in void formation.

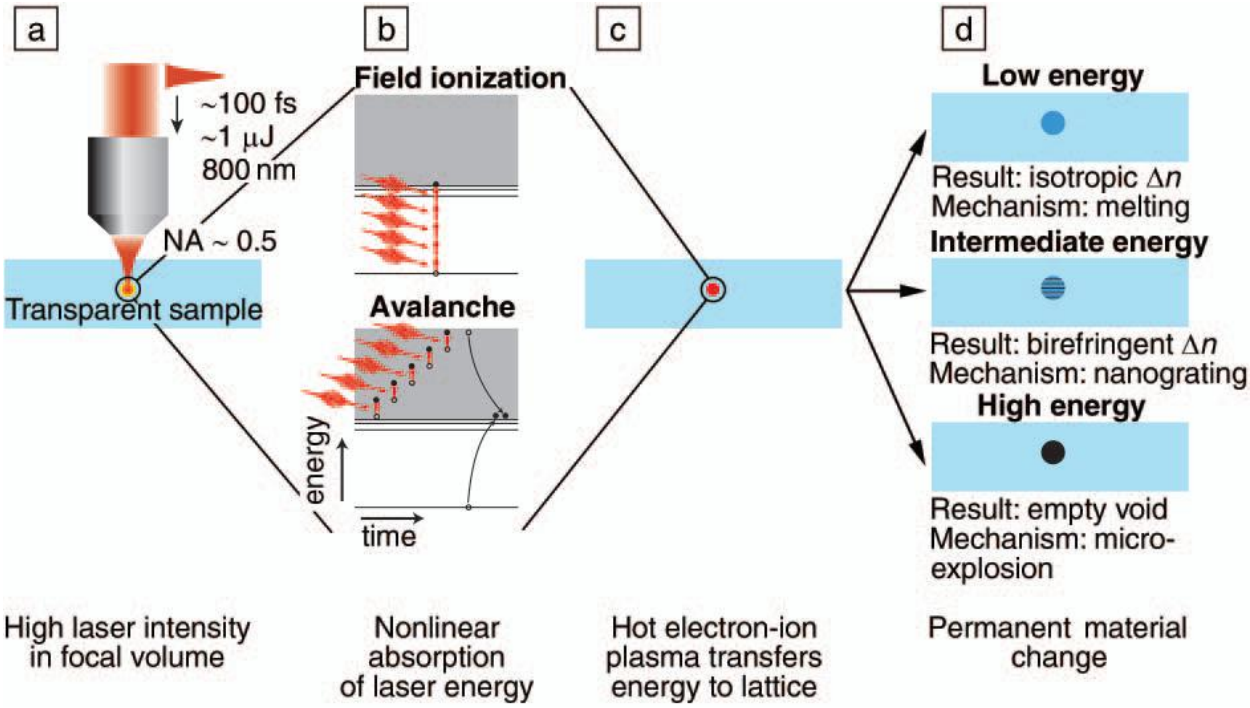

Figure 1. (a): Focusing a fs laser pulse inside a transparent dielectric with microscope objective (b) Nonlinear absorption of laser energy which is the cause for modification inside the material (c) The resultant hot electron-ion plasma transfers the energy to the lattice after nonlinear absorption of laser energy (d) Three basic permanent material changes reported in the literature after the modification.

Due to higher intensities associated with these ultrashort laser pulses, they find applications in material machining. The laser material machining is based on the local thermal action and subsequent ablation that is the removal of the material caused by its melting, evaporation, and shearing as resultant phenomena of the interaction between fs pulse with the material. UV excimer lasers are successfully used for micromachining as they have lower wavelengths which lead to minimum obtainable focal spots. But the disadvantage is that most of the transparent materials absorb this radiation and hence the surface of the materials is modified. Also, this radiation damages the focusing optics also. On the other hand ultrashort pulses of longer wavelengths can be used for both surface and bulk machining of transparent materials [4-5]. The experiments involved in references 4 and 5 were fabrication of holes of 0.3 μm in diameter produced in silver film and ~1 μm in fused silica using 790 nm Ti: Sapphire laser pulses with 200-fs pulse width in first case and 60-fs in second case. One can obtain smaller size features by choosing pulse carefully in such a way that the region near the center which exceeds the damage threshold of the material should be small. Thus, only the selected area leads to modification of the material leading to structures whose sizes are smaller than the diffraction-limited one.

Materials which are of interest for laser direct writing applications are of two types; absorptive and transparent. The applications found in the case of absorptive materials are hole drilling, removal of surface defects, and photolithographic mask repair [6-10]. Bulk refractive index change in transparent materials which is useful in the applications of the fabrication of waveguides has been reported [11-27]. Though there are several lithographic techniques with inimitable capabilities, fs laser direct writing (LDW) has been established to be a potential technique for precise structuring of well defined, three dimensional sub-micron features, especially in polymers, because of minimal damage arising from the generation of stress waves, thermal conduction, or melting [28-37]. A variety of materials including metals, dielectrics, polymers, and semiconductors have been successfully processed by the use of fs pulses [32-37]. Various applications are found in microfluidics [38-56], and photonic bandgap structures [57-59]. The main process involved in fs laser direct writing by which the energy is transferred from an optical field to material results in ionization of large number of electrons is called optical breakdown. Since, the first demonstration of the laser, Researchers at Ford Motor Company reported ionizing of air creating a very bright spark from a Q-switched ruby laser followed by the

observation of laser damage in glass [60-61]. As pulsed lasers achieve much higher intensities when compared to the continuous wave lasers, the light-matter interaction is different in these two regimes. Fabrication of waveguides is reported inside a piece of glass using 120-fs, 200-kHz Ti: sapphire laser system [17, 62]. Researchers used amplified fs laser systems with pulse energies of the order of μJ earlier followed by micromachining using nJ energy later in 2001. The first writing of waveguides in polymers using Ti: sapphire laser was reported in poly (methyl methacrylate) (PMMA) in 2004 [63].

As the energy per pulse is of the order of nanojoules in case of laser-oscillator systems, a higher numerical aperture objective lens is required to ensure high intensities to microstructure the sample. In case of micromachining with laser-amplifier systems where the energy per pulse is of the order of μJ, lower NA objective lenses are sufficient to microstructure the sample. The microscope objective is held fixed while the substrate or sample of interest is translated using 3 dimensionally arranged stages. Figure 1 shows a schematic diagram of a typical micromachining setup. The results of micromachining process depend upon laser parameters and material properties. Pulse energy, repetition rate, wavelength, and pulse duration are several laser parameters and bandgap; and thermal properties of the material that influence micromachining process.

1.2 Laser Intensity Distribution in a focal domain

When an fs laser beam is tightly focused inside a transparent material, deposition of high energy density occurs in a small volume which leads to the change in optical and structural properties of the material, where the beam is focused. If the resultant structure is very small ($<\mu m^3$), it can be used as a memory bit for applications involved in 3D optical storage. Every dielectric material has an ionization threshold above which the material gets ionized due to the generation of strong shockwave which propagates into the surrounding cold material. Thus a void is formed inside the material by processes of compression and decompression of the solid material at and behind the wave front [64-65]. Transparent dielectrics have a wide optical band-gap. For chalcogenide glasses it ranges from 2.2-2.4 eV, for polymers more than 2 eV, and 8.8 eV for sapphire. Hence they are transparent as they do not absorb any light in the visible and near infra-red at low intensity. Hence, the only way to modify the material is to increase the intensity through plasma

formation. Most of the dielectric materials can be easily ionized when the intensities are ~10^{14} W/cm^2.

The intensity distribution of a Gaussian beam can be represented in terms of field strength E(r, z, t) [66].

$$E(r,z,t) = E_0(t)\frac{1}{\sqrt{1+\frac{z^2}{z_0^2}}}\exp\{-\frac{r^2}{r_0^2(1+\frac{z^2}{z_0^2})}\}\times\exp\{-ikz - ik\frac{r^2}{2z(1+\frac{z_0^2}{z^2})} + i\tan^{-1}(\frac{z_0^2}{z^2})\} \quad (1.3)$$

r_0=Minimum waist radius at z=0 and z_0 is the Rayleigh length, and is given by $z_0=\pi r_0^2 n_0/\lambda$ where n_0 is the real part of the refractive index in the material. The minimum waist radius in the case of diffraction limited focusing by numerical aperture lens (NA) is given by $r_0=1.22\lambda/NA$. The cylindrical focal volume is given by

$$V_{foc,E} = 2\pi r_0^2 z_0 = \lambda z_0^2 \quad (1.4)$$

The incident laser intensity I_0 averaged over many light periods can be written as

$$I_0 = \frac{c}{8\pi}|E_0|^2 \quad (1.5)$$

where E_0(r=0; z=0) is the incident laser electric field. The volume where the intensity decreases approximately twice is given by (As $z_{1/2}= (2^{1/2}-1)z_0$; $r_{1/e}=2^{1/2}r_0$)

$$V_{foc,I} = 2\pi r_{1/e}^2 z_{1/2} = (\sqrt{2}-1)\pi)_0^2 z_0 = (\sqrt{2}-1)^2\lambda z_0^2 \quad (1.6)$$

Thus, the focal volume goes as the cubic order of the wavelength

$$V_{foc,I} \approx \lambda^3 \quad (1.7)$$

The volume reduces with the wavelength of light used for micromachining experiments. Thus, the modified crater (hole) can be treated as bit 1 whose applications can be found in data storage devices. However, most of the materials have absorption in UV region and hence only the surface of the material gets modified. This poses the limit over the usage of UV lasers in

micromachining. The only solution to the posed problem is to modify the material through nonlinear absorption scheme by using IR lasers.

1.3 Introduction to Optical Damage

The present laser technology can produce laser beams of sufficient intensity to exceed the damage threshold of different materials leading to optical damage. Several mechanisms that lead to optically induced damage are illustrated below [67].

a) Linear absorption, leading to localized heating and cracking of the optical material. This is the dominant damage mechanism for continuous-wave and long pulse laser beams (≥ 1 μs).

b) Avalanche breakdown is the dominant mechanism for pulsed lasers typically ≤ 1μs for intensities in the range of 10^9 W/cm^2 to 10^{12}W/cm^2.

c) Multiphoton ionization is the process of multiphoton dissociation of the optical material, which is the dominant mechanism for intensities in between 10^{12} to 10^{16} W/cm^2.

d) Direct (single cycle) field ionization is the dominant mechanism for intensities > 10^{20} W/cm^2.

The dominant mechanism for most pulsed lasers is avalanche-breakdown mechanism [67]. In this mechanism, a small number N_0 of free electrons initially present within the optical material are accelerated to high energies through laser mater interaction. These electrons can impact ionize other atoms within the material. This leads to generation of additional electrons which are subsequently accelerated by the laser field to produce more electrons. However, there has to be a few electrons (seed) to be present initially which are created by several processes including thermal excitation, quantum mechanical tunneling by means of the Keldysh mechanism, multiphoton excitation, or free electrons resulting from crystal defects. We follow the notation ~ (tilda) for describing time dependence. Here, we define the electric field strength as follows. cc stands for complex conjugate.

$$\tilde{E}(t) = Ee^{-i\omega t} + cc \tag{1.8}$$

Let us denote the energy with Q imparted to an electron which is at rest and subjected to an electric field $\tilde{E}$ for a time duration t is given by

$$Q = e\tilde{E}d \tag{1.9}$$

By substituting $d = (1/2)\, at^2 = (1/2)\, (e\tilde{E}/m)\, t^2$ (1.10)

We get

$$Q = e^2 \tilde{E}^2 t^2/2m \quad \text{for } t<\tau \tag{1.11}$$

τ is defined as the mean time between collisions. For longer time durations, the total energy imparted to the electron will be given approximately by the energy imparted to the electron in time interval τ multiplied by the number of such time intervals which results in

$$Q = e^2 \tilde{E}^2 t\tau/2m \quad \text{for } t>\tau \tag{1.12}$$

The rate at which the electron gains energy is given in this limit by

$$P = \frac{dQ}{dt} = \frac{e^2 \tilde{E}^2 \tau}{2m} \tag{1.13}$$

The number density of free electrons N (t) changes with time t according to the following relation

$$\frac{dN}{dt} = \frac{fNP}{W} \tag{1.14}$$

where W is the ionization threshold of the material under consideration, P is the absorbed power given by earlier equation, and f is the fraction of the absorbed power that leads to further ionization so that 1-f represents the fraction that leads to heating. Thus the solution becomes

$$N(t)=N_0 e^{gt} \text{ where } g = \frac{fe^2 \tilde{E}^2 \tau}{2Wm} \tag{1.15}$$

Optical damage will occur if the electron density N (T_P) at the end of the laser pulse duration T_P exceeds some damage threshold value N_{th} which is of the order of $10^{18}cm^{-3}$. Thus the occurrence for laser damage is given by the condition as follows:

$$\frac{fe^2 E^2 \tau T_P}{2mW} > \ln(N_{th}/N_0) \tag{1.16}$$

On the assumed values of N_{th} and N_0 the right hand side of the inequality can be taken to have a value of the order of 30. This result can be used to find out the threshold intensity for producing laser damage given by

$$I_{th} = n\varepsilon_0 c\langle E^2 \rangle = 2n\varepsilon_0 c \frac{Wm}{fe^2 \tau T_p} \ln(N_{th}/N_0) \tag{1.17}$$

1.4 Influence of pulse duration

Optical damage depends not only on laser fluence or on laser intensity but pulse duration also. The fluence or energy per unit area required producing damage increases with pulse duration and the intensity required to produce laser damage decreases with pulse duration. The nonlinear optical effects which arise due to laser pulses lead to thermal effects. Some fraction of the incident laser power is absorbed in passing through an optical material. The local temperature of the illuminated region increases which leads to change in refractive index which can be either positive or negative depends on the internal structure of the material. In order to arrive at some conclusions on the influence of pulse duration, let us assume $\tilde{T}_1$ which is laser induced temperature that obeys heat-transport equation as follows [67];

$$(\rho_o C)\frac{\partial \tilde{T}_1}{\partial t} - \kappa \nabla^2 \tilde{T}_1 = \alpha \tilde{I}(r) \tag{1.18}$$

($\rho_0 C$) denotes the heat capacity per unit volume, κ denotes the thermal conductivity, and α denotes linear absorption coefficient of the material. Thermal effects can be described by assuming refractive index n varies with temperature as follows

$$\tilde{n} = n_0 + \left(\frac{\partial n}{\partial T}\right)\tilde{T}_1 \tag{1.19}$$

$\left(\frac{\partial n}{\partial T}\right)$ describes the temperature dependence of refractive index of a given material.

By assuming a circular beam of laser intensity I_0 and radius R falls onto a slab of optical material of thickness L with linear absorption coefficient α, the power P can be written as

$P=\pi R^2 I_0$

The response time τ is defined as the time taken for the temperature distribution to reach its steady state after the laser pulse is suddenly switched off. Then the approximations to the equation (1.18) can be as follows;

The term $\frac{\partial \tilde{T}_1}{\partial t}$ can be replaced by T_1/τ and $\nabla^2 \tilde{T}_1$ as T_1/R^2

Thus the equation (1.18) becomes

$$\tau \approx \frac{(\rho_0 C)R^2}{\kappa} \tag{1.20}$$

Usually the response times are more for condensed matter as illustrated in reference 67. These response times are much longer than the pulse duration T produced by pulsed lasers. Thus, in conclusion when thermal effects are considered the power is the relevant quantity for continuous

wave laser beams and the pulse energy Q=PT is the relevant quantity for pulsed lasers where T is pulse duration, P is power and Q is energy.

Under steady state conditions for continuous wave laser beams, the heat transport equation (1.18) reduces to the following equation as

$$-\kappa\nabla^2 \tilde{T}_1 = \alpha \tilde{I}(r) \tag{1.21}$$

As center of the laser beam has more intensity I^{max}, it leads to maximum temperature rise T_1^{max}.Thus, equation (1.21) becomes

$$T_1^{max} = \frac{\alpha I^{max} R^2}{\kappa} \tag{1.22}$$

From equation (1.19), the maximum change in refractive index can be estimated as

$$\Delta n = \left(\frac{dn}{dT}\right)\frac{\alpha I^{max} R^2}{\kappa} \tag{1.23}$$

Thus an effective nonlinear refractive index coefficient n_2^{th} can be defined through $\Delta n = n_2^{th} I_{max}$.

$$n_2^{th} = \left(\frac{dn}{dT}\right)\frac{\alpha R^2}{\kappa} \tag{1.24}$$

For a short laser pulse with duration t_p much shorter than the thermal response time τ of equation (1.20), the heat transport equation (1.18) reduces to

$$(\rho_0 C)\frac{\partial T_1}{\partial t} = \alpha I(r) \tag{1.25}$$

Here, the term $-\kappa\nabla^2 T_1$ is dropped because in the regime $t_p << \tau$ only a negligible fraction of the absorbed energy can diffuse out of the interaction region. Then the partial differential term in the equation (1.25) can be approximated to T_1^{max}/t_p. Thus equation (1.25) further reduces to

$$T_1^{max} = \frac{\alpha I^{max} t_p}{(\rho_0 C)} \tag{1.26}$$

The change in refractive index can be either thermal or electronic which are described below.

$$\Delta n^{(th)} = \left(\frac{\partial n}{\partial t}\right) T_1^{(max)} \tag{1.27}$$

$$\Delta n^{(el)} = n_2^{(el)} I \tag{1.28}$$

From equations (1.25) to (1.28), the thermal contribution to the change in refractive index will exceed the electronic contribution if and only if

$$t_p \geq \frac{n_2^{(el)} (\rho_0 C)}{(dn/dT)\alpha} \tag{1.29}$$

By evaluating the above expression assuming different values as referenced in 67, the thermal effects become important for $t_p \geq 30$ ps. Also, by comparing equations (1.23) and (1.27), we can conclude that the thermal effects are almost negligible in case of ultrashort pulses.

By again invoking the equation (1.18), the local temperature distribution T(r, t) can be rewritten as

$$(\rho C)\frac{\partial \tilde{T}}{\partial t} - \kappa \nabla^2 \tilde{T} = N(1-f)\tilde{P} \tag{1.30}$$

Where f, N, P have been described in earlier section (1.3) and κ is the thermal conductivity, (ρC) is the heat capacity per unit volume. Here, we have replaced $\alpha \tilde{I}(r)$ by N (1-f) $\tilde{P}$ as (1-f) $\tilde{P}$ represents the fraction of power that leads to heating. By denoting l_{th} as the distance over which a temperature rise ΔT will diffuse a time interval T_p, and by replacing the derivatives with ratios and assuming diffusion in only one direction and by ignoring the right-hand side of the equation (1.30), we obtain

$$(\rho C)\frac{\Delta T}{T_p} = \kappa \frac{\Delta T}{l_{th}^{\ 2}} \tag{1.31}$$

From the above equation, we obtain

$l_{th} = \left(DT_p\right)^{1/2}$ where D=κ/ρC is the diffusion constant (1.32)

1.5 Linear and nonlinear absorption

Extending further, summarizing about the material parameters, we have materials other than metals and conductors have certain bandgaps. If the photon energy exceeds the bandgap energy, light can be absorbed by the material directly and the electrons are promoted from valence band to the conduction band [68]. Figure 2 (a) illustrates the absorption of a single photon by a valence electron. Deposition of sufficient energy into the surface of a material through linear absorption, material ablation can result. Materials which are transparent to the laser wavelength, absorption of a single photon does not excite an electron from valence band to the conduction band. Only through nonlinear absorption of photons (simultaneous absorption) it is possible to modify the material. In nonlinear absorption, the absorption probability is a nonlinear function of the laser intensity where the absorption is only confined to the bulk of transparent sample by tightly focusing the laser beam inside the sample, producing much higher intensity in the focal volume than at the surface. Two classes of nonlinear excitation mechanisms are reported which a play a role in nonlinear absorption and they are photoionization and avalanche ionization [69]. In photoionization, electrons are directly promoted from the valence to the conduction band by the laser field. There are two types of photoionization namely multiphoton and tunneling ionization regimes explained by the Keldysh parameter [70].

In tunneling ionization, the electric field of the laser suppresses the potential that binds a valence electron to its parent atom, forcing the electron to tunnel out. Thus the electron becomes a free electron. This kind of nonlinear ionization occurs for strong laser fields and low laser frequency. At higher laser frequencies multiphoton ionization occurs by simultaneous absorption of multiple photons by an electron as shown in figure 2 (b). The sum of energy of all the photons absorbed exceeds the bandgap energy that is $n\hbar\omega \geq E_g$, where E_g is equal to the bandgap energy (ω is the laser frequency, h is planck's constant, and n is the minimum number of required photons to cross the bandgap). In multiphoton absorption, 'n' photons interact simultaneously with a single electron so that the probability of absorption will scale as the density of the photons raised to the

power n. Since the photon density is proportional to laser intensity, I, the probability for multiphoton absorption scale as I^n. Avalanche ionization occurs in the conduction band of the material where it absorbs laser photons sequentially until its energy exceeds by more than bandgap energy followed by ionizing another electron in valence band through collisions. This results two electrons in the conduction band minimum. It is illustrated in figure 2 (c). Requirement of seed electrons in conduction band is essential for avalanche ionization provided by photoionization. For fs pulses, photoionization takes place during the leading edge of the pulse and avalanche ionization during the trailing edge of the pulse [71].The critical plasma density refers to the electron density that is grown through avalanche ionization until the plasma frequency of the electrons in the conduction band equals the frequency of the incident laser radiation. For ultrashort pulse durations, the absorption described above occurs on a time scale that is short compared to the time scale for energy transfer to the lattice, decoupling the absorption and lattice heating processes. After pulse is gone, the hot electrons and cold lattice are left.

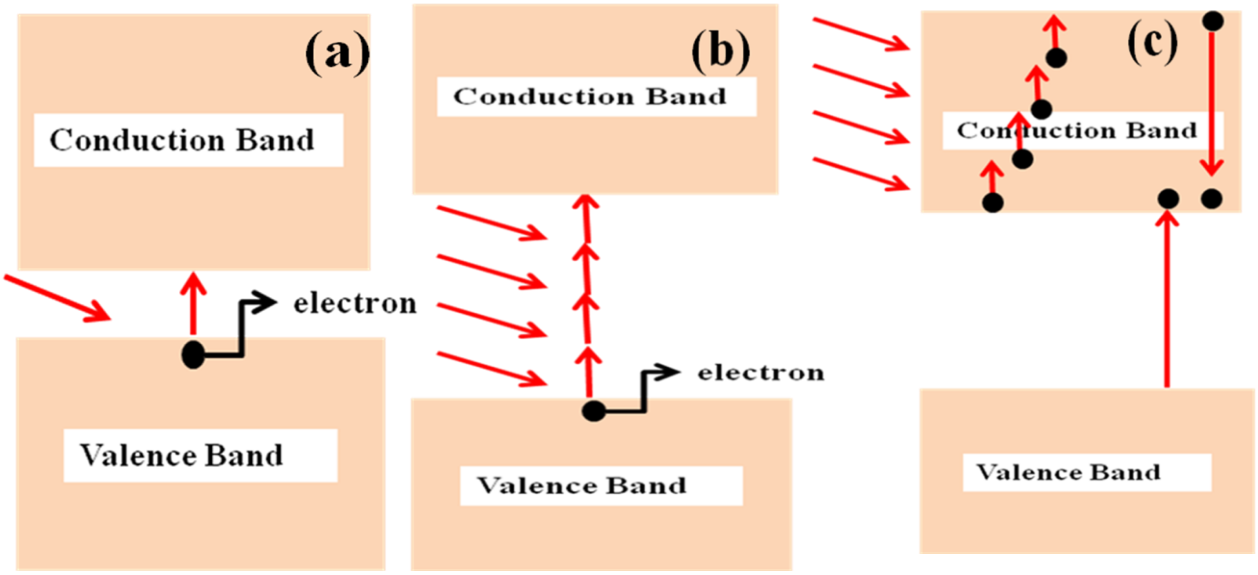

Figure 2. Schematic view of (a) linear absorption (b) multiphoton ionization and (c) avalanche ionization.

The Keldysh parameter (γ) which provides information about the dominant mechanism, is defined as

$$\gamma = \frac{\omega}{e}\left[\frac{mc\varepsilon_0 E_g}{I}\right]^{1/2} \tag{1.33}$$

m, e are reduced mass and charge of the electron, I is the intensity, ω is the laser frequency, ε_0 is the permittivity of free space, E_g is the band gap of the material, n is the refractive index of the material, and c is the velocity of light. Multiphoton ionization is dominant in case of γ >1.5, and tunneling ionization is favored in case of γ <1.5. If γ =1.5, then both ionizations take place [70-71].

Thus, the theoretical and experimental investigations of interaction of dielectrics with ultrashort laser pulses are a broad field which finds its applications in micromachining. Strong absorption of laser energy occurs when transparent solids are irradiated with laser intensities above a certain threshold. The formation of a free electron gas in the conduction band of the dielectric increases absorptivity of the material. Thus the advent of the ultrashort laser pulses of subpicosecond duration opens a new regime of laser matter interaction where the pulse duration compares with characteristic times of microscopic collision processes within the material. Study of these microscopic processes and their influence on free electron distribution by solving kinetic equations such as Fokker-Planck equation or Boltzmann equation are reported [72-73]. The temporal evolution of free electron density in a dielectric during ultrashort pulse laser irradiation plays a fundamental role. The free electron generation in dielectrics is described by a simple rate equation for the increase of the total free electron density in the conduction band n_{total} as

$$\frac{dn_{total}}{dt} = \dot{n}_{pi}(E_L) + \alpha(E_L)n_{total} \tag{1.34}$$

This equation combines the probability of photoionization $\dot{n}_{pi}$ depending on the amplitude of the electric laser field E_L, with the rate of impact ionization assumed to depend on total free electron density. Photoionization results in shifting of electrons from the valence band into the conduction band. If its kinetic energy is large it will transfer part of it to an electron in the valence band such

that the latter is enabled to overcome the ionization potential. The avalanche coefficient α depends on the effective energy gain of the free electron in the electric laser field E_L and can be estimated as

$$\alpha_{est} = \frac{W_{1pt}(E_L)\hbar\omega_L}{\varepsilon_{crit}} \tag{1.35}$$

Where W_{1pt} (E_L) is the probability of one-photon intraband absorption, $\hbar\omega_L$ the photon energy of laser light and ε_{crit} is the critical energy for impact ionization, which is on the order of bandgap between valence and conduction bands. Equation (1.34) was proposed and verified for laser pulses in nanosecond regime. The basic assumption made for equation (1.34) is that the impact ionization depends directly on the total density of free electrons but this impact ionization requires certain critical energy of the ionizing electron, thus the process depends on the energy of a particular electron in the conduction band. The photoionization generates electrons with low kinetic energy in the conduction band and impact ionization requires electrons of high kinetic energy and this additional energy is absorbed from the laser light by intraband absorption. On ultrashort time scales the shape of the electron distribution in the conduction band may change in time; the energy-averaged total electron density n_{total} is not an adequate parameter to describe the ionization process. By defining the density n_k of electrons above ε_{crit}, where k will be identified with the number of photons necessary to reach ε_{crit} a modified rate equation can be written as

$$\frac{dn_{total}}{dt} = \dot{n}_{pi}(E_L) + \tilde{\alpha} n_k \tag{1.36}$$

$\tilde{\alpha}$ represents the direct probability for impact ionization and this term can be estimated from the collisions and is independent of laser parameters unlike α. In the case of stationary shape of electron distribution in the conduction band, the fraction of high-energy electrons n_k/n_{total} is temporarily constant and the modified rate equation described in (1.36) reduces to standard rate equation with the substitution $\alpha(E_L) = \tilde{\alpha} n_k/n_{total}$. Equation (1.36) is the resultant of multiple rate equation introduced in references [72-73]. It provides a possibility to calculate the density of

high-energy electrons $n_k(t)$ and thus the transient evolution of free electron density $n_{total}(t)$. As per multiple rate equation (MRE), we have

$$\dot{n_0} = \dot{n_{pi}} + 2\tilde{\alpha} n_k - W_{1pt} n_0$$

$$\dot{n_1} = W_{1pt} n_0 - W_{1pt} n_1$$

$$\dot{n_2} = W_{1pt} n_1 - W_{1pt} n_2$$

....

....

....

$$\dot{n_k} = W_{1pt} n_{k-1} - \tilde{\alpha} n_k \qquad (1.37)$$

With $k = [\varepsilon_{crit}/\hbar\omega_L + 1]$. n_j denotes the density of electrons at a discrete energy level ε_j.

The k+1 energy levels ε_j are given by $\varepsilon_0 = 0$, $\varepsilon_{j+1} = \varepsilon_j + \hbar\omega_L$, where $k = [\varepsilon_{crit}/\hbar\omega_L + 1]$

The formulation of MRE is shown in figure (3). Photoionization generates electrons at the lower edge of the conduction band (CB) of a dielectric and with a certain probability W_{1pt}, that depends on ε_j absorb single photons from laser and reaches critical energy necessary for impact ionization. This results two electrons settling in lower edge of the CB starting the cycle of ionization fresh.

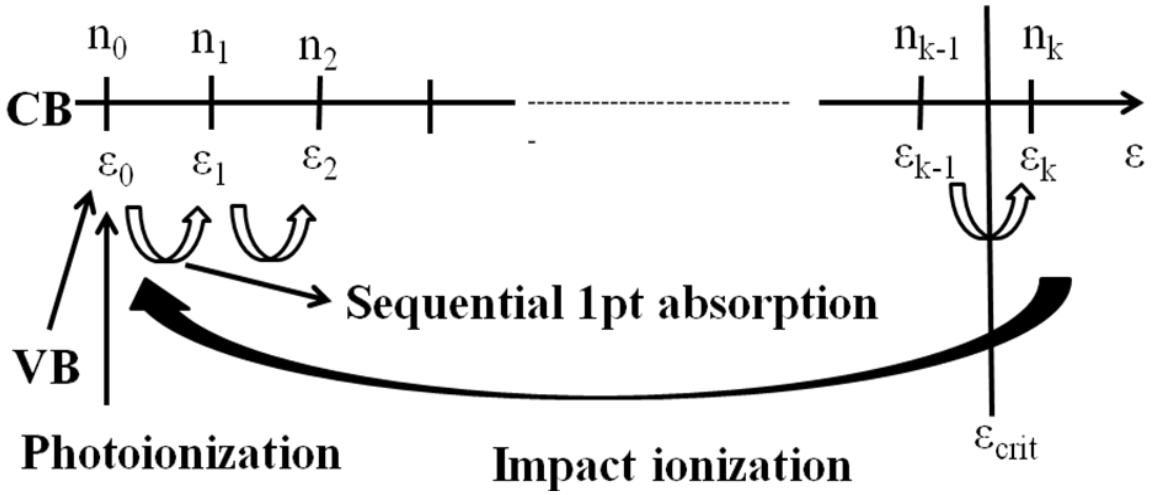

Figure 3. Schematic view of photoionization and impact ionization processes.

The MRE is solved with the help of Laplace transform and is given by

$$n_{total}(t) = \frac{\dot{n}_{pi}/W_{1pt}}{2k(\sqrt[k]{2} - 2 + \sqrt[k]{1/2})} \exp[t/t_{MRE}] \tag{1.38}$$

Equation (1.39) is valid for $t >> t_{MRE}$ with

$$t_{MRE} = [(\left|\sqrt[k]{2}\right| - 1)W_{1pt}]^{-1} \tag{1.39}$$

The transition time t_{MRE} characterizes the transition between the nonstationary regime on ultrashort time-scales and the asymptotic avalanche regime for longer times as described by equation (1.38). In this model constant intensity and constant ionization probabilities have been assumed. At the initial stage of ionization, photoionization is the dominant process. Later the shape of the free electron distribution becomes stationary and the probability of impact ionization which depends on the density of high energy electrons n_k, may be expressed through the total electron density n_{total}. Thus, the result of MRE indicates that for short times $t << t_{MRE}$ the electrons are provided by photoionization and for times $t >> t_{MRE}$ impact ionization plays an important role.

1.6 Long and short pulse interactions

If the pulse duration is longer typically of the order of ns, compared to the relaxation processes, then the whole system will be in equilibrium during the interaction process. Let us follow the terminology. T is the temperature, C_i be the specific heat of the material per unit volume. Then by considering the energy conservation in the system, any change in the internal energy U within a volume V either due to absorption of laser light within this volume (S.V) or due to energy diffusion out of the volume. Adopting the above terminology, we have in general

$$C\frac{\partial T}{\partial t} = \frac{-\partial Q(z)}{\partial z} + S \tag{1.40}$$

The above equation is called heat parabolic equation [74]. We have earlier arrived at the conclusion which follows the equation (1.32). The resulting heat waves after laser absorption will propagate for about l_{th} distance given by

$$l_{th} = \sqrt{DT_P} \tag{1.41}$$

l_{th} is called heat diffusion length, and $D=k/C_i$ is thermal diffusivity. The thermal conductivity which is characterized by the thermal diffusion coefficient, D, is an important feature of dielectrics which plays a major role. The value of D is typically 10^{-3} cm^2/s in case of dielectrics compared with ~ cm^2/s for metals. Hence, the micron-sized regions will cool in a time of 10 μs. For most metals, the thermal diffusivity ranges in between 0.1-1 cm^2/s. Hence, heat wave will travel about 0.1-1 μm within the pulse duration of 10 ns, which is much longer than the optical penetration depth α^{-1}, which is on the order of 10 nm for metals. Hence, it is appropriate to speak of a laser being a surface source of a heat [74].

The laser effect of multiple laser pulses focused into the same point in a dielectric will be an accumulation effect if the period between pulses is shorter than the cooling time. If the single pulse energy is too low to produce any structural modification in the material, a change can be brought by using a high pulse repetition rate, because of this accumulation phenomenon. The local temperature rise resulting from energy accumulation saturates as the energy inflow from the laser is balanced by heat conduction, which takes typically few thousand pulses at a

repetition rate of 10-100 MHz range. Due to this the size of a damaged zone inside a dielectric increases [75-76]. Thus the repetition rate becomes another parameter to control the size of structure produced by the laser.

For pulse durations of the order of ps and fs time scales, the heat diffusion length will become equal or smaller than the optical penetration depth. Hence, the laser pulse duration becomes shorter than the energy relaxation within the system leading to nonequilibrium conditions when heating is considered with ultrashort laser pulses. To explain the nonequilibrium conditions when interaction of the ultra-short pulses with material is considered, we need to invoke two-temperature model (TTM) proposed by Anisimov [74,77] as electrons and lattice have their own temperatures. The following equations represent two-temperature model equations.

$$C_e \frac{\partial T_e}{\partial t} = -\frac{\partial Q(z)}{\partial z} - \gamma(T_e - T_i) + S \tag{1.42}$$

$$C_i \frac{\partial T_i}{\partial t} = \gamma(T_e - T_i) \tag{1.43}$$

Te and Ti denote the electron and lattice temperatures, z is the direction perpendicular to the target surface, C_e and C_i are the heat capacities per unit volume of the electron and lattice subsystems. The parameter γ is electron-lattice coupling that is the energy exchange between the two systems. Q (z) (heat flux) can be written further as

$$Q(z) = -k_e(T_e)\frac{\partial T_e}{\partial z} \tag{1.44}$$

By dividing equations (1.42) and (1.43) by the corresponding heat capacities C_e and C_i respectively, we can observe two characteristic time scales; electron cooling time $\tau_e = C_e / \gamma$, and the lattice heating time $\tau_i = C_i / \gamma$. The values for τ_e and τ_i are 1 ps and 0.01-1 ns. There are three different regimes of interactions, where the laser pulse duration is shorter than τ_e, longer than τ_i or in between the two values. If the laser pulse duration τ_L is much longer than the lattice heating time, thermalization between the electron subsystem and the lattice takes place during

the laser pulse. Hence, common temperature $T=T_e=T_i$ is sufficient to characterize the system. Then equations (1.42) and (1.43) become equation (1.40).

Picosecond laser pulses can be represented by the condition $\tau_e << \tau_L << \tau_i$. For times $\tau >> \tau_e$, equation (1.42) becomes quasistationary, which implies that the energy loss due to heat transport and energy exchange with the lattice is compensated by the energy deposited due to the laser radiation. Also, $\partial T_e / \partial t = 0$ simplifies equation (1.42) further. For times $\tau >> \tau_i$, due to quasistationary character of the electron temperature, the lattice temperature will exponentially approach the electron temperature as follows.

$$T_i = T_e\left(1-\exp\left(-t/\tau_i\right)\right) = tT_e/\tau_i \tag{1.45}$$

The lattice temperature remains lower than the electron temperature during the pulse duration in picosecond regime. Hence, the equilibrium is obtained only after the pulse is gone. For femtosecond pulses, the pulse durations much shorter than the electron cooling time ($\tau_L << \tau_e$), results in negligible coupling between the electrons and the lattice for times $t << \tau_e$. In this case, the differential equation (1.42) can be easily solved, as it is identical with the parabolic heat eqn. (1.40). Now, the heat diffusion length becomes $l_{th} = \sqrt{D\tau_e} << \alpha^{-1}$ that is optical penetration depth. The electron heat capacity which can be written in terms of Fermi temparature when electron temparature remains smaller than the Fermi temperature ($T_F=E_F/k_B$ where E_F is the Fermi energy, k_B is Boltzmann constant, and T_F is the Fermi temperature) [70, 78-81]

$$C_e = C_e^1 T_e = \frac{\pi^2 n_e k_B^2 T_e}{2E_F} \tag{1.46}$$

where n_e is the electron density.

Within these approximations, equation (1.42) can be simplified further to (at the end of the laser pulse)

$$T_e(\tau_L) = \sqrt{\frac{2F_a \alpha e^{-\alpha z}}{C_e^1}} \tag{1.47}$$

Where $F_a = I_0 A\, \tau_L$ (I_0A is the absorbed intensity).

After the laser pulse the electrons are rapidly cooled due to the energy transfer to the lattice and as the cooling time is very short, equation (1.43) can be approximated using equation (1.45) as

$$T_i = \frac{t}{\tau_i} T_e(\tau_L) \tag{1.48}$$

The average cooling time of the electrons is given by $\tau_e^a = C_e^1 T_e(\tau_L)/2\gamma$

Now, the lattice temparature becomes

$$T_i = T_e^2(\tau_i)\frac{C_e^1}{2C_i} = \frac{F_a \alpha}{C_i}\exp(-\alpha z) = \frac{F_a}{C_i l_{th}}\exp(-z/l_{th}) \tag{1.49}$$

1.7 Material Ablation

Konig et al. have revealed that ultrashort laser pulse ablation is a process with emission of particles up to several hundred nanoseconds after the laser pulse is at least two steps [82]. Initially surface layer of the order of optical penetration depth is ablated by the following processes of electron emission, sublimation, and transition to the plasma state on a nanosecond time scale. The heat remaining diffuses into the surroundings and again leads to the emission of particles up to 10 ns by thermal boiling process. In order to obtain a significant ablation, the energy of the lattice $C_i T_i$ per unit volume has to exceed the threshold value. Let ρ be the density and Ω is the specific heat of evaporation per unit mass. Then the heat of evaporation is $\rho\Omega$. The condition for significant ablation is $C_i T_i \geq \rho\Omega$. Substituting the condition into equation (1.49), we have

$$F_a \geq \frac{\rho\Omega}{\alpha}\exp(\alpha z) \tag{1.50}$$

If the heat diffusion length for electrons is longer than optical penetration depth $l_{th} = \sqrt{D\tau_e} >> \alpha^{-1}$, then equation (1.50) is changed to

$$F_a \geq \rho\Omega\, l_{th}\exp(z/l_{th}) \tag{1.51}$$

Hence, the corresponding thresholds for the absorbed laser fluences are $F_{th} \sim \frac{\rho\Omega}{\alpha}$ and $\rho\Omega l_{th}$.

The ablation depths now can be derived from equations (1.50) and (1.51) as follows:

$$L=\alpha^{-1} \ln(F_a/F_{th}) \quad \text{as } \alpha^{-1}>l_{th} \text{ and } F_{th}=\frac{\rho\Omega}{\alpha} \tag{1.52}$$

$$L=l_{th} \ln(F_a/F_{th}) \quad \text{as } \alpha^{-1}<l_{th} \text{ and } F_{th}=\rho\Omega l_{th} \tag{1.53}$$

In the regime of lower fluences typically at much lower damage thresholds, there is no burr formation due to negligible heat affected zones. However, the absorption of laser radiation at higher fluences results in the creation of a dense, high-temperature plasma where the material is removed in plasma, liquid and vapor phases leading to heat penetration deep into the target. The expansion of plasma and vaporization process creates a strong recoil pressure which expels the molten material leading to the formation of droplets and debris on the target surface. Expelled liquid material, which re-solidifies at the edges of the hole results in the formation of burr. The high ablation pressure resulted due to higher fluences leads to strong mechanical deformations and cracks in the surrounding material [83].

1.8 Different Kinds of structural changes

In case of laser micromachining inside the transparent sample, the nonlinear absorption takes place at the focus owing to the high intensities and hence structural changes can occur at the focus without affecting the surface of the material as explained earlier. Thus, one can fabricate three dimensional structures by translating the sample in different directions across the laser focus. Three different structural changes have been reported in the literature so far and they are isotropic refractive index change, birefringent refractive index change, and void. These three phenomena are explained in figure 1 already. An isotropic refractive index change occurs due to localized melting and rapid resolidification reported [84-88]. In case of fused silica, isotropic refractive index changes are reported for the threshold energy values ranging from 40-150 nJ with 100-fs, 800-nm pulses with NA>0.65. It is found in case of fused silica that the density increases when the glass is quenched from high temperatures [89-90] that results in higher

refractive index in the modified regions [91-93]. This finds applications in waveguide devices [11-27, 84-93].

The birefringent refractive index changes occur by periodic nanometer-scale stripes with varying material composition and thereby density is formed in the irradiated volume [94]. These nano-gratings form as a result of interference phenomena that lead to periodic modulations in the electron plasma density. In experiments with fused silica, birefringent refractive index changes are observed for energies typically in the range of 150-500 nJ. Several reports on birefringent refractive index changes in the literature are in [94-96].

The voids are formed at still higher energies typically >500 nJ and have been attributed to an explosive expansion of material out of the focal volume and into the surrounding material, termed as "microexplosion" [65, 97-98]. This expansion occurs within the bulk of the material, the microexplosion leaves a less dense or hollow core (the void) surrounded by a densified shell of material [99-100]. Femtosecond laser irradiation of transparent samples also lead to other processes such as color center formation and migration of components in the glass [17, 101-102].

1.9 Role of focusing, aberrations, pulse duration and dispersion

a) Self- focusing

Intensity depends on the spot size of the laser beam as it is defined as the power within an area. In micromachining experiments lenses and microscope objectives are used to focus the laser beam down to spot sizes that ensure the intensities above the damage threshold. Self-focusing is one of the main phenomena that takes place and is defined as a process by which spatial variation in intensity across a laser beam leads to spatial variation in the refractive index through the nonlinear Kerr index $n=n_0+n_2I$, which acts as a lens and causes the beam to focus itself [103-105]. The coefficient n_2 is usually positive, leading to an increase of the refractive index in the presence of intense radiation. Assuming monochromatic incident laser beam with a Gaussian-beam intensity profile given by:

$I(r,t)=I_0 \exp\left(\frac{-2r^2}{\omega_0^2}\right)$, implying $n=n_0+n_2 I_0 \exp\left(\frac{-2r^2}{\omega_0^2}\right)$, can be expanded into infinite series;

Considering only first order term of the infinite series, the intensity of the beam, at the center of the beam is given by $\approx n_0 + n_2 I_0 (1-\frac{2r^2}{\omega_0^2})$

In such scenario the phase delay relative to the radial coordinate of the wavefront is given by

$$\varphi(r) = nk_0L = n_0k_0L - n_2k_0LI_0(\frac{2r^2}{\omega_0^2})$$

$$\Rightarrow \varphi(r) \approx const. - 2n_2k_0LI_0(\frac{r^2}{\omega_0^2})$$

which is very similar to that of a lens is involved, with the difference that here the effect is cumulative and can lead, in the absence of other saturating effects, to a catastrophic collapse of the beam on itself. This effect is represented in a diagrammatic way in figure 4. This would result in unwanted damage to the material while micromachining the structures. In order to avoid this problem, one can choose peak powers below that for self focusing and maintain the intensity more than the damage threshold of the material. This can be achieved by using high NA focusing lenses.

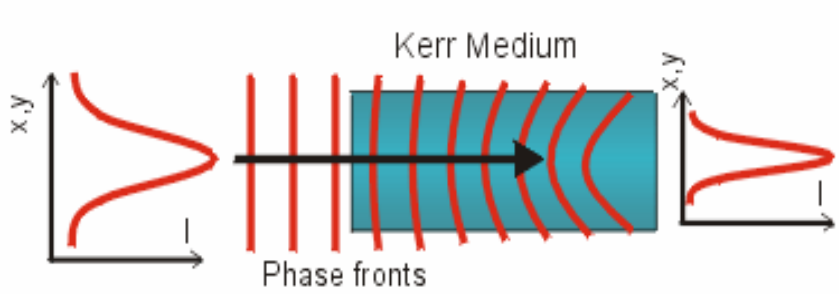

Figure 4. Distortion of the wave front of laser beam leading to self-focusing in a nonlinear medium for $n_2 > 0$

b) Aberrations

Aberrations arise as distortions to the laser beam at or near the focus and result of the focusing process. There are two types of aberrations namely spherical and chromatic. Chromatic aberration arises due to the fact that different colors of light (wavelengths) focus at different points and hence there is a distortion. Blue more refraction. If the bandwidth of the laser is narrow enough, chromatic aberrations can be neglected. Figure (5) depicts the chromatic aberration. The complex lens systems are often corrected for aberrations when used with a glass cover slip of a specific thickness. The change in the focus affects the threshold energy above which modification occurs. Spherical aberration is an optical effect that occurs due to the increased refraction of light rays when they strike a lens or a reflection of light rays when they strike a mirror near its edge, in comparison with those that strike nearer the centre.

Figure (6) shows spherical aberration due a lens. Rays that strike near the periphery of the lens, focus at B while rays that strike near the center of the lens (optic axis) refract more and focus at A. This leads to the spherical aberration. It signifies a deviation of the device from the norm, i.e., it results in an imperfection of the produced image. Higher NA objectives cause more spherical aberration compared with lower NA objectives. For surface micromachining, focusing should be aberration free to achieve the finest feature size.

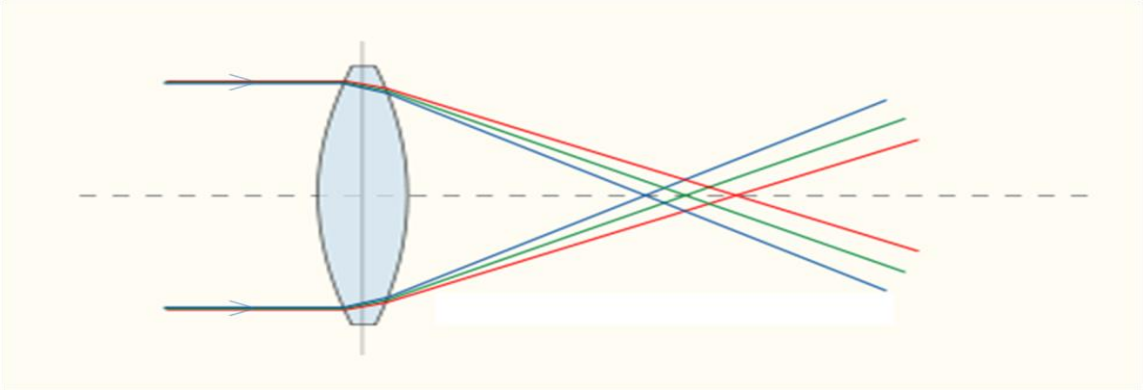

Figure 5. Chromatic aberration

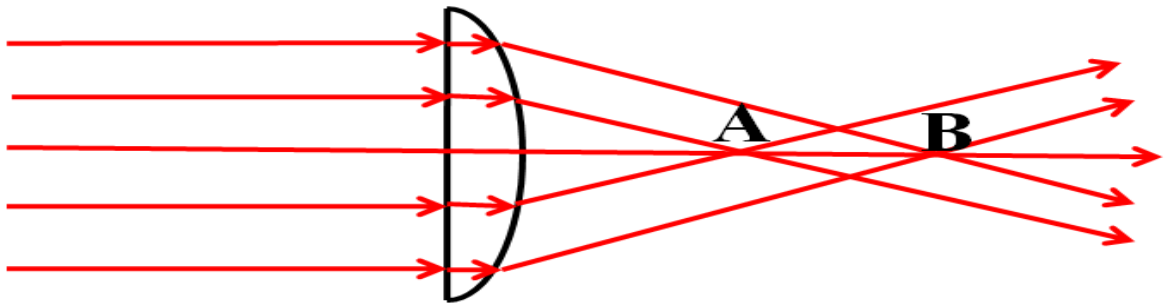

Figure 6. Spherical aberration

c) Pulse duration and dispersion

The laser intensity is equal to the pulse energy divided by the pulse duration and the area of the focal spot. Pulse duration is limited by the spectral width of the laser pulse. Since, different frequencies of light travel with different speeds inside a material, dispersion is caused. Dispersion increases the pulse duration as it separates the frequency components. Since pulse duration is increased which effectively reduces the intensity at the focus, it may not damage the material as intensity is below the required damage threshold. Figure 7 shows pulse broadening due to dispersion in the medium.

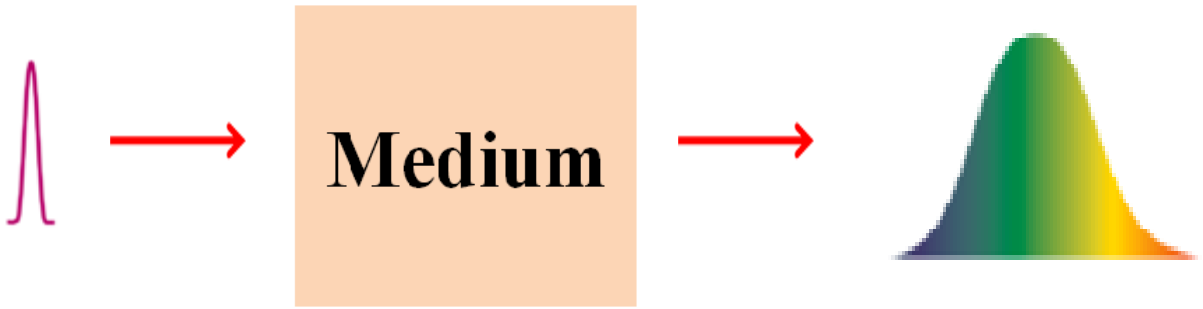

Figure 7. Dispersion in a pulse which causes broadening.

Chapter 2

Abstract

In this chapter, the details of various experiments carried out in this dissertation are explained. The femtosecond laser setup [MaiTai Oscillator+Spitfire] used to fabricate microstructures is explained. Newport stages, USA which was purchased and arranged three dimensionally is explained with its controller. We also describe very briefly all the other experimental techniques that have been utilized in the present study (Confocal microscope, Confocal micro-Raman spectroscopy, Absorption, fluorescence, and electron spin resonance spectroscopy techniques, Field emission scanning electron microscope (FESEM) with energy dispersive x-ray absorption spectroscopy (EDXAS) attachment, and Transmission Electron Microscope (TEM)).

2.1 Fs Oscillator [Mai-Tai^{TM} System]

The femtosecond (fs) oscillator used was *Mai Tai* which comprises of two lasers [106]: a continuous wave (cw) diode-pumped laser and a mode-locked Ti: Sapphire pulsed laser. The laser head has two chambers, a cw pump chamber and a pulsed output chamber. The cw pump chamber contains a diode-pumped, intracavity, frequency doubled, solid-state Nd: YVO_4 laser giving 532 nm laser output. As Ti: Sapphire's broad absorption band is in the blue and green, the 532 nm output of the cw laser is an ideal pump source for the Ti: Sapphire laser. The fluorescence band of Ti: Sapphire medium extends from 600 nm to wavelength greater than 1000 nm making it possible for wide broadband tunable laser. The mode locking is achieved by an acousto-optic modulator (AOM) to ensure reliable mode-locked operation when the laser starts up and provides smooth wavelength tunings. It also allows the laser to operate for extended periods without dropouts or shut-downs associated with pure Kerr-lens mode locking. The fs pulse laser can be wavelength tuned using a prism sequence and a slit where the prism sequence provides a region in the cavity and the wavelengths are spatially spread. The slit is placed in the dispersed beam and by changing the position of the slit in the dispersed beam; the output wavelength can be tuned.

The three factors that influence the pulse-width tunings characteristics of a Ti: Sapphire laser are generally influenced by three factors: (1) those inherent in the Ti: Sapphire material itself, (2) those from cavity parameters, and (3) the wavelength selection. By modifying the net group velocity dispersion (GVD) of the cavity, we can modify the pulse width. Temporal pulse spreading is caused due to the optical components present in the laser cavity that lead to positive GVD. Further pulse spreading is caused by self-phase modulation (SPM) in the Ti: Sapphire rod, which results from the interaction of the short optical pulse with the nonlinear refractive index. To obtain stable, short optical pulses, one needs to compensate these effects. Since, the positive GVD in the cavity changes with wavelength, the amount of compensating negative GVD must be varied with wavelength. In *Mai Tai* prism pairs are used to produce a net variable negative GVD in the cavity and are fully automated and results in an optimized pulse at any chosen wavelength. *Mai Tai* delivers a ~ 80 fs, 82 MHz pulse train with pulse energy of 1 nJ. The output spectrum with its peak at 800 nm is as shown in figure 1.

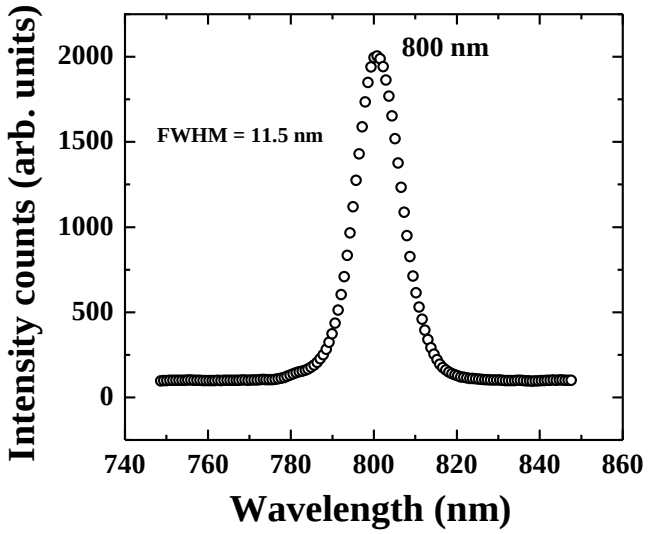

Figure 1. Mai Tai output spectrum

2.2 Fs amplifier [Spitfire]

Since the oscillator delivers low energy pulses of the order of nJ, S*pitfire* unit is used to amplify the energy without introducing much temporal broadening [106]. *Spitfire* is a regenerative amplifier system that employs the conventional chirped pulse amplification (CPA) technique. The general principle of regenerative amplification is as follows [107]: (a)Trap seed pulse in optical resonator, (b) Multi-pass pulse through the active medium (Ti:Sapphire rod) until amplified to desired energy level, and (c) Switch pulse out. Since, such short high energy pulses are always risk of laser induced damage of optics used for the amplification and other effects like self-focusing as explained in earlier chapter. To overcome this difficulty *Spitfire* employs Chirped Pulse Amplification (CPA) technique. The general principle of CPA is as follows: (a) pass the fs seed pulses from the output of the oscillator through a stretching mechanism that broadens the pulse to an order to 10^3 by introducing chirp using a grating (in most cases); (b) amplify the temporally broadened pulse; and (c) recompress the amplified pulse to its original pulse-width by pass it though a pulse compressor mechanism. Figure 2 shows the figurative explanation of the CPA technique used in *Spitfire.* Figure 3 shows a block diagram of Ti: Sapphire laser used in our experimental setup.

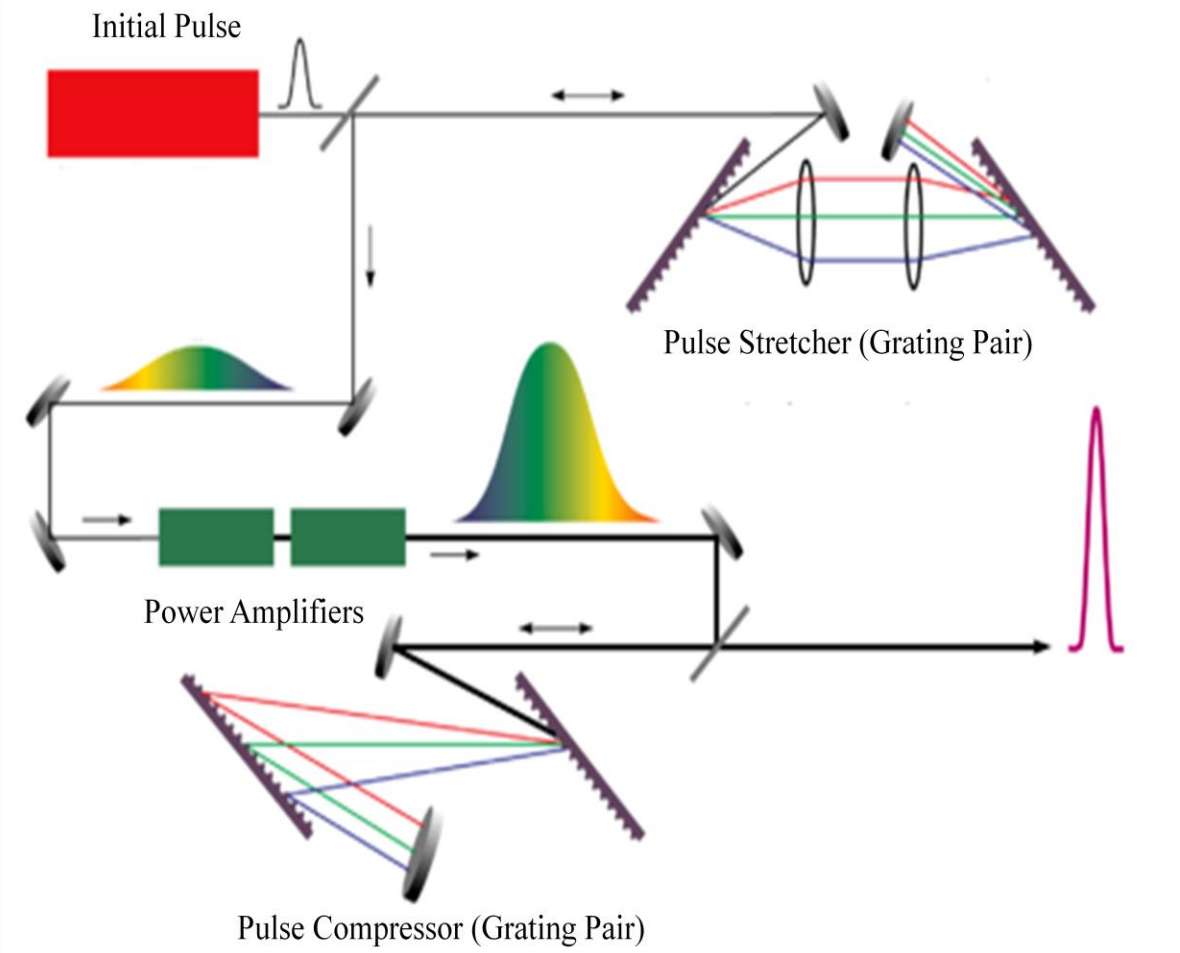

Figure 2. CPA technique basic principle

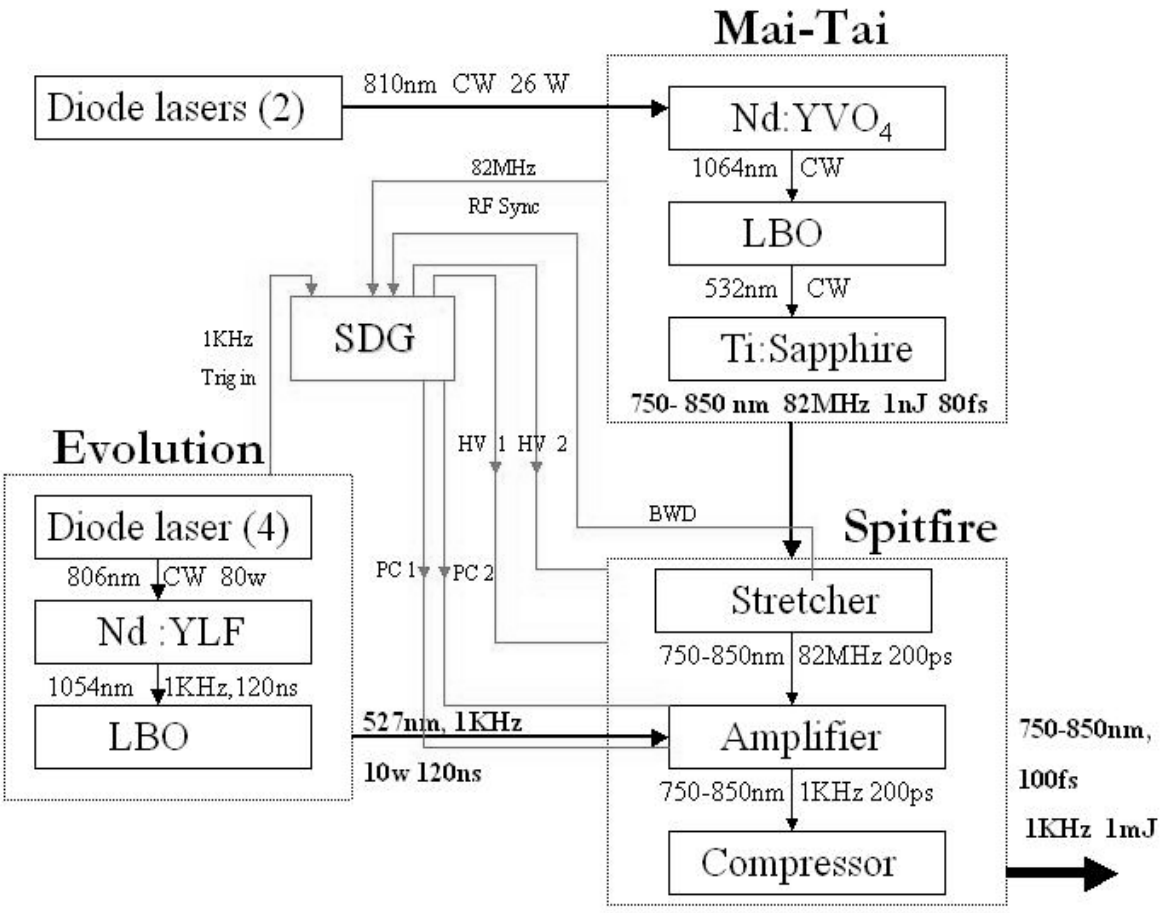

Figure 3. Complete fs laser setup

As shown in figure 3, the regenerative amplifier consisting of a Ti: Sapphire rod is pumped by the output of *Evolution* which is a 120 ns, 1 kHz rep. rate Nd: YLF laser delivering high power laser pulses of 532 nm. The amplification of the seed pulse from *Mai Tai* is obtained as follows:

1. The seed pulse from *Mai Tai* having a pulse-width of ~80 fs is stretched using a combination of grating and mirror to about 200 ps as shown in the top half of the figure 3.
2. The temporally stretched pulse is then made to oscillate in the regenerative cavity pumped by the laser pulses of *Evolution* laser head to attain maximum desired energy amplification. The entry and the exit of the seed pulse is achieved by the use of two high-voltage Pockel cells whose delay is adjustable by a Signal Delay generator (SDG) as shown in figure 3.

The amplified seed pulse exited from the regenerative cavity is then compressed following the reverse mechanism of stretching procedure to obtain amplified pulses of ~100 fs of a maximum of 1mJ average energy at a repetition rate of 1kHz.. The output of *Spitfire* is of 9

mm diameter with a spectral bandwidth of 9.4 nm at the peak wavelength operation at 800 nm as shown in figure 4. Table 1 summarizes the general and most important characteristics of the fs laser system used throughout the present studies in this thesis.

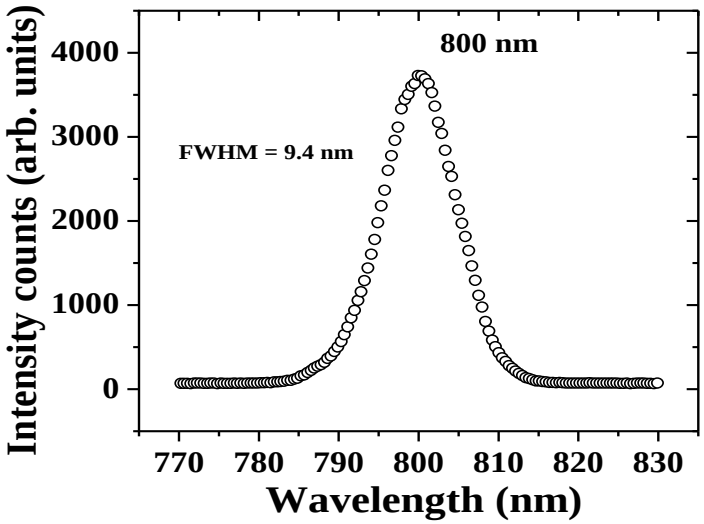

Figure 4. *Spitfire* output spectrum

Table 1. Summary of laser output characteristics of fs laser system used [105].

Particulars	***Mai Tai***	***Spitfire***
Pulse-width	~82 fs	~100 fs
Max output energy	1 nJ	1 mJ
Rep. rate	80 MHz	1kHz
Beam diameter	3 mm	9 mm
Polarization	Horizontal	horizontal

2.3 The autocorrelation technique

For measuring optical pulses of ps and fs order, an autocorrelator is the most common set-up used [107]. Here, an incoming optical pulse is split into two pulses of equal intensity using a beam splitter. An adjustable optical delay is imparted to one of the paths. The two beams are then again recombined within a nonlinear crystal for second harmonic generation (SHG). The efficiency of the SHG resulting from the interaction of the two beams is proportional to the degree of spatial and temporal pulse overlap within the crystal. One can monitor the intensity of SHG as a function of delay between the two pulses which produces the autocorrelation function that is directly related to pulse width. There are two types of autocorrelation configurations which are mentioned here. The first one is known as interferometric collinear autocorrelation as shown in figure 5(a). Here, the two beams are again made to recombine in a collinear fashion. This configuration results in an autocorrelation signal as the SH generated by each beam independently is added to the autocorrelation signal. In the second method, the beams are displaced from a common optical axis and then recombined in a noncollinear fashion as shown in figure 5(b). In this case, the background is eliminated because the SHG from the individual beams is separated spatially from the autocorrelation signal. This configuration is called "background-free" configuration. It is employed in the pulse-diagnostics of the amplified fs pulses from *Spitfire* used for all the experiments presented in this thesis. In the next section the details of the autocorrelation in the non-collinear geometry are explained.

A pair of mirrors as shown in figure 5 (b) are used as retro. While performing the retro-reflection in longer-pulse regime, retro-prisms are employed. But in the case of fs pulse regime, the retro-prisms are replaced by a pair of mirrors as shown in the figure 5 (b) to overcome dispersion-effects created within the fs pulses owing to the propagation in the prism-material medium that leads to temporal broadening of the pulses. The incoming beam is first split into two arms and passed through the retro-reflecting arrangement such that the two separated beams follow a parallel path before focusing into a 1mm Beta Barium Borate (BBO) crystal that is used for SHG. The retro-reflector on the delay stage can be moved with a resolution of 6 μm which corresponds to a minimum temporal resolution of ~ 20 fs. The autocorrelation signal that is generated as a resultant of temporal and spatial overlap of the two input beams is made to fall into a fast photodiode (FND100) after passing though a SHG filter to cut-off the residual input

pulses. To ensure that the photodiode does not get damaged, different neutral density filters are used for attenuation. The photodiode output is fed to a lock-in amplifier (SRS 830) and is recorded. The averaged signal is then sent to an interfaced ADC card and then to a computer. The autocorrelation signal trace is thus obtained as a function of delay obtained by translation of the stage.

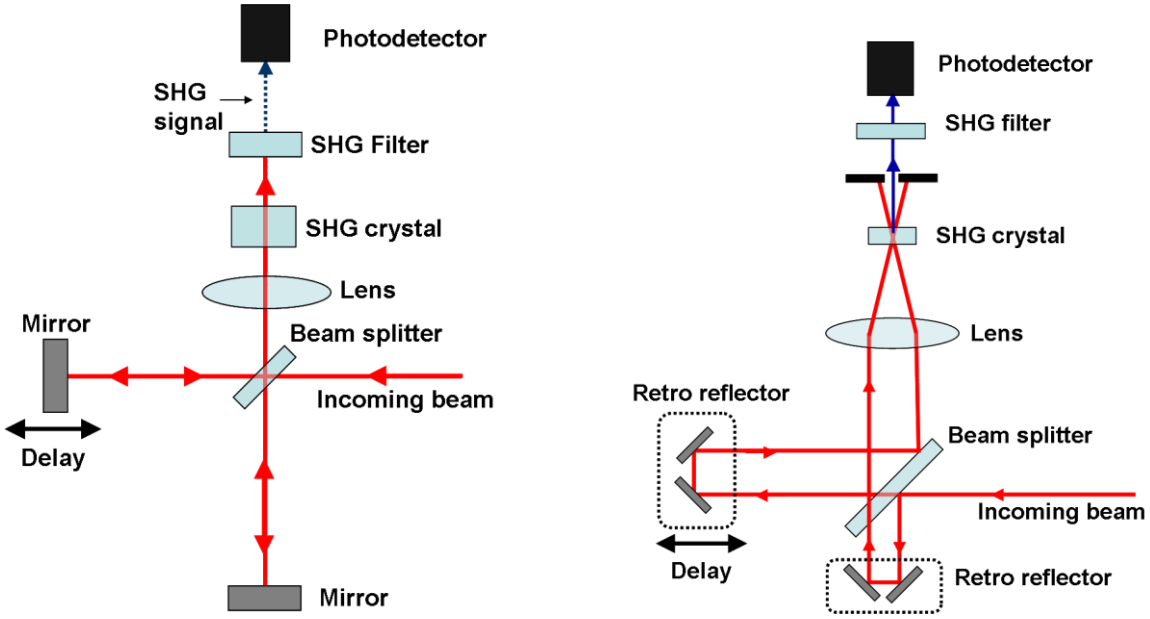

(a) collinear autocorrelation (b) Non-collinear autocorrelation

Figure 5. Interferometer autocorrelation set-up

To determine the actual pulse width from the obtained experimental autocorrelation data, it is necessary to know the pulse shape. Table 2 shows the relationship between the FWHM of the intensity envelope of the pulse (τ_p) and the FWHM of autocorrelation function of the pulse (τ_{ac}), for several pulse shapes. Figure 6 shows the autocorrelation signal from spitfire.

Table 2. Second-order autocorrelation functions and time-bandwidth products for various pulse shape models

Function	$I(\tau)$	$\frac{\tau_p}{\tau_{ac}}$	$\tau_p \Delta\upsilon$
Gaussian	$I(\tau)=\frac{\exp\left[-(4\ln 2)\tau^2\right]}{\tau_p^2}$	0.707	0.44
Hyperbolic Secant	$I(\tau)=\sec h^2\frac{(1.76\tau)}{\Delta\tau_p}$	0.648	0.315
Lorentzian	$I(\tau)=\frac{1}{1+\left(4\tau^2/\Delta\tau_p^2\right)}$	0.5	0.221

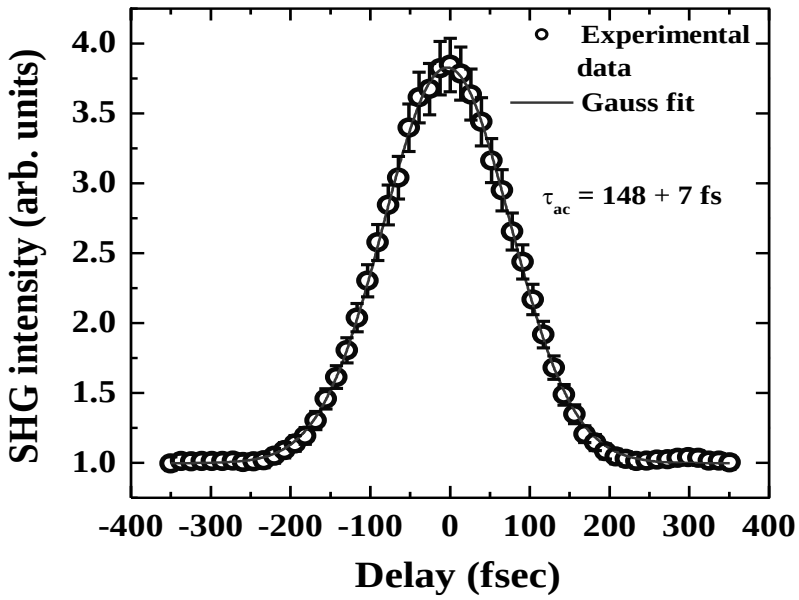

Figure 6. Autocorrelation trace obtained for the *Spitfire* amplified pulses fitted with Gaussian pulse shape

By taking Gaussian fit into account for the experimental autocorrelation signal, we obtained the FWHM, τ_{ac}, to be (148 ± 7) fs. From table 2, we have the relation for Gaussian pulse:

$$\frac{\tau_p}{\tau_{ac}} = 0.707 \quad \Rightarrow \quad \tau_p = 0.707\tau_{ac} \quad \Rightarrow \quad \tau_p = (104 \pm 7)$$

Thus the pulse-width obtained from the second-order intensity correlation is (104 ± 7) fs. Since the FWHM of the spectral envelope of *Spitfire* as shown in the previous section is $\Delta\lambda \sim 9.4$ nm with its peak at $\lambda_0 = 800$ nm.

$$\therefore \quad \tau_p \Delta\upsilon = \tau_p \frac{c\Delta\lambda}{\lambda_0^2} = 0.458.$$

Thus we have *nearly-transformed limited* pulses assuming Gaussian pulse shape.

2.4 Calculating pulse broadening due to Group Velocity Dispersion.

When optical pulses propagate through optical materials, they get temporarily broadened due to the group-velocity dispersion (GVD) since different frequency components travel with different velocities. Thus it is essential to calculate the broadening. B (broadening) is defined as the ratio defined as the ratio of the output pulse-width to the input pulse-width (in terms of fs) i.e.,

$$B = \tau_{out} \Big/ \tau_{in} \Rightarrow \tau_{out} = B \times \tau_{in}$$

For a transform-limited Gaussian pulse: $B = \left\{1 + \left[7.68\left(k_2 \times L \Big/ \tau_{in}^2\right)^2\right]\right\}^{\frac{1}{2}}$, where k_2 (in terms of fs^2/cm) is the second order dispersion coefficient. Table 3 gives the values of k_2 for different standard materials at 800 nm.

Table 3. Dispersion values of different materials at 800 nm.

Material	k_2 **(fs^2/cm)**
Fused silica	300
BK-7 glass	450
Ti: Sapphire	580
KDP crystal	25 (o – ray); 38 (e – ray)
SF-10	1590

2.5 Microfabrication setup

In this thesis, all microfabrication experiments are carried out using three nanopositioner stages capable of 15 nm resolution supplied by Newport, USA. The block diagram of typical experimental setup of the microfabrication is shown in figure 7.

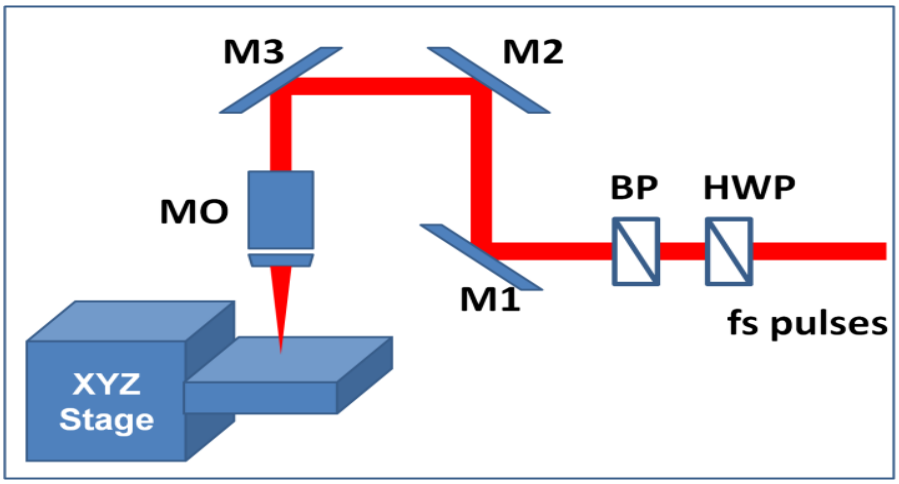

Figure 7. Block diagram of microfabrication experimental setup.

As shown in figure 7, fs laser pulses are made to pass through half-wave plate and polarizer (HWP,BP) combination so that one can vary the energy. The direction of propagation of these pulses is changed to vertical by the use of three mirrors (M1, M2, and M3). MO is the

microscope objective which is used to focus the laser pulses onto 3 dimensionally arranged XYZ nanopositioner stages. By moving these stages, one can obtain microstructures of interest. The experimental microfabrication setup which was used throughout the thesis is shown in figure 8.

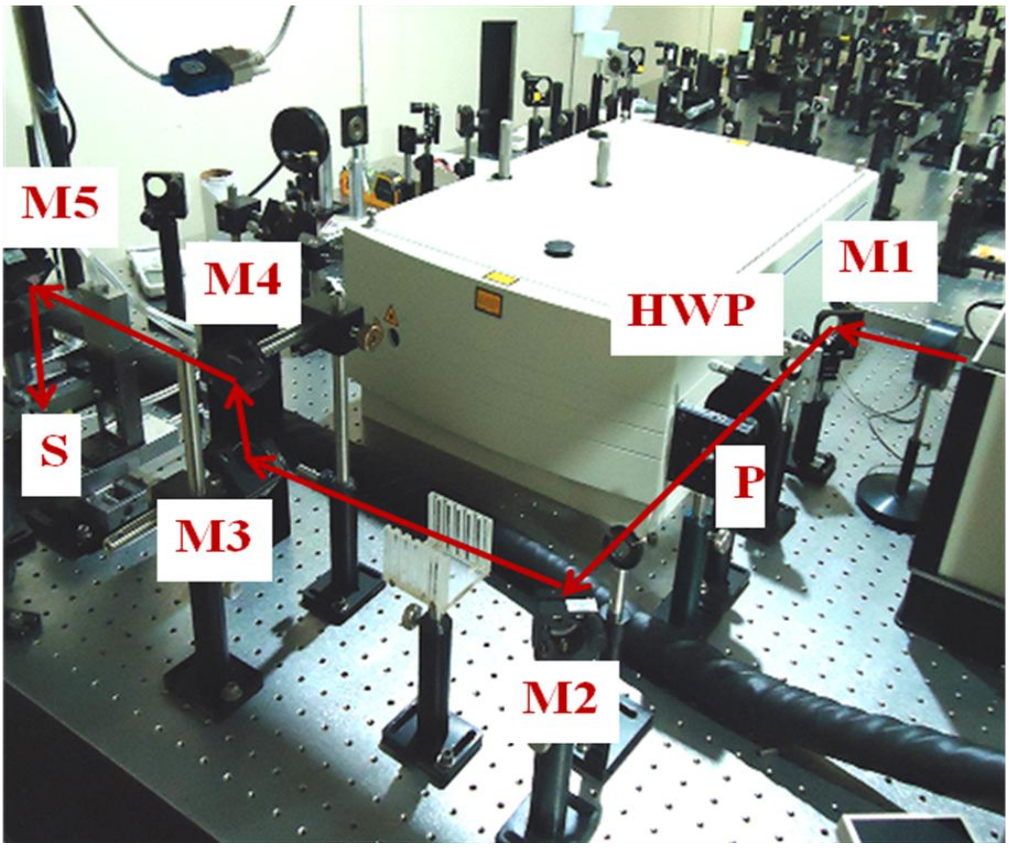

Figure 8. Experimental setup for microfabrication

As shown in figure 8, the laser pulses with 800 nm wavelength, 100 fs pulse width with 1 KHz repetition rate (after amplification from *Spitfire*) are made to pass through half wave plate (HWP) and polarizer (P) so that energy can be varied using this combination. Apertures are introduced in middle to align the beam. M1-M5 are the mirrors used to make the beam fall vertically onto the three dimensionally arranged Newport stages (S) as shown in the figure. Figure 9 shows the controller through which one can control the stages manually and through interface with computer or laptop [108].

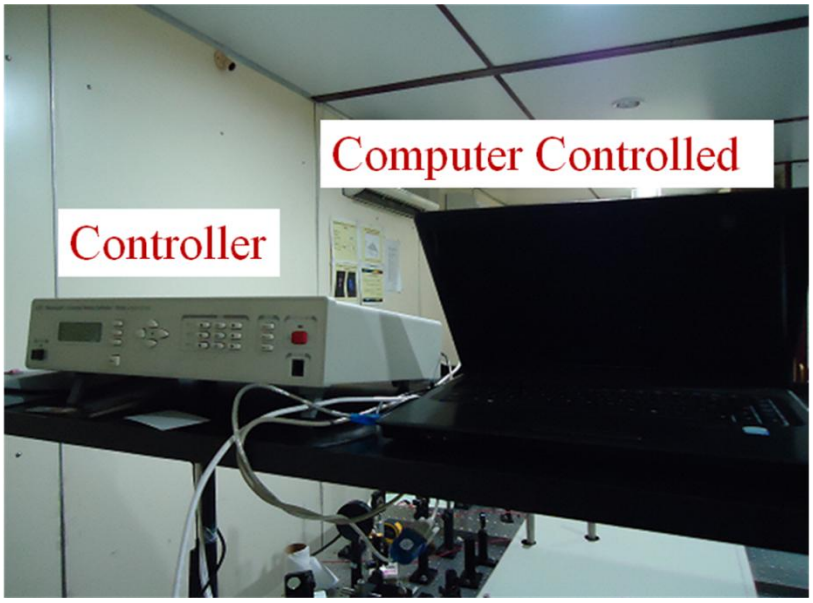

Figure 9. ESP 300 controller/Driver (Newport, USA)

2.6 Features of ESP 300 controller/Driver

There are three modes of operation to use the stages [108].

1) Local mode – stand-alone operation, executing motion from the front panel
2) Remote mode – executing commands received over one of the computer interfaces or the optional handheld keypad
3) Program execution mode – execution of a stored program.

Three home buttons are used to move X, Y and Z stages to respective starting positions. These three stages can be moved to 25 mm distance. The three stages (Axes) are connected to the rear panel of the controller. Also, RS-232 socket is provided to the rear panel of the controller so that one can transfer stored programs and commands through computer or laptop connected to RS232 socket of the rear panel using RS232-USB converter.

2.7 Confocal Microscope

In this thesis, confocal microscope is used to collect the images of microstructures fabricated. Confocal laser scanning microscopy (CLSM or LSCM) is a technique for obtaining high-resolution optical images with depth selectivity. The key feature of confocal microscopy is its ability to acquire in-focus images from selected depths. This process is called optical sectioning.

Images are acquired point-by-point and reconstructed with a computer, allowing three-dimensional reconstructions of topologically complex objects. For opaque specimens, this is useful for only surface imaging and for transparent samples, interior structures can be imaged. In ordinary conventional microscopy, the quality of image is blurred because the image information from multiple depths is superimposed. A conventional microscope collects all the light that can penetrate into the sample. However, these problems do not arise in case of confocal microscope. Confocal microscope images one depth level at a time with a controlled and highly limited depth of focus. Confocal microscopy relies on the principles of fluorescence microscopy.

In Fluorescence microscopy, reflected light gives much better results, so almost all fluorescence microscopes take this configuration. Figure 10 (a) shows the configuration of conventional fluorescence microscope. The light from source (1) passes through neutral density filter, aperture, and field stop (2, 3, and 4) to reach the excitation filter (5). After filtering away the unwanted wavelength, excitation light goes further and reaches a special and important filter called beam splitter (6), BSP. The excitation light selected by BSP is reflected to the specimen via objective (7) and excites fluorophores within the specimen (8). The fluorescence emission from the specimen comes back through the same path to BSP again. This time, the light should not be reflected away but passes through it and reaches emission filter (9). Being further filtered by emission filter, the emission light is either focused on the front focal plane of binocular or projected to infinite by tube lens in case of infinite corrected objectives(10). The final image is further magnified by binocular (11), or sent to a camera port, detected by devices coupled above the port: CCD camera or a photographic film camera. Filters 5, 6, 9 are usually installed together into a cube, called filter-set. It is the pivotal part of fluorescence microscope and will be discussed more in the following paragraph through figure 10 (b). As shown in figure 10 (b), arrow 1 represents the excitation light source of mixed wavelength. Filter A is the excitation filter, which is usually a band pass or long pass filter, allows light at certain wavelength range or wavelength longer than the cut-off value to go through. For a filter cube designed for simultaneous multiple fluorescence detecting, a long pass filter with cut-off value shorter than the shortest excitation has to be used. That leads more unwanted wavelength to specimen results in more nonspecific background fluorescence. Arrow 2 represents excitation light which passes through A and reaches the beam Splitter BSP. BSP reflects certain wavelengths away and permits other wavelengths to pass through. A multiple-bands reflecting filter or neutral

percentage splitter can be used for this role. Wavelength falling into the reflecting band or shorter than the cut-off value will be stopped and reflected to the specimen. The fluorescence light emitted from the specimen is illustrated as arrow 3. The emission is longer than excitation wavelength and cut-off value of the BSP, so the returned emission can go through the BSP towards emission filter C. Emission filter C is either a band pass filter or long pass filter, the cut-off value is longer than excitation wavelength so the residue of excitation light 2 is further prevented from reaching the image plane. Strict band pass results more specific but weaker signal, while long pass leads stronger signal but more background.

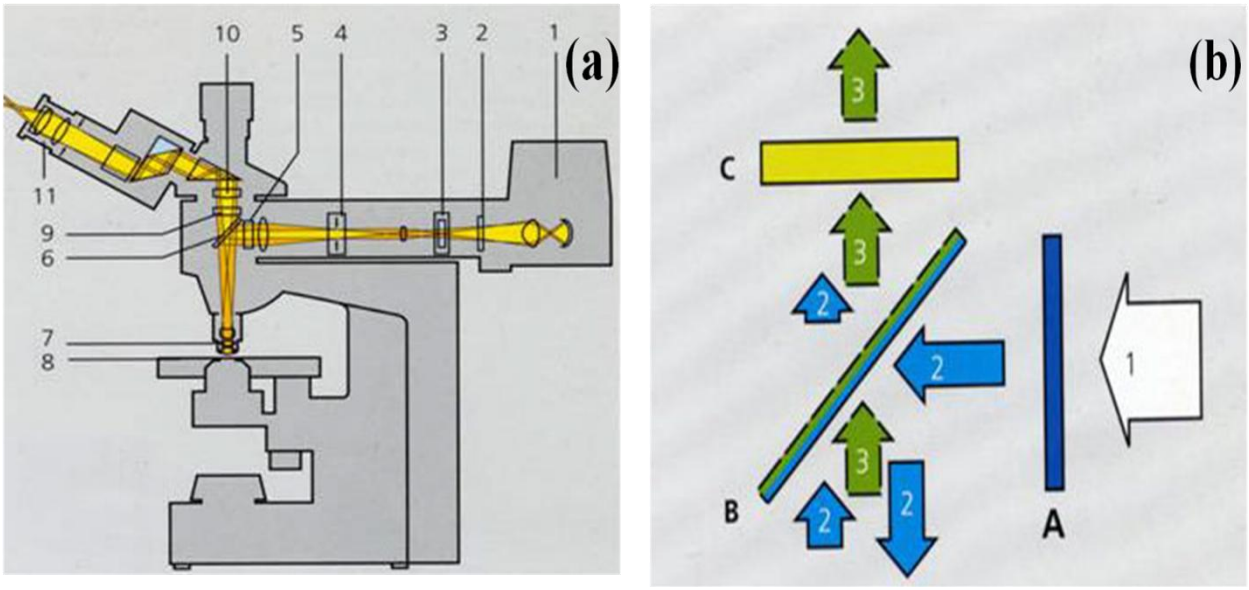

Figure 10. (a) A schematic diagram of conventional fluorescence microscope (b) Schematic representation of the role of filter set used.

In conventional wide field microscope, ordinary extended light is used as light source; the specimen is illuminated laterally and vertically at the same time. The resulting image is affected by all the illuminated spots, although it is centered at a given focal plane and local spot. These illuminated dots interfere with each other laterally and the stray light compromise image contrast. Image contrast, defined as the difference between the minimum and maximum intensity of two points in the image, is an important factor for an optical device to achieve its resolution, without proper contrast, the signal has little difference with background and the resolution of the

an optical lens cannot be realized. Improved contrast helps an optical device to reach its maximum resolution. If a point light source illumination is used, only one point in the specimen is illuminated at a time and the resulting image therefore is void of those lateral interference of dots as described in case of extended light illumination. The image from out-focal-planes overlaps on the focal plane, thus the image sharpness is compromised. To be worse, weak signals from a given plane of the specimen can be totally un-detectable because they are buried within the mixture. This is more dramatic in thick specimen where a sharp focus cannot be achieved at all. In another configuration, a plate with a small hole called pinhole is placed before the image detecting device. In this configuration, light from under-focal-plane will be focused at a plane behind the pinhole in such a way that it is blocked away by the pinhole plate. The light from above-focal-plane will be focused before the pinhole and is blocked away by the pinhole too. Only the light from focal plane is just focused at the pinhole thus can reach the image detector. This process simulates what is done with a microtome to cut some unwanted tissue away. This process is called "optical sectioning".

In practical, a point-like light source is achieved by using a laser light passing through an illumination pinhole. This point-like light source is directed to the specimen by a beam splitter (or AOBS in Leica's BSP-free system) to form a point-like illumination in the specimen. The point-illumination move or scan on the specimen by the help of a scanner. The reflected emission light from specimen's focal plane passes through the detecting pinhole and form point-like image on detector PMT (photon multiply tube). PMT converts detected photon into electron. These signals are amplified further by providing voltage to the tube. Thus the resulting electrons from photons form analogue current which is then digitized by analogue-digital converter (ADC) and pass to the digital image processor. Thus, the confocal microscope contains a point light source for illumination, a point light focus within the specimen, and a pinhole at the image detecting plane. Hence, Confocal affects result in supression of out-of-focal-plane light, supression of stray light in the final image. Figure 11 shows the configuration of confocal microscope with all essential components.

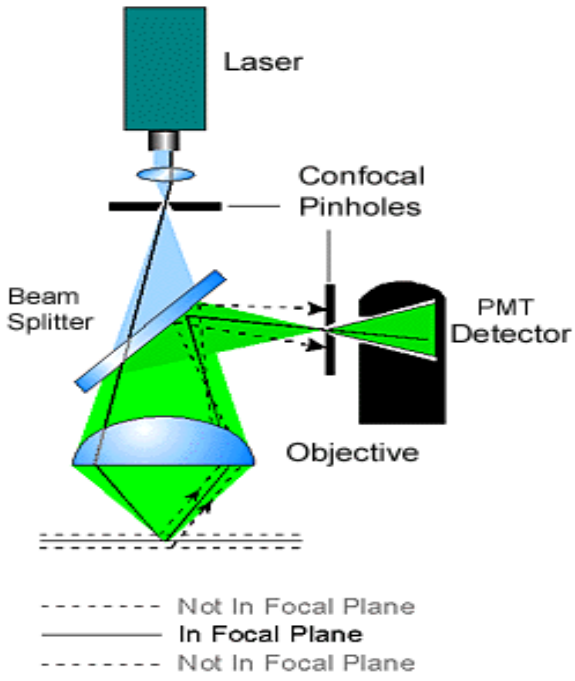

Figure 11. Confocal microscope configuration.

In the present dissertation, we have used laser scanning confocal microscope Leica Company with model TCSSP2AOBS as shown in figure 12. Three excitation laser sources are provided with tjis model. First one is Argon laser which supplies UV light for excitation ranging from 260-350 nm. This whole range is excited. The second excitation laser source is Argon Krypton

laser which supplies 458, 476, 488, 496, and 514 nm wavelengths. The third excitation laser source is He:Ne laser source which provides 543 and 633 nm wavelengths. The detectors used are photomultiplier tubes. It has both dry and wet microscope objectives for viewing. In this thesis, the usage of confocal microscope has two advantages.

a. Most of the structures fabricated in the polymers are buried. To image these structures with better resolution, we have used this microscope

b. The fs laser irradiated regions in polymers showed emission at excitation wavelengths of 458, 488, 514 nm wavelengths etc. We have used this confocal microscope to record the emission from these individual structures.

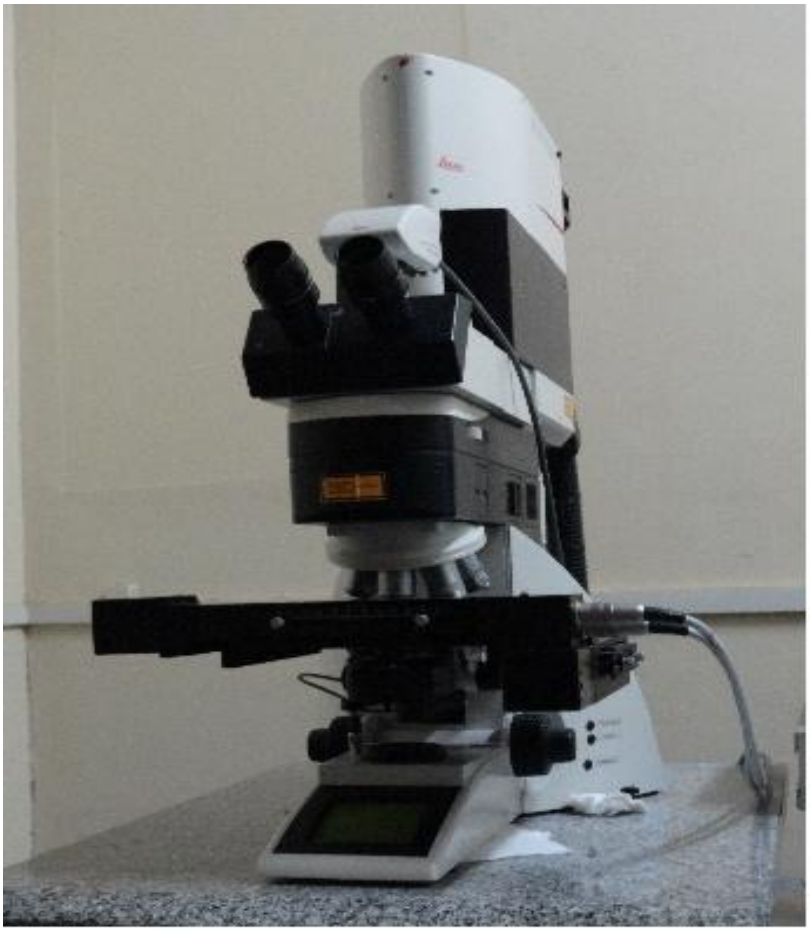

Figure 12. Leica TCSSP2AOBS laser scanning confocal microscope

2.8 Confocal Micro-Raman spectroscopy

Confocal micro-Raman spectroscopy relies on the same principle of confocal microscopy as discussed in the previous section. For an ideal microscope, each point of the specimen should be examined at a time and measure the amount of light scattered or absorbed at that point. This can be achieved by introducing a pinhole aperture in front of the light source as explained in earlier section. In this case the small pinhole aperture refocused by the microscope illuminates only a single point on sample. Thus, the first pinhole aperture greatly reduces scattered light and immensely improves the image quality and the second aperture eliminates any image degrading out-of-focus information, allows for controllable depth of field and gives the ability to collect series of optical sections from bulk specimens.

Using a spectrometer, it is possible to collect a signal from a single point on a sample, disperse it into a spectrum and detect the spectrum using a multi-channel detector such as CCD. The unique advantage of Raman spectroscopy is that it can be used to selectively excite a needed portion of the molecule by changing the excitation wavelength. Raman spectroscopy is also a convenient probe of the vibrational energy levels within a molecule which easily provides molecular fingerprints. Also it doesn't require any sample preparation, and samples are not destroyed. Water bands are usually small and easily subtracted and Raman spectra contain sharp bands that are characteristic of the specific molecular bonds in the sample. The intensity of the bands in a Raman spectrum is proportional to the concentration of the corresponding molecules and thus can be used for quantitative analysis. In the present work carried out, we investigated Raman peaks of polymers and crystals using HR 800 Horiba Jobin Yvon confocal micro-Raman spectrometer as shown in figure 13. It consists of three excitation laser sources. He:Ne laser which provides 632 nm wavelength, Argon ion laser which provides 514 nm, and diode laser which provides 785 nm wavelength. The detecting system is CCD. A notch filter is used in the HR 800 for the rejection of the exciting line. It is specific for one wavelength and it is changed when excitation wavelength source is changed. A silicon test sample which shows Raman characteristic spectrum at 520 cm^{-1} is provided to check for Raman signal before collecting any Raman signals for specimen. A joy stick is provided to position the sample exactly under the illumination spot. Also the sample holder is placed on a XY stage so that Raman mapping can be carried out for different samples.

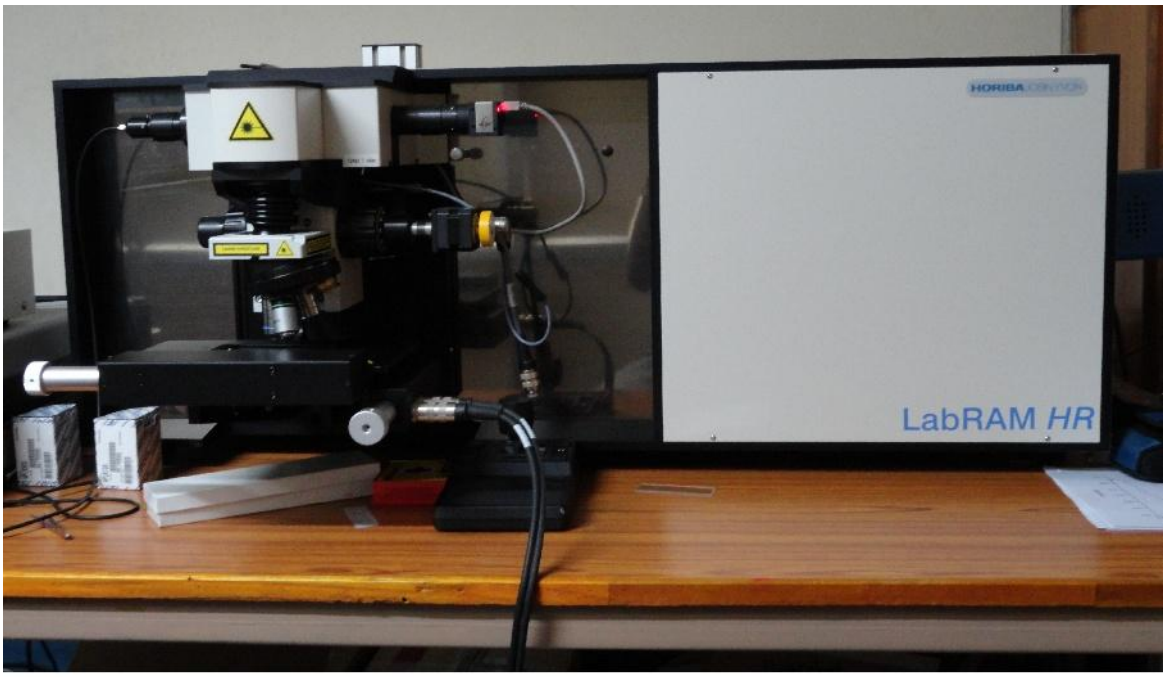

Figure 13. HR 800 Horiba Jobin Yvon confocal micro-Raman spectrometer

2.9 Absorption spectroscopy

Absorption spectroscopy is one of the spectroscopic techniques that measures the absorption of incident radiation, as a function of frequency or wavelength. The intensity of the absorption varies as a function of frequency, and this variation is called the absorption spectrum which is a plot of absorption versus wavelength of the light. Thus, a material's absorption spectrum is the fraction of incident radiation absorbed by the material over a range of frequencies Absorption spectroscopy is performed across the electromagnetic spectrum. The absorption spectrum arises by the atomic and molecular composition of the material. Radiation is more likely to be absorbed at frequencies that match the energy difference between two quantum mechanical states of the molecule. The absorption that occurs due to a transition between two states is referred to as an absorption line. The most common way of recording the absorption spectrum is to direct a light beam onto the sample and record the intensity of the transmitted light that passes through it. Thus, the transmitted energy can be used to calculate the absorption. The following illustrates the steps in recording the absorption spectrum.

First, the intensity of light (I_0) passing through a blank sample is measured as the intensity is the number of photons per second. The blank sample is a solution that is identical to the sample solution except that the blank sample does not contain the solute that absorbs light. If it is nanoparticles dissolved in water, water can be taken as blank sample. This measurement is necessary as the absorption cell itself scatters some portion of the light. Second, the intensity of light (I) passing through the sample solution is measured. Usually, instruments measure the power rather than the intensity of the light. The power is the energy per second, which is the product of the intensity (photons per second) and the energy per photon. Third, the experimental data is used to calculate two quantities: the transmittance (T) and the absorbance (A) as follows.

$$T = \frac{I}{I_0}$$

$$A = -\log_{10} T$$

The transmittance is simply the fraction of light in the original beam that passes through the sample and reaches the detector. The remainder of the light, 1 - T, is the fraction of the light absorbed by the sample. Figure 14 shows a typical schematic diagram of absorption spectrometer. A light source is used to illuminate the sample. Monochromator selects one wavelength at a time and the light of single wavelength now passes through reference arm and sample arm. The detectors used measure the power and the ration is taken which is fed to a computer. This gives us the amount of light transmitted.

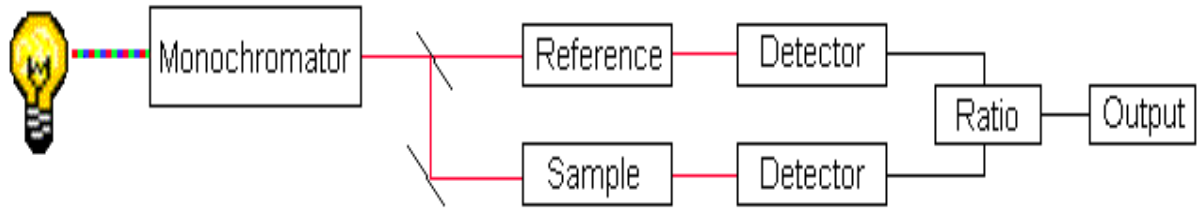

Figure 14. Schematic diagram of an absorption spectrometer.

In this dissertation, we used absorption spectrometer JASCO V-670. It provides wavelength range from 190 nm to 2.7 µm. Halogen lamp for visible to IR and Deuterium lamp for UV light

are provided for scanning the range. We used this spectrometer to record absorption and transmission of fs laser irradiated polymers and pristine polymers and to investigate silver nanoparticles for plasmon peaks.

2.10 Fluorescence spectroscopy

Fluorescence spectroscopy or fluorometry or spectrofluorometry, is a type of electromagnetic spectroscopy which analyzes fluorescence from a sample. It is a complementary technique to absorption spectroscopy, explained in earlier section. Molecules have various states referred to as energy levels. In fluorescence spectroscopy, the sample is first excited, by absorbing a photon, from its ground electronic state to one of the various vibrational states in the excited electronic state. Collisions with other molecules cause the excited molecule to lose vibrational energy until it reaches the lowest vibrational state of the excited electronic state. The molecule then drops down to one of the various vibrational levels of the ground electronic state by emitting a photon in the process. In a typical experiment, the different wavelengths of fluorescent light emitted by a sample are measured using a monochromator, holding the excitation light at a constant wavelength. This is called an emission or fluorescence spectrum. Also an excitation spectrum which is the opposite can be recorded, by keeping the emission light at a constant wavelength, and the excitation light is scanned through many different wavelengths (via a monochromator). Also fluorescence takes place from singlet states to singlet states. However, if there is a transition from triplet to singlet states which results in emission of photons having lower energies, this process is called phosphorescence. Usually transitions from singlet to triplet and vice versa are quantum mechanically forbidden.

In the present dissertation, we have used Fluorolog Horiba JOBIN YVON fluorescence spectrometer. We investigated emission and excitation spectra of pristine and fs laser irradiated polymers using this fluorescence spectrometer.

2.11 Electron spin resonance Spectroscopy

Electron paramagnetic resonance (EPR) or electron spin resonance (ESR) spectroscopy is a technique for studying chemical species that have one or more unpaired electrons, such as free radicals or inorganic complexes possessing a transition metal ion. Every electron has a magnetic

moment with spin quantum number s = 1/2. In the presence of an external magnetic field with strength B_0, the electron's magnetic moment aligns itself either parallel ($m_s = -1/2$) or antiparallel ($m_s = +1/2$) to the field, each alignment having a specific energy [109-110]. The parallel alignment corresponds to the lower energy state, and the separation between it and the upper state is $\Delta E = g_e \mu_B B_0$, where g_e is the electron's g-factor (see also the Landé g-factor) and μ_B is the Bohr magneton. This equation implies that the splitting of the energy levels is directly proportional to the magnetic field's strength, as shown in figure 15.

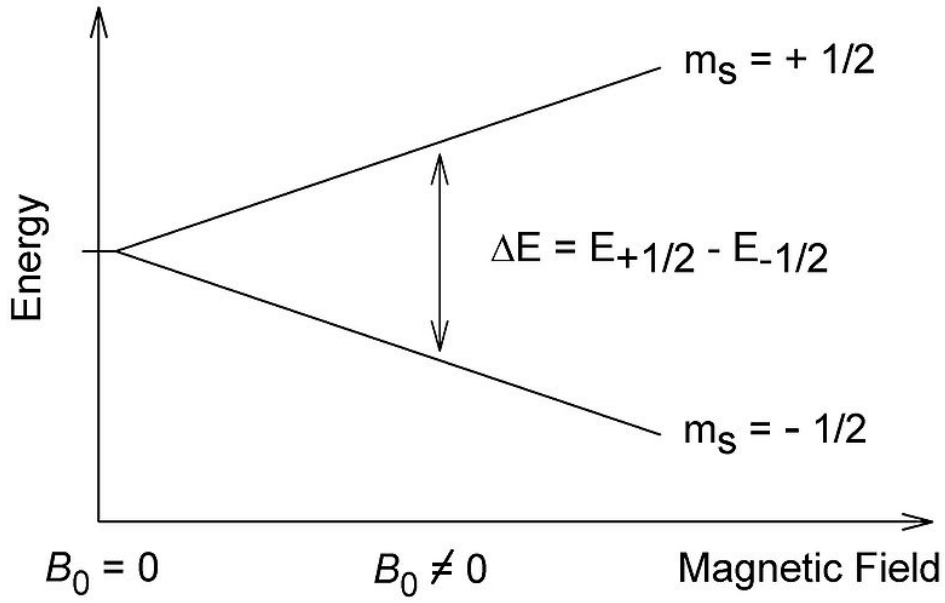

Figure 15. Splitting of levels [Zeeman Effect]

An unpaired electron can move between these two energy levels by either absorbing or emitting electromagnetic radiation satisfying the following relation.

$\Delta E = h\upsilon = g_e \mu_B B$, where h is Planck's constant and υ is the frequency of electromagnetic radiation.

EPR or ESR spectra can be generated by either varying the frequency of electromagnetic radiation incident on a sample while holding the magnetic field constant, or varying the magnetic field and keeping the frequency of electromagnetic radiation constant. Usually, the frequency of electromagnetic radiation is kept fixed and magnetic field is varied. Thus, a collection of paramagnetic centers, such as free radicals, is exposed to microwaves at a fixed frequency. By

increasing an external magnetic field, the gap between the $m_s = +1/2$ and $m_s = -1/2$ energy states is widened until it matches the energy of the microwaves, as represented by the double-arrow in the figure 15 above. At this point the unpaired electrons can move between their two spin states. Since there typically are more electrons in the lower state, due to the Maxwell-Boltzmann distribution, there is a net absorption of energy, and it is this absorption which is monitored and converted into a spectrum. Figure 16 shows a block diagram of ESR spectrometer. As shown in the block diagram, the electromagnet generates static/DC magnetic field when current is passed through it. Source for microwave frequency is klystron. Sample is placed in ESR tube with typically 3 mm in diameter. ESR tube is placed in between the electromagnets. The source is modulated and the resulting signal generated goes through phase sensitive detector and detector. The signal is amplified.

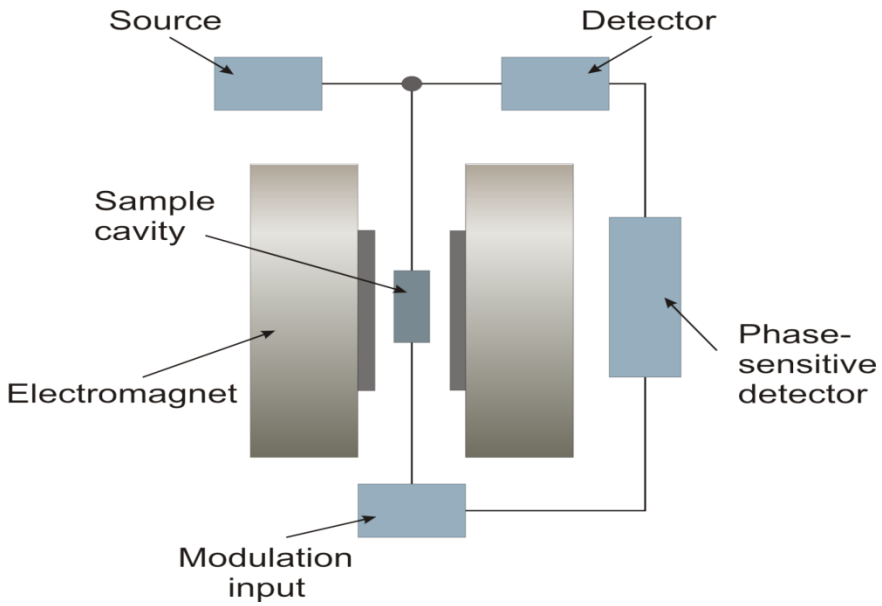

Figure 16. Block diagram of ESR spectrometer.

We have used JEOL company ESR spectrometer with version JES-FA 200 which is shown in figure 17. In this version, the microwave unit is X band unit which provides (8.65-9.75) GHz range. Magnetic field strength can be varied from 0-1 Tesla. In this dissertation, we have used the ESR spectrometer to investigate paramagnetic centers when polymers are treated with fs laser pulses.

Figure 17. JES-FA 200 version ESR spectrometer.

2.12 Field Emission-Scanning Electron Microscopy (FE-SEM)

A scanning electron microscope (SEM) is a type of electron microscope that images a sample by scanning it with a high-energy beam of electrons in a raster scan pattern. The electrons interact with the atoms that make up the sample producing signals that contain information about the sample's surface topography, composition, and other properties such as conductivity. The types of signals produced by SEM/FESEM include secondary electrons, back-scattered electrons (BSE), characteristic X-rays, light (cathodoluminescence), specimen current and transmitted electrons. Secondary electron detectors are common in all SEMs, but it is rare that a single machine would have detectors for all possible signals. The signals result from interactions of the electron beam with atoms at or near the surface of the sample.

A field-emission SEM provides narrower probing beams at low as well as high electron energy, resulting in both improved spatial resolution and minimized sample charging and damage. There are two classes of emission source: thermionic emitter and field emitter. Emitter type is the main difference between the Scanning Electron Microscope (SEM) and the Field Emission Scanning Electron Microscope (FESEM). Thermionic Emitters use electrical current to heat up a filament;

the two most common materials used for filaments are Tungsten (W) and Lanthanum Hexaboride (LaB6). When the heat is enough to overcome the work function of the filament material, the electrons can escape from the material itself. Thermionic sources have relative low brightness, evaporation of cathode material and thermal drift during operation. Field Emission is one way of generating electrons that avoids these problems. A Field Emission Gun (FEG); also called a cold cathode field emitter, does not heat the filament. The emission is reached by placing the filament in a huge electrical potential gradient. The FEG is usually a wire of Tungsten (W) fashioned into a sharp point. The significance of the small tip radius (~ 100 nm) is that an electric field can be concentrated to an extreme level, becoming so big that the work function of the material is lowered and electrons can leave the cathode. FESEM uses Field Emission Gun producing a cleaner image, less electrostatic distortions and spatial resolution < 2nm (that means 3 or 6 times better than SEM).

Figure 18 shows a schematic diagram of field emission scanning electron microscope. To cause field electron emission, a sharply pointed Schottky-type emitter is held at several kilovolts relative to nearby electrode which results in sufficient potential gradient at the emitter surface. Thermionic emission is enhanced by barrier lowering in the presence of high electric field for Schottky type emitter which is a thermal field emitter (TFE) cathode. A layer of zirconium oxide is coated on a tungsten tip to make a Schottky emitter. A high energy (typically 10-30 keV) electron beam, emitted from a tungsten tip is focused to a spot size of 1 nm to 5 nm by the condenser magnetic lenses and thereby it passes through a pair of scanning coils, which raster the beam across the surface.

Generation of low energy secondary electrons take place when these focused electrons are incident on the specimen, which are detected by a scintillator-photomultiplier device and the resulting signal is rendered into a two-dimensional intensity distribution that can be viewed and saved as a digital image. The most common imaging mode monitors low energy (<50 eV) secondary electrons which originates within a few nanometers from the surface. Back scattered electrons are those high-energy electrons which are elastically scattered and possess the same energy as the incident electrons. The probability of backscattering increases with the atomic number Z of the sample material. Back scatter electrons are used to detect contrast between areas

with different chemical compositions. Because these electrons are emitted from a depth in the sample, the resolution in the image is not as good as for secondary electrons.

Figure 19 shows a Photograph of the Field emission-scanning electron microscope (model: Carl ZEISS, FEG, Ultra 55) which is used in this thesis. Also, it has got EDXAS attachment where one can find out the percentage composition of various elements. The details are mentioned in the next section. We have used FESEM to image surface structures and cross-sections of gratings to know depths of the gratings.

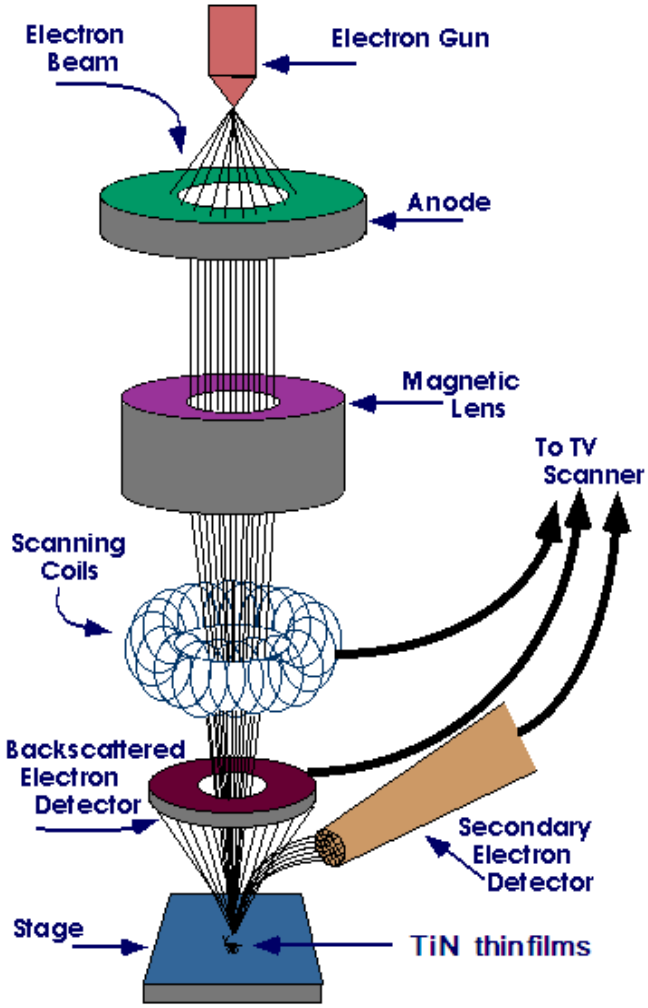

Figure 18 Schematic diagram of field emission scanning electron microscopy

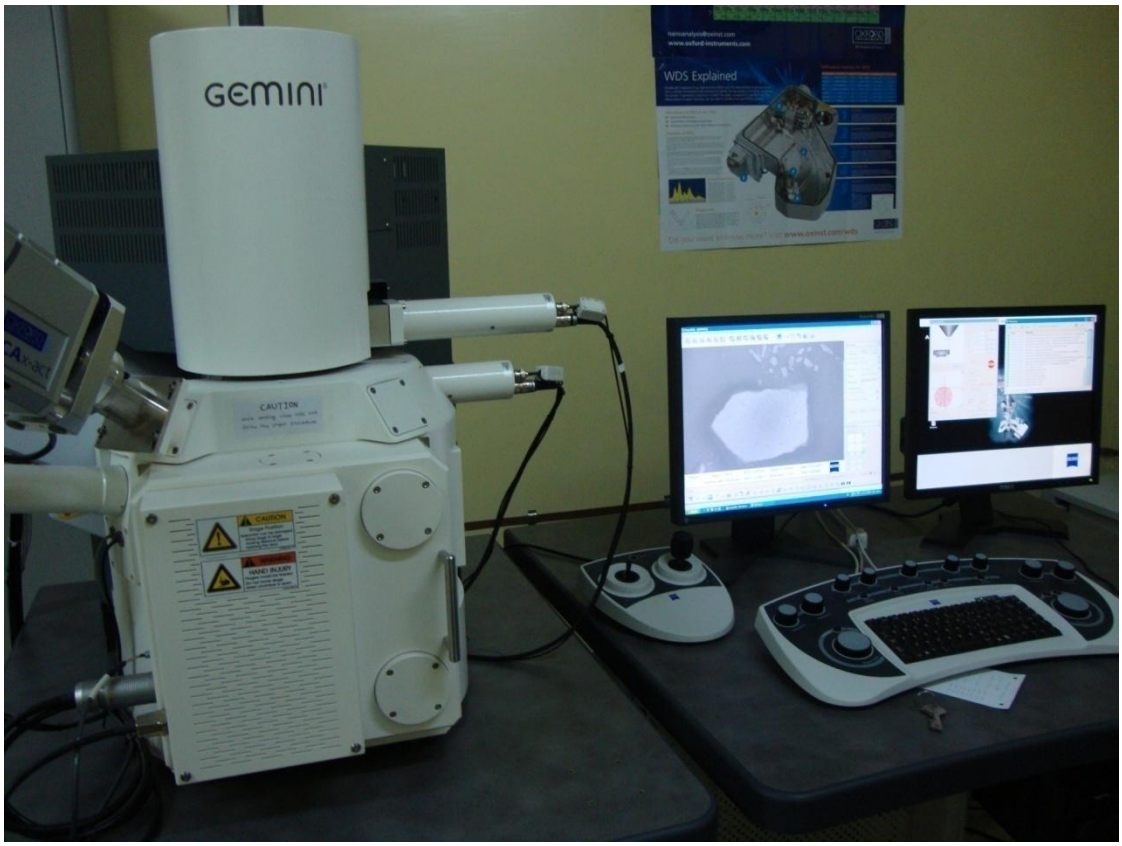

Figure 19. Photograph of the Field emission-scanning electron microscope (model: Carl ZEISS, FEG,Ultra 55) .

2.13 Energy dispersive x-ray absorption spectroscopy (EDXAS)

Energy Dispersive X-Ray Spectroscopy (EDXAS) is a chemical analysis technique used in conjunction with scanning electron microscopy (SEM). The EDXAS technique detects x-rays emitted from the sample during bombardment by an electron beam to characterize the elemental composition of the analyzed volume. Features as small as 1 μm or less can be analyzed. The process of x-ray emission from the sample surface is depicted in figure 20. When the sample is hit the electron beam from SEM, electrons are ejected from the atoms comprising the sample's surface. The resulting electron vacancies are filled by electrons from a higher state, and an x-ray is emitted to balance the energy difference. The x-ray energy is characteristic of the element

from which it is emitted. The EDXAS x-ray detector measures the relative abundance of emitted x-rays versus their energy. The detector is made up of lithium-drifted silicon, solid-state device. A charge pulse that is proportional to the energy of X ray is created when x-rays strike the detector. Using a charge sensitive preamplifier, the charge pulse is converted to a voltage pulse. This signal is then sent to a multichannel analyzer where the pulses are sorted by voltage. The energy, as determined from the voltage measurement, for each incident x-ray is sent to a computer for display and further data evaluation. The spectrum of x-ray energy versus counts is evaluated to determine the elemental composition of the sampled volume. In the thesis, the chemical composition of the bulk polymers, polymer thin films and crystals are determined using energy-dispersive x-ray spectroscopy (EDXAS) analysis. EDXAS spectrum is obtained from FE-SEM using an INCA EDX system, which is equipped with an Oxford Instruments. The operating voltage for EDXAS measurement is 20 kV.

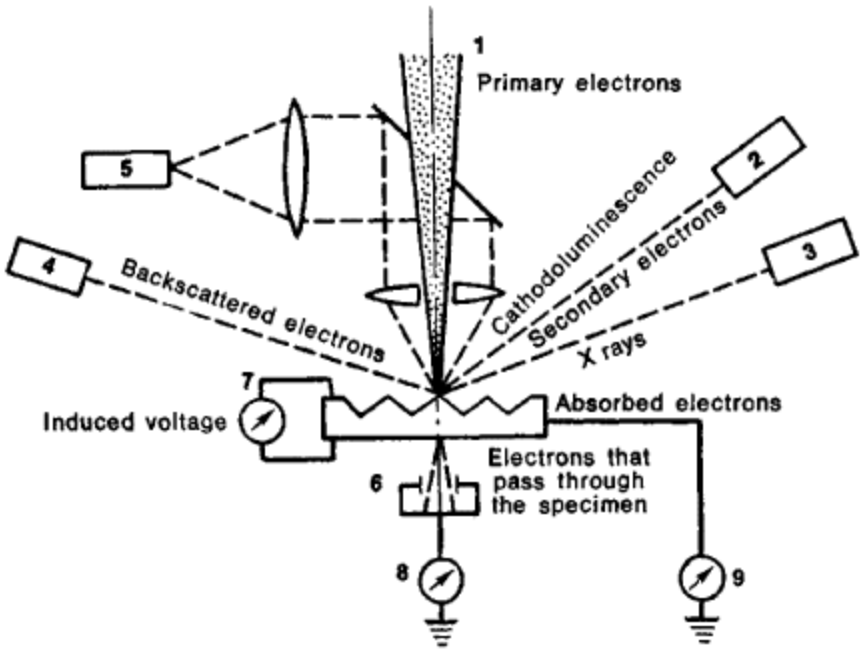

Figure 20. X-ray emission from the sample, when charged electron beam hits the sample surface.

2.14 Transmission Electron Microscopy (TEM)

Since, the wavelength of electron is much smaller than that of light, the optimal resolution attainable for TEM image is several orders of magnitude higher than that for a light microscope. In transmission electron microscopy (TEM), the specimen is bombarded with an electron beam. Few electrons are transmitted through the sample, some are also scattered or diffracted. The scattered and diffracted electrons form the image contrast as denser or thicker parts of the sample scatter as well as absorb, more electrons, thus appearing as darker areas in the image [111-112]. The imaging system of a TEM consists of at least three lenses as shown in figure 21: the objective lens, the intermediate lens (or lenses), and the projector lens. The intermediate lens can magnify the first intermediate image, which is formed just in front of this lens, or the first diffraction pattern, which is formed in the focal plane of the objective lens, by reducing the excitation [111]. Objective apertures α_o between 5 and 20 mrad, can be produced using the *bright-field mode* (BF) with a centered objective diaphragm which is the typical TEM mode, with which scattering contrast and diffraction contrast can be enhanced. For high-resolution phase contrast, the aperture should be larger ($\alpha_o \geq 20$ mrad) to transfer high spatial frequencies. The purpose of the diaphragm is to decrease the background by absorbing electrons scattered at very large angles. The resolution is limited by the attenuation of the contrast-transfer function (CTF) caused by chromatic aberration and not by the objective aperture α_o. Normally, the specimen is irradiated with small illumination apertures $\alpha_i \leq 1$ mrad. For high resolution, an even smaller aperture $\alpha_i \leq 0.1$ mrad is necessary to avoid additional attenuation of the CTF by partial spatial coherence.

In the *dark-field mode* (DF), the primary beam is intercepted in the focal plane of the objective lens. Different ways of producing dark-field conditions are in use. The shifted-diaphragm method as shown in figure 22 (b) has the disadvantage which worsens the chromatic aberration as scattered electrons pass through the objective lens on off-axis trajectories. To take into the account of chromatic aberration, the most common mode is that in which the primary beam is tilted as shown in figure 22 (c) so that the axis strikes the centered diaphragm. The image is produced by electrons scattered into an on-axis cone of aperture α_o. This mode has the advantage that off-axis aberrations are avoided. Thus, there is no increase of chromatic error. Asymmetries in the dark-field image can be avoided by using a central beam stop that intercepts the primary

beam in the back focal plane by employing a thin wire stretched across a circular diaphragm as shown in figure 22 (d). As there are fewer scattered electrons, DF micrographs need a longer exposure time. For high resolution, the contrast-transfer function (CTF) of DF is nonlinear, whereas the CTF of the BF mode is linear for weak-phase specimens. In the present thesis, we have used Transmission electron microscope as shown in figure 23 (model: Tecnai 20 G2 STwin, FEI electron microscope operated at 20 kV using Gatan CCD camera) to investigate the sizes of silver nanoparticles.

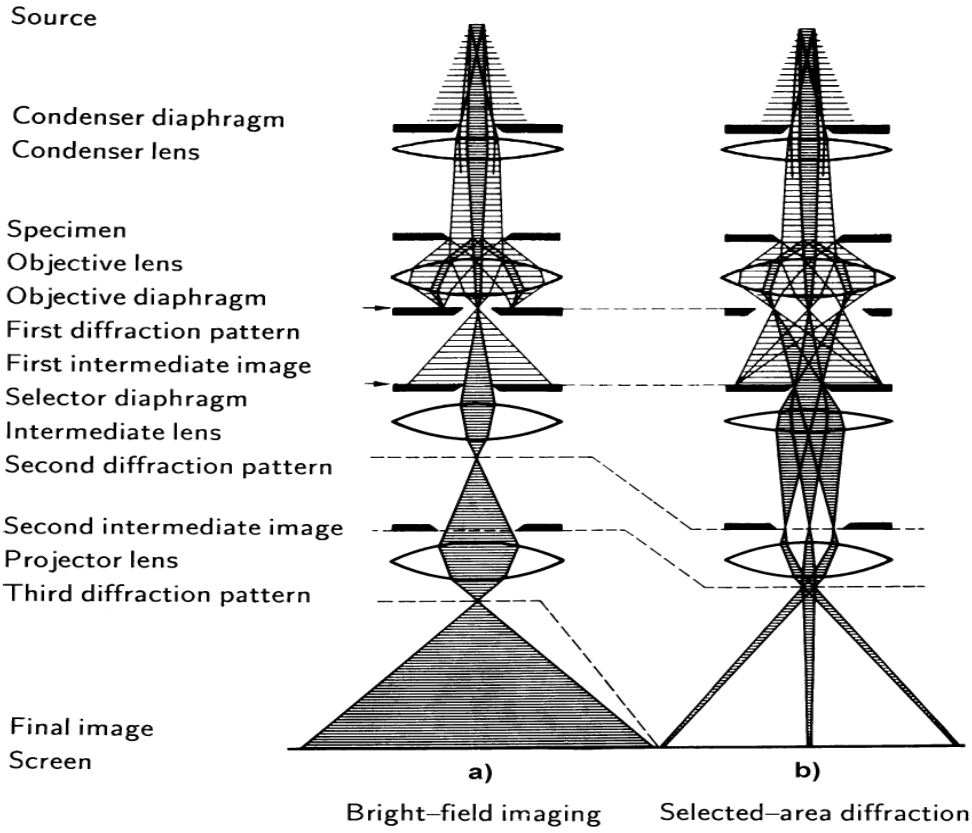

Figure 21. Ray diagrams for a TEM in (a) the bright-field mode and (b) selected area electron diffraction (SAED) mode. .

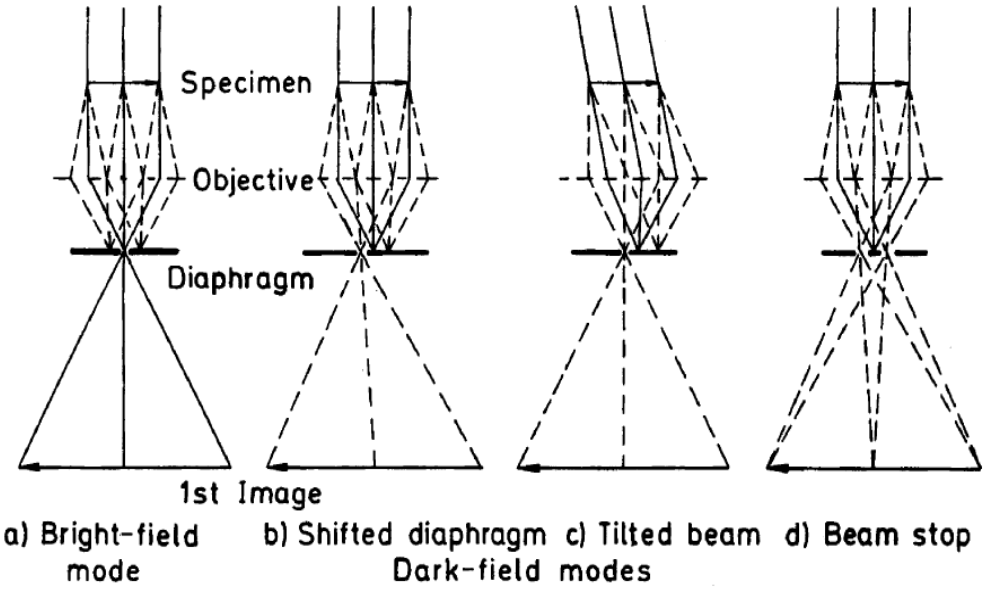

Figure 22. (a) Bright-field mode with a centered objective diaphragm and production of a dark-field mode by (b) a shifted diaphragm, (c) a tilted beam, and (d) a central beam stop. .

Figure 23. Photograph of the Transmission electron microscope (model: model: Tecnai 20 G2 STwin, FEI electron microscope operated at 20 kV using Gatan CCD camera).

Chapter 3

Abstract

Results obtained on microstructures, craters, gratings, and complex structures in different polymers using fs laser direct writing are explained. Role of fs laser pulses on optical damage and thermal diffusion length are highlighted. Keldysh parameter calculations are used to describe the dominant ionization process involved for polymers poly methyl methacrylate (PMMA), poly dimethylsiloxane (PDMS), polystyrene (PS), and polyvinyl alcohol (PVA) is investigated. Dependence of structure width with no.of scans, speed, energy and numerical aperture of the lens used are studied. Fabrication of micro-craters at high scan speeds and low energy irradiation dose is elucidated in the context of minimal pulse to pulse overlap. Results obtained with diffraction gratings fabricated in PMMA, PDMS, and PS are presented. The highest percentage diffraction efficiency (%DE) reported in our work are 34 % in PMMA and 10 % each in PDMS and PS are explained. Efforts to increase the %DE through thermal treatment are described. Photochemical and thermal models are briefly discussed. Also, the fabrication of complex structures such as Y couplers, double line waveguides, microfluidic channels, and 8 shape are illustrated by using simultaneous combined motion of stages.

3.1 Threshold Intensity for laser damage

The threshold intensity required for laser damage in different polymers investigated are presented herein. We use the equation (1.17) to find out the threshold intensity for laser damage at different pulse widths from ns to fs regime. The formula to calculate the threshold intensity is given by

$$I_{th} = n\varepsilon_0 c\left\langle E^2 \right\rangle = 2n\varepsilon_0 c \frac{Wm}{fe^2 \tau T_p} \ln(N_{th}/N_0) \tag{3.1}$$

I_{th} is the threshold intensity for laser damage. $\ln(N_{th}/N_0)$ can be taken as 30. All other parameters have their usual meanings as explained in chapter 1. W is the ionization potential for which we considered the bandgaps for various polymers. The bandgap of PMMA is 4.58 eV, PDMS is 2.84 eV, PS is 4.54 eV, and PVA is 2.4 eV [113-117]. We present summary of our results in table 1. From table 1, we see that the threshold intensity for producing laser damage increases with shortening the pulse as it is evident from the formula (3.1). We used 100 fs pulses throughout our research work with different polymers. The calculations obtained with 100 fs pulses in PMMA, PDMS, PS and PVA are highlighted in red color in the table 1. The order of magnitude is sub PW/cm^2 for almost all polymers that are investigated. Since fs pulsed lasers can produce PW/cm^2 intensities, micromachining with fs lasers is preferable.

These calculations give us rough idea about threshold intensity required for laser damage to be produced under several assumptions. In the calculations, we have assumed f≈0.01 [67]. f is defined as the fraction of the absorbed energy that leads to ionization. The value of f is different for different materials though we considered it to be equal to 0.01. τ is defined as the mean time between collisions which is taken as 10^{-15}s [67]. Under several such assumptions as referenced in 67, we calculated the threshold intensities for different pulse widths in these polymers.

Table 1. Threshold intensity for laser damage for different pulse durations in different polymers investigated.

S. No.	T_p	I_{th}			
		PMMA	PDMS	PS	PVA
1	1 fs	41.5 PW/cm^2	25.73 PW/cm^2	41.13 PW/cm^2	21.74 PW/cm^2
2	10 fs	4.2 PW/cm^2	2.573 PW/cm^2	4.11 PW/cm^2	2.174 PW/cm^2
3	100 fs	0.414 PW/cm^2	0.26 PW/cm^2	0.411 PW/cm^2	0.22 PW/cm^2
4	1 ps	41.49 TW/cm^2	25.73 TW/cm^2	41.13 TW/cm^2	21.74 TW/cm^2
5	10 ps	4.15 TW/cm^2	2.573 TW/cm^2	4.11 TW/cm^2	2.174 TW/cm^2
6	100 ps	0.415 TW/cm^2	0.26 TW/cm^2	0.411 TW/cm^2	0.22 TW/cm^2
7	1 ns	41.49 GW/cm^2	25.73 GW/cm^2	41.13 GW/cm^2	21.74 GW/cm^2
8	10 ns	4.15 GW/cm^2	2.573 GW/cm^2	4.11 GW/cm^2	2.174 GW/cm^2
9	100 ns	0.415 GW/cm^2	0.26 GW/cm^2	0.411 GW/cm^2	0.22 GW/cm^2

3.2 Thermal diffusion length calculations

Herein, we present our results on calculated thermal diffusion lengths for different pulse durations using the formula (1.32). By invoking the formula below, we have

$$L = \left(DT_p\right)^{1/2} \tag{3.2}$$

where D is the diffusion constant, L is thermal diffusion length and T_p is the pulse duration. The D values for PMMA and PS are taken as 0.11 and 0.525 mm^2/s [118-121]. The values of D typically will be of the order of 10^{-3} cm^2/s for dielectrics as explained in chapter 1. Table 2 shows the diffusion lengths for different materials at different pulse durations. We used 100 fs pulses and the calculated thermal diffusion lengths which are indicated in red color of table 2. From table 2, it is noticed that thermal diffusion length increases with the increase in pulse duration for almost all materials. Thus, thermal effects are almost negligible for fs pulses. It is

for the reason; fs pulses are preferred over ns, and ps pulses for micro structuring different materials. Since, value of D for PS is higher compared with PMMA; we could observe microstructures even at low energies of the order of nJ in case of PS. Thus the role of D and pulse duration cannot be avoided. Figure 1 shows the plot obtained between thermal diffusion lengths with pulse duration for different materials. Since the thermal diffusion lengths obtained for ps, and fs pulses are very less and nearly zero and cannot be seen in the graph, we have taken logarithm of the thermal diffusion length on the Y axis.

Table 2. Thermal diffusion lengths for different materials at different pulse durations.

S. No.	T_p	L(nm)		
		PMMA	PS	Dielectrics
1	1 fs	0.01	0.023	0.01
2	10 fs	0.033	0.073	0.032
3	100 fs	0.105	0.23	0.1
4	1 ps	0.3	0.725	0.32
5	10 ps	1.05	2.3	1
6	100 ps	3.32	7.25	3.2
7	1 ns	10.5	23	10
8	10 ns	33	72.5	32
9	100 ns	105	230	100

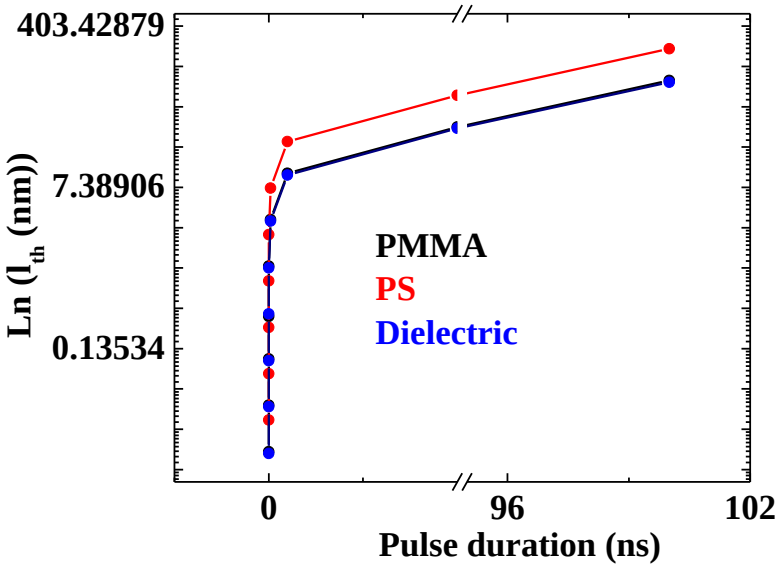

Figure 1. Logarithm of thermal diffusion length with pulse duration.

Also, in these calculations the role of repetition rate of the laser is neglected. There could be multiple irradiations at the same irradiated spot if repetition rate of the laser is high. In the calculations of threshold intensity for laser damage, several approximations and assumptions are made as explained earlier sections. In the calculations of thermal diffusion length also, we have neglected the intensity of the laser to arrive at the equation (3.2) as explained in chapter 1. If laser energy is very small, then intensities can be neglected. If laser energies are of the order of μJ, intensities associated with laser pulses (though pulse durations are of the order of fs) cannot be ignored and they lead to void formation. In our present study, we focused on fs pulses whose energies are of the order of μJ that resulted in the formation of defects.

3.3 Keldysh Parameter calculations

As explained earlier in chapter 1, Keldysh parameter is used to assess the ionization that is dominant when laser pulses interact with different materials. Most of the transparent polymers are wide bandgap materials. Their bandgap ranges from 2.2 to 2.4 eV for chalcogenide glasses and up to 8.8 eV for sapphire that ensures the transparency in the visible or near infrared spectral range at low intensity [122]. Most of the transparent polymers are also wide bandgap materials.

The Keldysh parameter (γ) which provides information about the dominant mechanism and is explained in chapter 1 through the equation (1.33) is defined as

$$\gamma = \frac{\omega}{e}\left[\frac{mc\varepsilon_0 E_g}{I}\right]^{1/2} \tag{3.3}$$

m, e are the reduced mass and charge of the electron, I is the intensity, ω is the laser frequency, ε_0 is the permitivity of free space, E_g is the bandgap of the material, n is the refractive index of the material, and c is the velocity of light. Multiphoton ionization is dominant in case of $\gamma > 1.5$, and tunneling ionization is favored in case of $\gamma < 1.5$. If $\gamma = 1.5$, then both ionizations are dominant [70-71, 123-124]. The energy of an 800 nm photon corresponds to 1.55 eV while the optical band gap of pure PMMA is 4.58 eV which implies that the nonlinear process involving at least three photons is responsible for structural modification at the focal volume [113]. The

bandgaps for PS, PVA, and PDMS are 4.3-4.54 eV, 2.92 eV, 2-2.84 [113-117] respectively. The information of bandgap suggests that multiphoton ionization is responsible for the modification of polymers as bandgap energies are more than each 800 nm photon energy. But the calculation of Keldysh parameter suggested that the tunneling ionization is main responsible for the modification process. For this, we calculated peak intensities for each pulse energy. Peak Intensity (I) is calculated as the peak power (P) divided by area of the focused spot. Area of the focused spot is given by

$$A = \pi r^2 \tag{3.4}$$

where r is the radius of the spot. For microfabrication experiments carried out with 40X objective with numerical aperture (NA) 0.65, the spot size is calculated as

$$d = \frac{1.22\lambda}{NA} \tag{3.5}$$

where λ is wavelength of the laser used (800 nm). The spot sizes thus estimated are 1.55 and 2.4 μm respectively for 40X and 20X microscope objectives. The peak power further is given by energy of the pulse multiplied by frequency of the laser which is 1 KHz (repetition rate). In our experiments with four different polymers PMMA, PDMS, PS and PVA we varied the energy from 150 μJ-460 nJ. Figure 1 shows the plot of Keldysh parameter with peak intensity for different polymers. The Keldysh parameter is less than 1.5 shows that the main mechanism responsible for modification is tunneling ionization. For polymers investigated in our experiments, the tunneling ionization is shown to be mainly responsible for modification process involved. Also, we extended our analysis to evaluate where Keldysh parameter nears 1.5. From the plot, we found that Keldysh parameter nears and becomes above 1.5 for pulse energies of 30 nJ. Thus for structures fabricated at and below 30 nJ, multiphoton ionization is the dominant mechanism for structural modification. However, we could not observed structures below 30 nJ (except for PS) for PMMA and PDMS as the resolution of confocal microscope is nearly a micron.

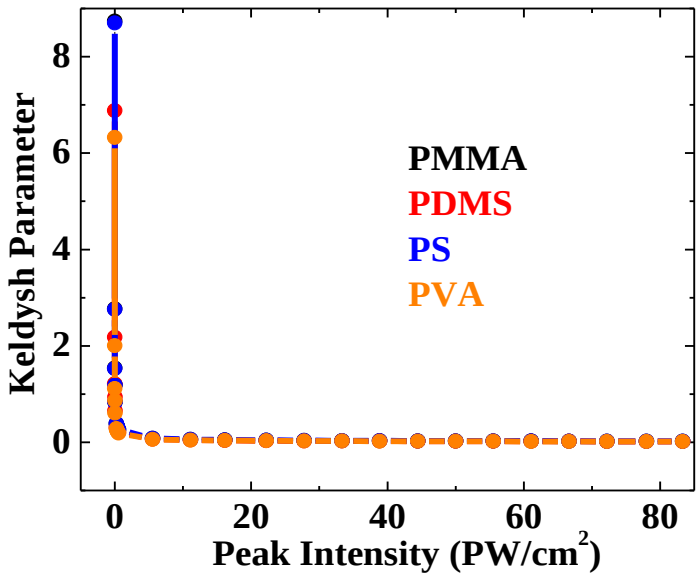

Figure 2. Keldysh parameter versus peak intensity for PMMA

In the present study, we did not carry out experiments at low energies typically of the order of nJ to create structures which are of refractive index change type as explained in chapter 1. Also, after the fabrication of structures, edges are supposed to be polished to carry out waveguide studies. In order to know the depth of the structures also, the quality of polishing is very important as the resolution of SEM is of the order of few tens of nm, one need to achieve polishing quality of the same order to view cross-sections of these structures. As polishing facility and waveguide setup is under construction, we could not carry out our studies at low energies towards waveguide studies. Hence, the present study focuses only on the formation of defects and hence higher energy pulses are used to fabricate the structures.

3.4 Factors influence structure width

For our experiments, we purchased PMMA sheet from Goodfellow, USA. PDMS was homemade. PS was purchased from Goodfellow, UK. PVA thin films were prepared by dissolving 8.56 grams of PVA beads in 100 ml of water and thin films were prepared using spin coating technique. Thin films of PS are made by preparing the PS solution first. Solution of PS was prepared by mixing 1 gram of polystyrene beads (ACROS) in 8 ml distilled water and stirred for 48 hours for complete miscibility. We prepared thin films of PS on a glass plate by spin coating the solution of PS. Initially, we fabricated several structures in polymers PMMA, PDMS, PS and PVA. We found structure width increasing with increase in the energy of the pulses and the no. of scans used. For structures fabricated at the same energy, structure width was found to be higher in PDMS compared with PMMA as PDMS is relatively soft and rubbery kind of material compared with PMMA. Also the tensile stress of PDMS is 2.24 Mpa, while for PMMA it is 70 Mpa. Figure 3 illustrates the confocal microscope images of structures obtained in PMMA polymer fabricated at different energies with 1 mm/s speed. Figure 4 shows the SEM images of cross-sections of the structures fabricated in PMMA. We observed structure width increasing with irradiation dose/energy.

To study the effect of energy and no. of scans on the structure widths that are obtained, we have fabricated microstructures in PMMA using single and double scan methods using 40X and 20X microscope objectives. For reproducibility, we have repeated for two sets of structures in PMMA and the data is in good agreement in both the cases. Typical confocal images and variation of the width with input energy for these structures are shown in figures 5 (a)–(b). Similar structures were achieved in PDMS (using 40X and 20X objective lenses) and figures 5 (c)–5 (d) show the structures and plots of structure width versus input energy. The structure width is found to be increasing with input energy and the number of scans. As stated above, 20X objective spot size is more than 40X objective; structures written at the same energy with the 40X and 20X are compared. For structures written at same energy, width is found to be more in PDMS compared PMMA as PDMS is relatively soft material compared to that of PMMA.

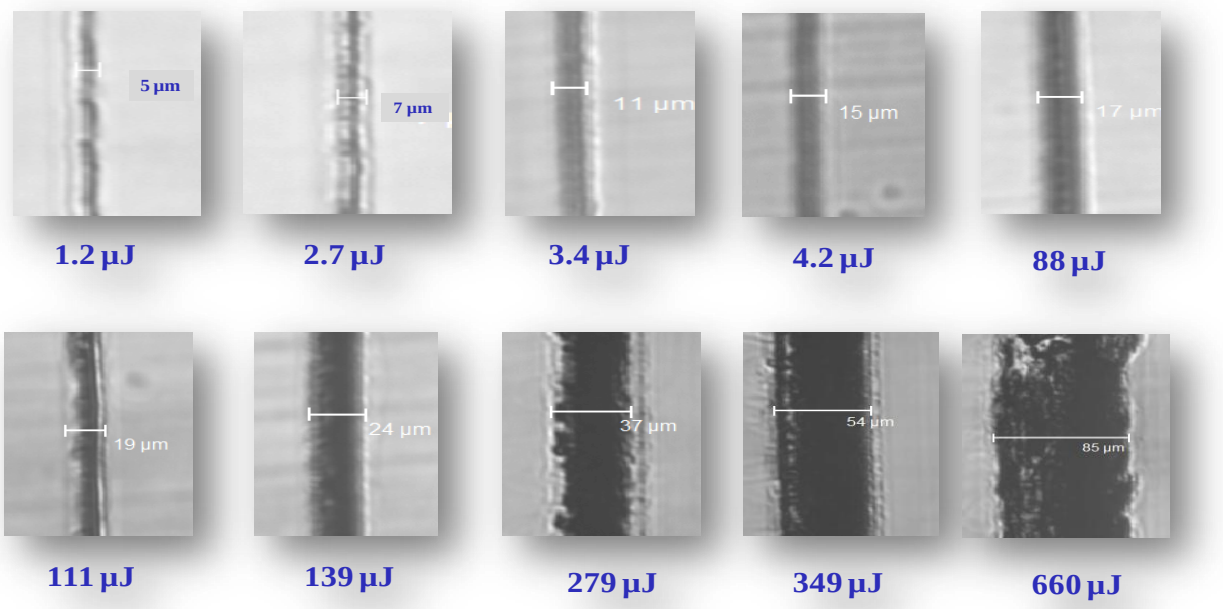

Figure 3. Confocal microscopic images of the microstructures written with 1 mm/s speed at different energies in PMMA (local grade).

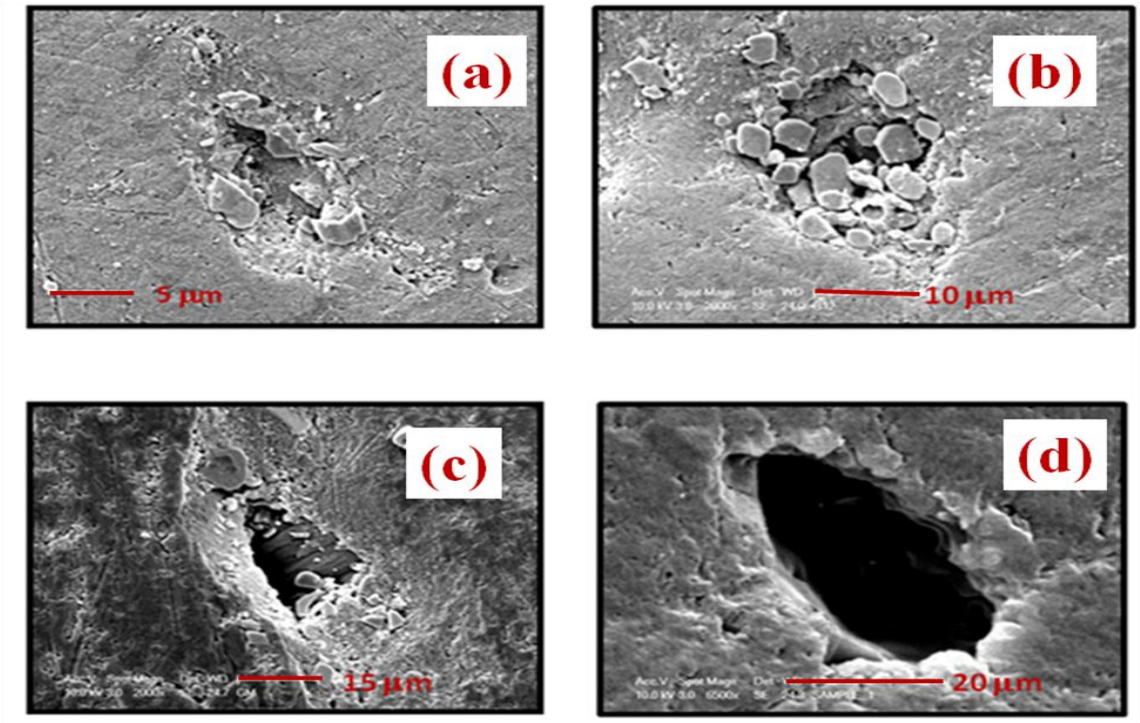

Figure 4. Typical cross-section image of a structure captured using SEM written with energy of (a) <2 µJ (b) ~20 µJ (c) ~40 µJ (d) SEM cross-sectional image of structure written with energy of ~75 µJ.

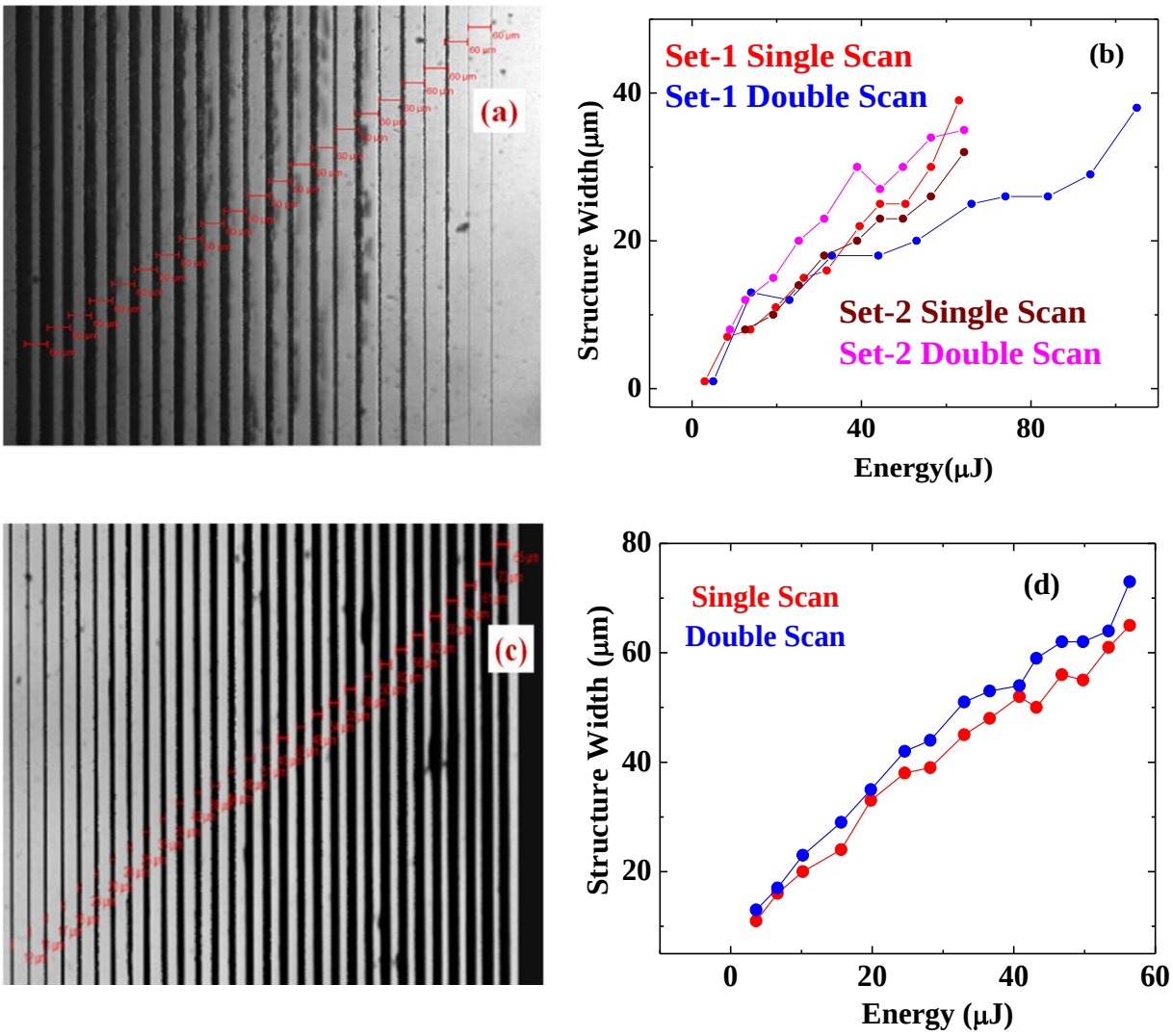

Figure 5. Microstructures obtained in PMMA using 40X objective in SET-1 **(a)** Confocal microscope image of the structures fabricated (Right to left structures were written with increasing energy in single and double scan methods) **(b)** Plot of structure width versus energy in SET-1 and SET-2 experiments **(c)** Microstructures written in PDMS using 40X objective **(d)** Plot of structure width versus energy in PDMS written with 40X objective.

Also, several microstructures are fabricated on the surface of PMMA and PDMS are fabricated. Figure 6 (a) – 6 (b) show the SEM images of the fabricated microstructures. The structure width is found to be different when we compared the data from confocal microscope with SEM owing to their resolutions. Through confocal microscope we could not establish the kind of

modification occurred at the focal volume. However, it is clear only when we viewed them through SEM. Figure 6 (a) clearly shows grooves in the irradiated region which indicates that the fabricated structure is of void type. However, we observed splitting of the microstructures written with 130-40 μJ (decreasing) energies as shown in SEM pictures. At lower energies (570 nJ), we have not observed any grooves. A structure fabricated at 570 nJ showed no grooves. At the edges of the structure, we clearly see small variation which indicates smooth refractive index variation in the region. The splitting behavior could be due to the damage in the 40X objective which we realized it later after careful observation.

Figures 6 (c)-6 (d) clearly shows the SEM images of PMMA and PDMS surface structures. Intermediate energies at the focal spot, possessing high peak intensities, eject the debris and is demonstrated through the SEM images of the surface structures. For buried structures, at intermediate energies, there is a possibility of debris settling within the structure since it cannot escape. These are hybrid structures with void regions followed by high density region and pristine region. Figure 7 (a) shows the confocal images of fabricated structures in PS thin films and 7 (b) shows the plot of structure width with energy. However, the energy values reported here are measured at the laser and do not take in to account of the reflection losses at different surfaces. Similar studies are carried out in bulk PS also on the surface and subsurface using 40X and 20X microscope objectives. We have obtained similar results such as increase in structure width with no.of scans and irradiation dose as observed in PMMA and PDMS. Furthermore, structures fabricated at a particular energy on the surface are found to be having more width compared to the structures fabricated inside the surface.

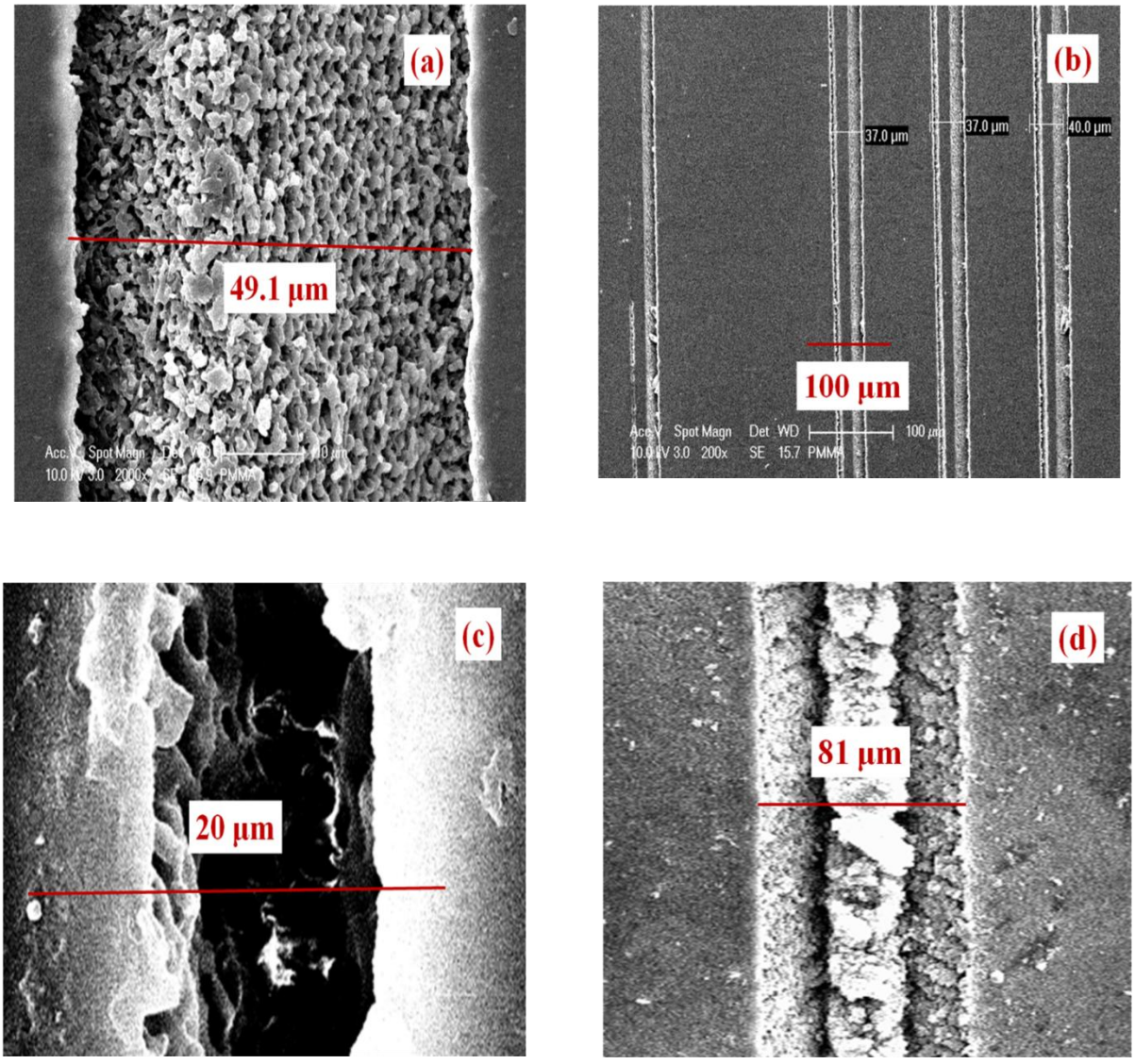

Figure 6. (a) Surface microstructures fabricated in PMMA at 150 µJ energy with 1mm/ s speed (b) 80-50 µJ energies from right to left in steps of 10 µJ energy. (c) SEM image of surface structure written at 54 µJ and 1mm/s in PMMA (d) SEM images of PDMS surface where structure is written at 54 µJ with scanning speed of 1mm/s.

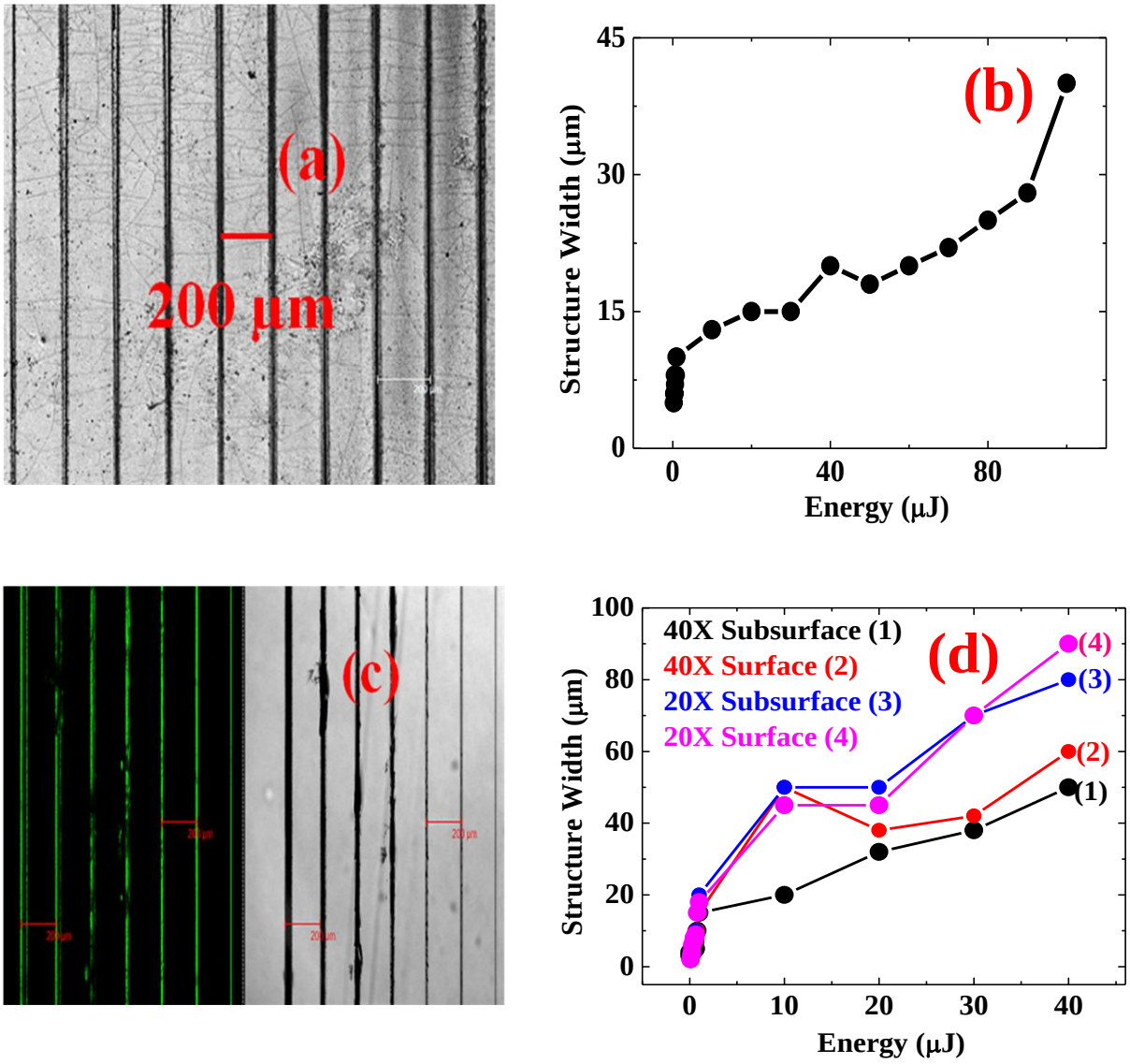

Figure 7. (a) Confocal microscope image of micro structures fabricated in thin films of PS with different energies using scanning speed of 1mm/s. (Right to left structures written at 100 µJ to lower energies in steps of 10 µJ, Scale bar is 200 µm); (b) Plot of structure width with energy; (c) Microstructures fabricated on the surface of bulk PS from 40 µJ to 10 µJ in steps of 10 µJ and 1 µJ, 798 nJ energies (From left to right). Pseudo green color shows emission from the modified regions when excited at 488 nm (Scale bar is 200 µm); (d) Structure width versus energy in case of 40X, 20X objectives on surface and subsurface of bulk PS.

3.5 Fabrication of micro-craters

Micro-craters are fabricated by exposing the surface of polymers to 800 nm laser at different exposures of time. Dimensions of craters are found to be increasing with energy and exposure time. The exposure time varied from 5 sec to 50 sec in steps of 5 seconds (10 craters). For the rows right to left, the energy varied as 50 μJ (column 3), 20 μJ (column 2) and 10 μJ (column 1). Figure 8 (a) and (b) show micro-craters fabricated on the surface of PMMA at different irradiation energies and exposure times. Figure 8 (c) and (d) show the same for the PDMS polymer.

Typical structure width (diameter of the crater) varied from 50 μm to 100 μm. The structures resulting from 0.4 NA (20X) objective were definitely larger in diameter than those exposed for the same time with 0.65 NA (40X) objective since the focused spot size was larger in former case. The position of the focal volume could be different in each case resulting in higher ablation rate and thereby induce cracks. Figure 8 (c) shows the micro-craters created on the surface of PDMS using 0.65 NA (40X) objective lens with exposure times as explained for the case of PMMA. Figure 8 (d) shows a typical SEM image of one such micro-hole elucidating the structure formed through high intensity pulses. The enormous strain created by the short pulse(s) is evident through the fine cracks. The crater was not well-defined since the debris has settled back imperfectly after the pulse has left. Fabricating such structures in conjunction with the flow of a liquid might reduce the debris and produce a well-defined crater, useful for microfluidic studies. The results from such studies support us in fabricating micro channels, reservoirs, etc. which are the building blocks for lab-on-a-chip devices.

Also, micro-craters are fabricated with a novel method by reducing the energy and increasing the scanning speed. When the input energy was reduced typically from μJ to nJ we obtained smooth structures and we perceive that the modification is of refractive index change type. Since polishing facility and waveguide setup are under construction, we could not carry out refractive index measurements in the present study. A buried grating is fabricated in PS with 33 nJ energy and with 0.5 mm/s speed. Figure 9 (a) shows the confocal microscope image of the polystyrene grating. When scanning speed is increased along with the reduced energy of the pulses we

observed the formation of micro-craters instead of straight line structures. Figure 9 (b) shows the confocal microscope image of polystyrene grating fabricated at 33 nJ energy with 3 mm/s speed. We found micro-craters arrayed throughout the fabricated grating structure instead of straight lines. Left side of the figure shows pseudo-green color that represents the emission when excited at 488 nm wavelength which will be explained in the next chapter. For clarity, one array of craters is shown in the inset of figure 9 (c). By decreasing the energy a weaker source for thermal diffusion is generated resulted in reduced modified size and by increasing the scan speed there was a reduction of pulse to pulse overlap [125]. Thus, one can achieve micro-craters instead of straight line structures at low energies and high scanning speeds. We have collected emission from the modified regions that are top and bottom surfaces of modification using confocal microscope as middle portion of the structure results in void formation and do not show any emission when fabricated at high energies. The schematic diagram for collecting emission is shown in figure 9 (d).

The material that is ablated from the center of the high energy Gaussian pulse gets deposited on the inner surface of the voids. The debris shows emission which can be seen when excited with 488 nm wavelength in the confocal geometry. Therefore top, bottom and sides of the irradiated region show emission. Figure 9 (d) shows field emission scanning electron microscope (FESEM) images of two surface structures fabricated in PS at 100 and 1 μJ energy with 1 mm/ s speed. Clearly we observed a trough and debris settled at the ends. The debris settled on the inner surfaces of the void along with the laser irradiated regions contributes to the observed emission. Right side of figure 9 (d) shows a schematic diagram with two regions of modification. Region 1 is completely of void type (due to middle portion of the incident Gaussian pulse) which is surrounded by region 2 of index change type which consists of ablated and modified material (in the tail portions of the incident Gaussian pulse).

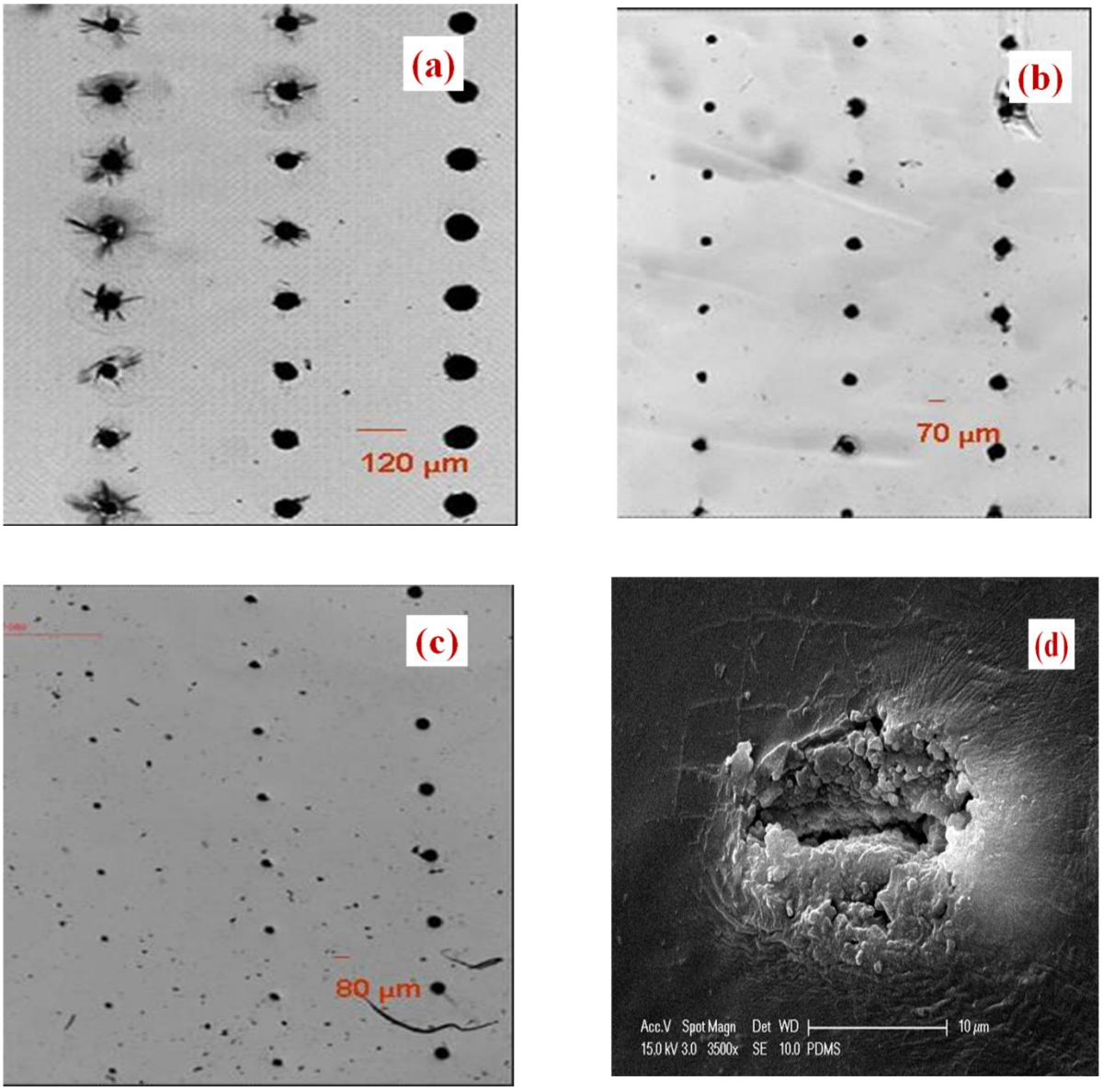

Figure 8. Micro-craters on the surface of PMMA with (a) 0.4 NA (20X) focusing (b) 0.65 NA (40X) focusing. Left to right rows: 10, 20, 50 µJ, Top to bottom: 5 sec to 50 sec in steps of 5 sec exposure time. (c) Surface structures in PDMS using 0.65 NA (40X) objective. Left to right rows: 10, 20, 50 µJ, Top to bottom: 5 sec to 50 sec in steps of 5 sec exposure time. (b) SEM image of a typical micro-crater structure on the surface of PDMS.

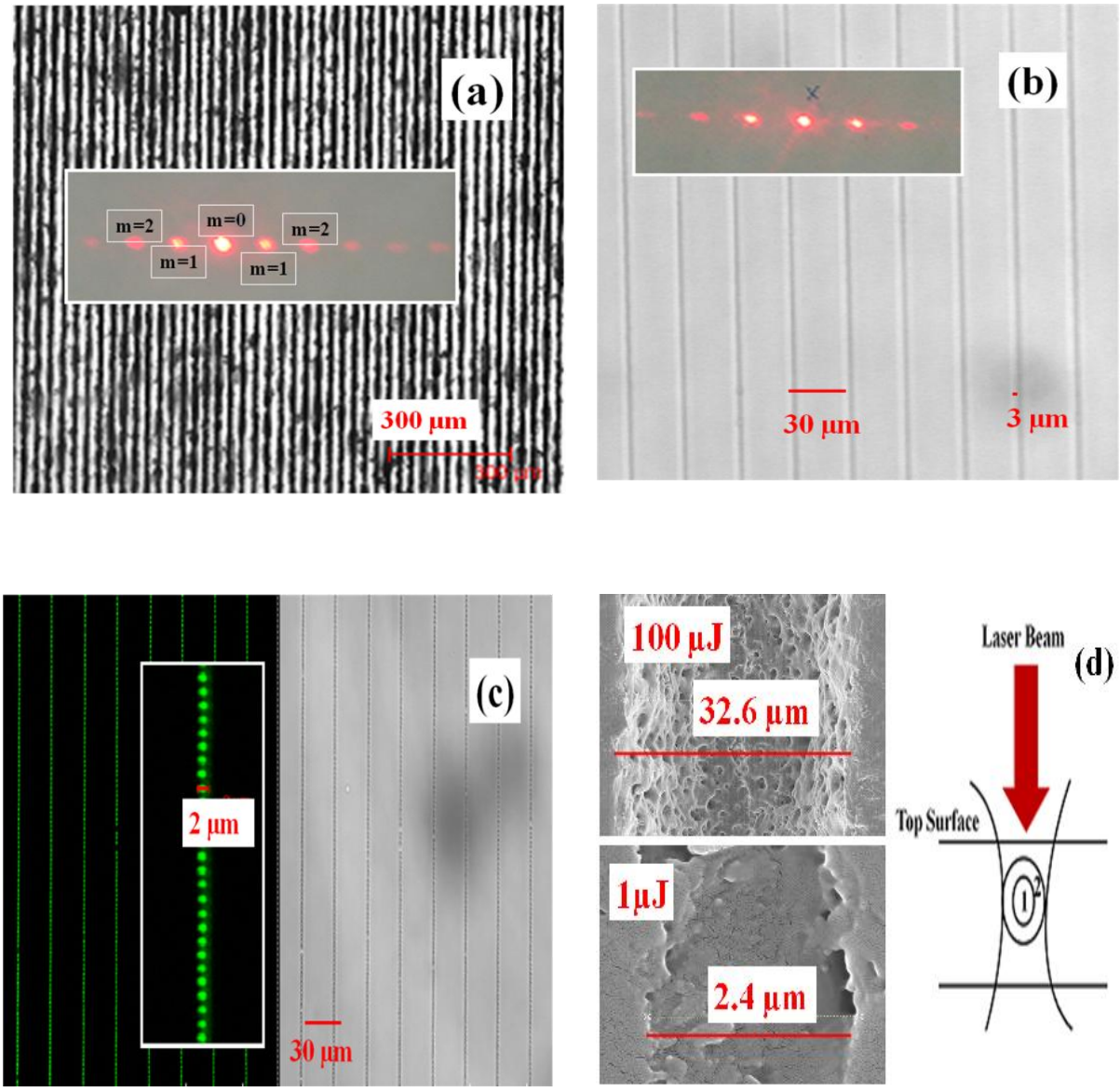

Figure 9. (a) Confocal microscope image of a typical buried PSG1 grating. Inset shows diffraction pattern with different orders. Scale bar is 300 µm. (b) Confocal microscope image of PSG3 grating and the corresponding diffraction pattern (period 30 µm and width 3 µm) (c) Confocal microscope image of PSG4 grating (period 30 µm). Pseudo green color indicates emission from the fs laser modified regions when excited at 488 nm wavelength. Array of luminescent micro-craters is depicted in middle with crater size of ~2 µm. (d) FESEM images of surface structures fabricated at 100 and 1 µJ energy with 1mm/s speed. Right side picture shows a schematic diagram showing the two regions from where the fluorescence is collected.

Structures are also fabricated at different energies (1 µJ, 635 nJ, 168 nJ, and 33 nJ) and different scanning speeds to study the formation of micro-craters in detail. The aspects of formation of craters (buried) at different energies and with different scanning speeds and size of craters obtained are tabulated in Table 3. Figure 10 (a) shows the confocal microscope image of a buried single micro structure in PS fabricated at 1 µJ energy and 1 mm/s speed. For the same energy we observed the appearance of craters when the scanning speed was increased to 2 mm/s. This is depicted clearly in the figure 10 (b), where the formation of microcraters is just onset. The process of formation of micro-craters is evident from the edges of figure 10 (b). Figures 10 (c) and 10 (d) illustrate the confocal microscope images of the craters formed at still higher scanning speeds of 3 and 4 mm/s. From these data we confirmed that by increasing the scanning speed one can reduce the pulse to pulse overlap and the micro-craters can be obtained similar to observations of periodic refractive index modulation observed earlier in glasses [126]. The same trend is noticed even at other energies also.

However, we found that the formation of craters at higher scanning speeds and lower energies show better profiles. This is obvious because the intensity of heat waves generated at each position where the pulse impinges depends on the pulse energy. Hence, at higher energies these intense heat waves travel and overlap with the waves generated at other positions. This leads to the formation of a line instead of a crater. This aspect is highlighted in table 3. As energy is reduced, micro-craters formation occurred at lower scan speeds, indicating the fact that the effect of pulse to pulse overlap controlled by scan speed and the phenomena of generation and propagation of heat waves at each position are important factors in the fabrication of microcraters. Inset of figure 10 (c) shows a model that represents the formation of micro-craters. The pitch '**p**' which is the distance from center to center can be varied by setting the scanning speed according to the relation **p=s/f** where '**s'** is scanning speed and '**f'** is laser repetition frequency which is 1 kHz in our case. L_0 is the overlap region between two consecutive focused spots which is (d-p) where d is the diameter of the spot. The spot size is calculated using the relation $D=1.22\ \lambda/NA$ where D is the diameter of the focused spot, λ is the wavelength and NA is the numerical aperture of the microscope objective used [127-129]. We had used a 40X microscope objective with NA of 0.65 in our experiments. The estimated spot size was 1.55 µm. In our experiments on micro-crater fabrication we observed clear micro-crater formation from 3

mm/s speed onward with different energies as tabulated in table 3. Hence the minimum pitch (**p**) can be taken as 3 µm. As the radius of the focused spot is ~0.75 µm, the micro-craters start appearing for speeds beyond 3mm/s. However, we could obtain minimum crater size of ~2 µm in our experiments owing to the size of the focused spot and continuous translation. The fabrication of these micro-craters is useful in the areas of memory storage devices and photonic crystals [125-135].

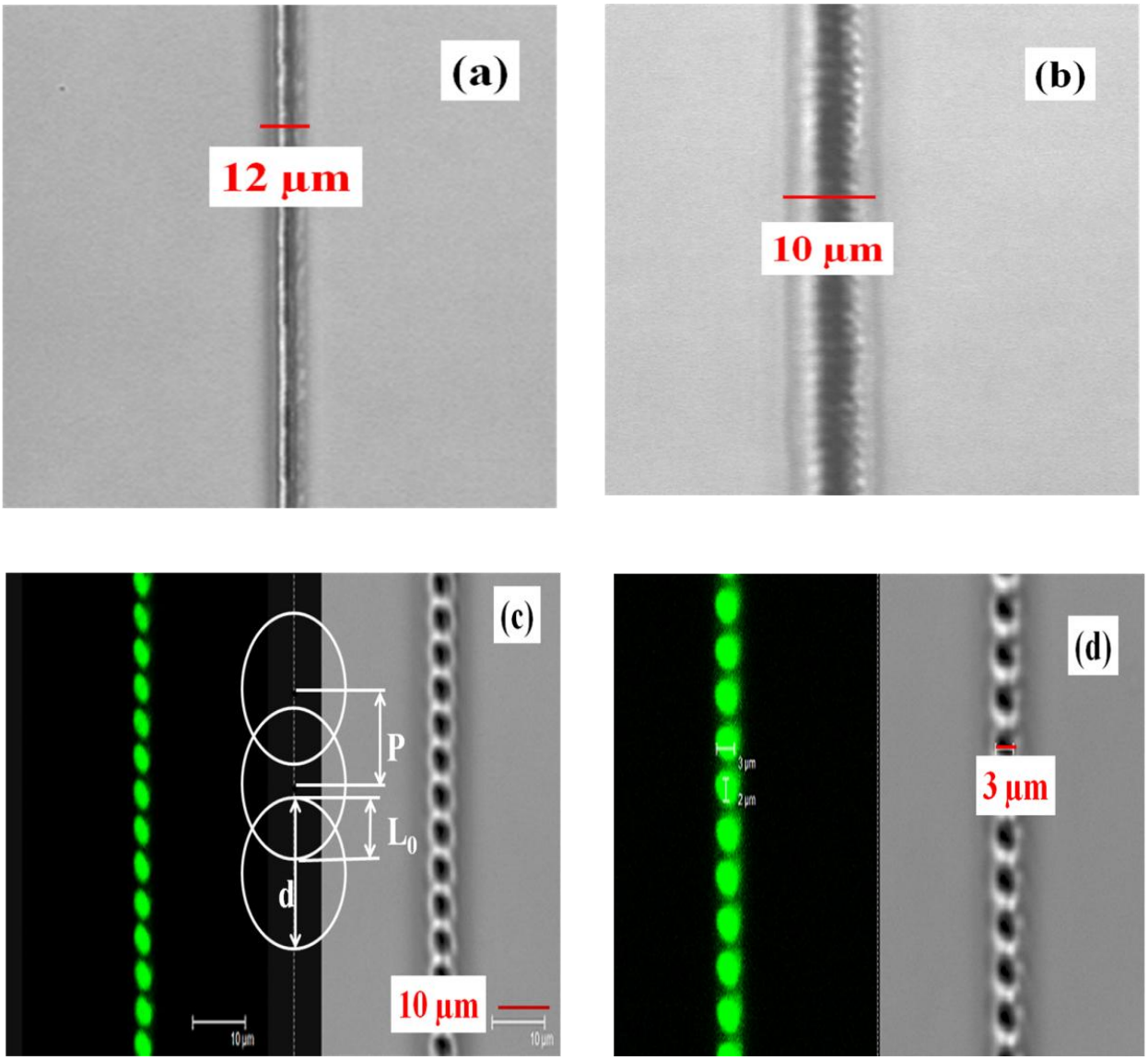

Figure 10. (a) Confocal microscope image of a buried single micro-structure in PS fabricated at 1 µJ energy and 1 mm/s speed. Structure width is ~12 µm. (b) Beginning of formation of micro-craters at the same energy when scanning speed is increased to 2 mm/s. Structure width 10 µm. (c) Scanning speed increased to 3 mm/s and the inset shows model used to fabricate micro-craters (d) Confocal microscope image of the craters formed at still higher scanning speed that is 4 mm/s. Pseudo green color indicates emission from the modified micro-craters when excited at 488 nm wavelength. Crater size is 3 µm.

Table 3. Details of micro-crater structures fabricated at different energies and scanning speeds.

S. No.	Energy (nJ)	Speed (mm/s)	Observation (Line/Crater)	Structure size (μm)
1	1000	1	Line	12
		1.5	Line	10
		2	Line	10
		2.5	Crater formation started	6
		3	Crater	6
		3.5	Crater	4
		4	Crater	3
		4.5	Crater	4
		5	Crater	3
2	635	1	Line	14
		1.5	Line	12
		2	Crater formation started	10
		2.5	Crater	3
		3	Crater	3
		3.5	Crater	3
		4	Crater	3
		4.5	Crater	3
		5	Crater	3
3	168	1	Line	4
		1.5	Crater formation started	3
		2	Crater	2
		2.5	Crater	2
		3	Crater	2
		3.5	Crater	2
		4	Crater	2
		4.5	Crater	2
		5	Crater	2
4	33	1	Line	3
		1.5	Crater formation started	3
		2	Crater	2
		2.5	Crater	2
		3	Crater	2
		3.5	Crater	2
		4	Crater	2
		4.5	Crater	2
		5	Crater	2

Formation of micro-craters is observed even in case of PVA polymer thin film also whose preparation method is described in section 3.4 . Structures are fabricated at different energies and the speed used for microfabrication experiment is 1mm/s. 40X microscope objective is used in these experiments. Three different sets of microstructures are fabricated by focusing the fs laser in different depths of the polymer thin film. Set (a) is when upper portion of the focused spot is inside the film as shown in figure 11. Set (b) is the middle portion of the focused spot is inside the film (50 μm above compared to set 1) and set (c) lower portion of the focused spot is above the film (100 μm above the set 1). These three different sets/configurations are shown as in figure 11 clearly.

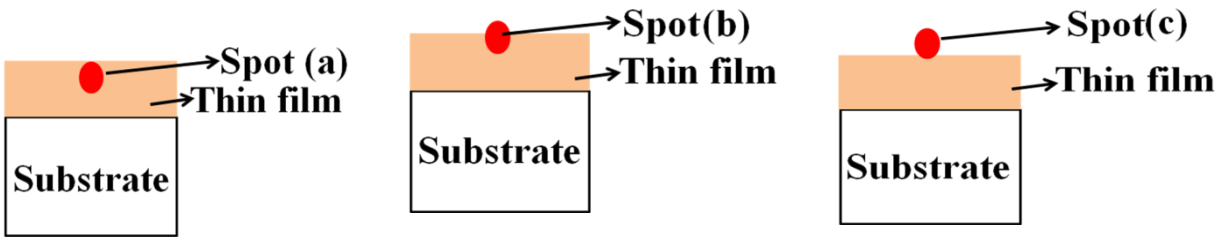

Figure 11. Three different sets/configurations of position of the focused spot.

Figure 12 (a) shows some of the FESEM images of the fabricated microstructures on PVA thin film (60-80 μm thickness). We clearly observed the formation of a trough in the central portion of each structure. It is evident as central portion of the incident Gaussian pulse has more intensity to remove the film which results in void formation. This phenomenon is observed for energies 100 μJ to 10 μJ. Figure 12 (b) shows clearly the formation of trough in the central portion of the microstructure fabricated at 100 μJ energy with 1 mm/s speed. For structures fabricated at low energies typically less than 10 μJ, formation of trough is not observed. Figure 12 (c) shows a plot of width of microstructure as well as trough at each energy for different sets. Widths of microstructures and troughs are found to be increasing with incident energy. For structures fabricated at the same energy, width is found to be more for set (a) compared with set (b) because the total intensity contained in the focused spot is utilized completely for the microfabrication process in case of set (a) unlike set (b) where partial amount of the intensity of the spot is used for the modification process. Formation of micro-craters is set at energy 1 μJ with 1mm/s speed. Structures fabricated at 635 and 564 nJ, clearly showed formation of micro-

craters. Figure 13 (a) shows the structure fabricated at 1 μJ energy, while 13 (b) and 13 (c) show the FESEM images of the microstructures fabricated at 635 and 564 nJ energies with 1 mm/s speed.

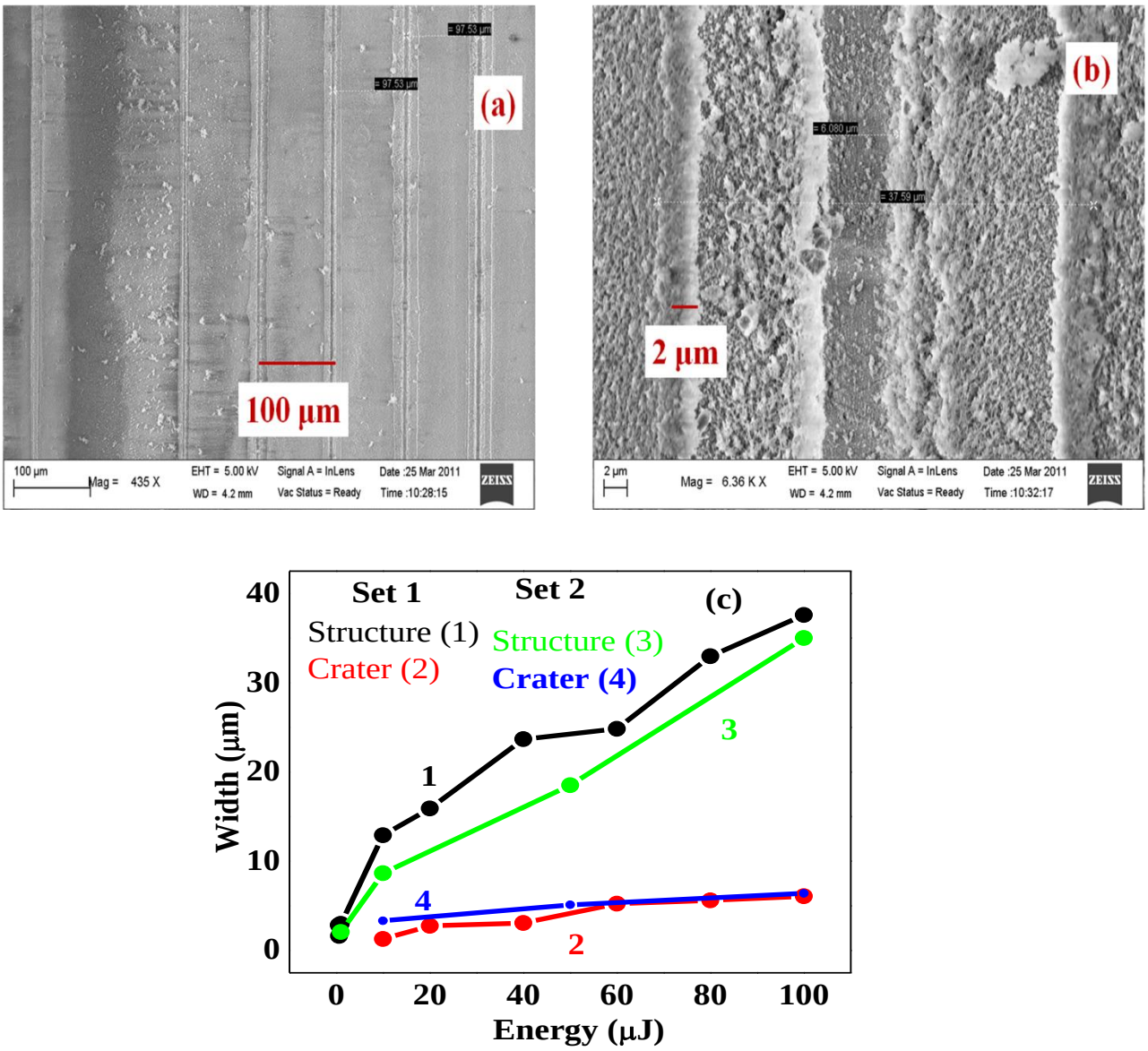

Figure 12. (a) FESEM images of structures fabricated. Structures from right to left indicate the energies from 100-10 μJ in steps of 20 μJ. (b) Microstructure fabricated at 100 J energy, 1mm/s speed. (c) Plot of structure and trough widths with energy.

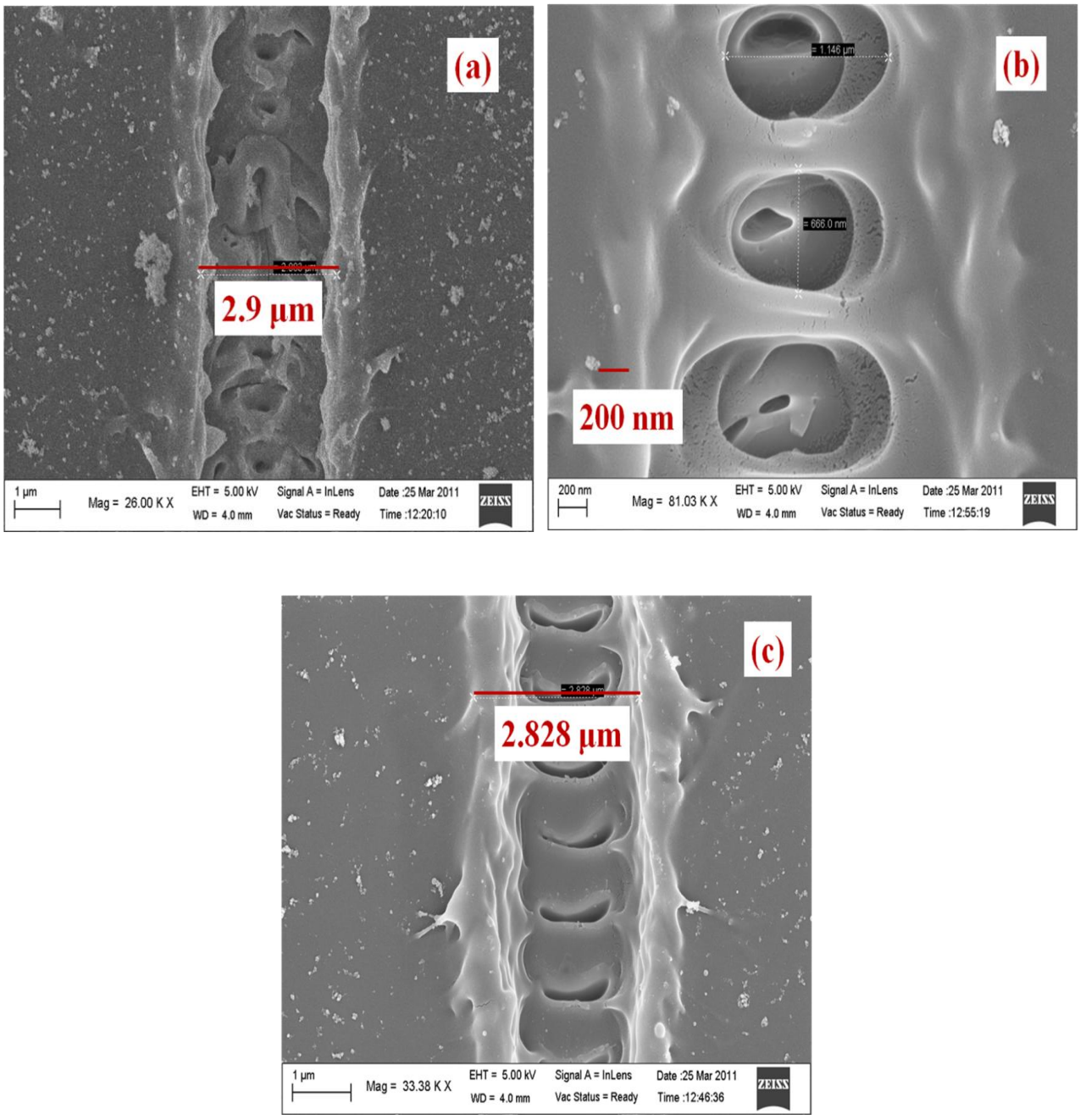

Figure 13. FESEM images microstructure fabricated at 1 mm/s speed, with energy of (a) 1 µJ, (b) 635 nJ, and (c) 564 nJ.

3.6 Fabrication of buried and surface gratings

Buried and surface gratings are fabricated at low and high energies in PMMA, PDMS and PS polymers. Fabricated diffraction gratings at higher energies in PMMA are studied and the dependence of diffraction efficiency (DE) with scanning speed, average energy, and grating period are compared. We follow the following abbreviations for different structures. First four letters represents the material (PMMA or PDMS). Next two letters represent grating type: whether buried (BG) or surface grating (SG). Next two numbers represent a particular writing condition (period, energy and scanning speed). Last character represents whether it is written at higher energy (H) or lower energy (L).Table 4 enlists the different writing conditions of fabrication and their diffraction efficiencies. The gratings that are fabricated at high energies result in the modification that is purely void type which is confirmed from SEM images of cross-sections of such structures (shown in figures 4 (c) and 4 (d)).

For structures written with typical energies <2 μJ in case of PMMA, we could confirm through confocal, SEM, Raman spectroscopic studies that the change is purely refractive index based without the presence of any voids as structures resulted at these energies do not lead to formation of any defects. For structures written with energies typically >2 μJ and <50 μJ the modification is refractive index change combined with voids formation. For structures >50 μJ there was clear indication of empty channel formation within the bulk. Even the empty channels obtained with such high energies enabled us to fabricate grating structures. The refractive index of bulk PMMA is taken as ~1.49 where as the refractive index of the empty channel is assumed to be ~1 (air) enabling the contrast sufficient to produce diffraction pattern. Thirteen gratings were fabricated with different writing conditions such as (a) energy varying from 50 μJ to 200 μJ, (b) speeds varying from 0.25 mm/s to 1 mm/s, and (c) variation with period.

Five of these thirteen gratings have not exhibited any diffraction pattern owing to overlap of the structures, which is later confirmed through laser confocal imaging studies. The estimated diffraction efficiencies ranged from 3.5% to 34% depending on the writing conditions. Diffraction efficiency (DE) of m^{th} order is calculated as the ratio of the power transmitted in the m^{th} order with the incident power. In all our experiments, we used a He:Ne laser (633 nm wavelength) to measure and calculate %DE. A highest diffraction efficiency of ~34% was

achieved for the grating written with ~50 μJ energy and 0.25 mm/s scanning speed. This represents one of the highest diffraction efficiencies reported in PMMA gratings achieved using femtosecond pulses. Figure 14 (a) shows a typical confocal image of the diffraction grating (60 μJ, 0.5 mm/s) achieved using 0.65 NA (40X) objective lens. Figure 14 (b) shows the confocal image of a single structure clearly demonstrating the formation of empty channel within the bulk. Figure 14 (c) shows the diffraction pattern obtained using a He-Ne laser. Table 5 enlists all the writing parameters and diffraction efficiencies obtained in PMMA gratings.

Table 5. Grating data written with high energies for PMMA using 40X objective.

S. No.	Code	Average Energy (µJ)	Speed (µm/s)	Period (µm)	First Order % DE
1	**PMMABG1H**	150	500	8	14.3
2	**PMMABG2H**	200	500	8	3.5
3	**PMMABG3H**	200	500	10	No Pattern
4	**PMMABG4H**	200	800	10	No Pattern
5	**PMMABG5H**	200	1000	10	No Pattern
6	**PMMABG6H**	60	500	50	14.0
7	**PMMABG7H**	60	500	25	20.0
8	**PMMABG8H**	60	500	10	5.6
9	**PMMABG9H**	60	500	5	No Pattern
10	**PMMABG10H**	50	1000	15	8.9
11	**PMMABG11H**	50	250	15	**34.0**
12	**PMMABG12H**	50	750	15	No Pattern
13	**PMMABG13H**	50	500	15	6.5

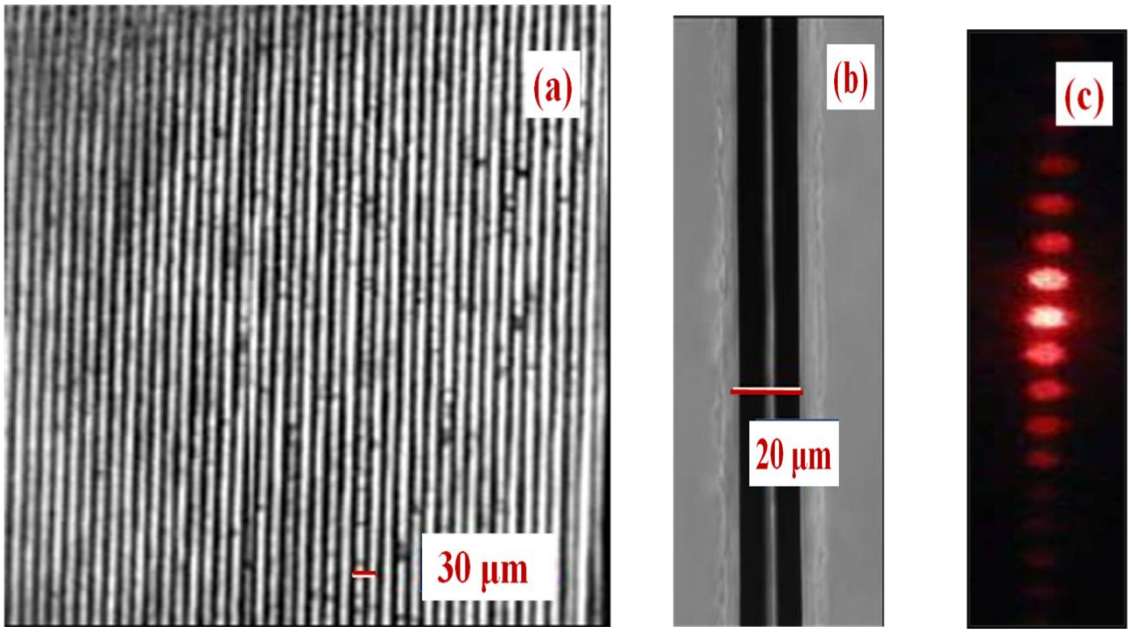

Figure 14. (a) Confocal optical microscopic image of buried grating (~60 µJ, 0.5 mm/s) (b) Zoomed optical image of a single structure indicating void/empty channel formed with a width of 20 µm (c) diffraction pattern with a first order efficiency of 20%.

At low input energies and by single scan method, six buried gratings were fabricated by means of different writing conditions in PMMA and PDMS samples. Table 6 summarizes the writing conditions used for all such gratings in PMMA, structure parameters determined, and the results obtained from diffraction efficiency measurements. The nomenclature followed for different gratings is as follows. For e.g., in PMMABG1 first four letters indicate the material, BG indicates buried gratings, 1 represents a grating written with particular writing conditions. Typical widths of the structures were 8-10 µm achieved with a writing speed of 0.5 and 1.0 mm/sec. A maximum first order diffraction efficiency (defined as the power in first order to the input power) of 7.55% was achieved using these conditions in PMMA.

Table 6. Grating data written with low energies [0.65 NA (40X) for BG1-BG3 and 0.4 NA (20X) for BG4-BG6] for PMMA (Goodfellow).

S. No.	Buried Gratings	Order	Left Side (mW)	Right Side (mW)	Average (mW)	%DE
1	**PMMABG1** (~3 μJ, 1 mm/s, 15 μm period, width 8 μm)	0	2.5			47.17
		1	0.5	0.3	0.4	**7.55**
		2	0.2	0.1	0.15	2.83
		3	0.1	0.1	0.1	1.89
2	**PMMABG2** (~3 μJ, 0.5 mm/s, 20 μm period, width 10 μm)	0	3.6			67.92
		1	0.3	0.2	0.25	**4.72**
		2	0.2	0.1	0.15	2.83
		3	0.1	0.1	0.1	1.89
3	**PMMABG3** (~6 μJ, 1 mm/s, 20 μm period, width 8 μm)	0	3.6			72
		1	0.2	0.3	0.25	**5**
		2	0.2	0.2	0.2	4
		3	0.1	0.1	0.1	2
4	**PMMABG4** (~3 μJ, 1 mm/s, 15 μm period, width 8 μm)	0	0.2			3.85
		1	0.1	0.1	0.1	**1.92**
		2	0.1	0.1	0.1	1.92
		3	**Very weak**			
5	**PMMABG5** (~3 μJ, 0.5 mm/s, 20 μm period, width 10 μm)	0	0.2			3.77
		1	0.1	0.2	0.15	**3.77**
		2	0.1	0.1	0.1	1.89
		3	0.1	0.1	0.1	1.89
6	**PMMABG6** (~6 μJ, 1 mm/s, 20 μm period, width 8 μm)	**No Pattern was observed**				

Figure 15 (a) shows another typical buried grating in PMMA while figure 15 (b) shows the emission, collected in the confocal geometry, from a single structure. The emission is absent in the data collected from pristine PMMA. The depths of the grating are 20-30 μm measured from the confocal images of cleaved and polished sample cross-sections. Figure 15 (c) shows the corresponding diffraction pattern obtained. Figure 15 (d) shows the geometry for collecting the emission from a single structure using confocal technique. We could clearly see that the top and bottom regions of the modified structure showed emission as middle portion results in void formation. The details of collection of emission and the origins of emission will be explained in the next chapter.

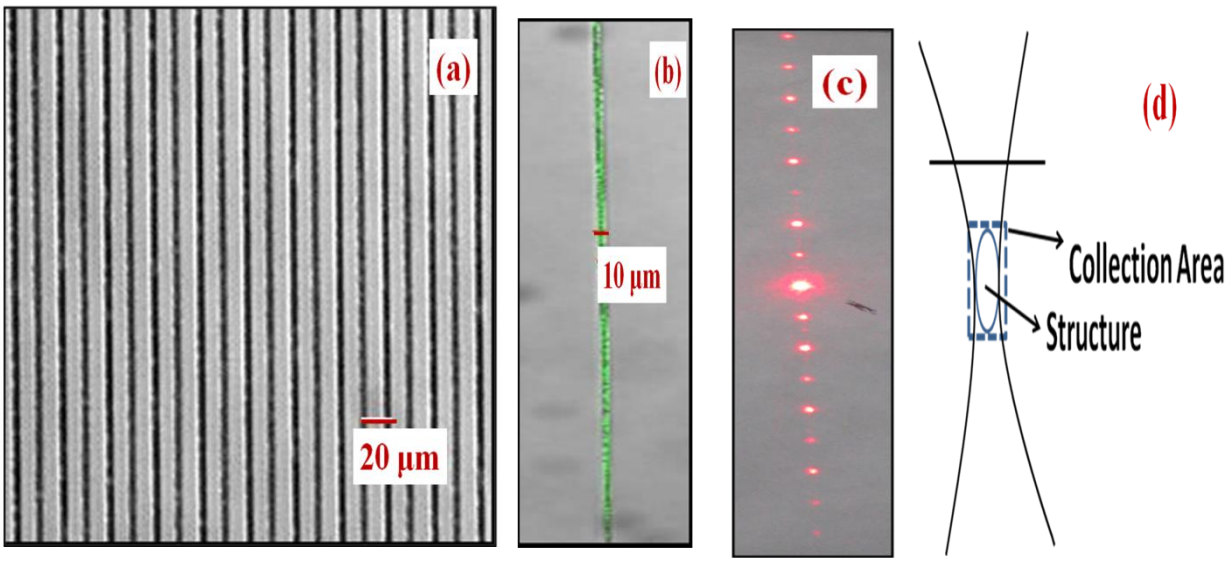

Figure 15. (a) Confocal optical microscope image of grating PMMABG2 (~3 μJ, 0.5 mm/s, 20 μm period, width 10 μm) and (b) Image of a single structure with emission from the irradiated regions indicated by the pseudo green color (c) Diffraction pattern from the grating (d) The geometry used in collecting the emission from the structures.

Surface gratings are achieved in PMMA with different input energies. We investigated the quality of these gratings and compared their performance with those of buried gratings. Figure 16 depicts typical gratings achieved on the PMMA surface. Table 6 illustrates surface gratings (SG) written with 0.65 NA (40X) objective in PMMA and PDMS (PMMASG1 to PMMASG3

and PDMSSG1 to PDMSSG3). PMMASG1 had a DE of 0.83% while the buried counterpart grating PMMABG1 (similar writing conditions) had a DE of 7.55%, probably due to better RI contrast in the latter case. The debris collected on the surface gratings could have influenced in reducing the RI contrast. However, PMMASG2 (~6 μJ, 1.0 mm/s) had a DE of 5.83% better than the DE of PMMABG2 (~3 μJ, 0.5 mm/s) which was 4.72%. With the identical conditions used for writing surface gratings, two dimensional crossed gratings (one set of structures and another set written perpendicular to the first one) were also attempted. Figure 17 and 18 display confocal and SEM images of such crossed gratings in PMMA and PDMS.

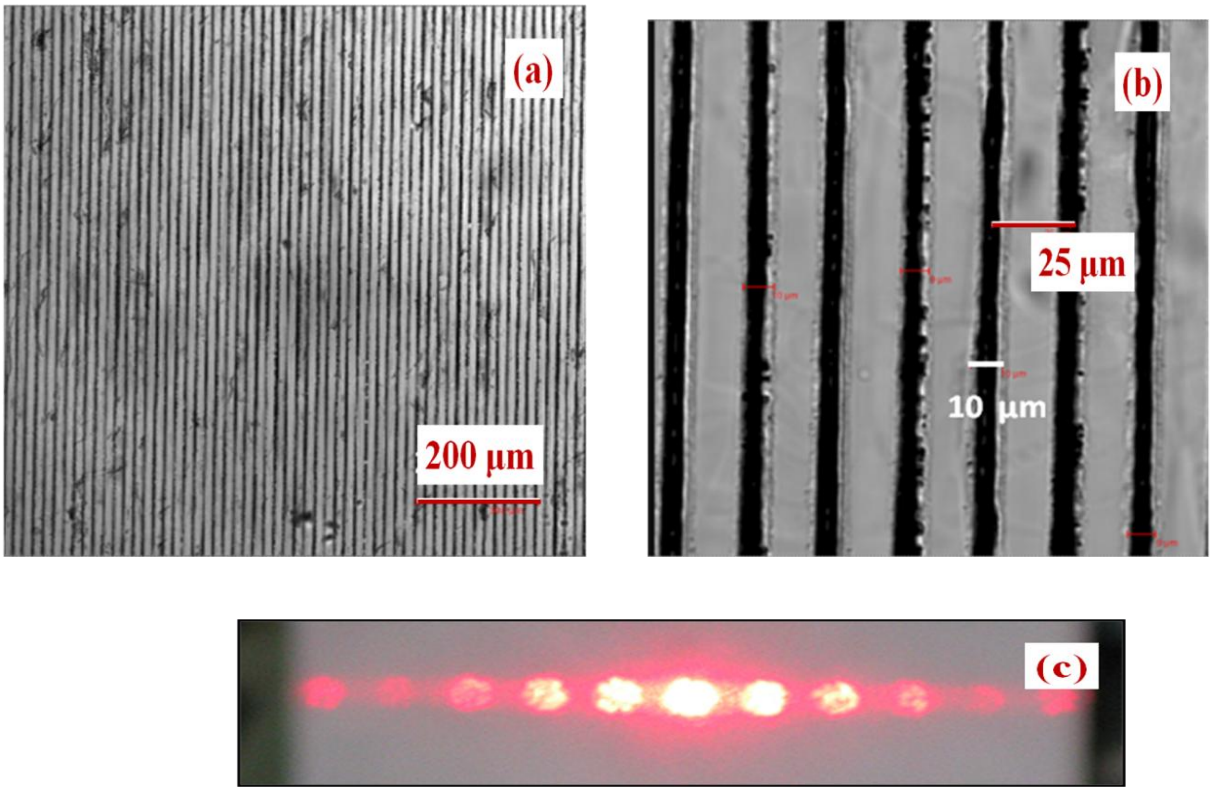

Figure 16. (a) Laser confocal images of surface gratings in PMMASG2 and their corresponding diffraction images. Scale bar in (a) is 200 μm. Energy used was ~6 μJ, writing speed of 1 mm/sec, width 10 μm, and spacing 25 μm with 0.65 NA (40X) objective (b) Magnified view of the grating (c) Diffraction pattern from the grating.

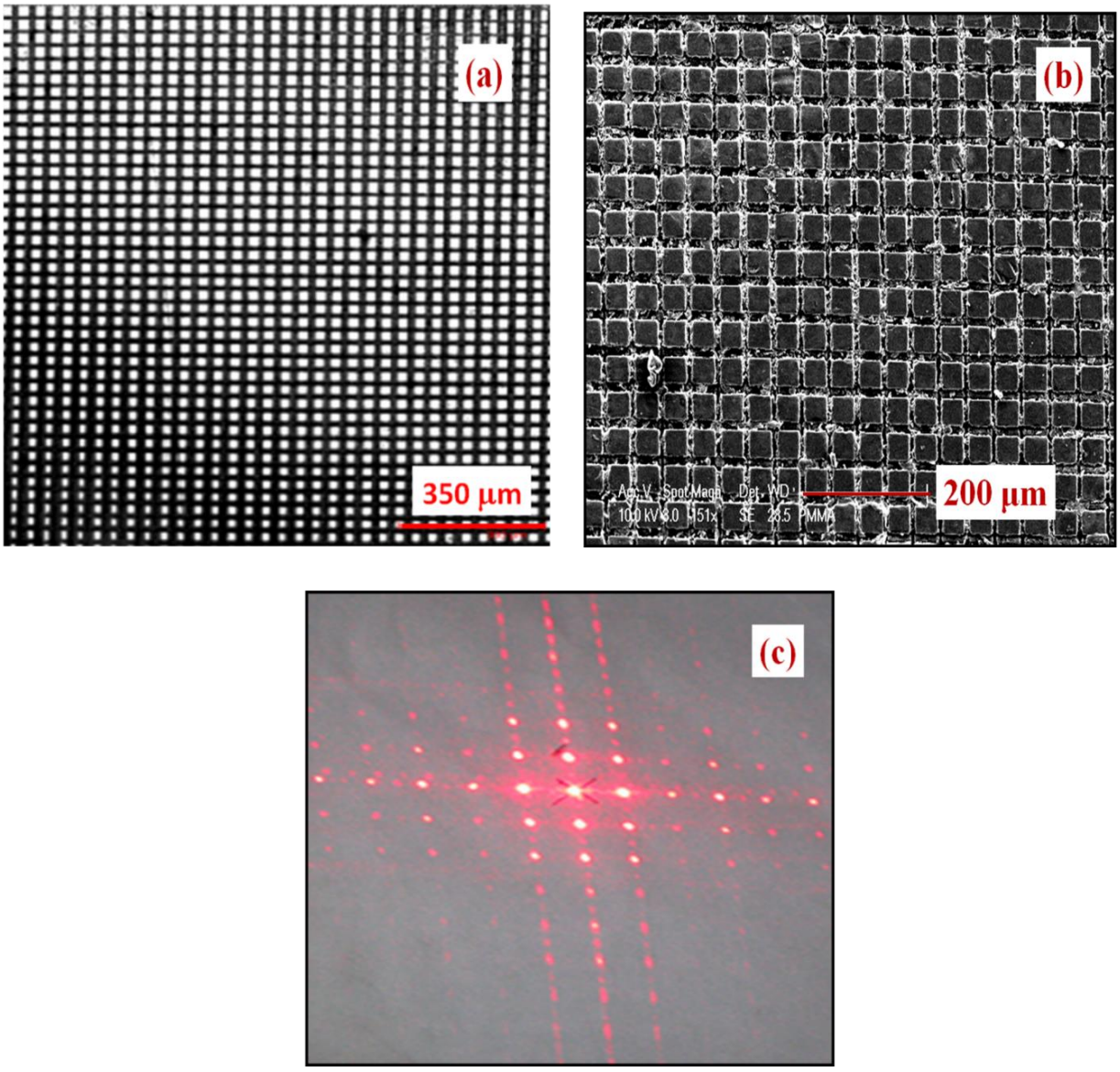

Figure 17. (a) Laser confocal images of two dimensional surface gratings in PMMASG3 (Goodfellow) using 0.65 NA (40X) objective. Scale bar is 350 µm (b) corresponding SEM image of the two dimensional surface grating. Scale bar is 200 µm (c) diffraction pattern observed from the grating. Energy used was <25 µJ, writing speed of 1 mm/sec, width 22 µm, and spacing 35 µm with 40 X objective.

Table 7. Data for surface gratings in bulk PMMA (Goodfellow) and bulk PDMS written with 0.65 NA (40X) objective.

Surface Gratings	Energy (~µJ)	Period (µm)	Speed (mm/s)	Width (µm)	0^{th} Order % DE	1^{st} Order % DE	2^{nd} Order % DE	3^{rd} Order % DE
PMMASG1	**3**	18	1	9	1.83	**0.83**	0.3	0.17
PMMASG2	**6**	25	1	10	46.83	**5.83**	2.17	0.83
PMMASG3	**30**	35	1	22	45.67	**4.66**	0.66	1.42
PDMSSG1	**3**	12	1	8	4.59	**2.6**	1.4	0.57
PDMSSG2	**6**	30	1	15	32.73	**9.6**	0.66	0.74
PDMSSG3	**30**	65	1	30	34	**7.7**	2.22	0.49

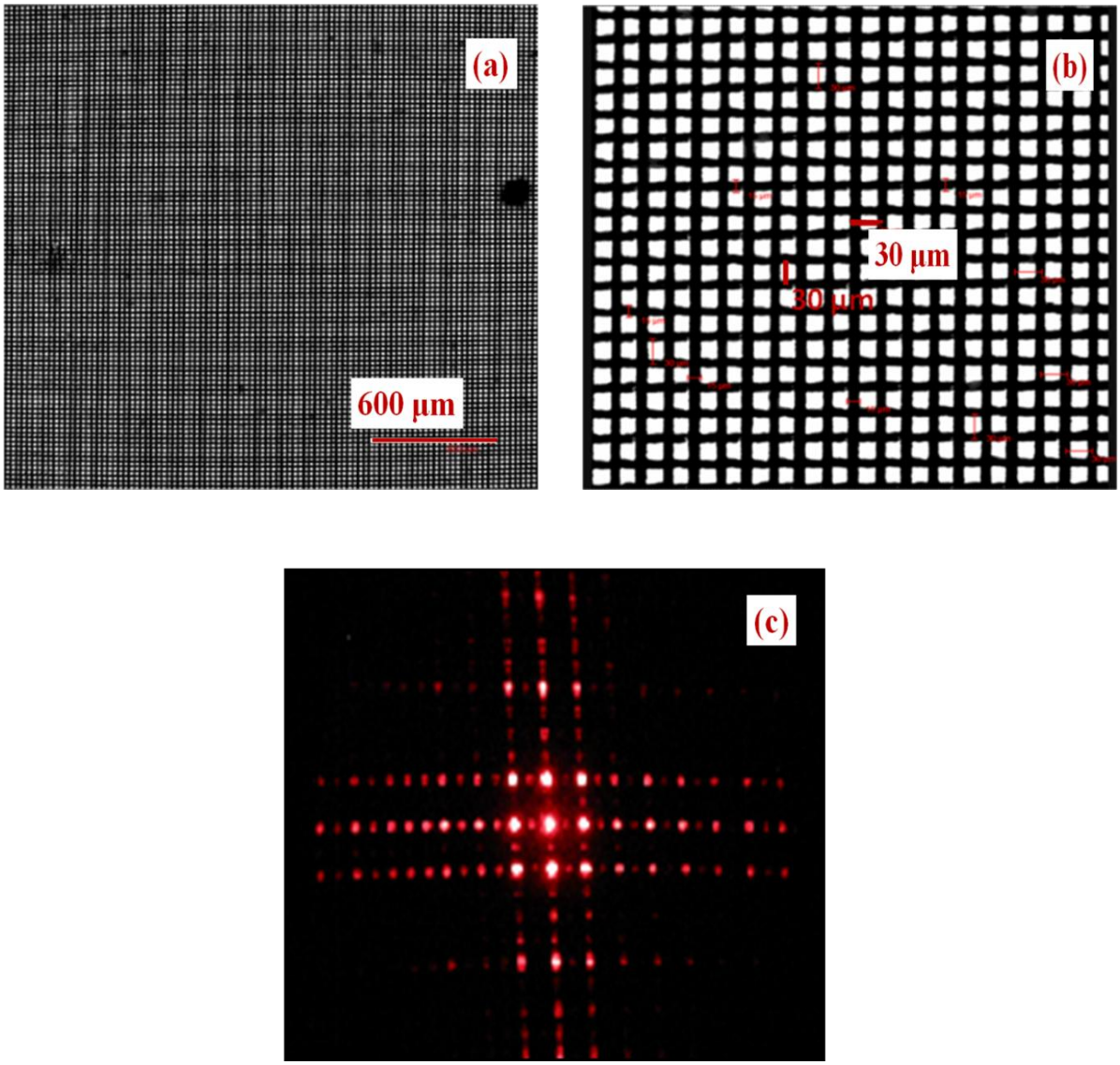

Figure 18. (a) and (b) A typical 2-d grating written in PDMS and (c) the corresponding diffraction pattern. Scale bar in (a) is 600 µm and typical period in (b) is 30 µm.

Six gratings are fabricated on PDMS (PDMSBG1 to PDMSBG6) using single-scan method with different writing conditions. The structural widths of PDMSBG1, PDMSBG2 and PDMSBG3 were ~9, 13, and 16 µm, confirmed through the confocal data. PDMSBG4, PDMSBG5 and PDMSBG6 were accomplished with similar writing conditions to PDMSBG1, PDMSBG2 and PDMSBG3 except that a 0.4 NA (20X) objective was used. We observed diffraction orders ranging from 8 to 12 for all the gratings. We calculated the diffraction efficiencies (DE) at 633 nm with a He-Ne laser. The first order DE (defined as the ratio of power diffracted into first order to the input power) of PDMSBG1, PDMSBG2 and PDMSBG3 were 10%, 7.7%, and 5%, respectively, while the second order diffraction efficiencies were 1.66%, 3.1%, and 1.66%, respectively. Our results obtained on buried diffraction gratings in PDMS are tabulated in table 5. These correspond to an enhancement in first order efficiency by ~70% compared to that reported by Cho et al. [136].

They had obtained a maximum diffraction efficiency of 6% for the first order, 1.9% for the second order, and 0.5% for the third order. They employed tighter focusing conditions (0.85 NA) while we used a 0.65 NA (40X) objective. We have also tried fabricating the gratings with 0.4 NA (20X) objective with similar conditions (energy, speed etc.) to understand the structure behavior with varying focal situations. For the case of PDMSBG4 and PDMSBG6 we could not observe any diffraction pattern and the reason, later confirmed through confocal images, was mixed up structures due to increased width. However, for the case of PDMSBG5 we observed good diffraction pattern and the efficiency calculated was 3.18%. Gratings written with larger spacing and using 0.4 NA (20X) objective lens were achieved recently and our recent optical studies point towards lower diffraction efficiencies compared to PDMSBG1, PDMSBG2, and PDMSBG3. These data suggests that the optimal focusing conditions were achieved with a 0.65 NA (40X) objective.

Baum et al. [137-138] reported diffraction efficiencies of 10% in PMMA obtained with ~110 fsec pulses but with 10 repeated scans. They noticed that as the pulse width decreased the efficiency of the gratings increased with the best efficiency of 35% obtained for gratings written with 45 fsec pulses and 14 repeated scans. Similarly for PDMS we expect to enhance the diffraction efficiency further through (a) repeated scans and (b) utilizing even shorter pulses.

PDMSBG3 (~5 μJ, 1.0 mm/s) had a DE of 5% while the corresponding surface grating PDMSSG2 (~5 μJ, 1.0 mm/s) had a diffraction efficiency of 9.6% clearly suggesting the RI contrast being higher in the latter case.The depths of buried gratings PDMSBG1, PDMSBG2, and PDMSBG3, measured from SEM images, were 34, 20, and 26 μm, respectively. We calculated the RI changes (assuming a smooth variation though the SEM images indicate the presence of small voids) for PDMSBG1, PDMSBG2 and PDMSBG3 to be ~1.9×10^{-3}, ~2.9×10^{-3} and ~1.8×10^{-3}, respectively according to the formula [139-140].

$$\Delta n = \frac{\lambda \cos\Theta \tanh^{-1}\sqrt{\eta}}{\pi d}$$

where Δn = refractive index change, λ = wavelength of light used, η = diffraction efficiency, d = grating thickness/depth, Θ = angle between normal and incident direction of light used = 0°.

Similar calculations were performed for PDMSBG5. These values were calculated from the diffraction efficiency data and structure parameters such as depth of the grating [139-140]. There could be an error of ±20% in the RI change estimates arising from uncertainties in depth measurements and DE calculations. Table 8 summarizes the data obtained for all the gratings studied. To gain knowledge about the physical changes in laser-modified region we cut the sample transversely, polished, and coated them with gold for conduction and viewed the structures with a scanning electron microscope (SEM). The result presented in figure 19 (a) portrays the depth of structures from the surface and figure 19 (b) illustrates the cross-sectional SEM image of a sliced structure. It is evident from these pictures that the gratings were formed ~400-600 μm below the surface and depth of the gratings varied from 20 to 30 μm. The pictures also ascertain, to an extent, that the physical changes such as localized heating, melting, and re-solidification at the focal volume (leading to higher density) to be the mechanism responsible for RI change.

Table 8. Summary of the structures written in PDMS using both 0.65 NA (40X) and 0.4 NA (20X) objectives. A highest diffraction efficiency of ~10% was recorded for PDMSBG1.

Buried Gratings	**Energy (~μJ)**	**Speed (μm/s)**	**Per. (μm)**	**Width (μm)**	**Depth (μm)**	**%DE 0^{th} Order**	**% DE 1^{st} Order**	**%DE 2^{nd} Order**	**Δn ($\times 10^{-3}$)**
PDMSBG1	**3**	1000	15	9	34	18.3	**10**	1.66	1.94
PDMSBG2	**3**	500	20	13	20	9.24	**7.7**	3.1	2.87
PDMSBG3	**5**	1000	20	16	26	5	**5**	1.66	1.76
PDMSBG4	**3**	1000	15	**No grating formed**					
PDMSBG5	**3**	500	20	14	10	4.61	**3.18**	1.86	3.50
PDMSBG6	**5**	1000	20	**No grating formed**					

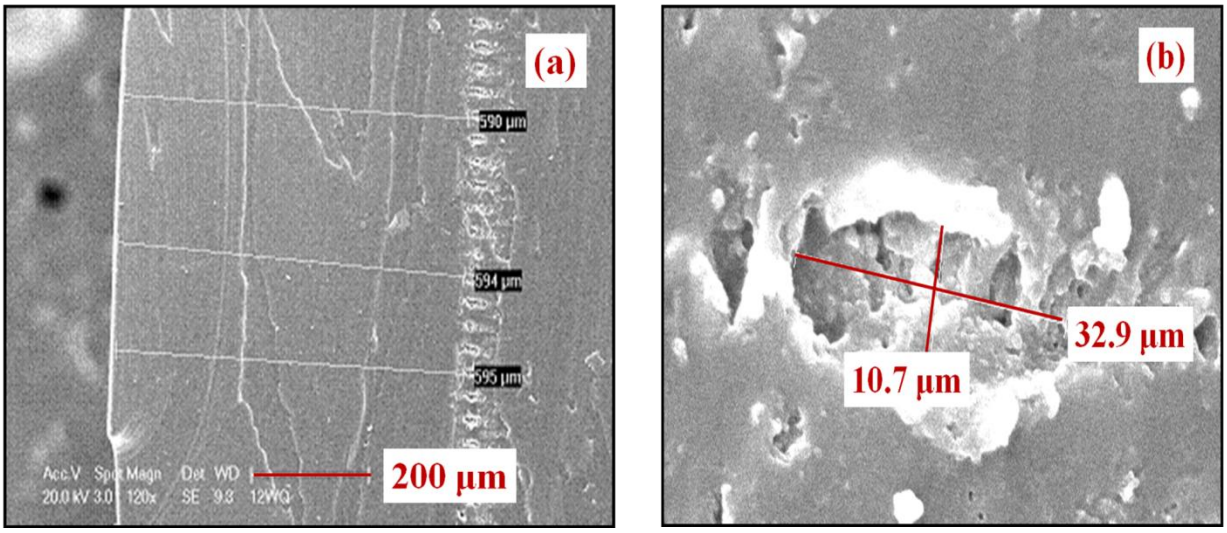

Figure 19. (a) SEM picture of PDMSBG1 grating and the modified region (595 µm below the surface) and (b) SEM picture of cross-sectional view of a typical microstructure.

Several buried diffraction gratings are fabricated in the bulk of PS using fs pulses at different scanning speeds, energies and periods. Details of various parameters used in the fabrication of these gratings are tabulated in Table 6. Each grating with its particular set of writing parameters is given a code for simplicity. The confocal microscope images of PSG1 and PSG3 are shown in figure 9 (a) and 9 (c). There are sparse reports in the literature available on the fabrication of diffraction gratings in PS. We obtained maximum %DE of 10% for a particular diffraction grating fabricated at 1 µJ energy, 1mm/s speed with 30 µm period. PSG3, PSG4, and PSG5 resulted in poor %DE as the resultant structures after fabrication were found to be arrays of microcraters instead of straight line due to minimal pulse to pulse overlap, explained already in earlier section.

Hirono et al. [141] have reported an increment in the DE of gratings in Poly Methyl Meth Acrylate (PMMA) obtained with 120 fs pulses through heat treatment at 70 °C for 500 hours. The efficiency recorded is 1.9% before heat treatment and increases to 72% after heat treatment. They attributed the increase due to the increase in induced RI change after heating and suggested the physical mechanism responsible could be volume contraction at the irradiated region. Table 9-10 show the writing conditions and %DE results obtained with gratings fabricated in PS before and after heat treatment. PS gratings are heated for 720 hours at 50°C. PMMA and PDMS

gratings are heat treated for 384 hours at 70°C initially and 552 hours at 80°C later to improve diffraction efficiency. We found no appreciable improvement in %DE upon thermal treatment given to these gratings. Since most of these gratings are fabricated at higher energies, the modification in the fs laser irradiated regions would be of void type. Therefore, we did not observe any appreciable increment in the DE with thermal treatment. Also, table 11 enlists the % DE incase of heated diffraction gratings in PMMA and PDMS.

Table 9. Details of micro fabrication of Gratings in PS.

S. No.	Terminology	Energy (μJ)	Speed (mm/s)	Period (μm)	Width (μm)	Type of structure
1	PSG1	1	0.5	30	16	Line
2	PSG2	0.635	0.5	30	21	Line
3	PSG3	0.033	0.5	30	3	Line
4	PSG4	0.033	3	30	2	Crater
5	PSG5	1	3	30	4	Line
6	PSG6	1	2	50	11	Line
7	PSG7	1	0.5	100	20	Line
8	PSG8	1	2	30	5	Line
9	PSG9	1	1	30	12	Line
10	PSG10	1	1	20	11	Line
11	PSG11	1	1	50	12	Line

Table 10. Details of gratings in PS before and after heat treatment.

S. No.	Grating type	Before thermal treatment (Percentage of DE)				After thermal treatment (Percentage of DE)			
		0^{th} order	1^{st} order	2^{nd} order	3^{rd} order	0^{th} order	1^{st} order	2^{nd} order	3^{rd} order
1	PSG1	27.1	8.3	0.65		14	4.96	0.4	
2	PSG2	21.2	7.95	0.40		46	6.87	1.7	0.26
3	PSG3	93	0.26	0.49		82	0.43	0.4	0.32
4	PSG4	96	0.19	0.17		90	0.43	0.18	
5	PSG5	85	0.13	0.74		96	0.328	0.3	
6	PSG6	66	3.65	1.5		72	2.21	1.6	0.89
7	PSG7	48	6.63	3.11	0.58	64	4.28	2.61	
8	PSG8	88	3.68	0.86	0.4	86	1.13	0.74	
9	PSG9	30	10	1.3		31	7.2	0.68	
10	PSG10	20	6.8	0.25		7	3	0.47	
11	PSG11	65	1.79	1.07	1	43	2.27	1.44	

Table 11. Data of DE of various gratings after heat treatment in PMMA and PDMS.

S. No.	Particulars		% DE for 0^{th} order	% DE for 1^{st} order	% DE for 2^{nd} order
1	PMMABG1L (40X, 3 µJ, 1mm/s, 15 µm period)	Initial	47	7.6	2.8
		Heat Treatment at 70°C for 384 hours	61	6.1	6.1
		Heat Treatment at 80°C after 552 hours	59	4.84	1.24
2	PMMABG2L (40X, 3 µJ, 0.5 mm/s,20µm, Period)	Initial	68	4.72	2.8
		Heat Treatment at 70°C for 384 hours	80	3.1	3.1
		Heat Treatment at 80°C after 552 hours	81	1.8	1.2
3	PMMABG3L (20X, 6 µJ, 1 mm/s, 20 µm period)	Initial	-	-	-
		Heat Treatment at 70°C for 384 hours	0.58	0.39	0.39
		Heat Treatment at 80°C after 552 hours	7.61	3.4	0.82
4	PMMASG1L (40X, 3 µJ, 1 mm/s, 18 µm period)	Initial	1.83	0.83	0.3
		Heat Treatment at 70°C for 384 hours	13.27	2.79	0.67
		Heat Treatment at 80°C after 552 hours	88.27	2.37	0.21
5	PMMASG2L (40X, 5 µJ, 1 mm/s, 25 µm period)	Initial	46.83	5.83	2.17
		Heat Treatment at 70°C for 384 hours	51.73	5.1	2.4
		Heat Treatment at 80°C after 552 hours	58.02	6.07	2.4
6	PDMSBG1L (40X, 3 µJ, 1mm/s, 15 µm period)	Initial	18	10	1.66
		Heat Treatment at 70°C for 384 hours	21	9.83	9.83
		Heat Treatment at 80°C after 552 hours	20	9.3	0.55
7	PDMSBG2L (40X, 3 µJ, 0.5 mm/s, 20 µm period)	Initial	9.3	7.7	3.1
		Heat Treatment at 70°C for 384 hours	12	7.24	7.24
		Heat Treatment at 80°C after 552 hours	11	6.54	2.95

3.7 Ablation models

Lippert et al. have reported different theoretical models to explain the ablation phenomena when materials, especially polymers [142] interact with laser pulses. These ablation mechanisms have been studied for more than two decades. As a result, the original separation of the models such as photo-chemical models by chemists and photo-thermal models by physicists is blurring. Ablation can change the chemical and/or physical properties of the polymer resulting in modified chemical composition, altered optical absorption and electrical conductivity [142]. Polymers consist of long molecular chains with strong covalent bonds binding the atoms and monomers. Also, at the same time, molecules belonging to different chains interact weakly. Thus the polymer material can be treated as a simple molecular solid. These polymer chains can easily be broken into small pieces by direct photochemical effect through UV photons as UV photons posses energy exceeding the energy of covalent bond. Hence, this model can be treated as photochemical model. But, in case of photothermal model the absorbed energy produces an elevated temperature high enough for thermal destruction of the polymer [142-145].If photons do not have sufficient energy to break covalent bonds, then photo thermal processes occur. Though these terms are used to describe the ablation process, a microscopic description of the processes involved in each mechanism is lacking as clarifying such details is complicated because of the fact that plethora of experimental conditions and material properties can influence an assortment of different molecular events [146].

Several fs photo-modification of PMMA in which an 800 nm wavelength is used and reported differing results about the sign of refractive index change (Δn). Negative Δn are found in the focal volume with a fs oscillator (25 MHz repetition rate) [147], where as positive Δn were observed with 1 kHz regenerative amplifiers [148-149] indicating that the repetition rate influences the modification through thermal effects. However, Baum et al. studied ultrashort-sub ablation threshold photo modification effects in PMMA at UV wavelengths (387 nm) that are not linearly absorbed [137]. They showed direct cleavage of the polymer backbone under formation of monomers, leading to a change in refractive index, Δn. In this way, one can expect that fs laser induced Δn in polymers leading to photochemical process depending on the irradiation parameters resulting in positive or negative Δn [150]. Photo physical model has both thermal and

nonthermal processes playing an important role and this is most adequate for short laser pulses in the ps and fs ranges [151].

In our research work carried out, as energy of the pulses are of the order of μJ, we expect photo thermal model which resulted in the formation of defects leading to emission and paramagnetic free radicals. These results are illustrated in next few chapters. Though we fabricated few structures in PS with nJ energy pulses, we could not carry out further experiment to estimate refractive index change as waveguide stages and polishing setup are under construction. Hence, at this point it is difficult to come to a conclusion whether photochemical model has any role to play in our results.

3.8 Fabrication of double channels and complex structures

As discussed earlier in chapter 1 that structures fabricated at low energy lead to refractive index change would be useful in waveguide applications if the change in positive. However, if the change in refractive index is negative then the region surrounded the fabricated structure has more refractive index. Thus, one can demonstrate waveguides by fabricating double line structures at high energies so that the region in middle (pristine) guides the light. Therefore, to demonstrate the versatility of fs direct writing technique we fabricated four sets of parallel structures in PMMA whose parameters are tabulated in table 12. SS stands for split structure and each set of parameters are given unique terminology to identify the parameters used for fabricating the structures. The exposed regions are expected to form voids with the energies used for writing. Our aim was to create regions of higher refractive index surrounded by regions of lower refractive index for wave guiding applications. If two such structures are fabricated close enough (few microns separation for single mode wave guiding) light can be guided. We used a He: Ne laser for coupling the light into such a structure. Figure 20 (a) and 20 (b) show the confocal microscope images of typical structures and light propagation captured by camera. Out of four structures fabricated three were found to be guiding light except the last one due to merging of the structures. Since these structures are buried, above and below portions of the central wave guiding region possess same refractive index as that of the substrate making it more like a 2-D waveguide.

Table 12. Details of split structures fabricated in PMMA.

Terminology	Energy (µJ)	Scanning Speed (µm/s)	Period (µm)	Width of each structure (µm)	Gap between two structures (µm)
SS1	30	1000	20	18	2
SS2	30	1000	30	14	16
SS3	30	1000	50	18	32
SS4	30	1000	10	MERGED LINES WITH OVER ALL WIDTH 30 µm	

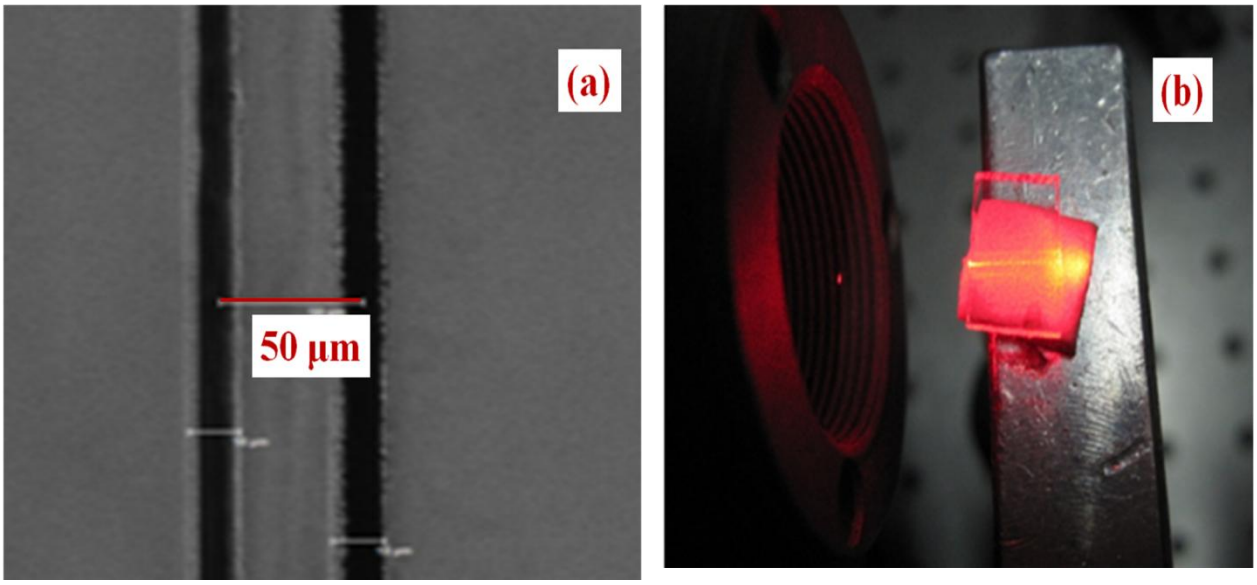

Figure 20. (a) Confocal microscope image of SS3 and (b) coupling of 633 nm light.

Applications in integrated optics require fabrication of waveguides, microfluidic channels, Y couplers and beam splitters. 1:8 beam splitters and Y coupler are fabricated in polymers PMMA, and PDMS. Figure 21 shows beam splitters and Y couplers fabricated in PMMA and PDMS polymers. Pseudo green color represents the emission when excited at 488 nm using confocal microscope. The Y coupler shown in figure 21 (c) was fabricated at 1 µJ energy. Since, the structures fabricated at these energies result in void formation, double lined Y coupler were

fabricated. As explained earlier, the central region which is unmodified between two modified regions will guide the light. This is useful in waveguide applications when (a) structures are fabricated at high energies (b) materials that show refractive index change negative even at low energies. Figure 22 shows the part of shape 8 fabricated in PMMA. Since the image is big, part of 8 shape which is curved is shown. Figure 23 shows a microstructure fabricated on the surface of a PDMS polymer with 15 μJ energy, 0.05 mm/s speed with 40X microscope objective. We prepared Rhodamine B solution to demonstrate the microfluidic channel. 4.79 mg of Rhodamine B was mixed with 200 ml of distilled water (5×10^{-5} M) and stirred for half an hour for complete miscibility. Rhodamine B solution is injected into the channel and excited at 543 nm wavelength. We observed emission of Rhodamine B in the channel when solution is slowly flowing into the channel. Pseudo red color represents the emission of Rhodamine B which is in the channel.

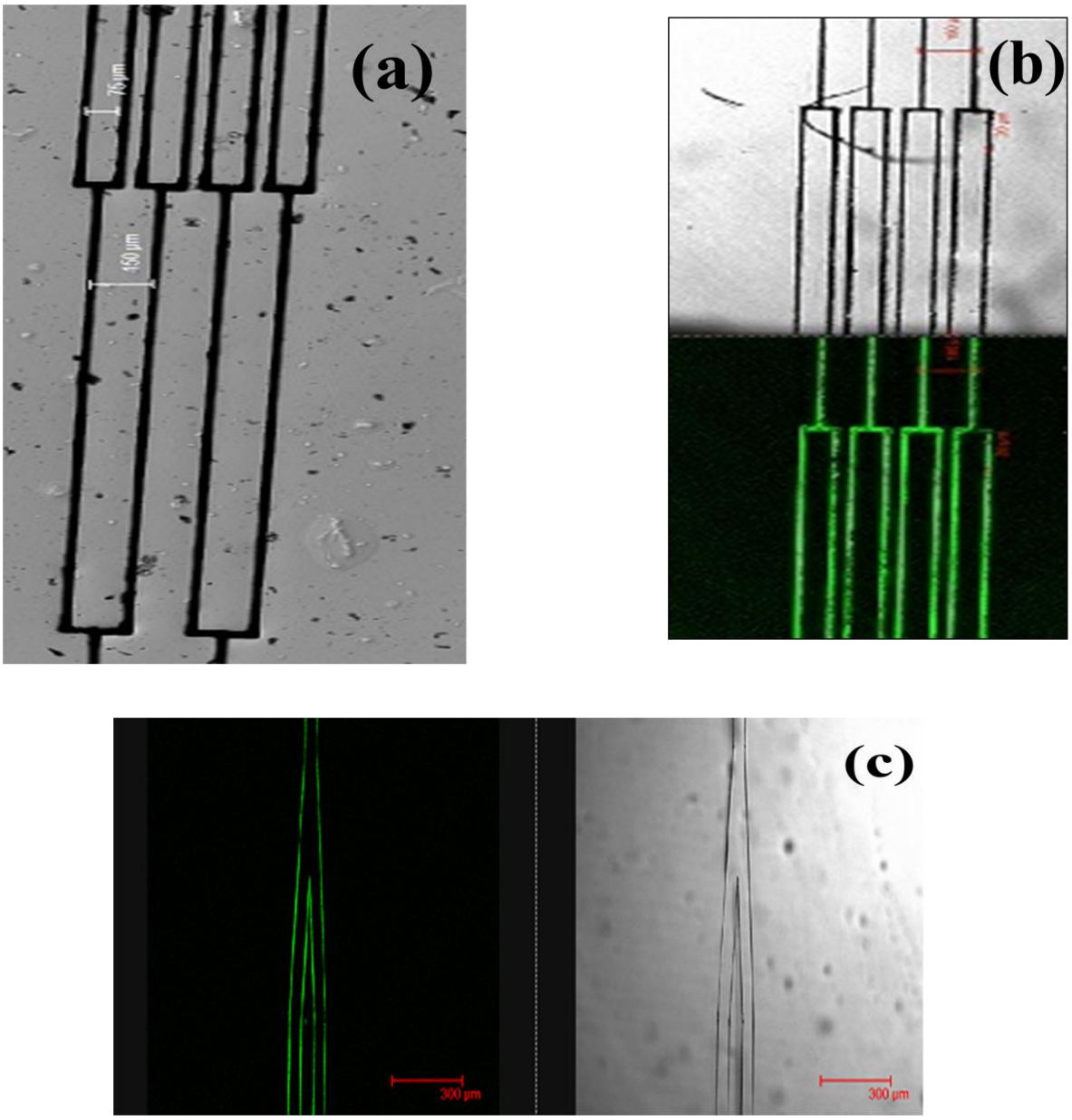

Figure 21. Confocal microscope image of (a) a branched surface structure (1:8 splitter) in PDMS (15 µJ and 0.05 mm/s speed, width 50 µm) (b) 1:8 splitter on surface PMMA (15 µJ with 0.05 mm/s). Pseudo green color represents emission when excited at 488 nm. Since image is large, part of the structure is shown. (c) Double Y coupler fabricated inside PMMA with 1 µJ energy, 1mm/s speed. Pseudo green color represents emission when excited at 488 nm. Pseudo green color represents emission when excited at 488 nm. Since image is large, part of the structure is shown.

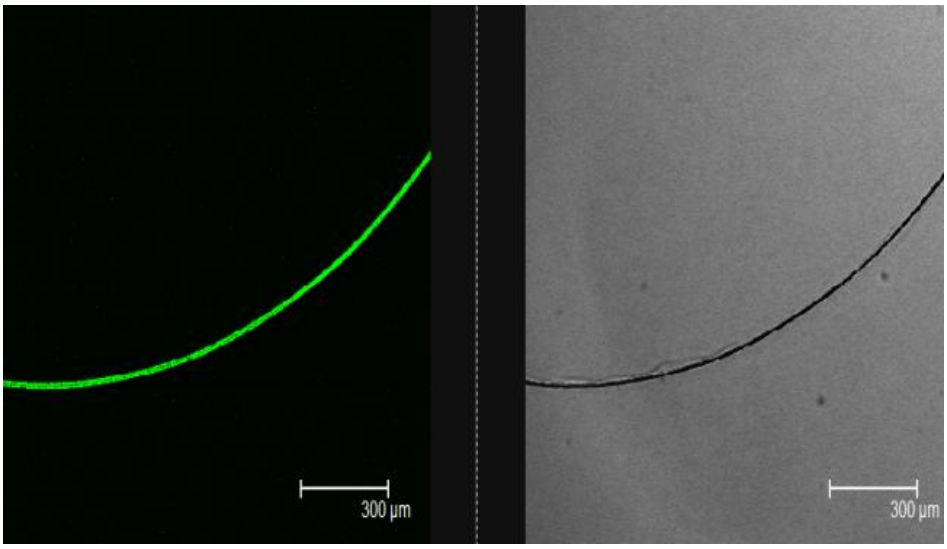

Figure 22. Part of the shape 8 fabricated in PMMA. Pseudo green color shows emission from the modified region excited at 488 nm. Scale bar is 300 µm. As image is large, only parts of image are captured.

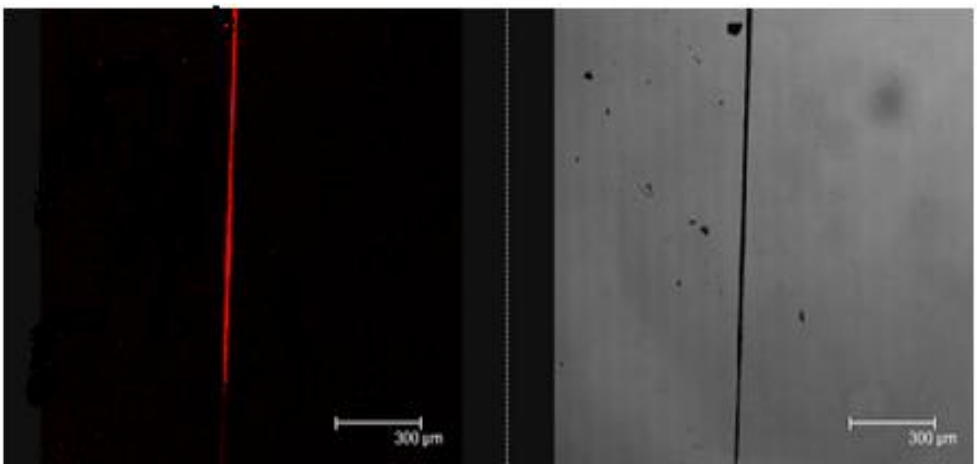

Figure 23. Fluorescence of Rhodamine B solution injected into the structure and excited at 543 nm in PMMA. Scale bar is 300 µm.

3.9 Conclusions

We presented our results on microstructures, craters, gratings, and complex structures in different polymers using fs laser direct writing technique. Role of pulse width and on optical damage and thermal diffusion length are calculated for different polymers. Tunneling ionization is shown to be mainly responsible for the modification at high energies in our case. Dependence of structure width with no. of scans, speed, energy and numerical aperture of the lens used are studied. Fabrication of micro-craters at high scan speeds and low energy irradiation dose is elucidated in the context of minimal pulse to pulse overlap. Results obtained with diffraction gratings fabricated in PMMA, PDMS, and PS are explained. The highest % DE reported in our work are 34 % in PMMA and 10 % each in PDMS and PS. Thermal treatment given to these gratings did not improve %DE as these gratings are of void type. Photothermal model is explained and assumed to be mainly responsible in our research work carried out as it resulted in the formation of defects. The fabrication of complex structures such as Y couplers, double line waveguides, microfluidic channels, and 8 shape are illustrated by using simultaneous combined motion of stages.

Chapter 4

Abstract

In this chapter, transmission, emission and excitation spectra collected from fs laser irradiated regions of polymers are presented. Brief survey of the literature on emission in case of glasses and PMMA, PS polymers is described. The observation of emission and the change in emission peak with the excitation wavelength are explained in the context of formation of myriad optical centers or defects. The increase in emission intensity with irradiation dose in bulk and thin films of polymers is explained in the context of formation of more number of optical centers with irradiation dose. Also, the increase in emission intensity with heating is explained through the formation of optical centers due to polymer chain scission. The transitions such as $n \rightarrow \pi^*$, $\pi \rightarrow \pi^*$ *in the functional groups such as aldehyde or ketone after breaking up of polymer due to fs laser irradiation are mainly responsible which lead to emission. The shift in the emission peak with excitation wavelength on the red side of the excitation spectrum is explained in the context of localization effects such as "Red-edge Effect" in which the classical Kasha's rule fails.*

4.1 Brief Survey

Pristine polymers do not show emission in the visible region as their band gaps lie in the range of 3-7 eV [122]. These polymers are transparent to visible light. But upon irradiation with UV-Visible or IR light, defects or optical centers and or free radicals are generated which exhibit luminescence behavior. Thus, one can fabricate micro craters which are luminescent. Each luminescent micro crater can be treated as bit 1. Thus the fabricated micro craters find its applications in realizing the applications in memory based devices. Watanabe et al. have shown the luminescence through defect formation in vitreous silica [152] and Kudrius et al. have shown a similar effect in sapphire [153]. In both these cases, it is the formation of luminescent defects or optical centers that are responsible for the observation of photoluminescence behavior. However, such reports on the luminescence of fs laser irradiated polymers are sparse and yet to be explored and investigated.

Nie et al.reported multilayered optical bit memory in fluorescent Poly Methyl Meth Acrylate (PMMA) irradiated with fs pulses. Irradiated with fs laser the PMMA exhibited fluorescence when excited it at 442 nm which they attributed to the defects generated by bond scission. The excitation spectrum had a peak near 360 nm [40, 133-135]. R. N. Nurmukhametov et al. [154] have exposed PS films and solutions with UV laser light beam (λ=248 nm) and observed changes in absorption and luminescent properties. They observed formation of optical centers with absorption band from 280-460 nm with fluorescence band from 330-520. The absorption and emission spectra due to the fs laser irradiation in the present study match nearly with their reported work indicating the creation of similar optical centers. Thus there are reports in the literature that show observation of emission after treated with different irradiations. However, the origin of emission is still not pin pointed. In the present study, four polymers are investigated namely Poly Methyl Meth Acrylate (PMMA), Poly Di Methyl Siloxane (PDMS), Poly Styrene (PS), and Poly Vinyl Alcohol (PVA). Photoluminescence is observed in all these cases when treated with fs laser irradiation [128-132, 155-156]. Pure polymers have absorption in UV region. Hence, in order to modify these polymers, they have to be irradiated with UV light as

Nurmukhametov et al. [154] have analyzed the spectra of solutions and thin films of polystyrene after treated with UV light. The investigations carried out by different groups show that the emission could be due to the formation of defects such as optical centers, the absorptions or excitations associated with the functional groups such as $n \rightarrow \pi^*$, $\pi \rightarrow \pi^*$ etc, which lead to emission and or due to photo selective excitation called the "Red Edge Effect". We focus on our investigations of emission in the irradiated regions of polymers below.

4.2 Parameters influencing the emission

The parameters that influence emission are the irradiation dose, temperature and excitation wavelength. These parameters result in variation of emission intensity or change in emission peak. As irradiation dose or temperature is increased, emission intensity is also found to be increasing. As excitation wavelength is changed, emission wavelength is also found to be changing which will be explained in the next section. In the present analysis, PMMA bulk is purchased from Goodfellow, USA. PDMS is homemade and PS is purchased from Goodfellow, UK. Solution of PS is prepared by mixing 1 gram of polystyrene beads (ACROS) in 8 ml toluene and stirred for 48 hours for complete miscibility. We prepared thin films of PS on a glass plate by spin coating the solution of PS. PVA thin films are prepared by dissolving 8.56 grams of PVA beads into 100 ml of water and made thin films. Figure 1 (a) shows the confocal microscope image of a buried structure in PMMA and the emission from the fs laser modified region when excited with 488 nm wavelength. Pseudo green color represents the emission. Figure 1 (b) shows the confocal microscope image of a surface structure fabricated typical ~25 µm wide micro channel inside the bulk of PMMA. 30 µJ energy used and scanning speed of 1 mm/sec, 40X objective lens. Pseudo color (green) indicates the fluorescence from the laser-modified regions.

In figures 1 (a) and (b), emission is observed from the edges. As central portion of the fs laser pulse has more intensity, it resulted in void type of structure in the middle region of the structures fabricated. Hence no emission is observed in the middle portion of the structure. However, if it is focused onto top or bottom surface of the microstructure, one can observe the emission which is explained in earlier chapter. This shows the usefulness of confocal microscope in selectively exciting different planes of focus which is illustrated in chapter 2. Figure 1 (c)

shows the confocal geometry used to collect emission. The mechanism responsible for the observed emission is the formation of defects generated in the polymer. Emission is recorded for structures fabricated at different irradiation doses. Figure 2 (a) shows PMMA emission data with excitation at 458 nm, 40X objective lens, 1 mm/sec scanning speed with different energies and

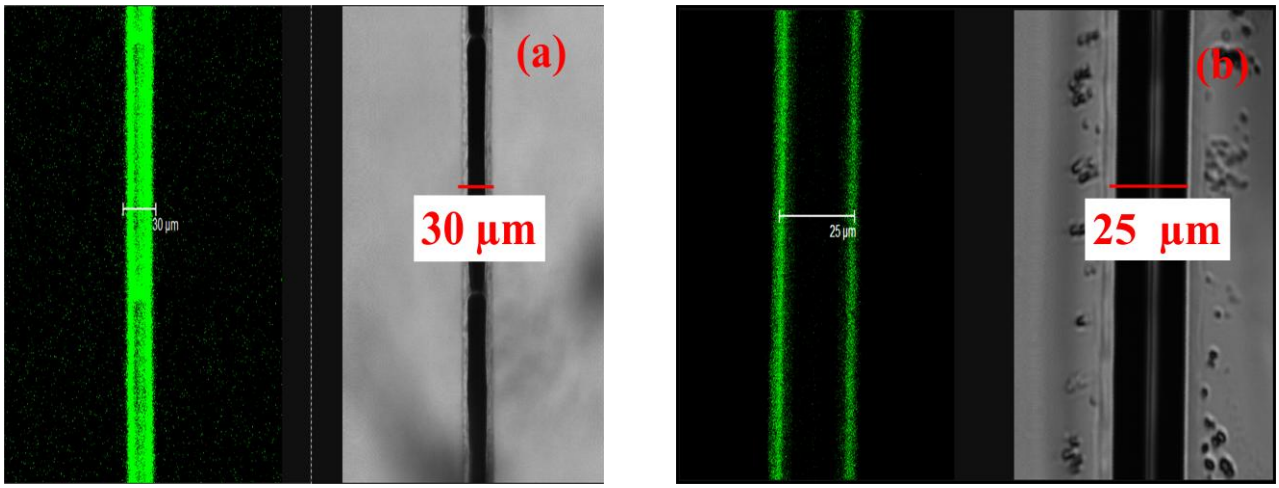

(b) shows the PMMA emission data with excitation at 488 nm, 40X objective lens, 1 mm/sec scanning speed with different energies.

Figure 1. (a) Confocal microscope images of PMMA (Goodfellow). ~20 µm wide micro channel inside the bulk of PMMA. 30 µJ energy used and scanning speed of 1 mm/sec, 40X objective lens. (b) A typical ~25 µm wide micro channel inside the bulk of PMMA. 30 µJ energy used and scanning speed of 1 mm/sec, 40X objective lens. Pseudo color (green) indicates the fluorescence from the laser-modified regions. (c) Collection of emission in confocal geometry.

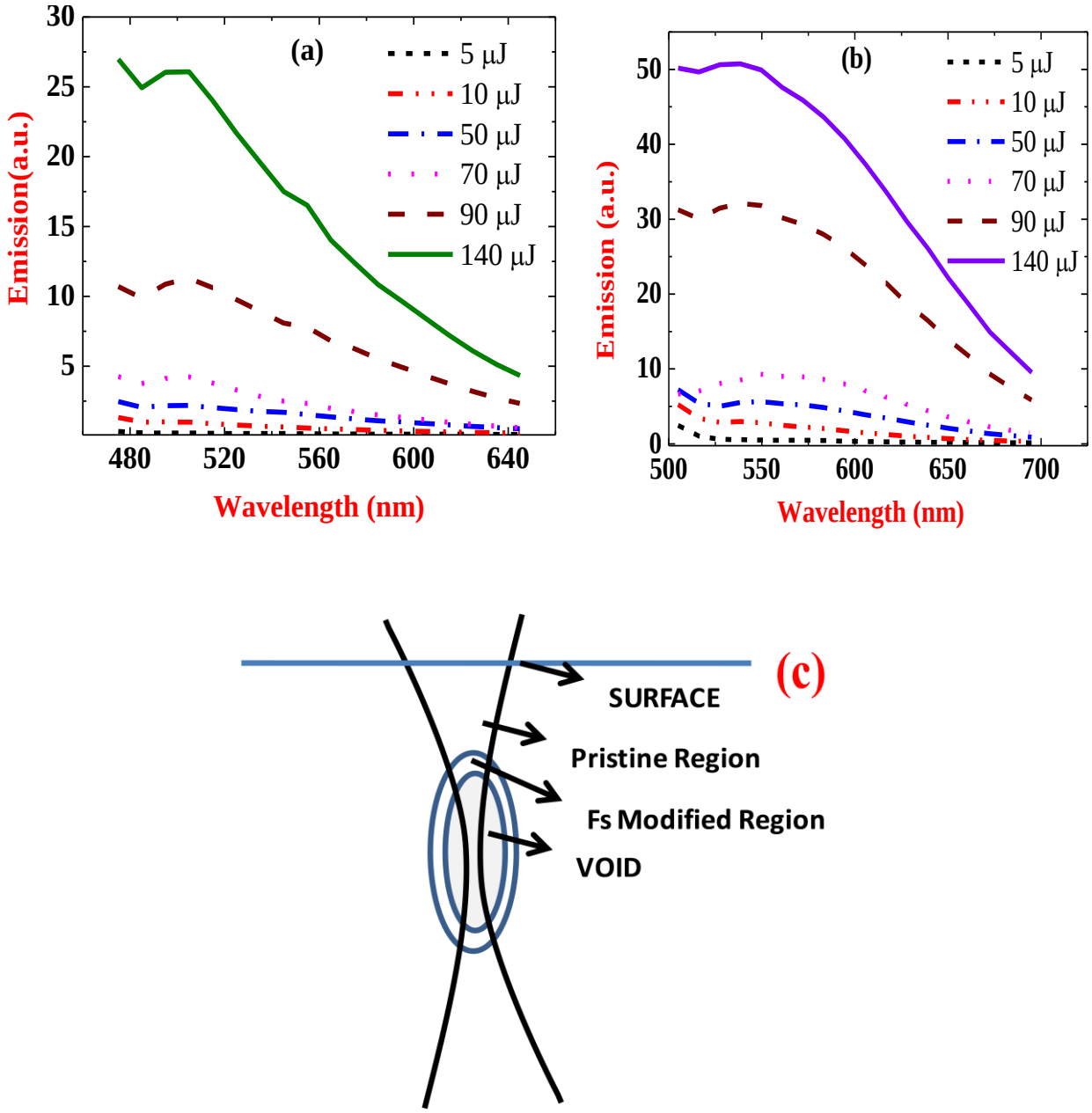

Figure 2. (a) PMMA fluorescence data with excitation at 458 nm, 40X objective lens, 1 mm/sec scanning speed with different energies. (b) PMMA fluorescence data with excitation at 488 nm, 40X objective lens, 1 mm/sec scanning speed with different energies.

Emission is observed in case of thin films of PS, bulk PS and PVA thin films when excited at different wavelengths. Figures 3 (a)-(c) show emission plots for the structures excited at 458, 488 and 514 nm wavelengths using confocal microscope. We found emission intensity increasing with the energy used for fabricating the structures from all the emission plots at different excitation wavelengths as structures fabricated with more energy are modified more compared with the structures fabricated at low energy. It is clearly observed that the structures fabricated at high energies show more emission compared with structures fabricated at low irradiation doses. Pristine polymers do not show any emission as there are no defects present.

The second parameter that influences the emission intensity is temperature. Since the emission from a microstructure cannot be recorded using conventional fluorescence spectrometer in which the spot size is more compared with structure width. Hence we fabricated several lines close by such as grating in bulk PS with energy of 1 μJ, 0.5 mm/s speed with 40X microscope objective (we termed this grating as PSG1). We explained the fabrication parameters used in earlier chapter for PSg1. As confocal microscope generates pseudo color for emission, fluorescence spectrometer is used to record emission. Heat treated PSG1 grating showed more emission intensity as number of defects and or optical centers formed are increased. These lead to increase in excitation intensity also as number of generated defects participate in absorption at a particular monitoring wavelength. Figures 4 (a) to 4 (d) show the results obtained. Several reports on thermal degradation of polymers leading to chain scission and the formation of more radicals are reported in literature [157-162].

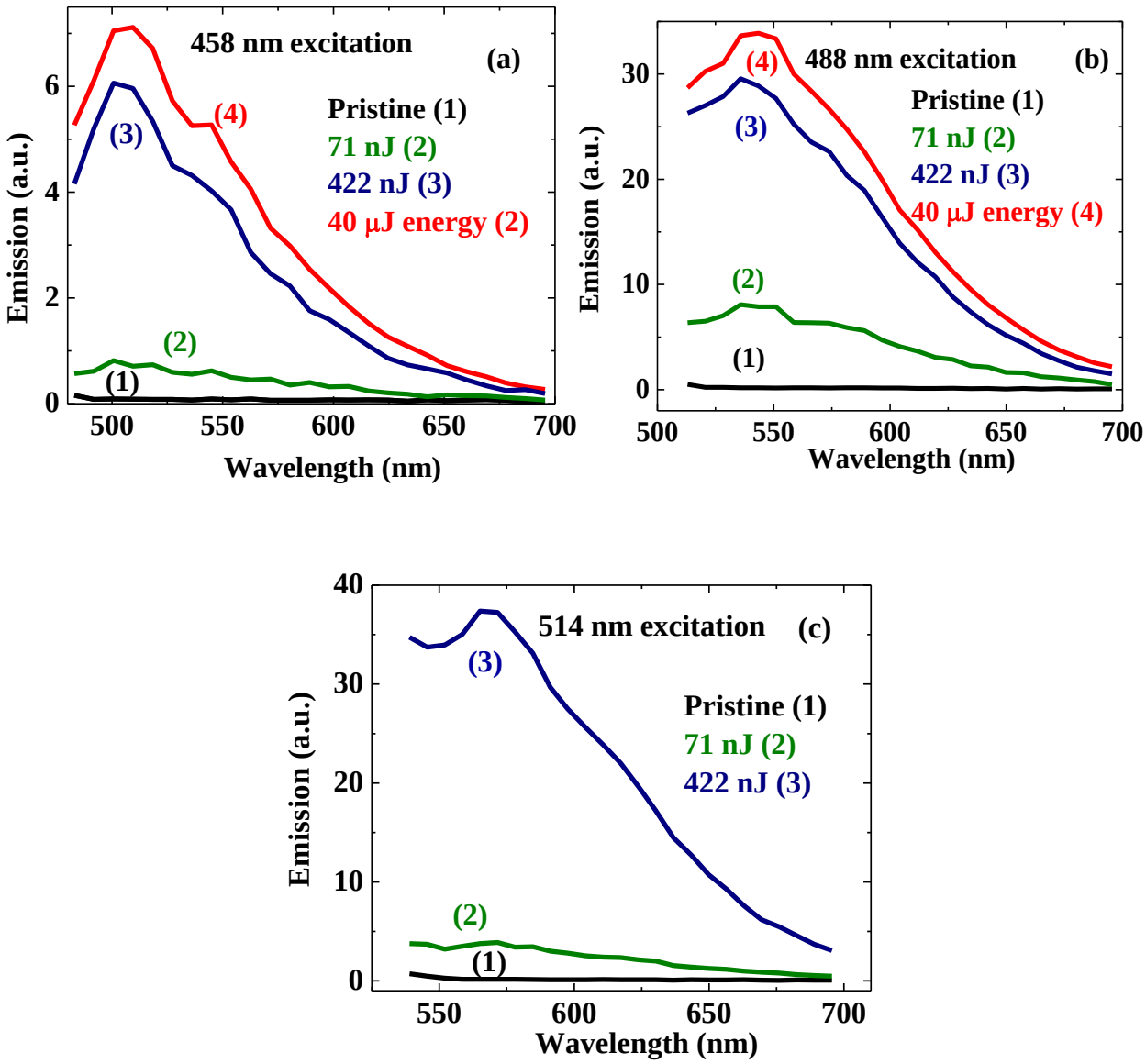

Figure 3. (a) (Color online) Plots of emission when structures fabricated at 40 µJ, 422 nJ, 63 nJ and pristine region of PS excited at 458 nm;(b) (Color online) Plots of emission when structures fabricated at 40 µJ, 422 nJ, 63 nJ and pristine region of PS excited at 488 nm; (c) (Color online) Plots of emission when structures fabricated at 422 nJ, 63 nJ and pristine region of PS excited at 514 nm.

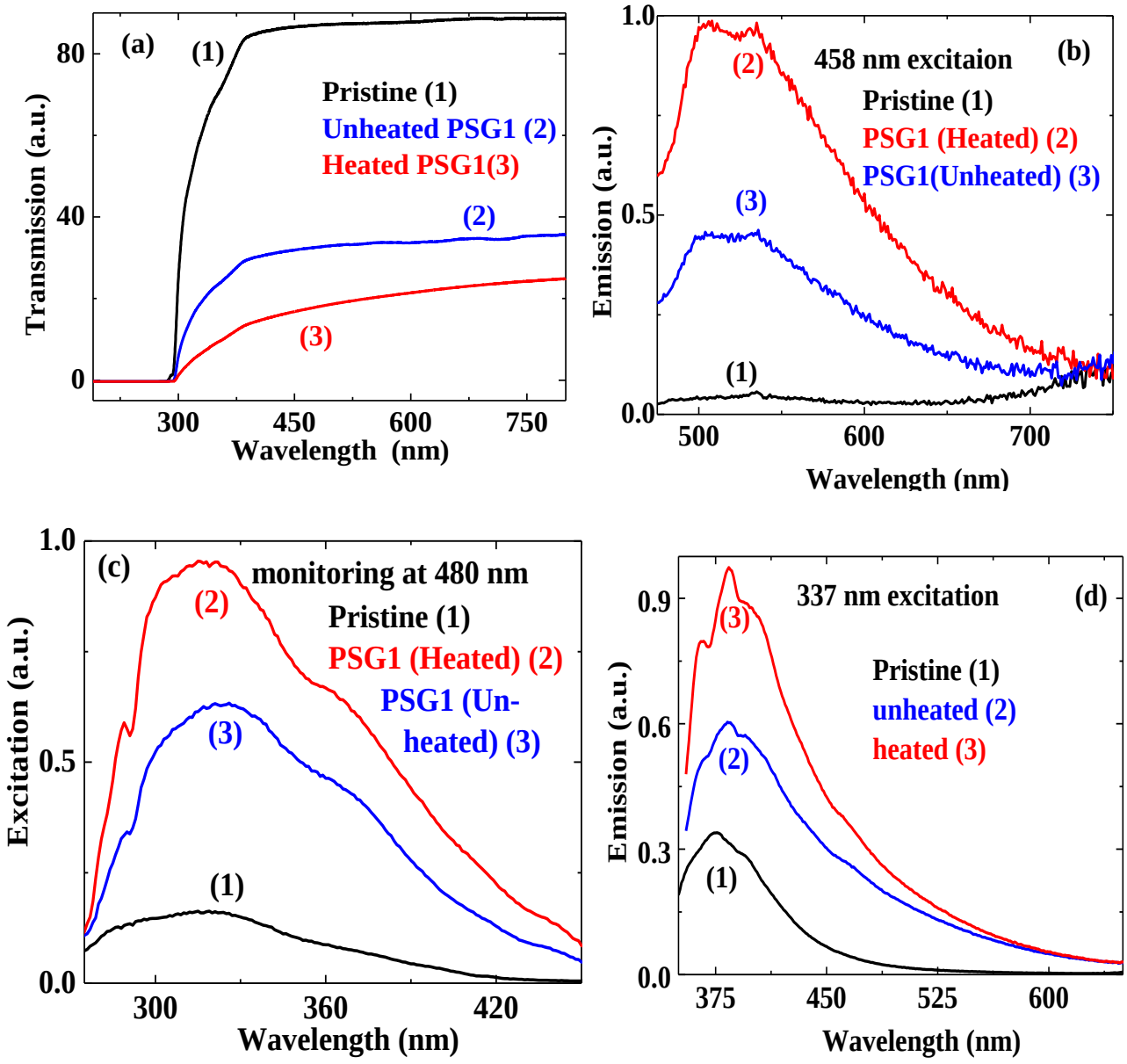

Figure 4. (a) Transmission spectra obtained for pristine PS, fs laser irradiated, and thermally treated + fs laser irradiated PSG1 (b) Emission spectra obtained for pristine PS, fs laser irradiated, and thermally treated + fs laser irradiated PSG1 when excited at 458 nm wavelength (c) Excitation spectra obtained for pristine PS, fs laser irradiated, and thermally treated + fs laser irradiated PSG1 monitoring emission at 480 nm (d) Emission spectra obtained for pristine PS, fs laser irradiated, and thermally treated + fs laser irradiated PSG1 when excited at 337 nm wavelength.

4.3 Origins of emission

The observation of emission can be explained through different possible mechanisms explained below.

a) Optical centers

Nurmukhametov et al. [154] have exposed PS films and solutions with UV laser light beam (λ=248 nm) and observed changes in absorption and luminescent properties. They observed formation of optical centers with absorption band from 280-460 nm with fluorescence band from 330-520. They established different optical centers being responsible for such a behavior and hypothesized their results more close to the spectrum of diphenylbutadiene (DPBD). The absorption and emission spectra due to the fs laser irradiation in the present study match nearly with their reported work indicating the creation of similar optical centers. Plots 3 (a) – 3 (c) show that the emission peaks and were different for different excitation wavelengths. In present study, the modification of PS was due to 800 nm (infrared) laser through multi-photon absorption process. Hence, fs laser irradiation results in bond scission followed by the formation of large number of defects that act as optical centers for emission. This resulted in shift in emission peak with excitation wavelength. The observed spectral peaks are mentioned in Table 1. Observed spectral peaks from fluorescence spectrometer and the confocal microscope are also compared in the table.

Figure 4(a) shows the transmission spectrum of irradiated PS (PSG1) with pristine PS. We observed decrease in the transmission of irradiated PS at longer wavelengths which could be due to the creation of different optical centers in the medium due to fs laser irradiation. As the polymer is like an amorphous medium, each optical center experiences a different local field. Thus there is a possibility of an extended state of optical centers with different energies. Figure 4 (b) shows the emission plot of PSG1 obtained with 458 nm wavelength excited. The peak around 530 nm is due to toluene solution. When used to dissolve the PS, the peak shifts to longer wavelengths. The plot shows that fs irradiated PS has more emission compared with pristine PS. Though any kind of emission is unexpected from the pristine PS, it may be noted that even the carefully prepared films contain scratches and surface defects that lead to this observation of weak emission. In order to confirm this, the florescence from a dense PS solution was recorded. The emission reduced from the solution. This confirms that the surface defects and scratches lead

to the emission from the pristine polymer films. Similar trend is noticed in case of other excitations also.

Table 1. Comparison of emission data obtained in irradiated PS (PSG1).

S. No.	Excitation Wavelength (nm)	Emission peak (nm) in confocal microscope	Emission peak (nm) observed in fluorescence spectrometer
1	458	509, 544	505,536
2	488	535	550
3	514	565	563
4	400	Excitation source is not available	454, 462, 476

By monitoring different regions of emission spectrum, excitation spectra are recorded which looked alike and showed maximum absorption at around 337 nm, which means that the optical centers have almost similar absorption spectrum. This is logical as all the optical centers are of the same monomer unit. Figure 4(c) shows excitation spectra at monitoring wavelength 480 nm with a maximum around 337 nm. Figure 4(d) shows emission spectrum of irradiated PS excited at 337 nm. The tail in the transmission spectrum clearly indicates the low concentration of the optical centers, which are in a way localized in the polymer matrix. This leads to a shift in the emission spectrum with different excitation energies due to localization.

In the process of polymerization of styrene molecules, they can be chemically bonded with each other by not only "head to tail" as by usual procedure of the monomer units shown in figure 5(a), but also through "head to head" and "tail to tail" bonds. This results in the formation of defective units in the PS chain. These bonds are also weak which can get modified easily due to photo degradation. We expect the photo degradation in our case is due to multiphoton absorption. In order to estimate the lifetime of the emission from the optical centers formed, we used third harmonic of Nd: YAG laser at 355 nm, 10 Hz repetition rate and 6 ns pulses for the excitation. The emission was collected at 90^0 to excitation. The emission was observed with a 0.5 m Jobin

Yvon spectrometer with a PMT attachment. The lifetimes are seen on an oscilloscope. The lifetime measured at 536 nm is around 40 ns. Figure 5 (b) shows the lifetime plot.

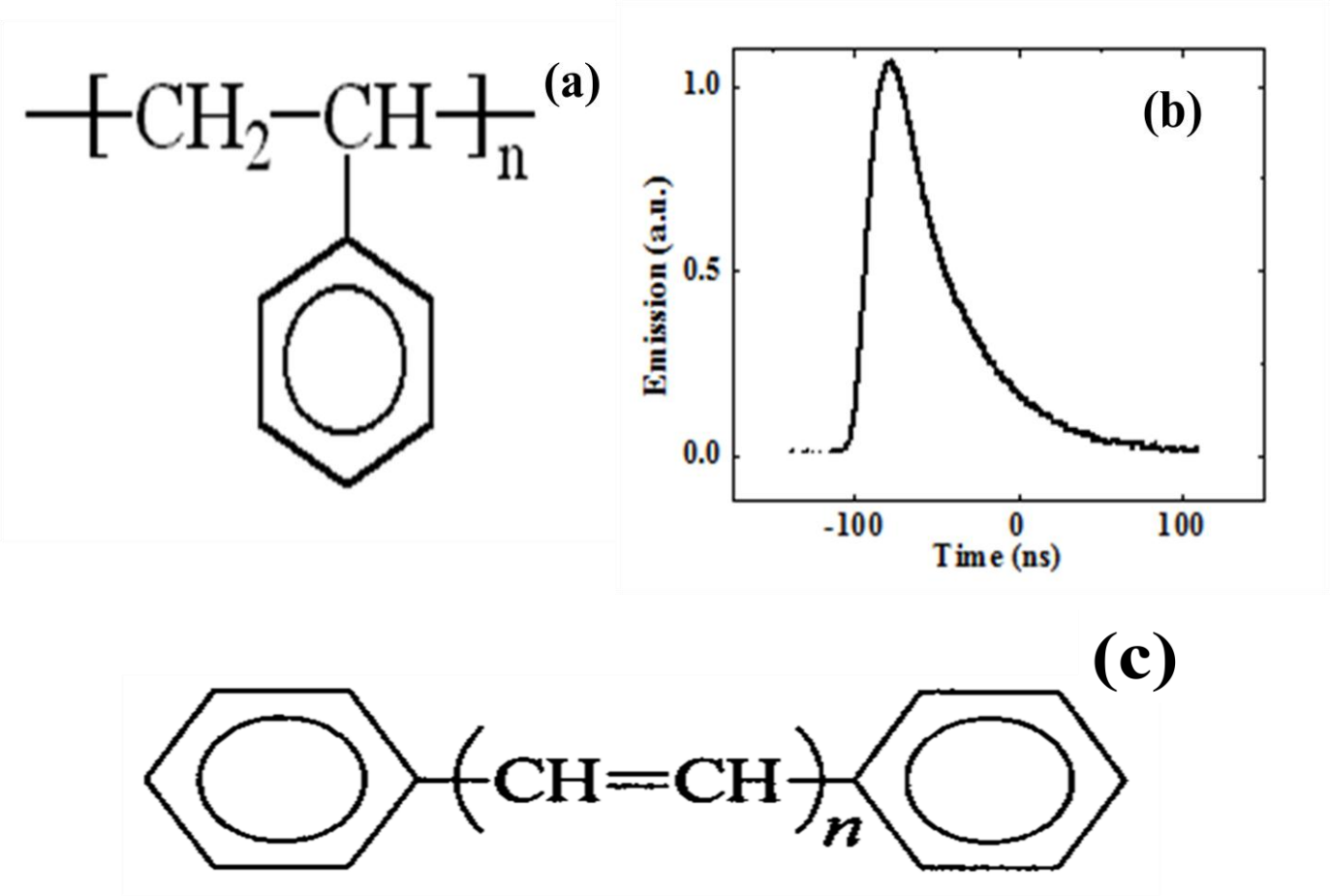

Figure 5. (a) PS monomer (b) Lifetime of irradiated PS (c) Optical centers chemical formulae

Figure 4 (d) shows our results obtained at excitation of 337 nm. The observed emission peaks are at 367, 383 (broad peak) and 458 nm (less intense). These observed peaks were compared with the available literature [154]. 367 nm peak in the emission spectrum is interpreted as due to *trans*-stilbene, observed earlier through UV irradiation [154] and also matches well with the *trans*-stilbene emission. The broad emission peak around 383 nm is interpreted as due to diphenylbutadiene (DPBD). The excitations at 337 and 400 nm showed the peak around 458 nm which is interpreted as due to diphenylhexatriene (DPHT) optical center. As fs laser carries intense energy, the structural modifications are much more easily achieved in a polymer matrix

than with the UV light irradiation. Figure 5 (c) shows the structure of *trans*-stilbene, DPBD and DPHT [154]. When n=1,2 and 3 it is trans-stilbene, DPBD and DPHT respectively.

Emission spectra with different excitations are shown in figure 6. Different excitations showed different emission peaks in our work which is an indication of the formation of different optical centers. However, the absorption characteristics of these optical centers thus formed showed maximum absorption around 337 nm. As the defect centers are distributed over wide range of energies, the emission spectrum too gets distributed over the entire fluorescence spectrum contribution coming from all types of defects. This results in the spectra being the same in the excitation spectra recorded by monitoring different emission wavelengths. However the emission, when excited at long wavelength side, due to localization of energy we observe different emission spectra.

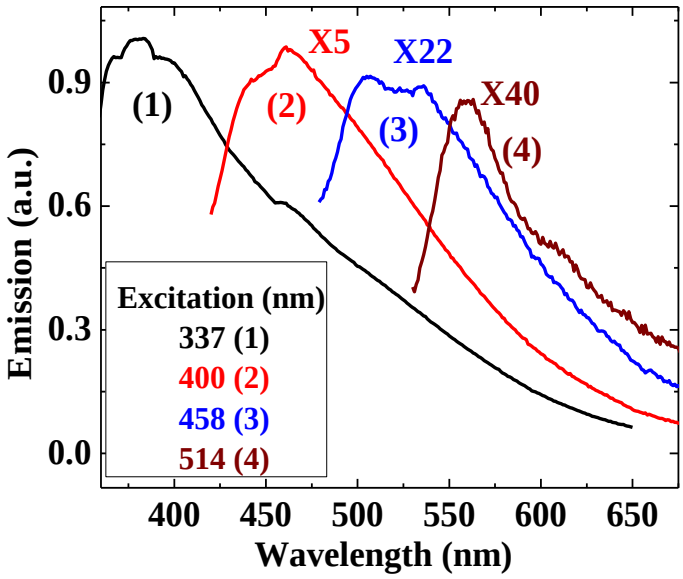

Figure 6. Emission from PSG1 grating excited at different wavelengths. Emissions with longer wavelength excitations are enhanced for clarity.

In order to examine the same effect, microstructures over a large area were fabricated to record the emission and excitation spectra from these laser irradiated regions. To accomplish this an array of closely spaced lines were fabricated in PMMA (energy 10 μJ, speed 1mm/s, period 30

μm), PDMS (50 μJ, 1mm/s, 10 μm), PS (1 μJ, 0.5 mm/s, 30 μm), and PVA (10 μJ, 1mm/s, 20 μm). All the four polymers are transparent to visible light before fs laser irradiation and hence do not show any emission when excited with visible light. However, due to multiphoton absorption overcoming the large band gaps of these polymers, they get modified and optical centers are produced that exhibit emission when excited at different excitation wavelengths. Figures 7(a), 7(c), 8(a) and 8(c) depict the observed emission due to different excitation wavelengths in PMMA, PDMS, PS, and PVA. It was noticed that the strong emission from the modified regions of all polymers was observed when excited with any of 458, 488, and 514, 543 nm (except for PS) light. The formation of optical centers resulting from fs laser irradiation is responsible for the emission observed. The change in emission peak with the excitation wavelengths is interpreted as due to the formation of diverse optical centers. The sharp peaks observed in the emission spectra of pristine PDMS [depicted in figure 7(c)] could be attributed to the defects and/or impurities or radicals in the sample. This emission was amplified when irradiated with fs laser. Also it is noticed that the excitation spectra collected by monitoring different emission wavelengths show similar spectrum for these polymers. In this analysis, the role of Raman modes cannot be ignored which will be explained in next few sections.

The emission peaks in our study differed considerably with the excitation wavelength recorded at room temperature. Low temperature studies of spectral narrowing were reported earlier in some of the organic molecules [163]. By monitoring different wavelengths of the emission peaks, the excitation spectra for all polymers which are illustrated in figures 7(b), 7(d), 8(b), 8(d) for PMMA (maximum at 366 nm), PDMS (maximum near 300 nm), PS (maximum at 337 nm), and PVA (maximum below 300 nm) look alike. This is understandable because of the wide distribution of the energies of all the optical centers, leading to similar excitation spectrum as explained earlier. In case of PDMS and PVA excitation spectra [figures 7(d) and 8(d)] the maximum peaks were not well resolved since the second order of excitation coincided with the monitoring wavelengths. Insets of these figures show the modifications of transmission spectrum due to fs irradiation. It is noticed that the small decrease in transmission, and thus increase in absorption, towards UV region for fs laser irradiated polymers. This change is attributed to the formation of different optical centers due to nonlinear absorption process resulting in polymer chain scission. The change observed beyond 400 nm is due to scattering/diffraction losses from

the irradiated regions in polymers. Figures 9 (a) and 9 (b) show emission from fs irradiated polymers when excited near excitation peaks.

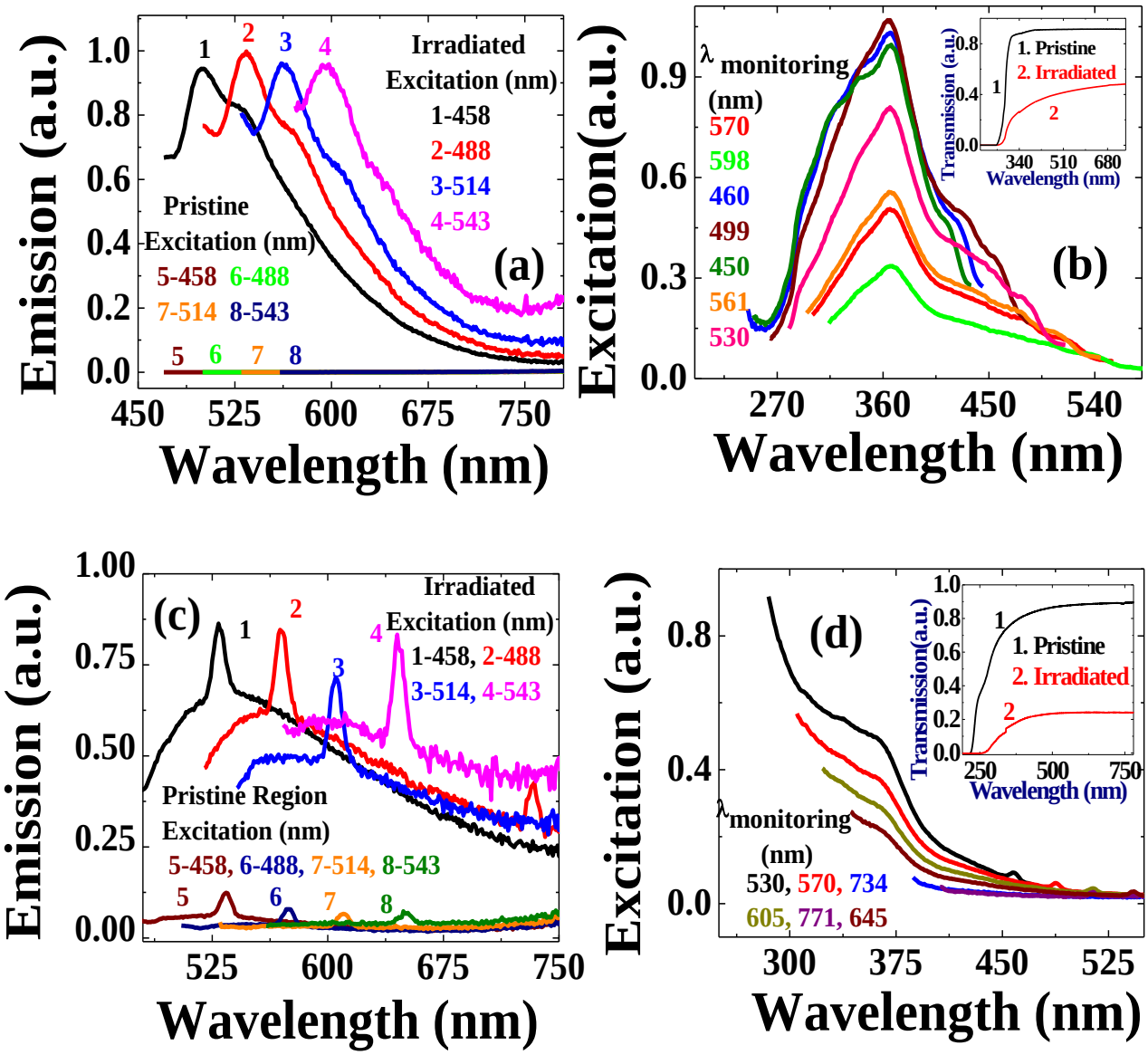

Figure 7. (a) Emission spectra of pristine and irradiated PMMA (energy 10 µJ, speed 1 mm/s, period 30 µm) (b) Excitation spectra of irradiated PMMA (Inset shows the transmission spectra of the same irradiated and pristine PMMA) (c) Emission spectrum of pristine and irradiated PDMS (energy 50 µJ, speed 1 mm/s, period 10 µm) (d) Excitation spectra of irradiated PDMS (Inset shows the transmission spectrum of irradiate PDMS with 30 µJ energy, 1 mm/s speed and 60 µm period and pristine PDMS).

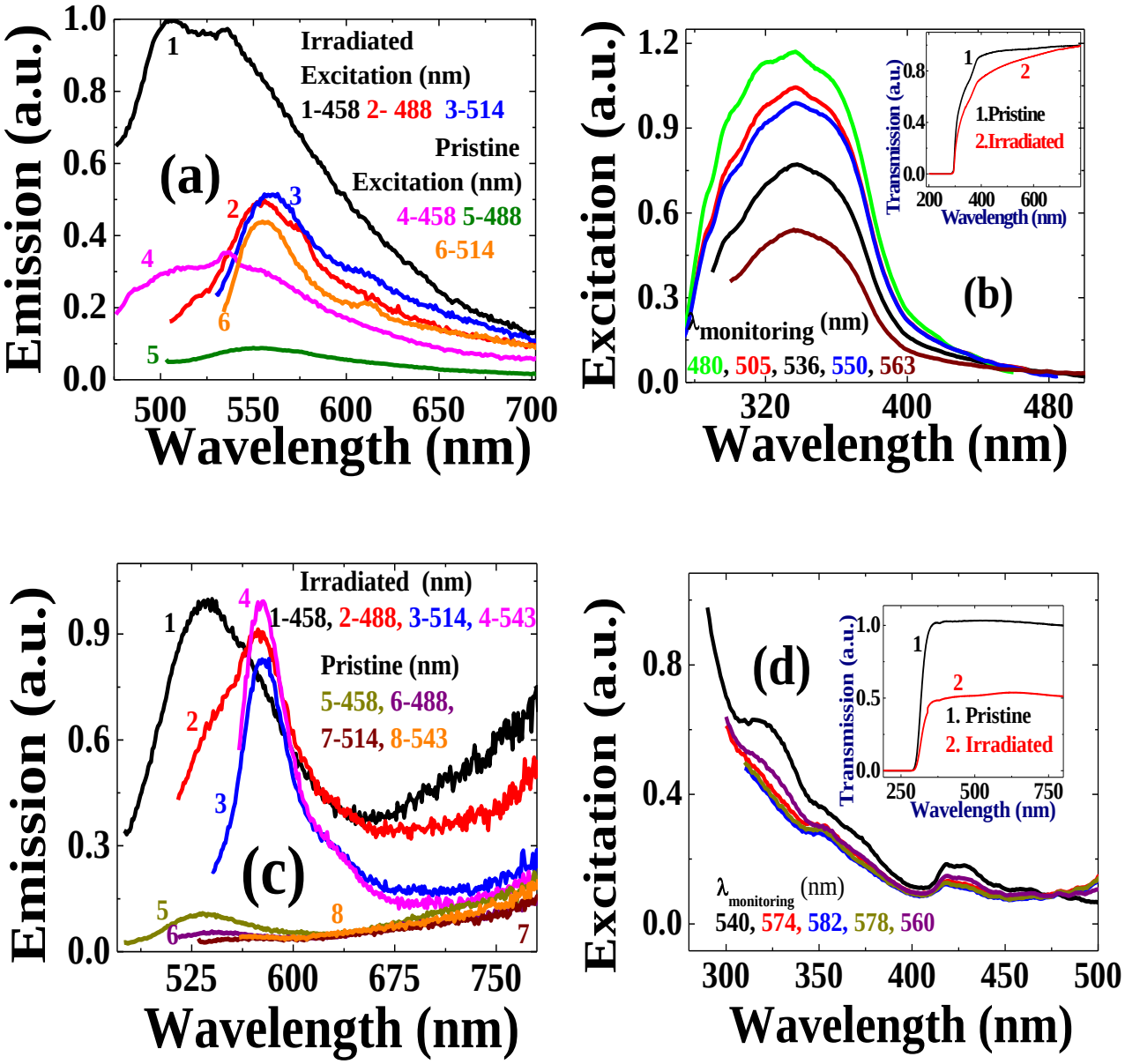

Figure 8. (a) Emission spectra of pristine and irradiated PS (energy 1 µJ, speed 0.5 mm/s, period 30 µm) (b) Excitation spectra of irradiated PS (Inset shows the transmission spectra of the same irradiated PS and pristine PS) (c) Emission spectra of pristine and irradiated PVA (Energy 10 µJ, speed 1mm/s, period 20 µm) (d) Excitation spectra of irradiated PVA (Inset shows the transmission spectra of same irradiated PVA and pristine PVA).

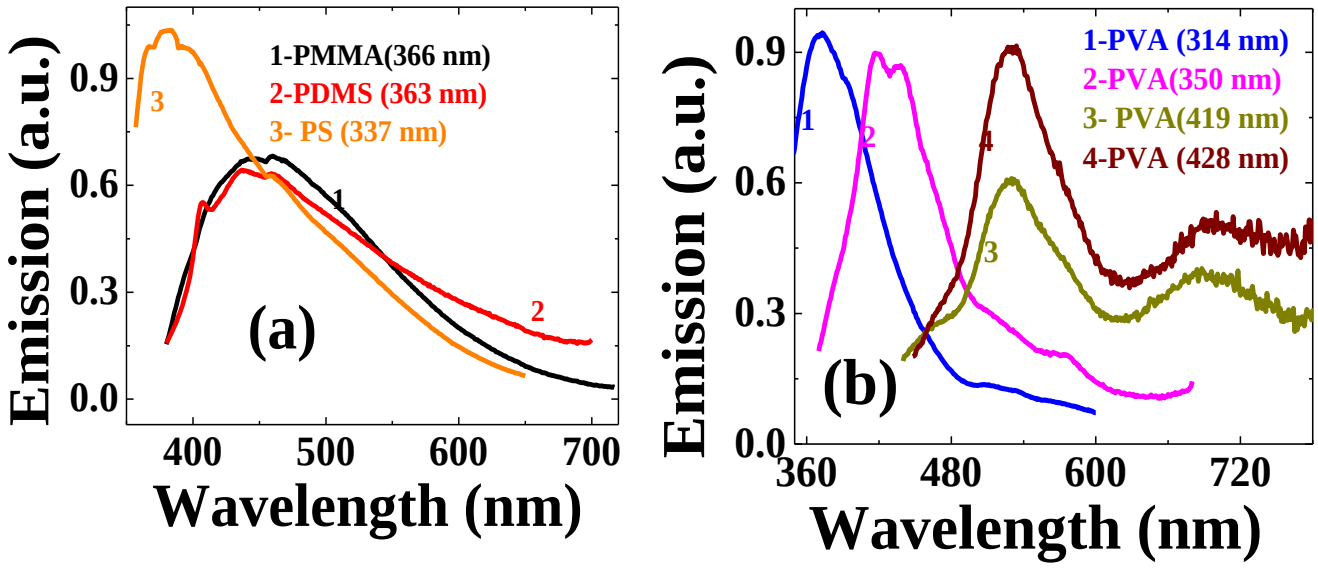

Figure 9. (a) Final emission spectra of irradiated PMMA, PDMS, PS. (b) Emission spectra collected from irradiated regions of PVA excited with different peak wavelengths observed from the excitation spectra. Excitation wavelengths are enclosed in parentheses for different polymers.

b) Transitions in functional groups

Nie et al. [40, 133-135] have fabricated three dimensional multilayered optical bit memory in PMMA using fs laser at 800 nm wavelength with 1 KHz repetition rate and 100 fs pulses. They observed the maximum excitation at 375 nm. This is ascribed to the absorption of some unsaturated aldehyde or ketone groups, which undergo $n \rightarrow \pi^*$ transitions near 380 nm [162]. The maximum excitation or absorption in PMMA in our investigation occurs at 366 nm which can be ascribed to the same absorption of aldehyde or ketone groups undergoing $n \rightarrow \pi^*$ transition (Figure 7 (b)). PDMS shows similar emission spectrum [figure 9 (a)] to PMMA when excited at 363 nm as it is perceived that PMMA and PDMS both contain similar groups except for the presence of silicon in PDMS. The excitation spectra of PS is already explained through different optical centers formation such as *trans*-stilbene, DPBD and DPHT. However, the inter electronic transitions involved with in the functional groups present among bonding, antibonding, and nonbonding molecular orbitals cannot be ruled out [40,133-135,164-166].

Figure 10 (a), (b), and (c) show the chemical structures of PMMA, PDMS, and PVA to understand the possible transitions involved which leads to the observation of emission after absorption of suitable wavelength in UV-Visible spectrum through inter electronic transitions. The chemical structure of PS is shown in figure 5 (a). Figure 10 (d) shows energy level diagram for possible transitions among molecular orbitals.

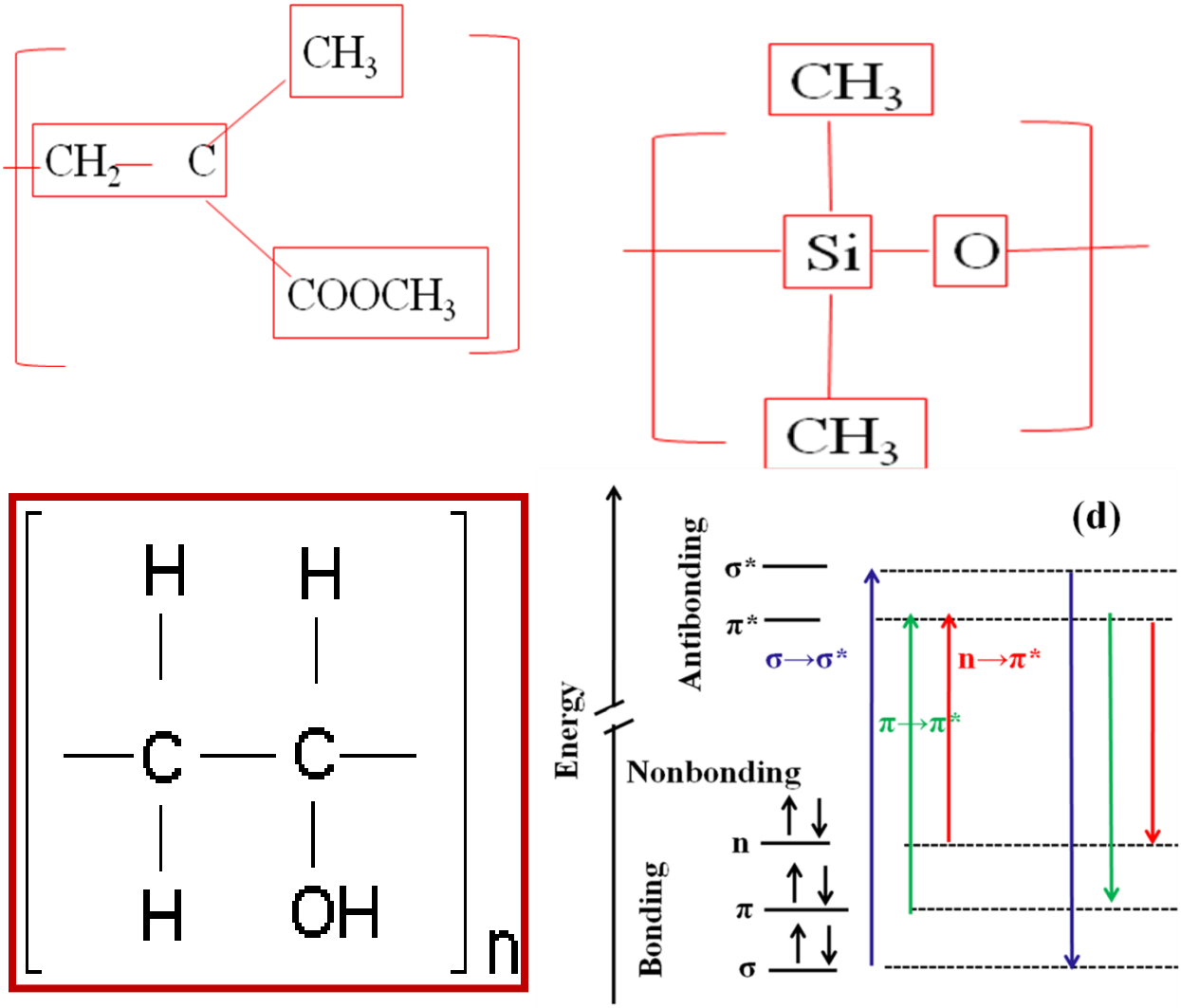

Figure 10. Chemical structures of (a) PMMA (b) PDMS (c) PVA (d) Energy level diagram

The transitions involved in σ→σ* require more energy and hence they appear in deep UV (lower wavelength). The transitions involved in π →π*, and n→π* take less energy and thus appear on

higher wavelength side of UV- Visible absorption spectrum [165-166]. Usually the atoms that have lone pairs present undergo nonbonding to antibonding transitions [165]. In case of PMMA, as explained earlier the unpaired electrons on oxygen present in ketone group undergoes n $\rightarrow\pi^*$ transition. In case of PDMS, as oxygen is present it could be due to n $\rightarrow\pi^*$ transition of Si=O [164,166] which occurs around 200 nm. In case of PVA, due to the presence of OH group (alcohol group), it could be due to n $\rightarrow\sigma^*$. In case of PS, due to the presence of aromatic ring, the more probable absorption transition could be $\pi \rightarrow\pi^*$ among C=C groups. There are several absorption transitions possible according to figure 10 (d). Polymers are macromolecules containing several functional groups (such as aldehyde, ketone, or OH groups) which are activated when UV or visible light is shown on them. Also there is a possibility for the polymer to break into several species which contain these functional groups upon irradiation of UV or visible light. There are several transitions which are possible out of which only one or few are active which depends upon the chemical environment of the polymer and selection rules. After these active functional groups are excited, they can get deexcited to any of the possible states which can be also one of the reasons for the observed emission.

c) Interference of Raman modes

To understand whether the presence of Raman modes appear in the analysis of emission, emission spectra are rerecorded over a broad range for every 20 nm increment from 280 nm onwards using fluorescence spectrometer. However, only those excitation wavelengths that showed emission are presented in figures 11 and 12 for PMMA, PDMS, PS and PVA. Tables 2 to 5 show the excitation wavelengths and the corresponding emission wavelengths for the investigated polymers PMMA, PDMS, PS, and PVA after fs laser irradiation. Also, secondary and higher emission peaks are enlisted in these tables. Emission peak is found to be changing with excitation wavelength though excitation spectra recorded at different monitoring wavelengths look alike. Interestingly, some of the emission peaks coincided with Raman peaks of these polymers. Emission is indicated as broad curve over which sharp Raman peaks appeared in case of PDMS (Figure 11 (c) and (d)). Same PDMS polymer did not show any sharp peaks for excitation wavelengths below 400 nm. The Raman shift is calculated with the wave number difference as follows.

$$\Delta\lambda(cm^{-1}) = \frac{1}{\lambda_{ext}} - \frac{1}{\lambda_{em}}$$

where $\Delta\lambda$ is wavenumber difference or Raman shift between excitation and emission wavelengths. λ_{ext} and λ_{em} are excitation and emission wavelengths respectively. For PMMA, the excitation wavelengths at 458, 488, 530, and 560 nm nearly match Raman mode of characteristic peak at 1736 cm^{-1} of γ (C=O) of (C-COO) mode [167]. Excitations at 380, and 400 nm nearly matched with Raman mode of 3454 cm^{-1} which is $2\gamma_2$ overtone of 1730 cm^{-1}. Excitation at 543 nm matched with another Raman peak of Combination band involving γ (C = C) and γ (C-COO) of PMMA which is at 1736 cm^{-1}. The spectra therefore contain the Raman peaks over the broad emission spectrum shown in figure 11 (d).

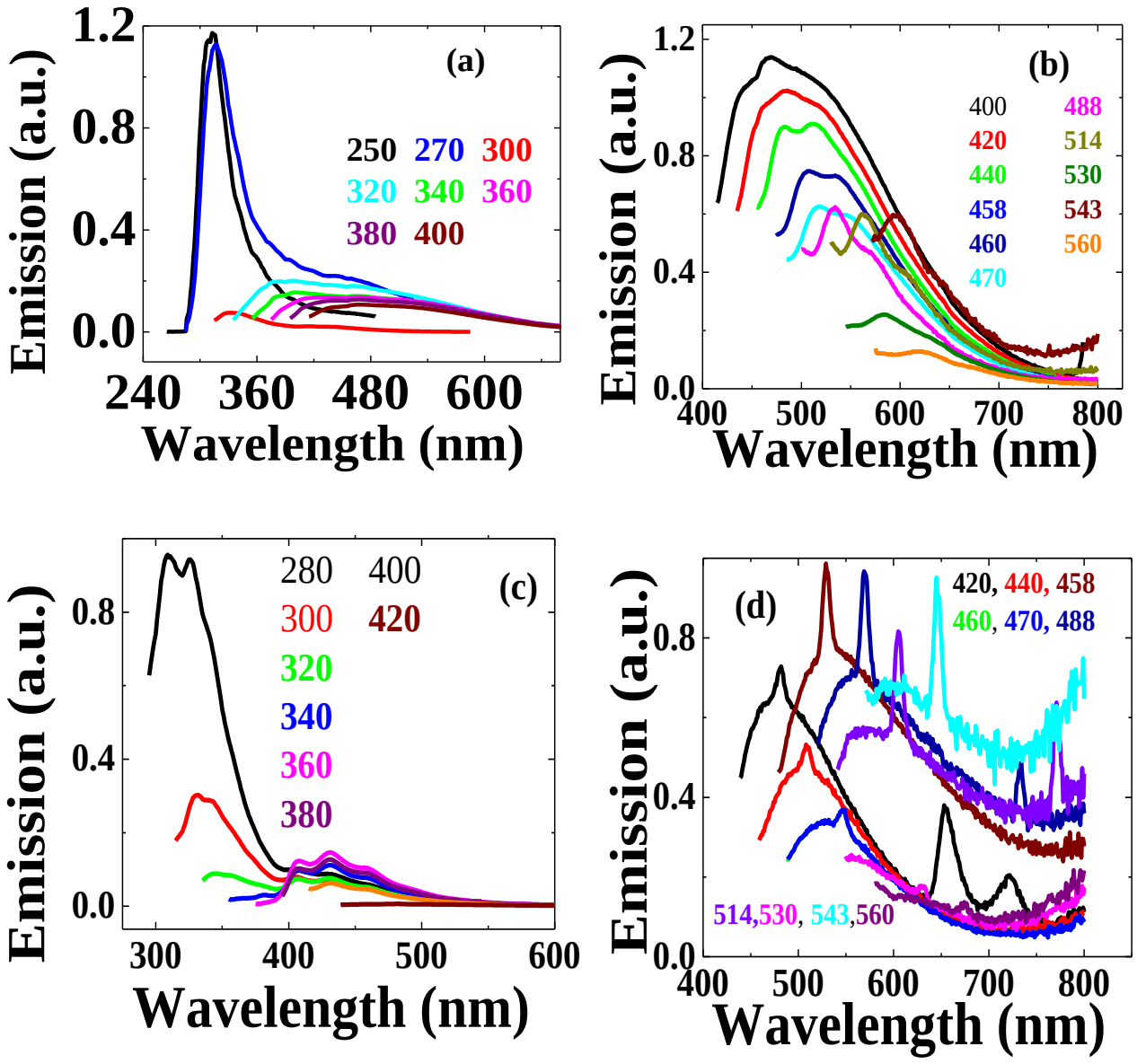

Figure 11. Plot of emission spectra of (a) PMMA at excitation wavelengths from 250-400 nm (b) PMMA at excitation wavelengths from 400-560 nm (c) PDMS at excitation wavelengths from 280-420 nm (d) PDMS at excitation wavelengths from 420-560 nm

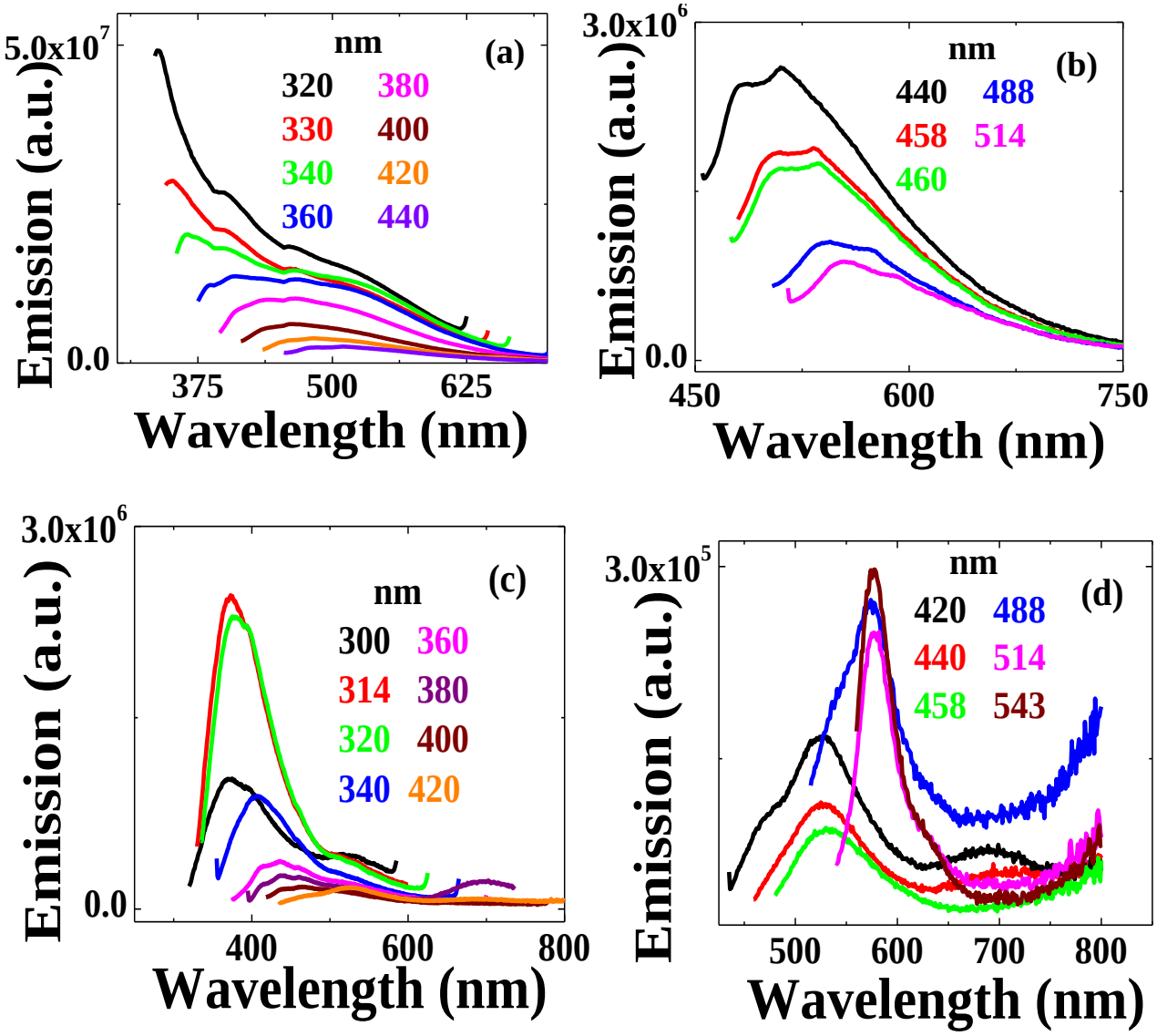

Figure 12. Plot of emission spectra of (a) PS at excitation wavelengths from 320-440 nm (b) PS at excitation wavelengths from 440-514 nm (c) PVA at excitation wavelengths from 300-420 nm (d) PVA at excitation wavelengths from 420-543 nm.

Table 2. Excitation, emission, and Raman shift observed in fs laser irradiated PMMA.

S. No.	λ_{ext} (nm)	λ_{em} (nm)	$\Delta\lambda$ (cm^{-1}) = λ_{ext}^{-1} - λ_{em}^{-1}
1	250	309	7638
		313	8051
2	270	317	5491
3	300	326	2658
4	320	381	5003
		398	6214
		461	9558
5	340	398	4286
		464	7860
6	360	427	4359
		465	6272
7	380	437	3432
		467	4903
8	400	464	3448
9	420	484	3148
10	440	483	2023
		511	3158
11	458	499	1794
		529	2930
12	460	507	2015
		535	3048
13	470	518	1972
		551	3128
14	488	534	1765
		568	2886
15	514	561	1630
16	530	584	1745
17	543	598	1694
18	560	621	1754

Table 3. Excitation, emission, and Raman shift observed in fs laser irradiated PDMS

S. No.	λ_{ext} (nm)	λ_{em} (nm)	$\Delta\lambda$ (cm^{-1}) = λ_{ext}^{-1} - λ_{em}^{-1}
1	280	309	3351
		326	5040
2	300	332	3213
		340	3921
3	320	345	2264
4	340	408	4902
		431	6210
		457	7530
5	360	408	3270
		431	4576
		457	5896
6	363	407	2965
7	380	407	2965
8	400	407	2965
9	420	482	3063
		653	8496
		722	9959
10	440	508	3042
11	458	529	2931
12	470	549	3524
13	488	569	2917
		734	6868
14	514	605	2926
		771	6485
15	543	645	2912

Table 4. Excitation, emission, and Raman shift observed in fs laser irradiated PS

S. No.	λ_{ext} (nm)	λ_{em} (nm)	$\Delta\lambda$ (cm^{-1}) = λ_{ext}^{-1} - λ_{em}^{-1}
1	330	352	1894
		398	5177
		462	8658
2	340	365	2015
		400	4412
		462	7767
3	360	380	1462
		408	3268
		468	6410
4	380	439	3537
		462	4671
		467	4903
5	400	461	3308
6	440	486	2151
		512	3196
7	458	508	2149
		532	3037
8	460	511	2170
		536	3082
9	488	544	2019
		574	3070
10	500	554	1950
		589	3022
11	514	564	1734
		612	3115

Table 5. Excitation, emission, and Raman shift observed in fs laser irradiated PVA

S. No.	λ_{ext} (nm)	λ_{em} (nm)	$\Delta\lambda$ (cm^{-1}) = λ_{ext}^{-1} - λ_{em}^{-1}
1	300	373	6524
		393	7888
2	314	374	5109
3	320	373	4403
		395	5934
4	340	408	4902
5	360	435	4789
		461	6086
6	380	439	3537
		460	4577
		704	1211
7	400	464	3448
		602	8389
8	420	527	4834
9	440	525	3680
10	458	540	3316
11	488	574	3070
12	514	576	2094

In case of PDMS, the excitation wavelengths at 300, 420, 440 nm matched with Raman peaks of PDMS with Raman mode of 3106 cm^{-1} which is CH stretching vibration mode [168]. Also excitations at 363, 458, 488, 514, 543 cm^{-1} nearly matched with two Raman modes of PDMS at 2907, and 2965 cm^{-1} which are CH_3 symmetric and asymmetric stretch modes [169]. Also, compared with PMMA, it is very clear in PDMS that sharp peaks appear on broad emission background which indicates the component of emission along with Raman signal. In case of PS, the excitation at 360 nm matches with that of 1454 cm-1 of Raman peak of PS which is CH_2 or CH_3 bending mode. Also, secondary emission peaks of excitation at 440, 458, 488, 500, 514 nm wavelengths match with 2907, 2986 cm^{-1} of SP^3 CH group or 3004, 3056 cm^{-1} of SP^2 CH group [168,170]. In case of PVA, the third emission peak of 380 nm excitation wavelength matched with one of the Raman modes of PVA which is at 1232 cm^{-1} ascribed as CH vibrational mode. It is usually a weak mode [168,171].

However, for the observed phenomena to be completely Raman, $\Delta\lambda$ should remain constant. From tables 2 to 5, it is found to be varying. In order to confirm, water Raman spectra was recorded at different excitation wavelengths. Water molecule has three modes. They are O-H symmetric stretching, O-H asymmetric stretching and, H-O-H bending. These modes occur respectively at 3585, 3506 and 1885 cm^{-1}. Table 6 illustrates excitation and emission wavelengths recorded using fluorescence spectrometer for water. From table 6, it is clear that Raman shift observed is constant throughout the analysis and matches with OH vibration mode. In earlier analysis for fs laser irradiated polymer the observed Raman shift is found to be varying. The reason for not observing a constant Raman shift could be because when one varies the excitation wavelength, it may be resonantly exciting different centers that might be under different stress or defects.

Table 6. Excitation, emission, and Raman shift observed in water.

S. No.	λ_{ext} (nm)	λ_{em} (nm)	$\Delta\lambda$ (cm^{-1}) = λ_{ext}^{-1} - λ_{em}^{-1}
1	280	311	3560
2	300	334	3393
3	320	359	3395
4	340	385	3438
5	350	397	3383
6	360	410	3388
7	380	436	3380
8	400	464	3448
9	420	489	3559
10	440	519	3460
11	460	546	3424
12	480	574	3412
13	500	605	3471
14	520	634	3458
15	540	665	3481
16	560	696	3489
17	580	722	3391
18	600	763	3561
19	620	794	3535

d) Red Edge Effect (REE)

Unusual spectroscopic behavior was reported earlier in case of organic fluorophores in rigid and highly viscous environments by W. Galley in Canada [172] and Rubinov in Belarus [173]. The unusual phenomena are the observation of the shift of fluorescence spectra with longer wavelengths of excitation that is red edge of the absorption spectrum in case of low temperature glasses. Varieties of fluorophores in different media with frozen or relatively slow structural dynamics from vitrified and highly viscous solutions to polymer matrices have shown similar effects. These phenomena did not account for concepts of independence of emission energy on excitation energy within the absorption band (Vavilov's law) and the occurrence of emission irrespective of excitation band, always from the lowest electronic and vibrational state of same multiplicity called Kasha's Rule [174-175].

These effects originate not from the violation of fundamental principles, but from their operation in specific conditions, when the ensemble of excited molecules is distributed in interaction energy with molecules in their surroundings. In a condensed medium, this distribution always exists at the time of excitation, but its display in a variety of spectroscopic phenomena depends on how fast the transitions are between the species forming this ensemble of states. Thus, REE is a site-selective effect which allows probing of the dynamics of redistribution of fluorophores between different environments [176]. The first observation of static REE in polymeric media were made with DMABN in PMMA and pyridine merocyanine dye in PVA [177-178]. REE effect was also reported in glassy polar polymer matrices [179], polymer solutions [180], and hydrogels [181]. Excitation at the red edge results in the loss of vibrational structure and a shift to longer wavelength of fluorescence spectra, leaving the excitation spectra emission-independent.

In the present study, the fs laser irradiated polymers (whose details are explained above) are investigated. A plot of excitation wavelength with emission wavelength is shown in figure 13. Clearly, it is observed that the shift in emission peak with excitation wavelength in irradiated polymers show the REE phenomena.

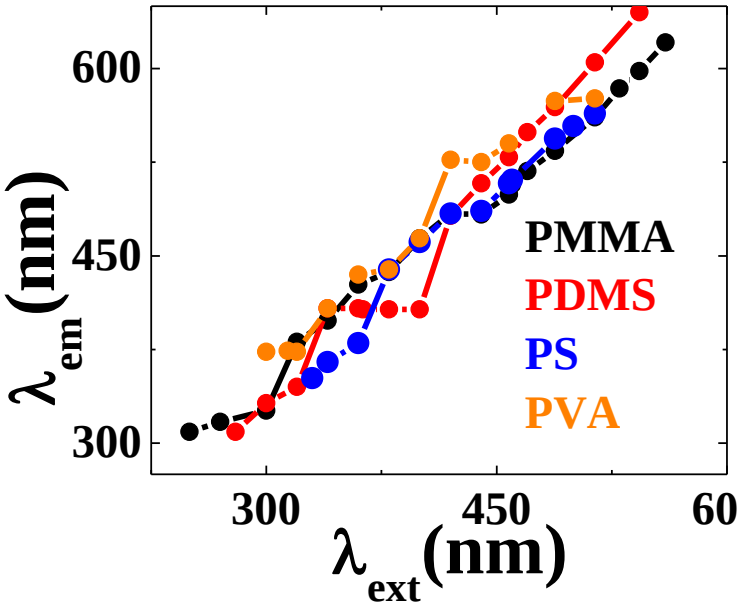

Figure 13. Plot of emission wavelength dependence on excitation wavelength in different polymers investigated after fs laser treatment.

4.4 Conclusions

In this chapter, observation of emission in four polymers PMMA, PDMS, PS, and PVA after fs laser irradiation is reported. The change in emission is ascribed to the formation of different optical centers and the main absorption which is responsible for emission behavior is attributed to the transitions such as n→π*, π→π*. Interference of Raman peaks over emission peaks is investigated. The shift in the emission peak with excitation wavelength on the red side of the excitation spectrum is explained in the context of localization effects such as “Red-edge Effect”.

Chapter 5

Abstract

The formations of free radicals that are paramagnetic in nature are explained in the polymers PMMA, PDMS, and PS after fs laser irradiation. The observation of peroxide type, alkoxy type of free radicals in fs laser modified regions of polymers is carried out and confirmed with electron spin resonance (ESR) technique. The role of interaction of the surface with the atmosphere is highlighted to determine the stability of these free radicals. The amorphous nature of the materials which are independent of orientation is explained. The observation of change in the percentage of elements in the modified regions due to the formation of optical centers explained in earlier chapter and paramagnetic centers is carried out by the elemental analysis of the investigated polymers using Energy Dispersive X-ray Absorption Spectroscopy (EDXAS) technique which showed the distribution of various elements after fs laser interaction with the investigated polymers.

5.1 Introduction

Majority of stable molecules are held together by bonds in which electron spins are paired in which there is no net electron spin which leads to no net electronic magnetic moment. Hence, no interaction between the electronic spins and applied magnetic field. Atoms or molecules which contain one or more electrons with unpaired spins are expected to show electron spin resonance (ESR) spectroscopy. Since these materials are called paramagnetic materials, this spectroscopy also refers to electron paramagnetic resonance (EPR) [165]. Substances with unpaired electrons may either arise naturally or produced artificially. Unstable paramagnetic materials also called as free radicals or radical ions are formed either as intermediates in a chemical reaction or by irradiation of a normal molecule with ultra-violet or X-rays or a beam of nuclear particles. One can detect these radicals provided these radicals life time is more than a μs. Species shortlived at room temparature may also be studied at a low temparature either in solid state or trapped in a solid matrix of a host material. This is called matrix isolation and it increases lifetime of the trapped radical. When unpaired electrons exist in a substance their spins are aligned randomly. When a magnetic field is applied, they will have a preferred direction spinning either clockwise or anticlockwise about the field direction. ESR spectroscopy thus measures essentially the energy required to reverse the spin of an unpaired electron. The intensity of ESR absorption is proportional to the concentration of the free radical or paramagnetic material present. The width of ESR resonance depends upon the relaxation time of the spin state under study. Spin-spin interaction is very efficient unless the sample is extremely dilute and gives a relaxation time of 10^{-6}-10^{-8} s. The spin-lattice interaction is efficient at room temparature but will be less effective at reduced temperatures.

The spin energy levels of an electron are separated in an applied magnetic field B by an amount as

$$\Delta E = h\upsilon = g\mu_B B \qquad (5.1)$$

Where μ_B is Bohr Magneton, g the Lande splitting factor and h is Planck's constant. The value of μB is given as 9.273×10^{-24} JT^{-1}. Resonance absorption occurs at a frequency mentioned below as

$$\upsilon = \frac{\Delta E}{h} \qquad (5.2)$$

To study the role of radical species as intermediates in polymerization process and polymer degradation process, ESR spectroscopy offers a solution [182]. ESR spectroscopy enables both the identification of radicals and their concentration and also it is a non-destructive technique. The spectra can be recorded both during polymerisation and degradation of polymers [183]. Degradation of polymers is a deterioration in the polymer materials leading changes in molecular structure, molecular weight etc. This degradation takes place when these polymer materials interact with high-energy radiation, gamma rays and electron beams. The degradation reactions usually involve free radical intermediates, and therefore ESR spectroscopy is a valuable technique for investigating the chemical mechanism of degradation. In this chapter we present our results on the effect of fs laser irradiation with polymers PMMA, PDMS, PVA and PS. Free radicals which are paramagnetic in nature are formed when these polymers are treated with fs pulses. Role of surface and environment is discussed. Formation of optical centers explained in earlier chapter and paramagnetic centers lead to change in chemical composition in fs laser irradiated regions compared with pristine regions.

5.2 Observation of free radicals

Polymers are cut into 3 mm×10 mm area and edges are polished before micro fabrication experiments being carried out. In order to increase the effective area, two dimensional grating structures (grid) are fabricated on the surface of bulk PMMA and PDMS. For collecting the Electron Spin Resonance (ESR) spectra we have written two dimensional grids on the surface of PMMA at 5, 10, 50 μJ energies, scanning speed of 1 mm/s and collected ESR after 5 days as ESR spectrometer in the institution was not functional at that time and samples were to be carried out to a different place. Table 1 shows the parameters used to fabricate the structures. Figure 1 (a) and 1 (b) show the confocal microscope images of such grids fabricated in PMMA and PDMS polymers.

Table 1. Parameters used to fabricate surface grids in polymers PMMA and PDMS.

Code	Energy (μJ)	Period (μm)	Speed (mm/s)	Width (μm)
PMMA1	5	18	1	9
PMMA2	10	25	1	10
PMMA3	50	35	1	22
PDMS1	5	12	1	6-8
PDMS2	10	30	1	15-16
PDMS3	50	65	1	30

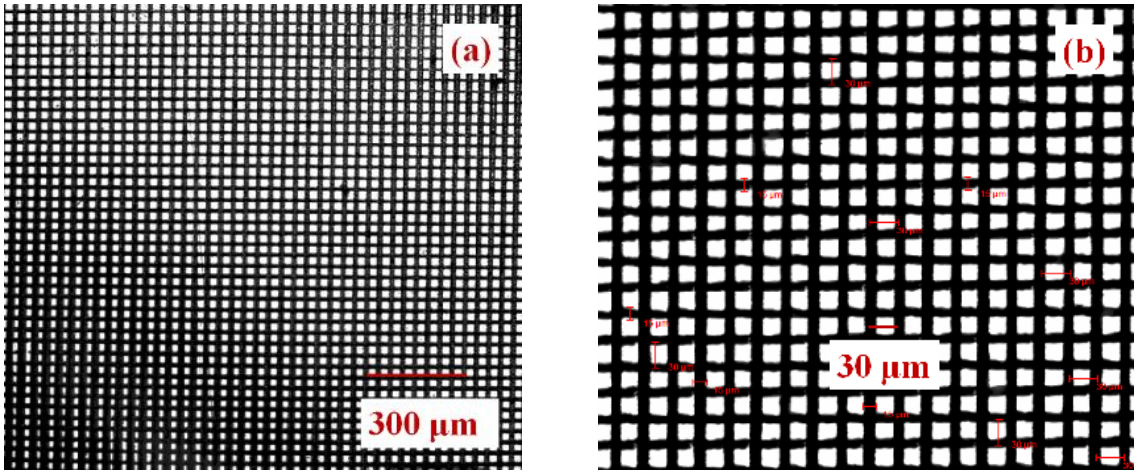

Figure 1. Confocal microscope images of surface grids in (a) PMMA3 (b) PDMS2

Figure 2 (a) shows the ESR spectrum of pristine PMMA, while figure 2 (b) shows the ESR spectrum of irradiated/modified PMMA at 50 μJ energy. Figure 2 (c) depicts the ESR spectrum of mechanically scratched PMMA and figure 2 (d) shows the same spectrum (of figure 2(c)) recorded after one and half hours. We could not observe any ESR signal as we suppose that the lifetime of free radicals, responsible for the ESR peaks, are too short. However, mechanically

scratched PMMA showed ESR signal as mechano-radicals are generated. As samples were taken to a different Institute, the radicals which we were supposed to observe in ESR spectrometer were not found due to short life time. Nie et al. [40] revealed 9 line ESR spectrum of PMMA immediately after irradiation and reported generation of free radicals immediately after irradiation. We could not observe in our case as our investigations are carried out at room temperature. There are reports available in literature on PMMA treated with different radiations. Earlier studies [40, 184-185] suggest that when these polymers are irradiated with ionizing radiation free radicals are generated. If a polymer is irradiated in vacuum the radical concentration produced in the polymer depends on the irradiation dose. When these vacuum-irradiated polymers are exposed to air, the free radicals trapped in the material are transformed into peroxide radicals through the reaction with molecular oxygen. Kaptan et al. [185] have irradiated PMMA with γ radiation in a vacuum and reported a nine-line ESR spectrum. They have shown the transformation of nine line ESR spectrum into a single peak anti-symmetric peroxide type free radical formation with exposure to air. Velter-Stefanescu et al. [184] have collected ESR spectra for electron-irradiated PMMA and observed single peak ESR signal at 326.5 milliTesla (mT). ESR signal obtained from mechanical scratching was found at the same magnetic field and the same authors report it to be single radicals which are responsible for ESR signal in case of electron beam irradiation on PMMA.

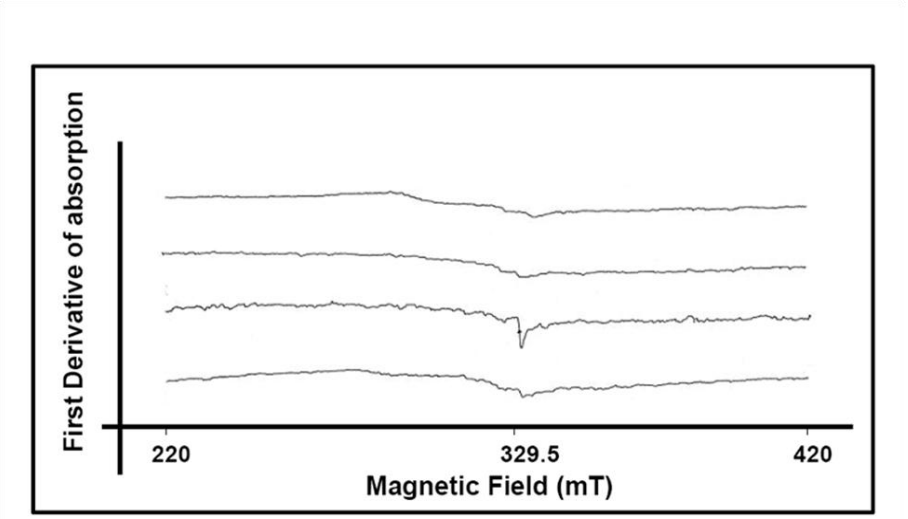

(a) Pristine PMMA.
(b) Irradiated PMMA at 50μJ, 1mm/s speed.
(c) Scratched PMMA
(d) Scratched PMMA after 90 minutes.

Figure 2. ESR signal of PMMA

Similar experiments were carried out in PDMS also. Figure 3 shows the ESR spectra of pristine PDMS, fs-modified PDMS, and mechanically scratched PDMS. We have observed one peak near 330 mT in the ESR spectra of fs-modified PDMS, for the first time to our knowledge, indicating the presence of free radicals. However, unlike in PMMA, the mechanically surface scratched PDMS did not show any ESR peaks. As mechanically scratched PMMA and fs laser irradiated and modified PDMS exhibited ESR signals at the same magnetic field and their g values are approximately equal to 1.9, we confirm that same free radical is responsible for both the ESR spectra. However, lifetimes are different because the host materials are different for PMMA and PDMS.

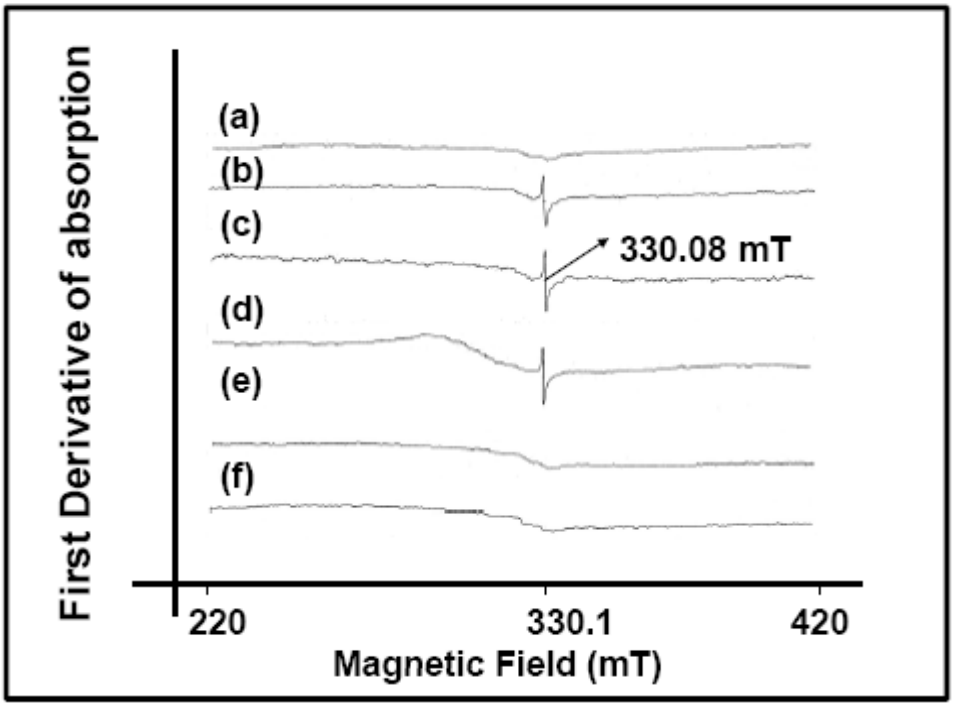

(a) Pristine PDMS.
(b) Irradiated PDMS at 5 µJ, 1mm/s.
(c) Irradiated PDMS at 10 µJ, 1mm/s.
(d) Irradiated PDMS at 50 µJ, 1mm/s.
(e) Scratched PDMS.
(f) Scratched PDMS after 15 minutes.

Figure 3. ESR spectra collected from fs-irradiated PDMS, pristine PDMS, and mechanically scratched PDMS

We carried out similar experiments when ESR spectrometer was functional at our Institute to comprehend our results. We have repeated our investigations and recorded the spectra immediately after fs laser irradiation. Figures 4 (a) and 4(b) show fs laser modified PMMA (50 µJ energy, 1 mm/s speed) and PDMS where structures were fabricated inside the surface (3, 6 µJ energy with 1 mm/s speed) . We could not observe free radicals in fs modified PMMA during our earlier studies since the ESR spectra were recorded after few days as ESR spectrometer was not functional. However, fs laser irradiated PMMA exhibited free radicals when the ESR spectrum was collected within two days of exposure. In the case of PDMS we observed free radicals even after 6 months. This demonstrates the dependence of life time and stability of free

radicals in different host environments. We have also extended our studies to PS. Figure 4(c) shows the ESR spectrum recorded in PS irradiated grating fabricated with 30 μJ energy, 1 mm/s speed with period 15 μm. We observed no ESR signal in case of pristine PS. We collected several spectra after 1 hour of fabrication in different time intervals. Irradiated PS demonstrated decrease in ESR signal with time. Irradiated regions of PMMA and PDMS polymers also showed ESR signal at the same magnetic field. All these polymers exhibited ESR signal at the same magnetic field of 326 mT with **'g'** value of 2 from which we predict the existence of peroxide type free radicals. PMMA and PS illustrated decrease in ESR signal in few days of time while the PDMS showed ESR signal even after six months indicating that the free radicals are stable in this polymer. However, the emission from the irradiated regions of polymers explained in earlier chapter did not vanish even one year after the exposure. This clearly suggests that the free radicals which contributed to ESR signal do not lead to the emission except in the case of PDMS. Graubner et. al has treated PDMS with 172 nm irradiation. They reported the abstraction of hydrogen (which is initial step) followed by reaction of methylene radicals with oxygen leading to peroxy radical formation. This peroxide radical rearranges to silanol group. We strongly feel that the silanol group is mainly responsible for its stability for long time [186]

Nie et al. [40] have reported typical characteristic 9 line spectrum of PMMA immediately after fs laser irradiation. However, our data depicted a single peak in the ESR spectra for PMMA, PDMS and PS since the experiment/irradiation was carried out in the atmospheric environment and room temperature.

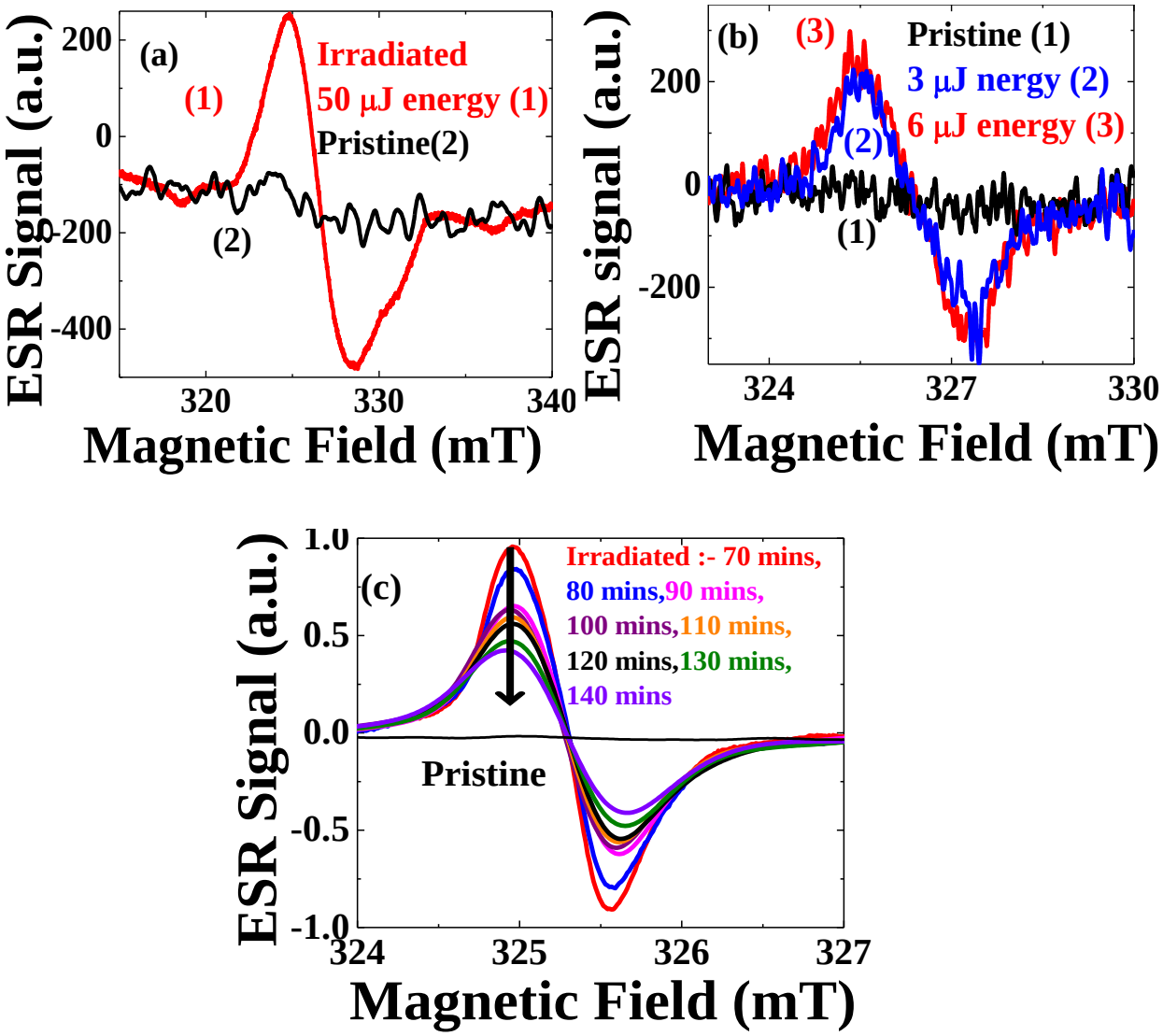

Figure 4. (a) ESR spectrum of irradiated PMMA at 50 μJ energy, 1mm/s speed. (b) ESR spectrum of irradiated PDMS at 3, and 6 μJ energy and a speed of 1 mm/s. (c) ESR spectrum of irradiated PS varying with time. Decrease in ESR signal intensity is indicated by the arrow.

Figure 5 shows the ESR signal of fs irradiated bulk PS. Pristine PS did not show any free radicals and or paramagnetic centers. After fs irradiation, bulk PS has shown peroxide type free radical. We found ESR signal becomes stronger with the incident energy as high energy irradiation modifies more compared to the low energy case. The ESR peak can be attributed to peroxide type free radical in fs irradiated PS with g value of 2 as it matches with our earlier investigations with PMMA. But reports in the literature suggest that irradiated PS under liquid nitrogen temperature transforms to asymmetric peroxy radicals when it is brought to room

temperature. Also several reports suggests that alkoxy radicals which could be main responsible for ESR signal as reported in literature [187-189].

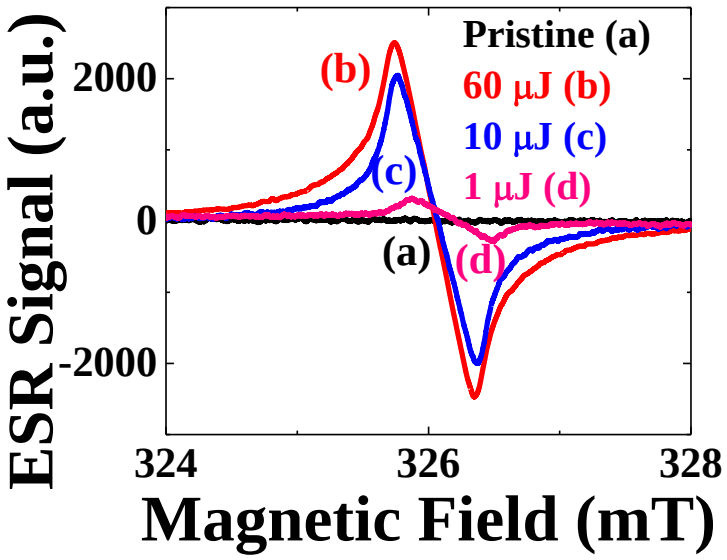

Figure 5. ESR spectrum recorded for fs-irradiated bulk PS at different energies 1, 10 and 60 μJ.

Interestingly, fs irradiated regions of PVA did not show any ESR signal. The polymers PMMA, PDMS, and PS are bulk materials. However, in our investigations, we prepared PVA solution and then made thin films before fabricating structures. Since the radicals generated can easily interact with atmosphere if structures are fabricated either on the surface or thin film, we feel that the same case would happen in PVA polymer thin film also. In order to understand the role of a surface, we fabricated similar structures on the surface and buried in PMMA and PS polymers and compared the radical concentrations. Figure 6 (a) shows a microscope image of a fabricated grating structure on the surface of PS fabricated at 30 μJ energy, 1mm/s speed with 40 μm period. Figure 6 (b) shows a plot of ESR signal of fs laser irradiated PS (buried and surface) and pristine PS. From figure 6 (b), we clearly see that radical concentration of PS is almost negligible when grating is fabricated on the surface when compared with inside. Similar trend is observed in case of other polymers also. Also, we observed the ESR signal almost constant when ESR tube is oriented at different angles w.r.t. the magnetic field as depicted in figure 6 (c). Since these polymer materials are amorphous there is no symmetry present and ESR signal is independent of the orientation.

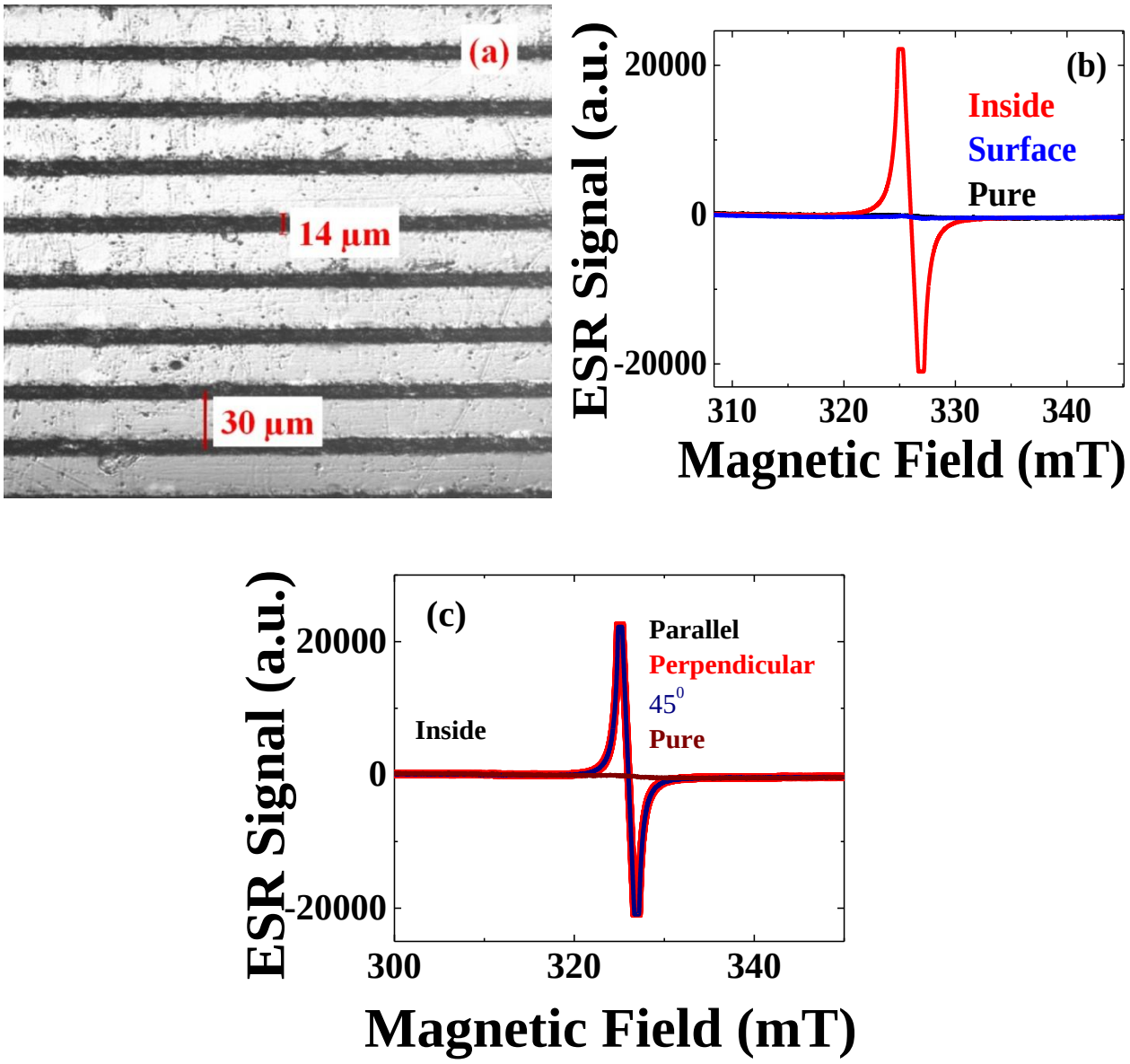

Figure 6. (a) Microscope image of a surface grating structure on PS (b) ESR signal of fs irradiated PS a pristine PS (c) ESR signal with orientation of sample.

5.3 EDXAS analysis

In our effort to understand the composition after the polymer chain scission due to radiation affects that resulted in possible defect formation we collected the FESEM and EDXAS data from the fs laser irradiated PMMA and PDMS. The main elements in PMMA are carbon (C) and oxygen (O) and silicon (Si), carbon (C), and oxygen (O) for PDMS. Since these structures are fabricated on the surface of polymers, the ablated materials consisting of different compositions and main elements cannot escape anywhere but settle at the edges of the structures. Hence, there will be a variation in weight percentage/atomic percentage of these elements compared with pristine regions. We fabricated different micro structures on the surface of PMMA at 50, 40, 30, 20, and 10 µJ energies with 1mm/s scanning speed. Figure 7 (a) shows FESEM images of micro structures fabricated on the surface of PMMA. We observed void type regions at the centre from FESEM pictures for all the irradiation energies above 10 µJ. Figures 7 (b) and (c) show the pristine region of PMMA and the plot that shows percentage of elements present through EDXAS analysis.

Figure 8 (a) shows the modified region with average energy pulses of 40 µJ, 1 mm/s speed while figure 8 (b) shows the plot of percentage of elements. The weight percentages of C and O are 60 and 40 in pristine regions. The percentage of C and O found to be are 81 and 19 in the end regions. This is due to the settling of the ablated material from the modified regions as can be observed in FESEM pictures. In case of middle portion of the structure the percentage contents of C and O are 87 and 13 respectively. As the middle portion of the structure is influenced by higher intensities, one would expect material getting carbonized completely and hence there is a slight enhancement in percentage of C. This is illustrated in the figures 8 (c) and (d).

Extending the same elemental analysis to PDMS, we focused our attention to elements C, O, and Si. For pristine regions of PDMS, we found the contents of C, O, and Si in the percentage weight ratios of 26, 40 and 34. Figures 9 (a) and (b) show FESEM and EDXAS pictures. Figure 9 (c) and (d) show FESEM picture of a microstructure on the surface of PDMS fabricated at 40 µJ energy with 1 mm/s scanning speed and weight percentage contents of different elements in the middle portion of the structure obtained with EDXAS analysis. We found the weight percentage of these elements is 13, 27 and 60. Figures 9 (c) and (d) show the middle portion of the structure

fabricated and EDXAS analysis. There is slight decrement in carbon and oxygen elements unlike silicon, whose percentage content is increased. We found similar trend in other cases that include at different regions of interest with different energies. Silicon is heavier element compared with carbon and oxygen and hence it may not escape from the same regions.

Tables 2 and 3 show weight percentage of different elements in PMMA and PDMS obtained with fs laser irradiation. We observed that for the structure fabricated at 1 μJ energy the percentage composition of C, O, and Si showed no difference between end and central regions (see table 3). As the structure is narrow due to low energy irradiation dose, there is not much appreciable gap left between end and middle regions. Also from the data presented in table 1 and 2 we could not establish a particular trend due to the complexity involved in the problem. At higher energies, we observed the ablated material getting settled on microscope objective that leads to loss of the material, which cannot be accounted for the analysis part to study the distribution of various elements after fs laser treatment. Also, there could be decrease in irradiation energy as the settled ablated material on the microscope objective does not transmit all the light and lead to losses. Similar studies are carried out in PVA and PS polymers also. In case of PVA, pristine regions contain 55 % carbon and 45 % oxygen. As structures are fabricated on PVA thin film, we do not observe any major changes in chemical composition when end and middle regions are compared. Figure 10 (a) and 10 (b) show the FESEM image of a microstructure fabricated on the surface of PVA thin film and EDXAS plot of the structure. Table 4 lists the chemical compositions for different structures fabricated at different energies with 1 mm/s speed. However, in case of polystyrene, since only two elements carbon and hydrogen are present, we could not record as hydrogen cannot be detected with EDXAS.

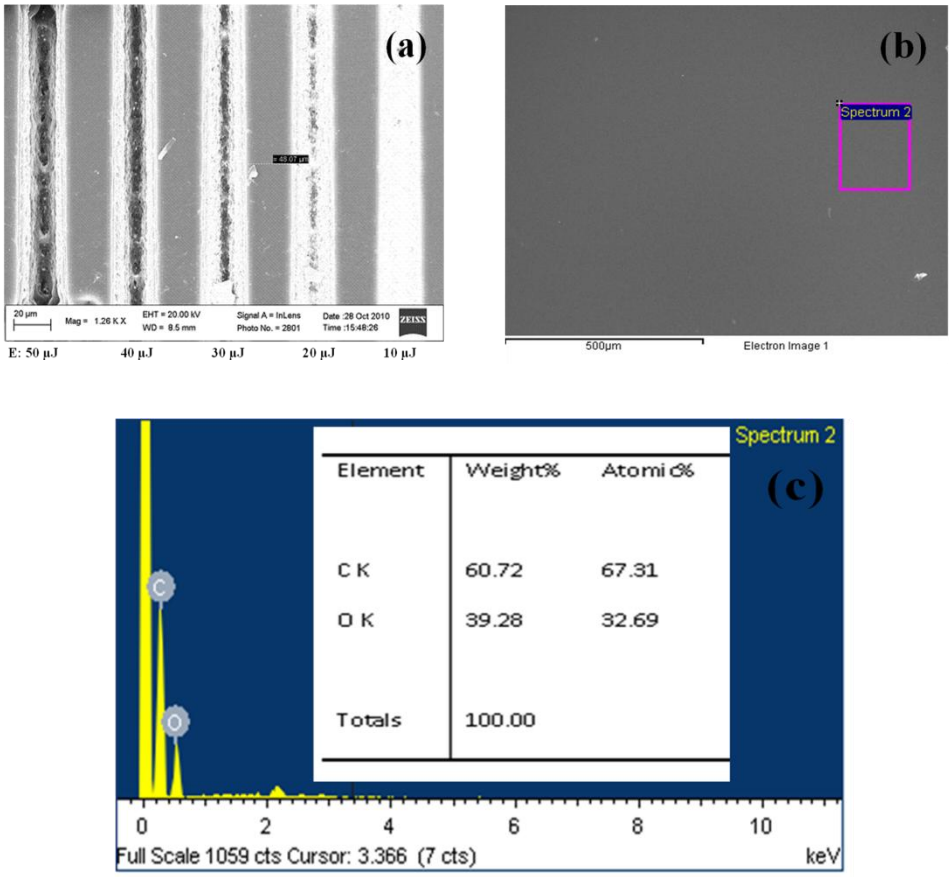

Figure 7. (a) FESEM image of a micro structures fabricated on the surface of PMMA with a period of 50 µm for elemental analysis using EDXAS. Energies of the fabricated structures is clearly mentioned below the picture. (b) Pristine region of PMMA where EDXAS is performed (c) Percentage of various elements of carbon and oxygen in pristine PMMA.

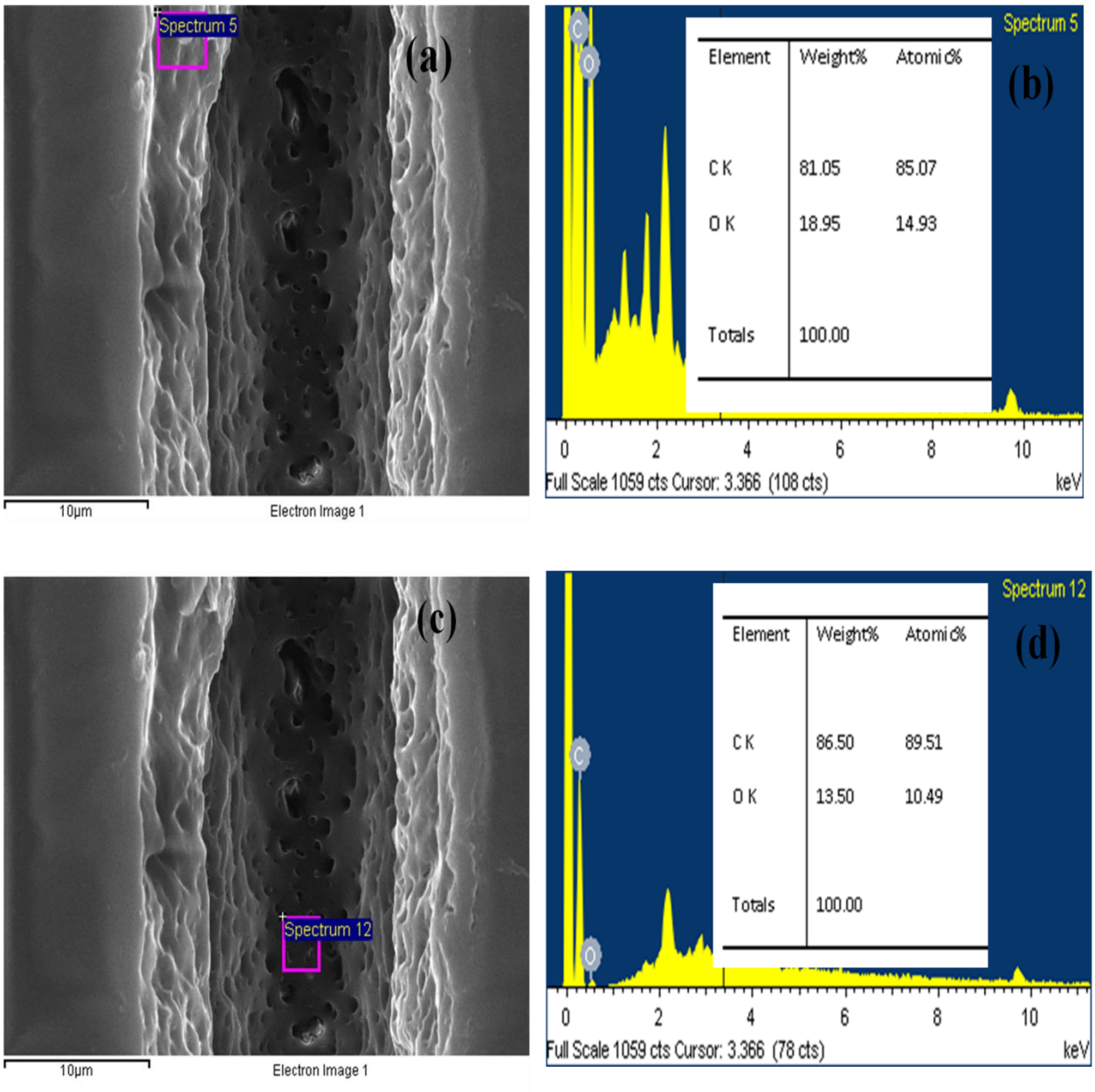

Figure 8. (a) FESEM image of a micro structure fabricated at 40 µJ energy, 1mm/s speed and the rectangle shows the region where EDXAS is collected (Scale bar 10 µm).(b) % contents of C and O in the end region (c) The middle portion of the structure where EDAX is performed (Scale bar 10 µm).(d) The % contents of C and O.

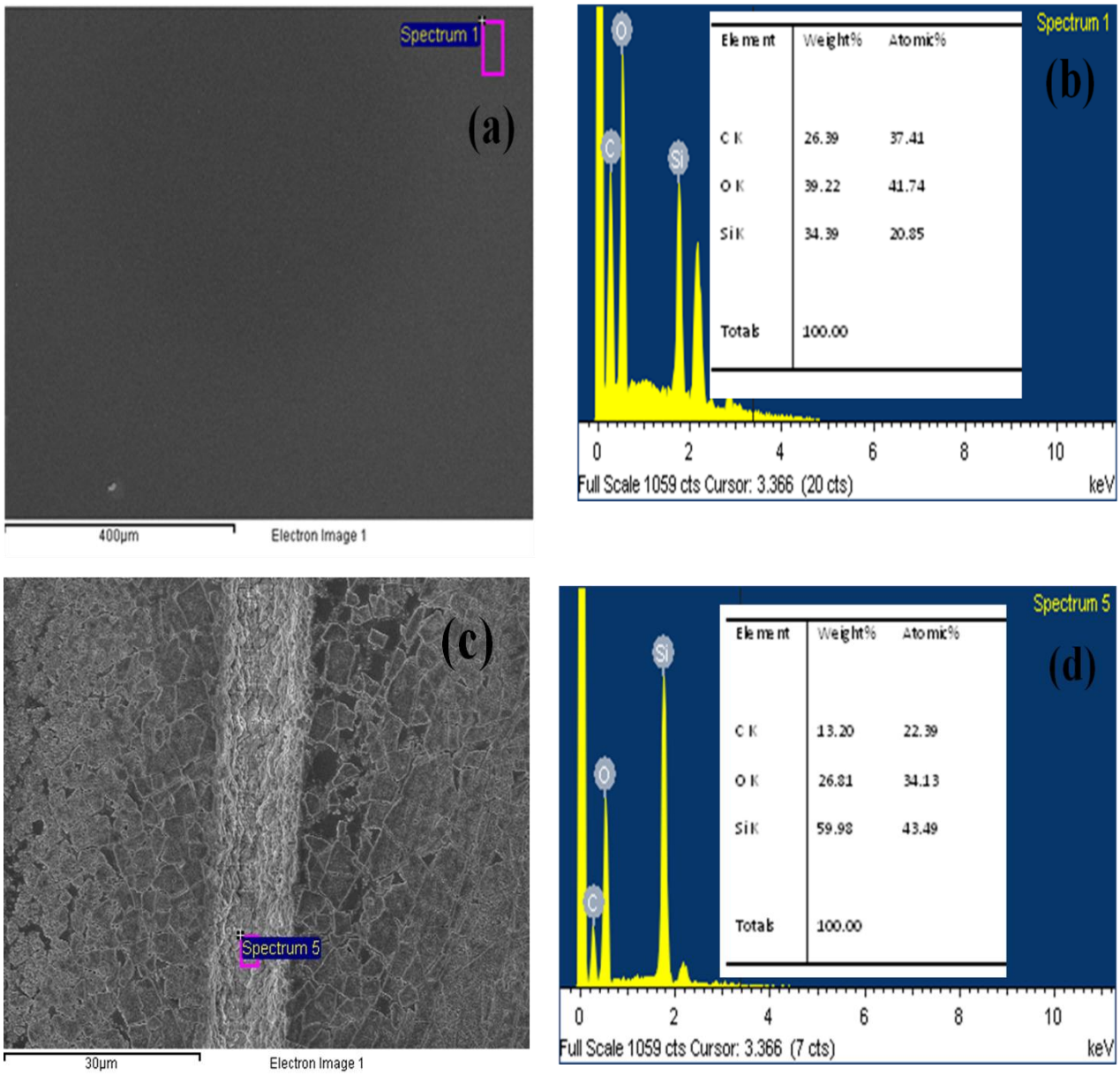

Figure 9. (a) FESEM image of a micro structure fabricated at 40 µJ energy, 1mm/s speed and the rectangle shows the region where EDXAS is collected.(b) % contents of C and O and Si in the pristine region (c) The middle portion of the structure where EDXAS is performed (Scale bar is 30 µm) (d) The % contents of C and O and Si.

Table 2. Weight % of elements C and O at different energies in PMMA collected in different regions using EDXAS analysis.

S. No.	Energy (μJ)	Region	%C (%Weight)	%O (%Weight)
1	Pristine		60-64	35-40
2	50	End	70-84	16-30
		Middle	63-83	17-37
3	40	End	71-86	18-25
		Middle	67-87	12-34
4	30	End	67-87	12-33
		Middle	70-88	12-29
5	20	End	65-84	16-35
		Middle	88-97	3-13
6	10	End	79-83	17-21
		Middle	86-89	11-14

Table 3. Weight % of elements C, O, and Si at different energies in PDMS collected in different regions using EDXAS analysis.

S. No.	Energy (μJ)	Region	%C (%Weight)	%O (%Weight)	%Si (%Weight)
1	Pristine		26-30	39-41	30-35
2	50	End	18-24	19-27	54-57
		Middle	31-41	19-26	54-57
3	40	End	7-18	10-39	44-83
		Middle	7-15	12-31	53-80
4	10	End	12-20	24-35	46-63
		Middle	13-15	18-20	67-68
5	1	End	23-25	30-32	44-46
		Middle	23-25	30-32	44-46

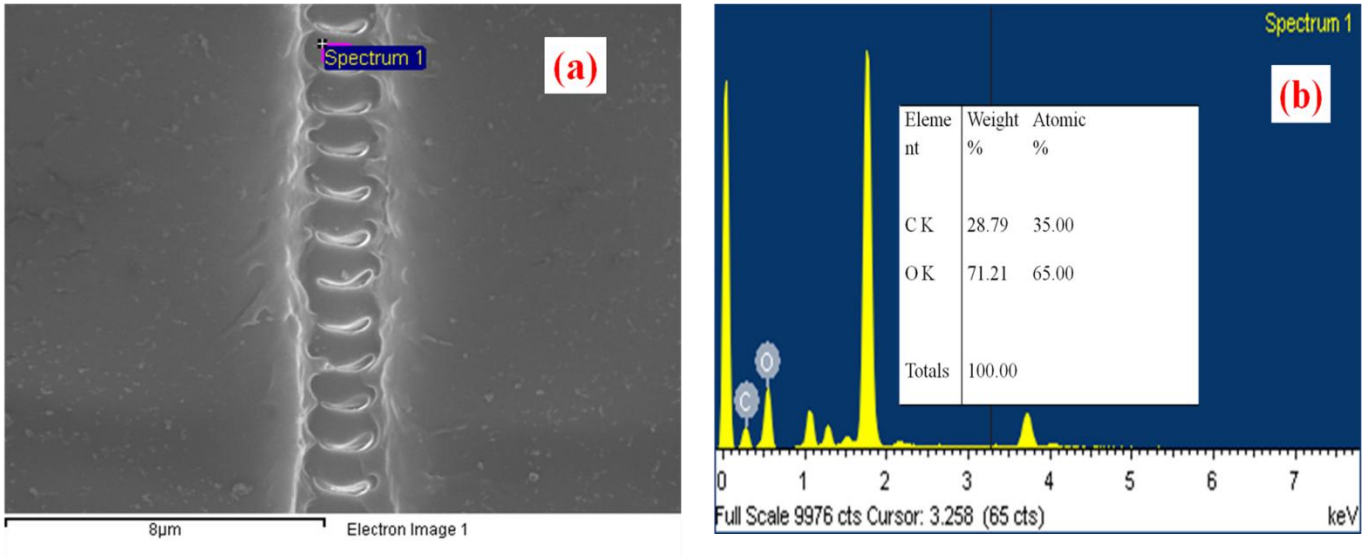

Figure10. (a) FESEM image of a micro structure fabricated at 564 nJ energy, 1mm/s speed and the rectangle shows the region where EDXAS is collected.(b) % contents of C and O in middle portion of the fabricated structure.

Table 4. Weight % of elements C, and O at different energies in PVA collected in different regions using EDXAS analysis.

S. No.	Energy (μJ)	Region	%C	%O
1	Pristine		55	45
2	100	End	10	90
		Middle	8	92
3	80	End	9	91
		Middle	11	89
4	60	End	12	88
		Middle	10	90
5	40	End	8	92
		Middle	5	95
6	20	End	10	90
		Middle	12	88
7	10	End	15	85
		Middle	9	91
8	1	End	40	60
		Middle	31	69
9	0.634	End	39	61
		Middle	32	68
10	0.564	End	39	61
		Middle	35	65

5.4 Conclusions

In this chapter, the formation of free radicals that are paramagnetic in nature are explained in the polymers PMMA, PDMS, and PS after fs laser irradiation. The observation of peroxide type of free radicals in fs laser modified regions of polymers is carried out and confirmed with electron spin resonance (ESR) technique. For structures fabricated on the surface of polymers do not show ESR as radicals that are generated on the surface interacted with atmospheric oxygen and escaped. The observation of change in the percentage of elements in the modified regions is investigated and reported through Energy Dispersive X-ray Absorption Spectroscopy (EDXAS) technique.

Chapter 6

Abstract

In this chapter Raman spectra collected in pristine and fs laser modified regions are investigated. Assignments of various Raman modes of these polymers are presented. Broadening and suppression of Raman modes in case of structures fabricated at high energies is explained by modification of the material due to its interaction with high intensity laser pulses which essentially leads to the formation of defects. Thermal effects are also discussed. Raman-mapping carried out across the structure showed the same effect as the center of the structure is influenced by huge intensity of the Gaussian pulse which produces more number of defects at the center compared with edges.

6.1 Introduction

Raman spectroscopy provides information about molecular vibrations that can be used for sample identification and quantization. The technique involves shining a monochromatic light source (i.e. laser) on a sample and detecting the scattered light. The majority of the scattered light is of the same frequency as the excitation source; this is known as Rayleigh or elastic scattering. A very small amount of the scattered light is shifted in energy from the laser frequency due to interactions between the incident electromagnetic waves and the vibrational energy levels of the molecules in the sample. Plotting the intensity of this "shifted" light versus frequency results in a Raman spectrum of the sample. Generally, Raman spectra are plotted with respect to the laser frequency such that the Rayleigh band lies at 0 cm^{-1}. On this scale, the band positions will lie at frequencies that correspond to the energy levels of different functional group vibrations. The Raman spectrum can thus be interpreted similar to the infrared absorption [165, 168].

Raman scattering is a spectroscopic technique that is complementary to infrared absorption spectroscopy. Raman offers several advantages over mid-IR and near-IR spectroscopy, including:

- Little or no sample preparation is required
- Inexpensive glass sample holders are ideal in most cases
- Fiber optics (up to 100's of meters in length) can be used for remote analyses
- Since fundamental modes are measured, Raman bands can be easily related to chemical structure
- Raman spectra are "cleaner" than mid-IR spectra - Raman bands are narrower, and overtone and combination bands are generally weak
- The standard spectral range reaches well below 400 cm^{-1}, making the technique ideal for both organic and inorganic species
- Raman spectroscopy can be used to measure bands of symmetric linkages which are weak in an infrared spectrum (e.g. -S-S-, -C-S-, -C=C-)

It is important to note that Raman scattering is not the absorption of the photon, followed by the emission of a photon of less energy that instead describes fluorescence. The difference between

Raman scattering and fluorescence is that, in Raman scattering the incident photon is not fully absorbed but it perturbs the molecule exciting or de-exciting vibrational or rotational energy states. But, in fluorescence the photon is completely absorbed causing the molecule to jump to a higher electronic state, and then the emitted photon is due to the molecule's decay back to a lower energy state. One advantage that Raman scattering has over infrared absorption however, is that since it is represented as a shift in frequency from the incident light, it can be done with visible light, which it is possible to create detectors with much higher efficiencies than infrared radiation. Furthermore, information about the molecule can be gained from the polarization of the Raman scattered light, information which is not easily accessible via infrared absorption. This made us to carry out our experiments with confocal micro-Raman to analyze the effect of fs laser in different polymers.

6.2 Raman Analysis of Polymers

For Raman analysis and investigation, structures are fabricated in PMMA, PDMS, PS, and PVA. The method of preparation of the samples is explained in earlier chapters. All the polymers investigated showed similar results. Figure 1 (a) and 1 (b) show the Raman spectra collected in different regions of the fabricated structures at high and low energies. Figure 1 (a) shows the Raman spectra recorded for a grating structure fabricated in PMMA with 50 μJ, 0.25 mm/s speed using 40X NA objective lens. Figure 1 (b) shows Raman spectra collected from a PMMA grating fabricated at ~3 μJ energy with 500 μm/sec scanning speed with 0.65 NA (40X) objective.

From figure 1 (a), we observed that various peaks in the spectrum collected from the fs modified regions are broadened probably due to huge strain created by the enormous peak intensities leading to the formation of defects at the focal volume. At high intensities, the broadening of Raman peaks could be due to the defects. SEM images of these structures confirmed formation of voids/empty channels explained in chapter 3. The debris from the voids region is re-deposited which contributed to the Raman signals. Raman spectra collected from regions far away from the focal volume (unmodified regions) did not reveal any peak broadening. For this, we recorded Raman for a structure fabricated at low energy. Figure 1(b) shows the Raman spectrum from low energy laser irradiated (3 μJ) regions, which clearly indicates that the changes in the

peak widths are minor unlike in the high energy case. Figure 2 demonstrates the micro-Raman spectra collected for grating PDMSBG3 (whose fabrication details are indicated in chapter 3) from the unexposed region (dashed line), exposed region (solid line), and the central regions (dotted line). It is noticed that there is no variation in the peak positions and widths in different spectral regions. A slight change in Raman intensity of the modified regions compared to unmodified regions is noticed which probably suggests that there are no major chemical alterations to the polymer at the focal volume. Table 1 and 2 show the Raman assignments of various modes in PMMA and PDMS [167-169].

Extending the same analysis in case of thin films also, the confocal micro-Raman spectra are collected from the modified regions of thin films of PS in order to predict the effect of fs pulses on Raman modes of PS. Figure 3 (a) shows Raman spectra collected for a structure fabricated at 90 µJ energy, 1mm/s speed using 40X objective. The spectra are collected from the middle portion and edge portion of the microstructure as shown in figure 3(b). The circles shown in figure 3(b) depict the middle and edge portions of the structure where Raman spectrum was collected. We used 50X objective with 0.75 NA to collect Raman with excitation wavelength 514 nm. Hence, the spot size of the 514 nm beam is approximately 850 nm. It may be noted that the circles shown is slightly larger in figure 3 (b) for clarity sake (while the scale bar is 65 µm width). 1001 cm^{-1} Raman mode corresponds to ring breathing mode. We noticed similar trend (broadening and suppression of Raman modes) like earlier case with PMMA and PDMS. Also, similar tendency has been noticed in the middle of the structure as it is influenced by the central portion of the incident Gaussian pulse which has more intensity resulting in larger stress or void formation that essentially leads to the formation of defects. In figure 3(c) since, the microstructure is fabricated at lower energy; there is no appreciable change in ring breathing mode in both the regions (middle and edge) of the microstructure. Table 3 shows the assignment of different Raman modes [168,170]. PVA thin film which is prepared earlier also showed similar results depicted in figure 4 and table 4 [68,171].

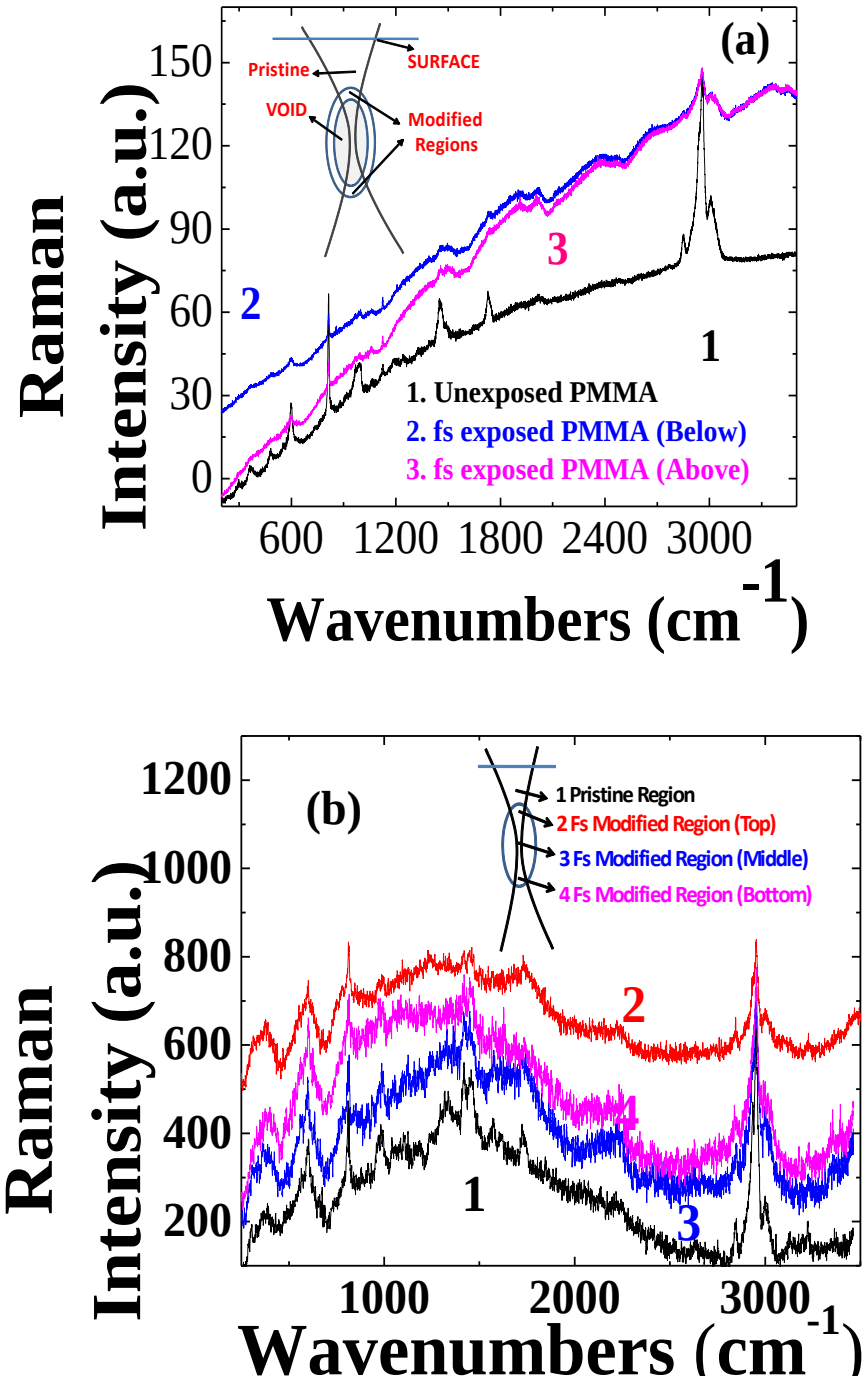

Figure 1. (a) Raman spectra from a PMMA grating (50 μJ, 0.25 mm/s) with the bottom curve representing the spectrum collected from unmodified regions of PMMA while the middle and top curves from the fs modified regions. (b) Micro-Raman spectrum of PMMA grating (~3 μJ, 500 μm/sec) achieved with 0.65 NA (40X) objective. The curves have been shifted for clarity. Inset shows the regions from which the spectra are collected.

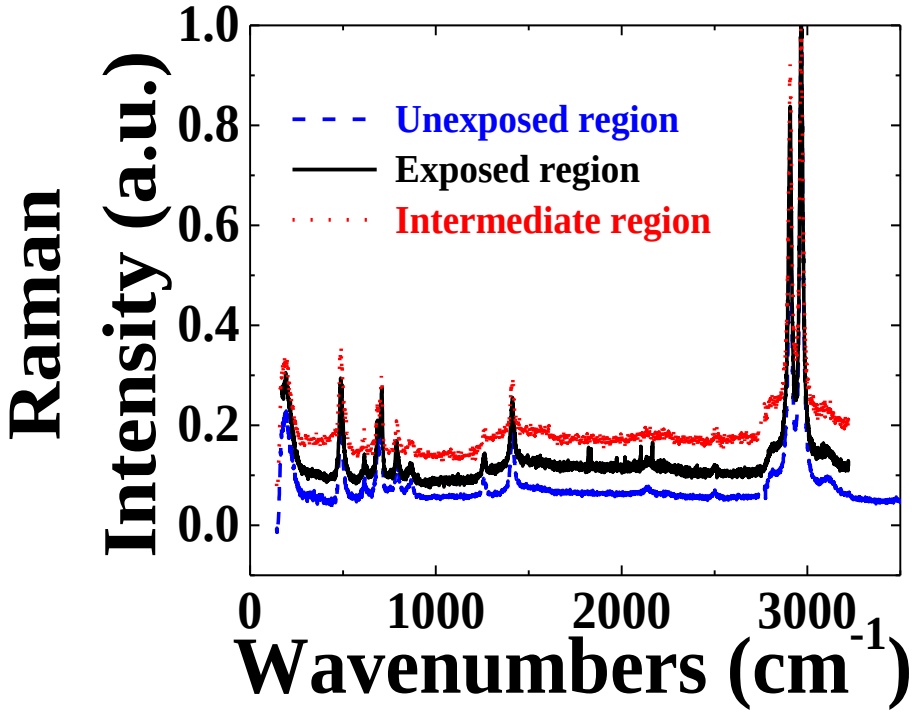

Figure 2. The Raman spectra of modified and unmodified regions of PDMS grating fabricated with 5 µJ energy, 1mm/s speed with 20 µm period.

Table 1. Raman modes of PMMA polymer

S. No.	Raman Band (cm^{-1})	Assignments
1	602	γ (C-COO), γ_s (C-C-O)
2	853	γ (CH_2)
3	925	γ (CH_2)
4	999	O-CH_3 rock
5	1081	γ (C-C) skeletal mode
6	1264	γ (C-O), γ (C-COO)
7	1460	δ_a (C-H) of α-CH_3, δ_a (C-H) of OCH_3
8	1648	Combination band involving γ (C = C) and γ (C-COO)
9	1736	γ (C=O) of (C-COO)
10	2848	Combination band involving O-CH_3
11	2957	γ_s (C-H) of O-CH_3 with γ_s (C-H) of α-CH_3 and γ_a of (CH_2)
12	3001	γ_a (C-H) of O-CH_3, γ_a (C-H) of α-CH_3
13	3454	2 γ_2 overtone of 1730 cm^{-1}

Table 2. Raman modes of PDMS polymer

S. No.	Raman Band (cm^{-1})	Assignments
1	488	Si-O-Si Symmetric Stretching
2	687	Si-CH_3 Symmetric rocking
3	708	Si-C symmetric stretching
4	787	CH_3 asymmetric rocking + Si-C asymmetric stretching
5	862	CH_3 symmetric rocking
6	1262	CH_3 symmetric bending
7	1412	CH_3 asymmetric bending
8	2907	CH_3 symmetric stretching
9	2965	CH_3 asymmetric stretching

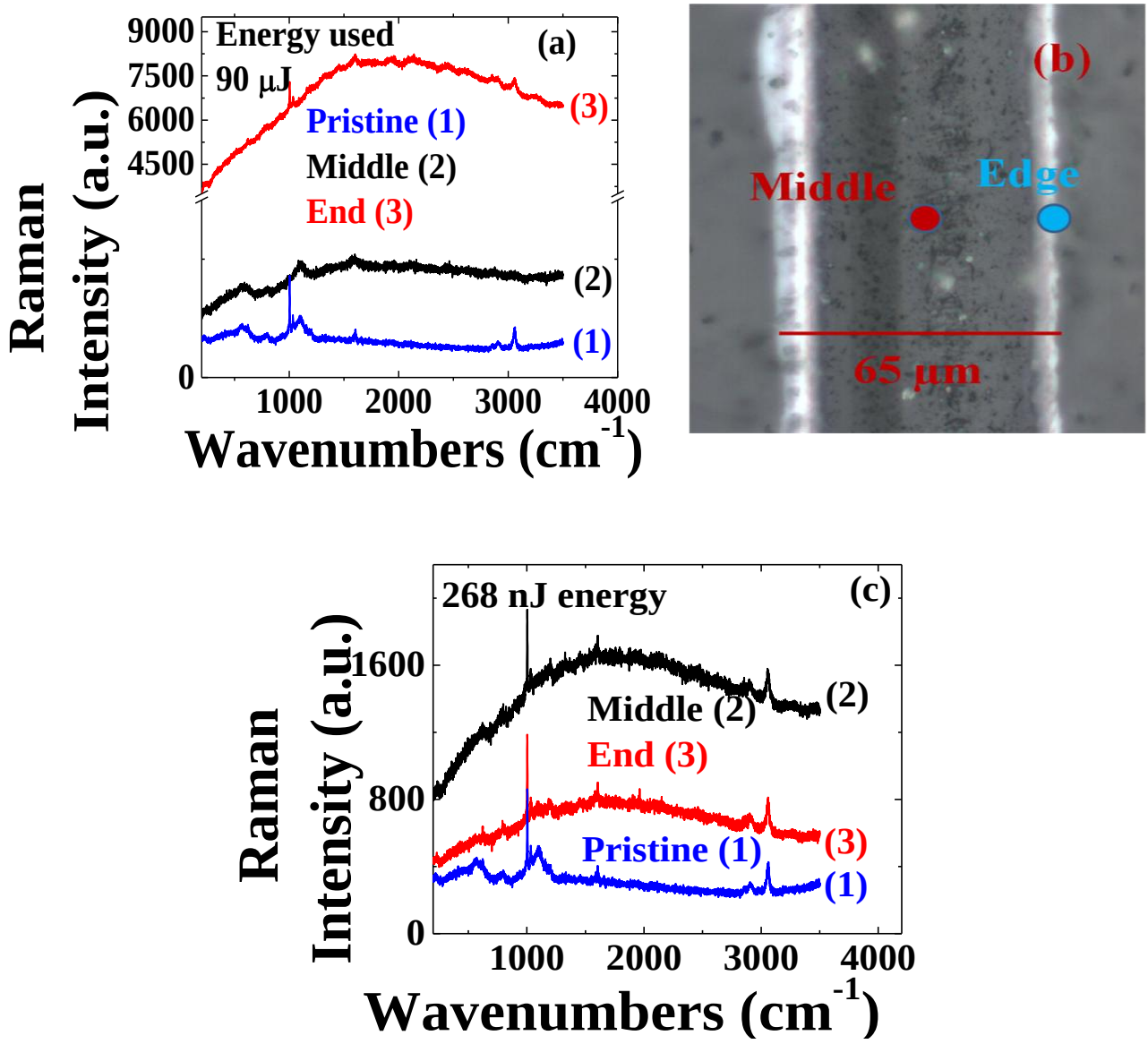

Figure 3. (a) Raman spectra collected from a microstructure fabricated in PS thin film using 40 X objective with energy 90 µJ, 1mm/s speed; (b) 65 µm width (Scale bar) structure obtained with 90 µJ energy. The spot sizes used to collect Raman are 836 nm (For clarity spots are shown in bigger size); (c) Raman spectra recorded for similar structure fabricated with 268 nJ energy in PS thin film.

Table 3. Raman modes of PS

S. No.	Raman shift (cm^{-1})	Assignment
1	398	No reference found
2	624	Ring mode (υ_{6b}) which supports either mono or para substitution
3	761	Out of plane CH bend for mono or para substitution
4	800	Finger print band of styrene
5	1004	Ring breathing mode
6	1032	Styrene group bands
7	1158	
8	1201	
9	1332	No reference found
10	1454	CH_2 or CH_3 bending modes
11	1587	υ_{8a} and υ_{8b} aromatic ring stretch (Aromatic ring deformation)
12	1604	
13	2853	SP^3 CH group
14	2907	
15	2980	
16	3004	SP^2 CH group
17	3056	

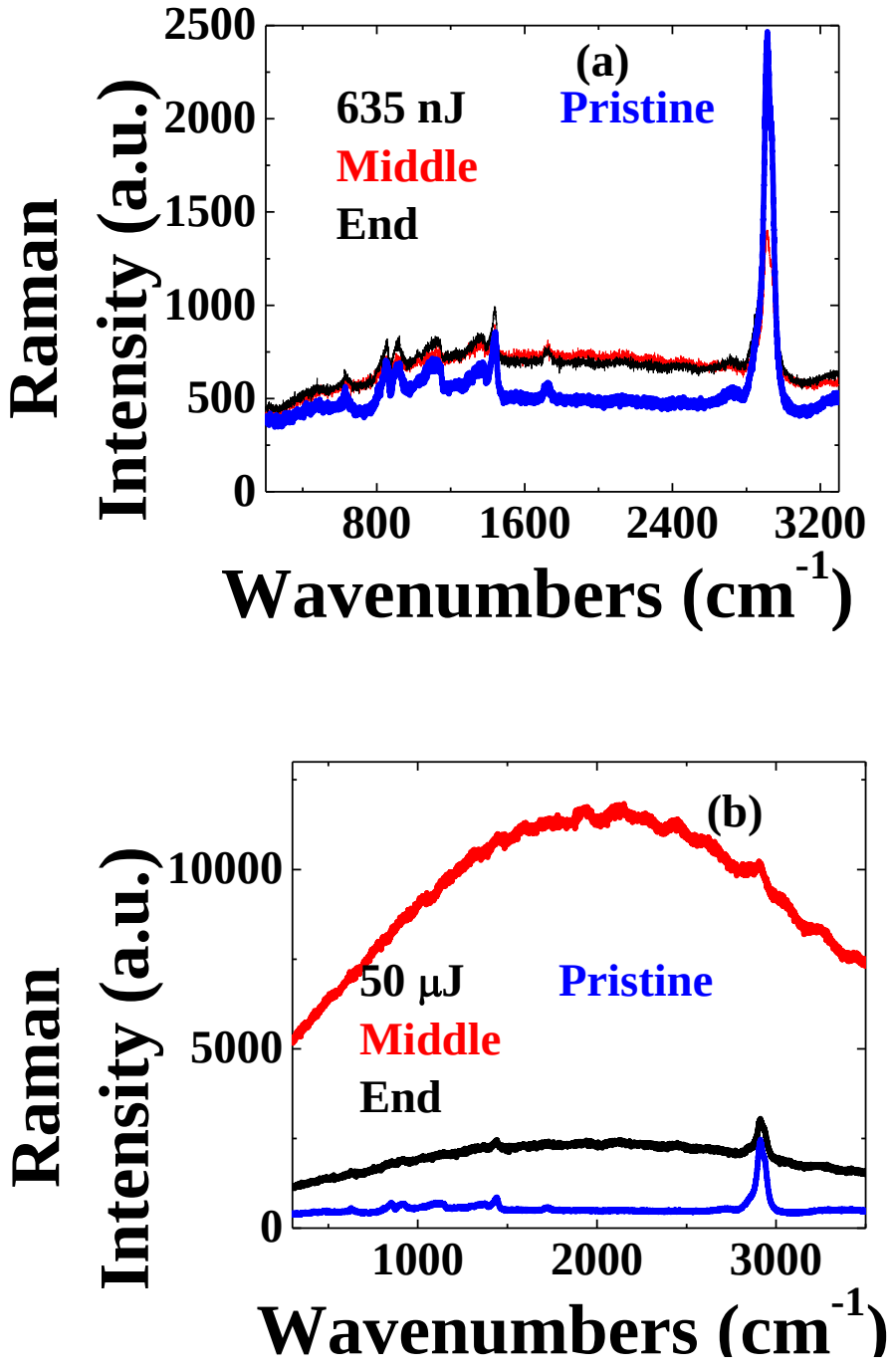

Figure 4. (a) Raman spectra of a structure fabricated in PVA thin film at 635 nJ energy, 1 mm/s speed (b) Raman spectra of a structure fabricated in PVA thin film at 50 µJ energy, 1 mm/s speed.

Table 4. Raman modes of PVA

S. No.	Raman shift (cm^{-1})	Assignment
1	310	C-C torsion and bending
2	410	γ_w(C-O)
3	477	δ(C-O) CH out of plane
4	563	γ_w(OH), CH out of plane
5	856	γ(C-C)
6	918	γ(C-C)
7	1095	γ(C-O)
8	1145	γ(C-O), γ(C-C)
9	1232	γ_w(CH)
10	1356	γ_w(CH2), δ(OH)
11	1440	δ(CH2), δ(OH)
12	1710	γ(C=O) Residual acetate
13	2721	γ(CH) weak band
14	2910	γ(CH) of CH_2

6.3 Thermal Effects

In order to understand the effect of temperature, the heated PSG1 grating whose details are mentioned in chapter 3 is used to record Raman. The PSG1 grating is thermally treated at 50C for 720 hours. We compared the recorded micro-Raman spectra in the confocal geometry for pristine PS and fs laser irradiated PSG1 without and with heat treatment. Figures 5 (a) and (b) show the microscope image of PSG1 and Raman plots. Some of the Raman plots have been shifted (vertically) for clarity. Raman spectra are collected from the centre and edge portions of the lines fabricated in the PSG1 grating. The intensity of Raman modes are suppressed in case of fs laser irradiated PS. We observed that the intensities of two main Raman modes are affected drastically due to the formation of defects in the fs laser irradiated regions. 1001 and 1603 cm^{-1} modes of PS correspond to ring breathing and C=C vibrational modes respectively [168, 170]. The two modes at 2980 and 3004 cm^{-1} corresponding to SP^3 and SP^2 CH groups disappeared completely in case of fs laser irradiated PS. Though we expect voids in the middle portion of the fabricated structures, there could be debris ablated and resettled in the middle portion of the structures which contribute to the Raman signal. Part of this signal could be from top and bottom portions of the line structures. There is slight decrease in intensity upon thermal treatment given

to PSG1 grating. No major peak alteration is observed due to minimal temperature which is used to heat the grating.

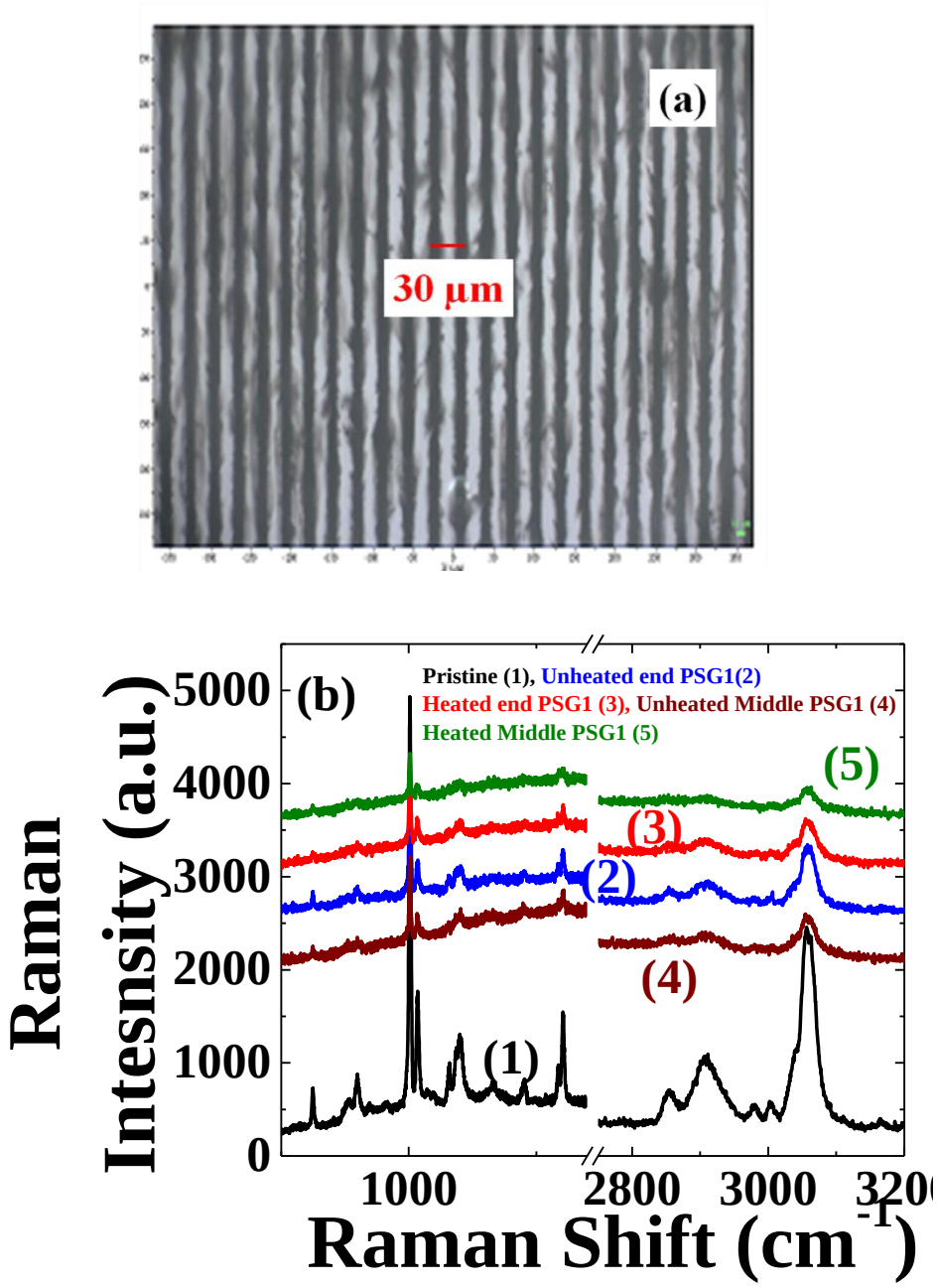

Figure 5. (a) Microscope image of PSG1 grating. Scale bar and period is 30 µm (b) Raman plot of pristine PS, irradiated PSG1, heated and irradiated PSG1 with central and end regions of the modifications.

6.4 Raman mapping

In earlier sections, Raman signals collected in middle and end portions of the structures fabricated is investigated. To study the variation of Raman signal intensity across the structure to understand the effect of the high intensity Gaussian laser pulses, Raman mapping is carried out. Here, the data obtained through Raman mapping technique for a surface structure fabricated in PDMS (15 µJ energy, 0.05 mm/s speed) is presented. Figure 6(a) shows the region of 50 µm over which the mapping was performed in the steps of 1 µm increment (The portion of single structure of figure 6(a)). The two peaks at 2904 and 2963 cm^{-1} correspond to CH_3 symmetric and asymmetric stretching modes [169]. It clearly shows lower Raman intensity at central regions compared with the regions near the edges with slight broadening in the middle portion of the structure. Since these structures are fabricated using Gaussian pulses, portions of the structures modified by the central portion of the Gaussian pulse, get modified to a maximum extent due to large intensities associated with the centre of pulse. Hence, there is slight broadening in the middle region compared to those near the edges. Figure 6(b) shows Raman mapping plot for 2904 cm^{-1} mode. It clearly indicates that the number of defects generated in the middle portion is more compared with the edges as the middle portion of the Gaussian laser pulse has more intensity and leads to the formation of more defects in the central portion of the microstructure compared with the edges. Figure 6(c) shows how Raman intensity falls in 50 µm fs exposed region as the region experiences different amount of intensity in various places. This suggests us that the number of defects generated is not uniform within the structure as intensity distribution across the pulse is not uniform. This effect can be observed in figure 6 (b) where the modification leading to reduction in intensity almost resembles Gaussian profile as the incident pulse is Gaussian. Similar trend has been noticed even in other polymers also.

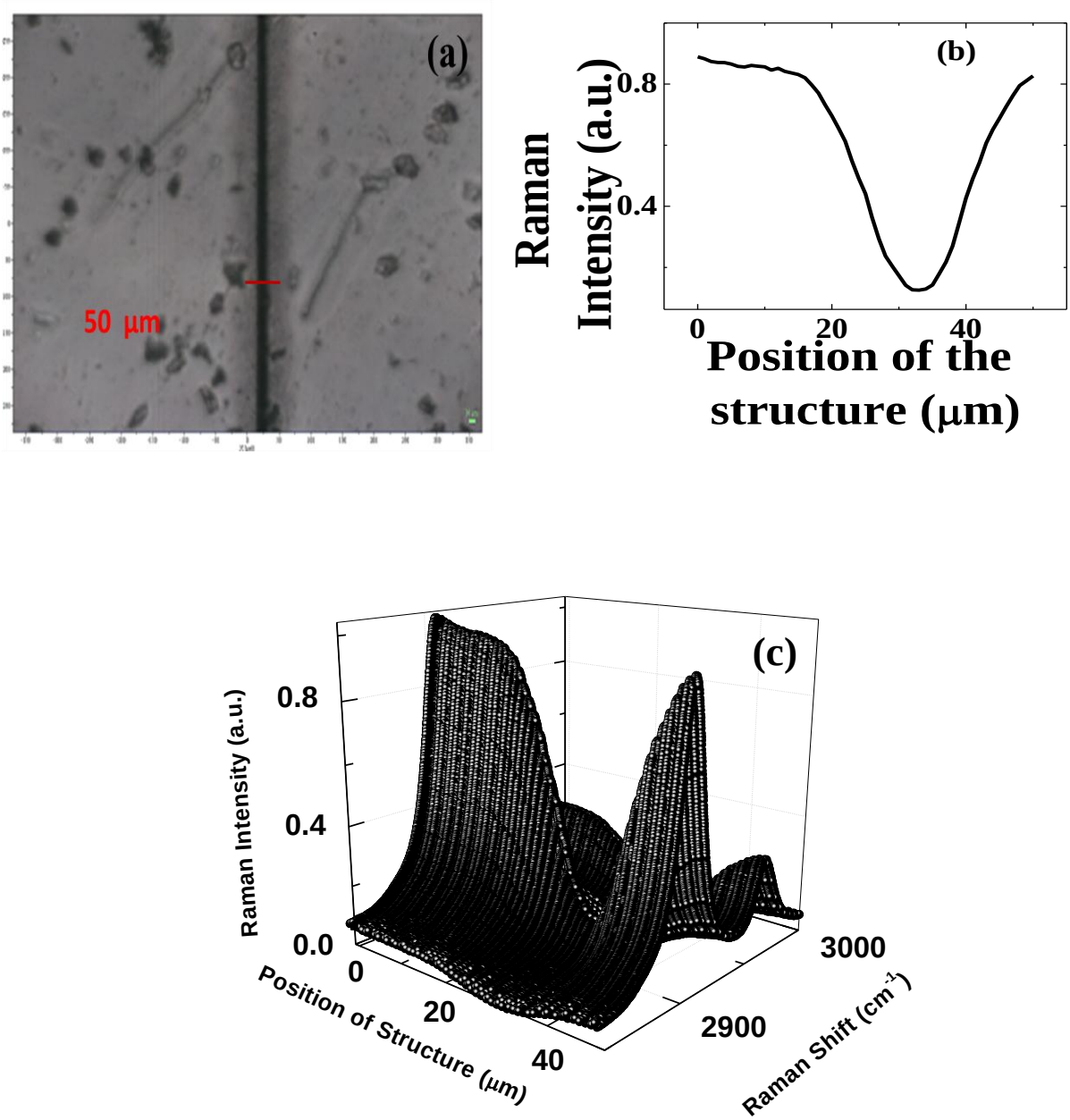

Figure 6. (a) Microscope image of the structure in PDMS fabricated using 15 µJ energy, 0.05 mm/s speed (Scale bar 50 µm) (b) Raman Intensity versus position of the structure (c) Raman mapping plot of the PDMS structure.

6.5 Conclusions

In this chapter, Raman spectra collected in pristine and fs laser modified regions of four different polymers (PMMA, PDMS, PS, and PVA) investigated are presented. Broadening and suppression of Raman modes in case of structures fabricated at high energies is explained by modification of the material due to the formation of defects. All the four polymers investigated showed similar results. Raman-mapping carried out across the structure showed the variation in Raman intensity due to the formation of defects caused after interaction with incident Gaussian pulse whose intensity is not same at the center and edges.

Chapter 7

Abstract

Preliminary results on the fabrication of simple microstructures at different scan speeds in lithium niobate ($LiNbO_3$) are presented. Dependence of structure width with irradiation dose and scan speed are given. Keldysh parameter calculations are highlighted to describe the dominant ionization process. Formation of micro-craters at low irradiation dose and high scan speed is analyzed through minimal pulse to pulse overlap. Fabrication of double structures leading to double waveguide, and double Y coupler is demonstrated for applications in waveguides. Raman spectrum collected for modified $LiNbO_3$ crystal is explained.

7.1 Introduction

Lithium Niobate (LNB) is one of the most widely used dielectric materials in photonics and optoelectronics due to its excellent nonlinear optical, electro-optical, acousto-optical, piezoelectric and photorefractive properties [190-191]. Hence, LNB has emerged as promising material for fabricating integrated optoelectronic circuits because of its favorable physical properties such as large anisotropy, high electro-optic coefficients and large second order nonlinearity. LNB crystals are positively birefringent and, hence, the extraordinary refractive index n_e for z-plane polarized light is higher than the ordinary refractive index n_o along the x and y direction. We refer to the crystal as X-cut or Z-cut depending on which crystal axis is perpendicular to the top surface. In many of the applications compact active components are required that can form into optical waveguides, integrated optical circuits, and other light control systems. LNB waveguide fabrication therefore demands positive refractive index changes while avoiding crystal defects that increase optical losses or diminish the nonlinear crystal responses. In literature several methods that include metal and rare earth in-diffusion, ion implantation, proton exchange are reported [31, 192-201]. Among all the preparation methods, fs LDW turned out to be the best method because of the relative ease of realization of the microstructures and possibility of 3D photonic devices and integration. Incident intensity of the focused ultrashort pulses determines the type of modification in LNB: (a) an increase in refractive index n_e (type I) (b) a decrease of both n_o and n_e (type II) and (c) formation of micro voids [31,199]. Thomas et al. have recently achieved a hybrid fs laser written chip in lithium niobate that comprised a rare-earth-doped laser section, a frequency doubling unit, Bragg reflectors, waveguide splitters, and an amplitude modulator [199]. However, detailed studies with different pulse durations and writing conditions are essential and enable us to identify the optimal conditions for achieving low loss (insertion, propagation etc.) photonic structures in lithium niobate [31, 192-201].

Though there is widespread interest, little is known about the photo physical and photo chemical mechanisms responsible for the formation of this laser induced optical waveguide, and the micro-structural lattice modifications underlying the positive refractive index change. $LiNbO_3$ has a complex crystal structure into which the extreme interactions of ultra short pulsed lasers can drive defects, incubation processes, local compression and dilatation of the $LiNbO_3$ unit cell, non symmetric heat flow, spontaneous polarization changes, submicron-scale explosions and

localized amorphization [202-206]. In this chapter, fabrication of microstructures, craters, dominant ionization processes, and spectroscopic analysis of the modified regions are discussed.

7.2 Fabrication of microstructures

Structures are fabricated in X-cut $LiNbO_3$ crystal. Three different sets of experiments are performed using 40X microscope objective. In set 1, structures are fabricated at 1 mm/s speed while in set 2, structures are fabricated at 0.5 mm/s speed. In set 3, energy used is kept constant while the scanning speed is changed. All these three sets are carried out below 300 µm from the surface of the $LiNbO_3$ X-cut crystal. Figures 1 (a) and 1 (b) show the confocal microscope images of two structures fabricated at 100 µJ, and 50 µJ energies at 1 mm/s speed.

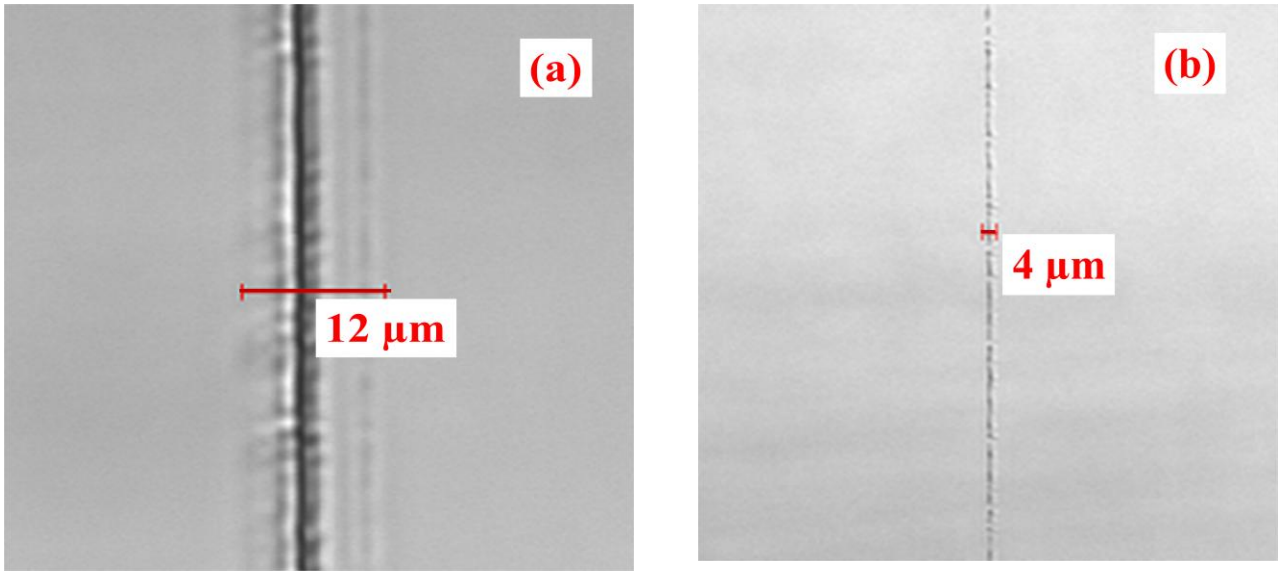

Figure 1. Confocal microscope images of a structure fabricated with 1 mm/s speed at energy of (a) 100 µJ (b) 50 µJ.

Figure 2 (a) shows the confocal microscope image of structures fabricated at different energies with 0.5 mm/s speed. Figure 2 (b) shows a confocal microscope image of a structure fabricated at 635 nJ energy. From figure 2 (a), it can be inferred that there is a reduction in structure width with decrease in energy. Structures fabricated at low energies are found to be smooth as indicated in figure 2 (b). Structure widths and energies used for fabrication set 1 and set 2 are plotted in figure 2 (c). An increment in structure width is found with energy in each set and

structures fabricated in set 2 with scanning speed 0.5 mm/s are found to be having more width when compared with set 1 at the same energy. As scanning speed is reduced, material is exposed to the laser for a larger period and leads to an increase in structure width.

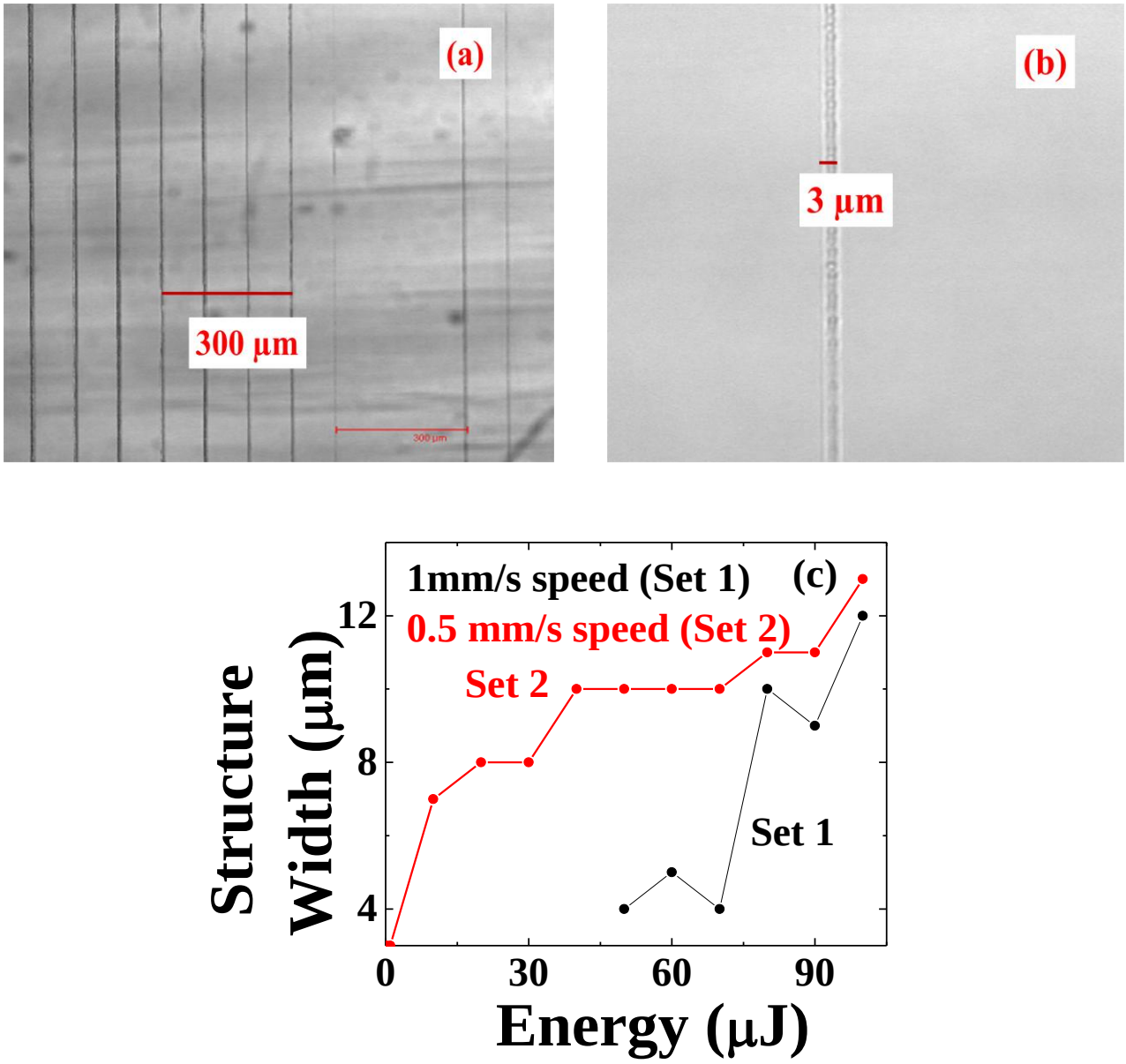

Figure 2. (a) Confocal microscope image of microstructures fabricated at 0.5 mm/s speed. Left extreme structure is fabricated at 100 µJ energy. Left to right, energy is decreasing. Speed is 0.5 mm/s. (b) Confocal microscope image shows the structure fabricated at 635 nJ energy. (c) Plot of structure width versus energy for set 1 and set 2.

Figure 3 (a) shows confocal microscope images of set 3 structures fabricated at a particular energy of 40 μJ with different writing speeds as 0.1, 0.2, 0.5, 0.8, 1, 2, 4, 6, 8 and 10 mm/s (from left to right). Figure 3 (b) shows confocal microscope image of a structure fabricated at 4 mm/s speed. It clearly shows the formation of pearl like structure (formation of microcraters) which was described in earlier chapters. This phenomenon is observed from 2 mm/s speed to higher scanning speeds. There is monotonous decrease in structure width with increasing writing speeds. For structures written with higher speeds, we observed the formation of 'pearl like' structure. This effect can be attributed to the reduction in number of incident pulses on the material at higher writing speeds as pulse to pulse overlap is minimal at high scanning speeds. Figure 3 (c) shows a plot of structure width with scanning speed of the translation stage. Structure width can be changed by either continuous modifications or a chain of pulses depending on energy and scan speeds. From figure 3 (c), it is clear that structure width starts decreasing at high scan speeds as exposure at a spot in the material is reduced. Since the bandgap of $LiNbO_3$ is 3.75 eV [207-208], it is transparent to the visible light. Each 800 nm photon carries 1.55 eV energy. This implies that minimum three photons are required for modification of the crystal. To top the three photon absorption process, Keldysh parameter is used to estimate the dominant mechanism responsible for ionization process [70]. In the present study, it is tunneling ionization which is mainly responsible for the modification process as Keldysh parameter is less than 1.5. Figure 3 (d) shows the plot of peak intensity versus Keldysh parameter. Peak intensities are calculated for energies ranging from 0.46-100 μJ. For all these energies, Keldysh parameter is still less than 1.5. The fabricated structures are found to be having less width when compared with polymers due to the reasons given in earlier chapters. This is due to higher damage threshold of the LNB crystal. The ablation threshold of the lithium niobate crystal is 3.92 J/cm^2 [209] for single shot. As polymers are soft materials compared with glasses, and crystals, polymers exhibit low damage threshold.

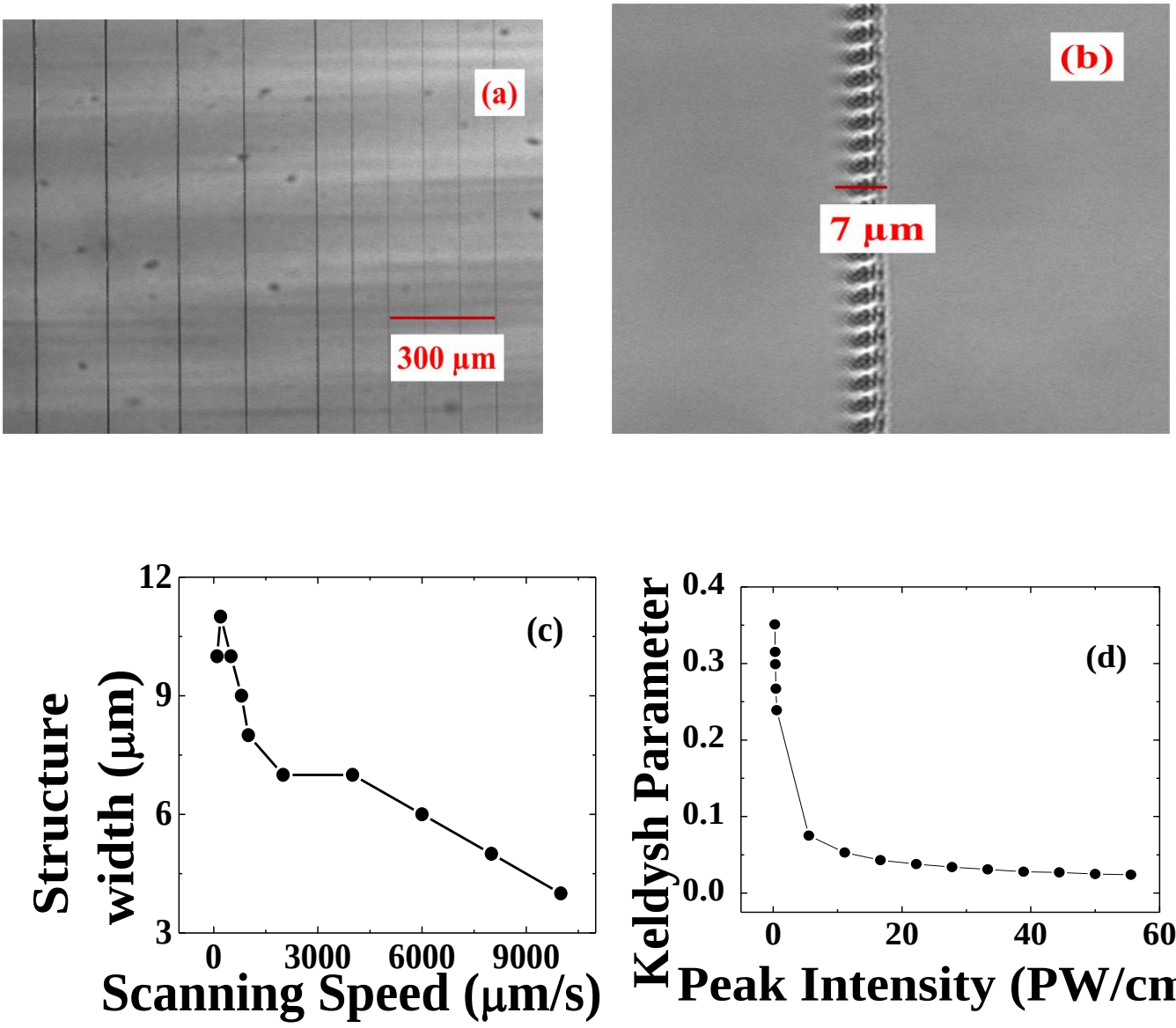

Figure 3. (a) Confocal microscope image of microstructures fabricated at different scan speeds with 40 µJ energy. Left extreme structure is fabricated at 0.1 mm/s speed. (b) Pearl like structure fabricated at 40 µJ energy, 4 mm/s speed. (c) Plot of structure width with scanning speed. (d) Plot of Keldysh parameter with peak intensity.

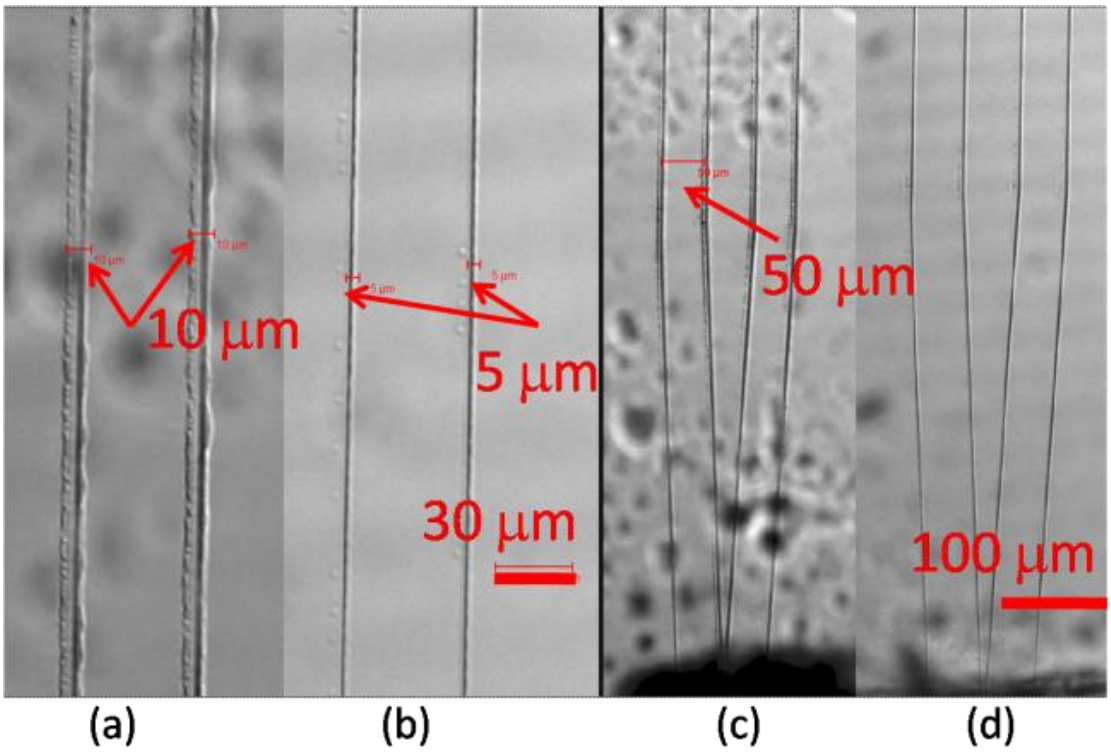

Figure 4. (a) and (b) are confocal images of double line structures written with line width W = 10 µm and waveguide width (WW) = 50 µm with energies of 5 µJ and 635 nJ respectively. The confocal images (c), (d) are Y branch structures written with energies of 1 µJ and 635 nJ respectively.

We also fabricated the Y couplers in LNB as shown in figure 4 (c) and 4 (d). Figure 4 presents images of typical 2-mm long double line structures and Y branch structures fabricated in $LiNbO_3$ wafers. As the fabricated structures are found to be having negative refractive index change, a double line waveguides and Y couplers are written in order to guide light through the region that is in between these laser modifications. This central portion is found with higher refractive index.

7.3 ESR analysis of $LiNbO_3$

In chapters 4 and 5, formation of free radicals, optical centers and paramagnetic centers in polymers were discussed. Similar investigations are carried out in lithium niobate crystal to find out whether any free radicals form after fs laser irradiation. We did not observe any optical centers after fs laser treatment. To carry out ESR analysis, we fabricated gratings underneath and on the surface of the lithium niobate crystal. Energy used is 100 µJ with 40 X microscope objective and 1 mm/s as the scanning speed. Grating structure has 20 µm period. Figure 5 (a) and 5 (b) show the confocal microscope images of the fabricated gratings in the crystal.

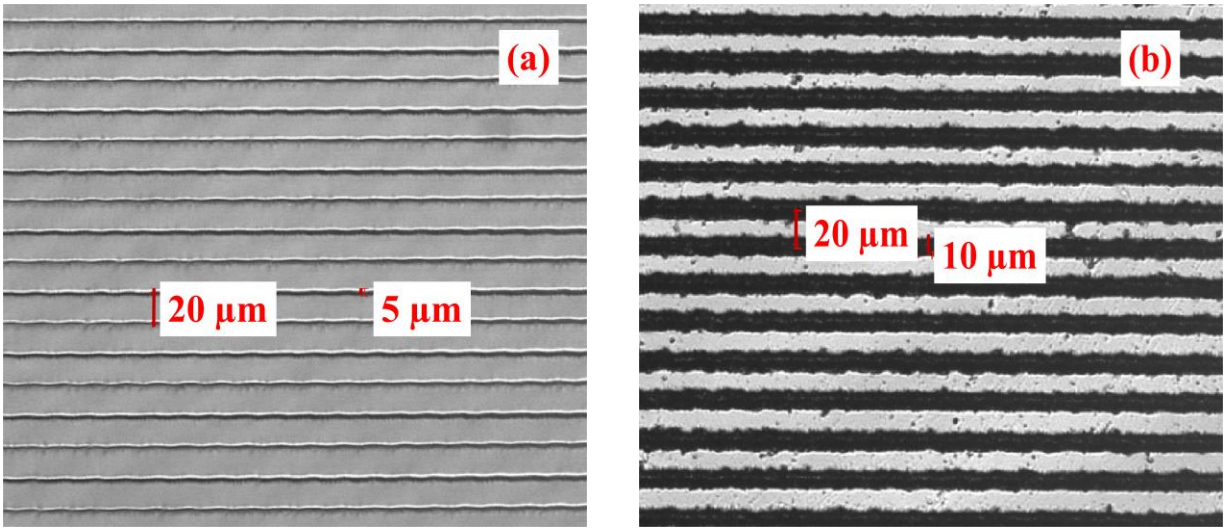

Figure 5. Confocal microscope image of (a) grating structure fabricated inside lithium niobate crystal (b) on the surface of lithium niobate crystal.

In case of polymers we observed paramagnetic radicals in all orientations of the sample with respect to the direction of magnetic field (Parallel, Perpendicular and 45°). Since the properties of the crystals are anisotropic due to symmetry involved in the crystal structure, we observed orientation dependent ESR signal. Interestingly, pristine LNB crystal has also shown ESR signal when sample was oriented parallel to the magnetic field direction. Figure 6 (a) shows the ESR signals in three different orientations of the crystal with respect to the direction of magnetic field applied. Only parallel orientation of the crystal with respect to the magnetic field has shown the existence of paramagnetic radicals. Figure 6 (b) shows the results obtained with irradiated sample (for buried grating). Similar results were obtained, since the irradiated crystal also

contains maximum volume of pure crystal, It has exhibited ESR signal in parallel configuration. Figure 6 (c) compares ESR signals of irradiated and unirradiated samples in parallel configuration.

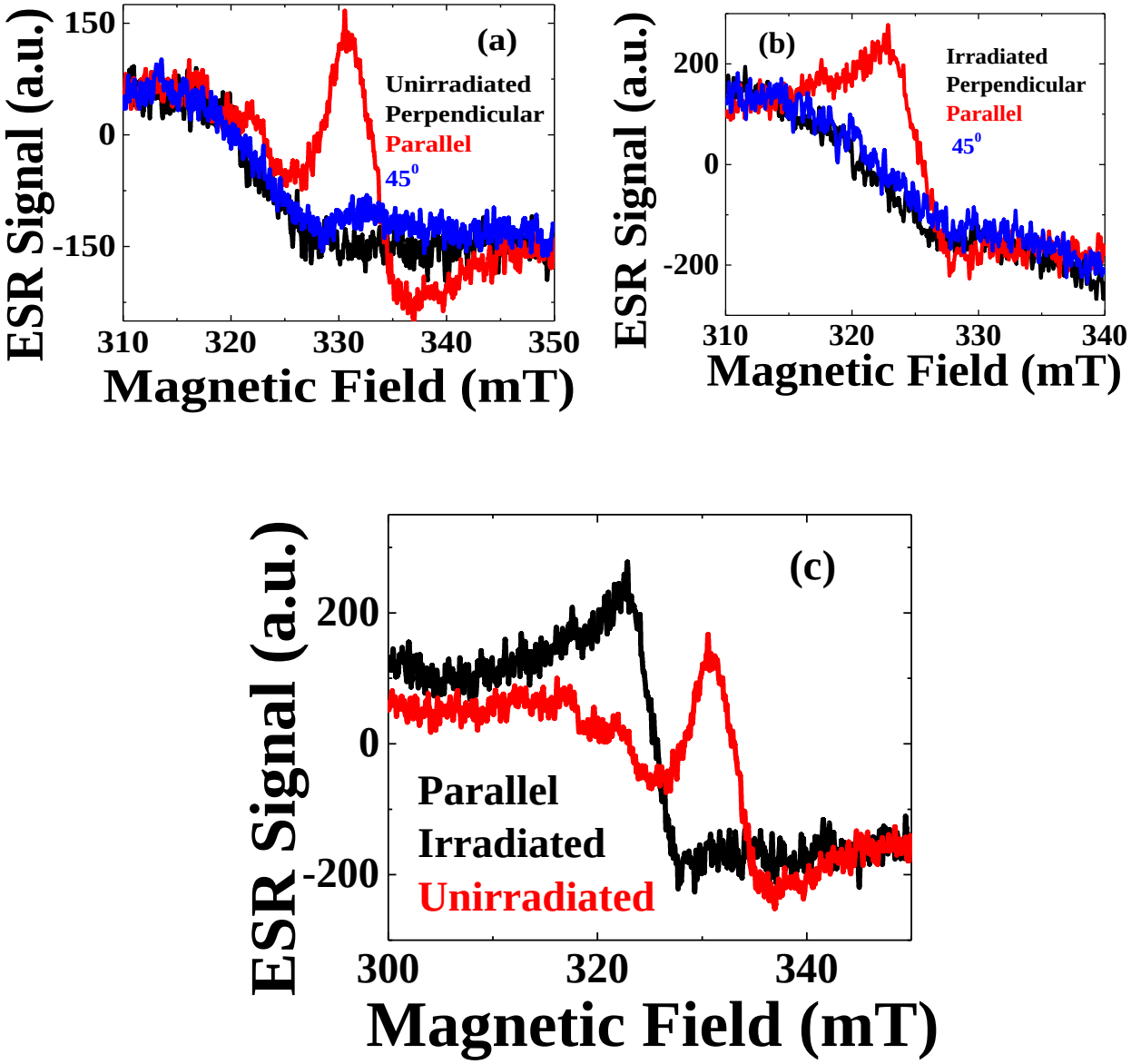

Figure 6. ESR signal of (a**)** Unirradiated pure LNB crystal in different orientations (b) Unirradiated pure LNB crystal in different orientations (c) Irradiated and pure crystals in parallel orientation.

7.4 EDXAS analysis of $LiNbO_3$

EDXAS Analysis is carried out to investigate the distribution of elements after fs laser irradiation. For this, surface structures are fabricated at different energies with 1 mm/s speed. Figure 7 (a) shows a SEM image of a microstructure fabricated on the surface of lithium niobate crystal at 100 µJ energy with 1 mm/s speed using 40 X objective. Middle portion of the structure clearly show void formation as central region of the Gaussian pulse has more intensity compared with the rest of the pulse which leads in removal of the material. Also, it can be clearly observed that the ablated debris has settled around the void region. Figure 7 (b) shows a SEM image of a microstructure fabricated at 389 nJ with 1 mm/s speed. Thus, it can be shown that fabrication of structures at high energies lead to void formation and at lower energies, it leads to minimal modification (Refractive index change) which is explained in chapter 3. Figure 6 (c) shows the fabricated structure widths with energy. EDXAS analysis is carried out for structures to study the distribution of elements.

Pristine LNB crystal showed 28% of Nb and 72% of O. We observed variation in the % contents of Nb and O as material gets ablated and modified due to interaction with fs pulses. For a structure fabricated at 60 µJ energy with 1 mm/s speed, the % contents of Nb and O are 41% and 59% in the end regions of the fabricated structure. In middle portion of the structure the contents are 21% and 79%. Figure 8 (a) shows the EDXAS data obtained in end regions of a structure fabricated at 60 µJ energy. Figure 8 (b) shows the same data for middle portion.

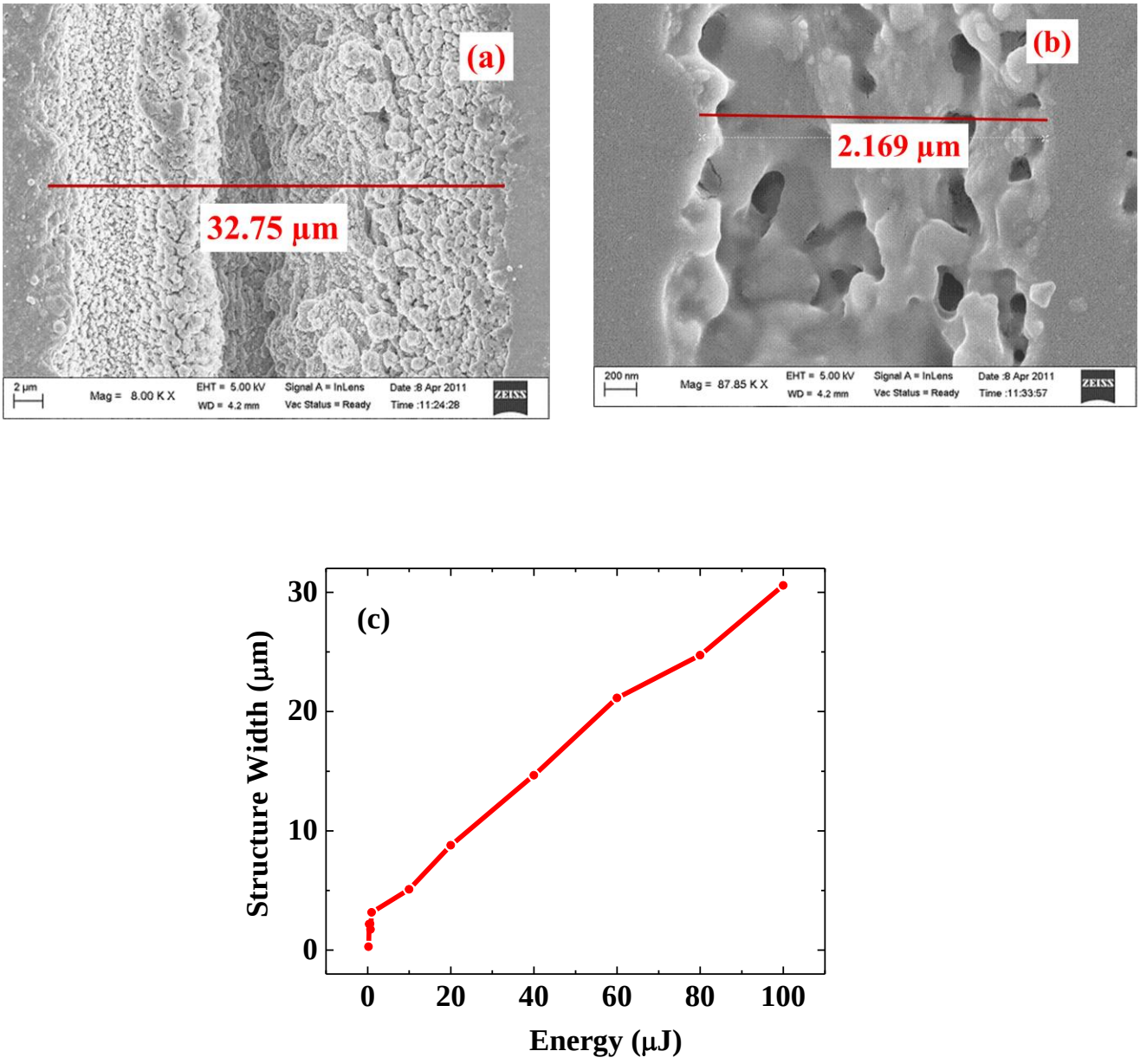

Figure 7. (a) SEM image of a microstructure fabricated at 100 µJ energy, 1 mm/s speed (b) SEM image of a microstructure fabricated at 389 nJ, 1 mm/s speed (c) Plot of structure width with energy.

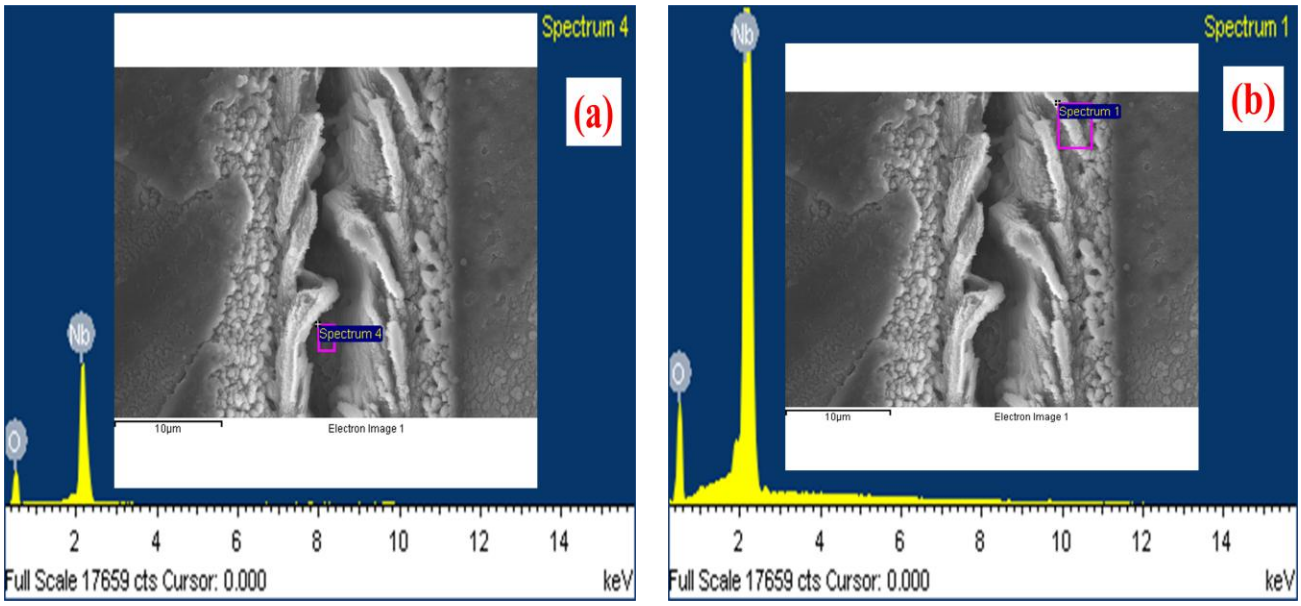

Figure 8. EDXAS data obtained for a microstructure fabricated at 60 µJ energy with 1 mm/s speed in (a) middle portion and (b) end portion.

7.5 Raman analysis of $LiNbO_3$

We carried out Raman analysis for the fabricated structures. There were three main transverse optical phonon modes reported in the literature [191, 210-216]. Figure 9 (a) shows the three phonon modes $A_1((TO_1)$, $A_1((TO_2)$, and $A_1((TO_4)$. $A_1((TO_1)$ phonon mode corresponds to the motion, along the z axis, of Ni ions against the O sub-lattice, while Li ions remain relatively static [213]. This mode is considered to be important and more sensitive to changes in Nb sub-lattice. Spectral broadening and low frequency shifting can determine the Li/Nb content as Li content is locally reduced [211, 213-215]. $A_1((TO_2)$ mode is related to displacements along z axis between Li and Nb ions while the O ions are stationary [211].$A_1((TO_4)$ mode corresponds to distortions of the octahedral only in xy plane. This mode has high relevance in assessing the compaction, and hence refractive index changes [191, 211-213]. Raman spectral analysis is a powerful technique for the detection of local modifications in chemical composition, unit cell volume, ionic displacement, local disorder, and defects. We adapt some of the mechanisms

leading to changes in Raman modes from the reference 2. Table 1 shows various mechanisms and the Raman modes response in lithium niobate crystal.

We fabricated several structures in LNB crystal and carried out Raman analysis. Figure 9 (a) shows the Raman modes of LNB crystal. We collected Raman spectra for a structure fabricated at 100 μJ energy in middle and end regions and also for a structure fabricated at 40 μJ energy with 0.5 mm/s scanning speed and using 40X objective. In order to analyze the Raman modes, we enlarged figure 9 (a) and plotted in figure 9 (b) which shows the changes in Raman intensities of $A_1(TO_1)$ and $A_1(TO_2)$ modes. Though there is a slight Raman shift by 1 cm^{-1} for the structure fabricated at 100 μJ with pristine region, it cannot be accounted for reduction in the Li content as the spectral resolution of the instrument we used is ±1 cm^{-1}. These results show that there is only Raman intensity change from figures 9 (b) and 9 (c). This could be due to lattice deformity leading to creation of defects.

Rodenas et al. [191] have fabricated waveguides by laser direct writing technique in Z-cut LNB crystal with a commercial fiber-fiber chirped pulse amplified laser with wavelength 1045 nm, 600 fs pulse duration with repetition rate 100 KHZ-1.5 MHz. Pulse energies varied were 120-700 nJ. They have postulated that the waveguide forms as a consequence of a slight rearrangement of the oxygen octahedron of the $LiNbO_3$ lattice. In their case, the waveguide has been created in a defect free zone as its propagating mode can spatially overlap with the nearby directly laser-modified zone, characterized by a large defect concentration, which induces optical losses in the penetrating evanescent tail of the guided mode. In our case, since structures are fabricated at high energies of the order of μJ, the modified region mostly resulted in void formation. Due to large intensities associated with the laser pulses, the material was ablated and lattice was deformed heavily which lead to decrease in Raman intensity for various modes. In earlier chapters, we observed the formation of defects such as optical centers and paramagnetic centers when fs pulses interact with polymers. This led to the broadening of Raman modes. In the present study, defect formation and structural modifications to the crystal structure must be minimal.

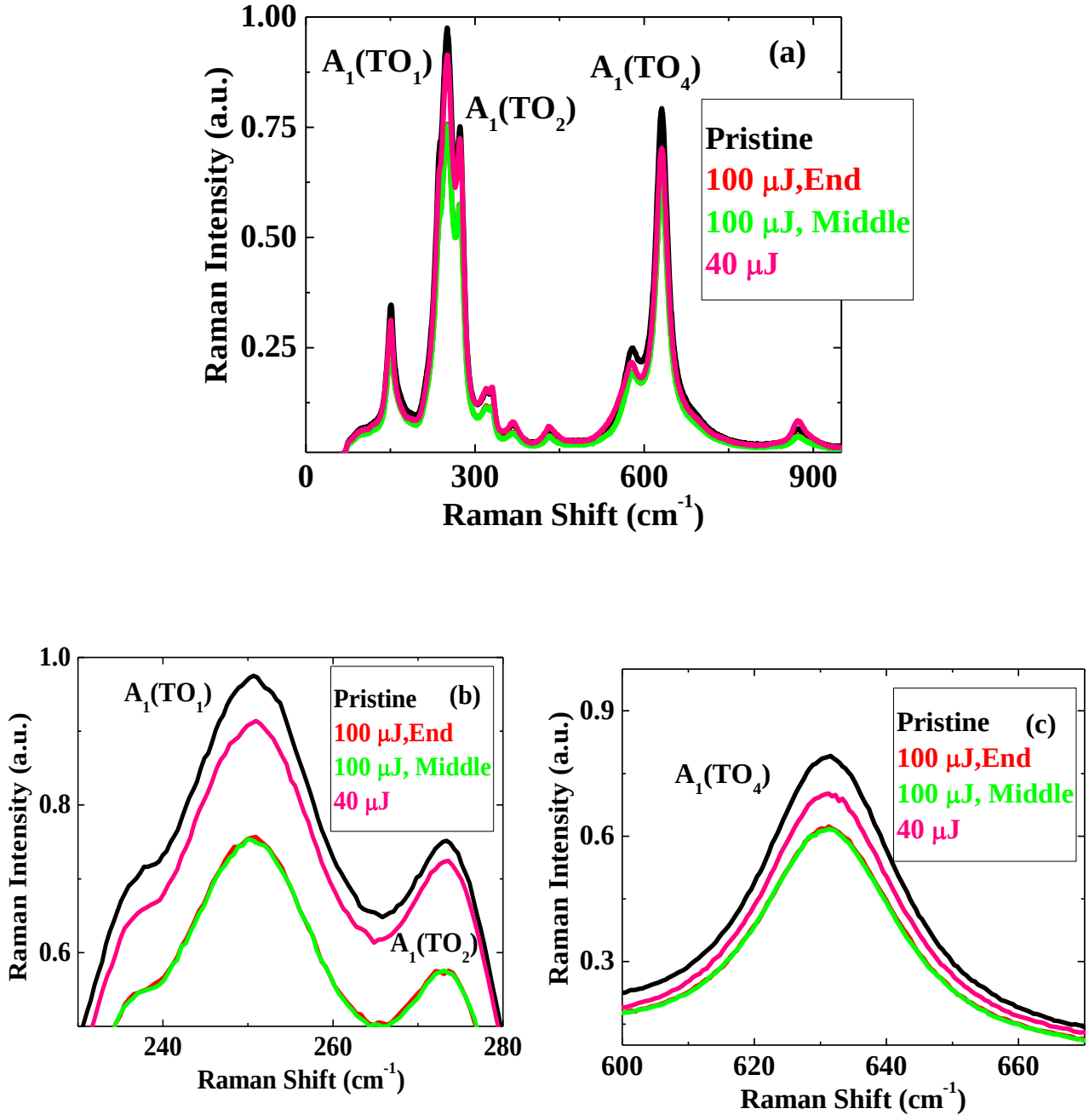

Figure 9. (a) Raman plots of pristine LNB and modified regions of LNB (b): Enlarged modes of $A_1(TO_1)$ and $A_1(TO_2)$ (c): Enlarged Raman modes of $A_1(TO_4)$.

Table 1. Adapted table represents some of the reported mechanisms from Reference 191.

S. No.	Mechanism	Raman mode response	Reference
1	Local environment densification and compressive stress	Increase in phonon mode frequencies especially for $A_1((TO_4)$	215
2	Reduction in the Li content	Broadening of Raman modes especially for $A_1((TO_1)$ and Raman shift for $A_1((TO_1)$	211, 213-214
3	Reduction in spontaneous polarization due to large-scale defects	Broadening of Raman modes and Reduction in Raman intensity	204, 216-217
4	Ionic rearrangement	Changes in Raman shifts	204, 211

7.6 Conclusions

Fabrication of microstructures, craters is explained. Dependence of structure width with energy and scan speed is investigated. Keldysh parameter calculated showed tunneling ionization is mainly responsible for the ionization during the modification process in addition to three photon absorption process. Fabrication of double waveguides and Y couplers has been demonstrated using the present laser direct writing set up. EDXAS analysis showed that the modified regions lead to redistribution of the elements of Nb, and O. Raman spectra recorded for pristine and modified regions exhibited decrease in Raman intensity for all three transverse optical phonon modes which could be due to the formation of defects and voids due to large intensities associated with high energy fs pulses.

Chapter 8

Abstract

Brief survey of literature is given on the synthesis of silver nanoparticles. The most popular method of ablation of silver target by using different lasers is also surveyed. Our earlier works on silver nanoparticles is also briefly mentioned. A novel method to synthesize silver nanoparticles through laser irradiation of silver precursor $AgNO_3$ in PVA polymer matrix is presented. The preparation of silver nanoparticles and results obtained by irradiating the mixture of silver nitrate ($AgNO_3$) and PVA solution with nano, pico and femtosecond lasers is investigated. The plasmon peak around 400 nm is confirmed through UV-Visible absorption spectroscopy. The results obtained in the preparation of silver nanoparticles in liquid phase are extended to thin films also using laser irradiation technique. Femtosecond laser inscription of microstructures is also presented. Linear and nonlinear optical properties are studies using UV-visible absorption spectroscopy and Z scan technique. The nonlinear absorption coefficient (α_2) was found to be 140 cm/GW at an input intensity of 0.143 GW/cm^2.

8.1 Introduction

The surface Plasmon band absorption is main key role in deciding the optical and electronic properties of metal nanoparticles. Just as photons are quantized for light waves, phonons are quantized for sound waves; plasmons are quantized particles for plasma oscillations. These plasmons are collective vibrations of of an electron gas (called plasma) surrounding the atomic lattice sites of a metal. When these plasmons are coupled with photons, the resulting particle called polaritons comes into picture. In classical explanation of plasmons, Drude model of metals play an important role. The metal is treated as three dimensional crystal of positively charged ions, and delocalized electron gas is moving in a periodic potential of the ion grid. A light of frequency which is below the plasma frequency will be reflected when it falls on the metal as electrons in the metal screen electric field of the light. Light of frequency above the plasma frequency will be simply transmitted as electrons cannot respond fast enough to screen it. Most of the metals have plasma frequency in the UV region making them shiny (reflective) in the visible region. Metals such as copper and gold have electronic interband transitions in the visible where only specific light energies are absorbed. The plasmon energy which is defined as

$$E_P = \hbar\sqrt{\frac{d_{ve}e^2}{m\varepsilon_0}} \tag{8.1}$$

where d_{ve} is the valence electron density, e is the charge, m is mass and ε_0 is the permittivity of free space. These surface plasmons are also referred as surface plasma polaritons. Surface plasmons are those plasmons that are confined to surfaces and interact with light resulting in a polariton. Surface Plasmon frequency depends mainly on the number of surface atoms. Surface atoms play an important role in catalysis, as the reaction takes place at the surface of particle. Surface plasmons are electron oscillations [218-219] at optical frequencies which are localized to the interface of a material with a positive dielectric constant and that of a negative dielectric constant. The surface plasmon resonance is the coherent motion of the conduction band electrons caused by interaction with an electromagnetic field [220-223]. In a classical sense the electric field of an incoming light induces a polarization of the electrons with respect to the much heavier ionic core of a spherical nanoparticle. A net charge difference is only felt at the nanoparticle

surface, which in turn acts as a restoring force. This leads to a dipolar oscillation of all the electrons with the same phase. When the frequency of the electromagnetic field becomes resonant with the coherent electron motion, a strong absorption in the spectrum is seen in the observed spectrum. The frequency and width of the surface plasmon absorption depend on the size and shape of the metal nanoparticle as well as the medium that surrounds it. The optical properties of metals involve both interactions of light with the free electrons and the electron transitions from one band to another. When the particle size decreases, the mean free path of free electrons also reduces consequently the optical properties of metal change. Small nanoparticles such as Au, Ag, and Cu show a plasma absorption band in visible light of a particular wavelength and this surface plasmon absorption (SPA) band broadens as the particles become smaller than the mean free path of the free electrons. This is captured in Mie equation for optical absorption of spheres [224] and the optical properties of free electrons. Modified Mie equation for the small particle size is given by [225]

$$\alpha = \frac{18\pi Q n^3 \varepsilon_2}{\lambda((\varepsilon_1 + 2n^2)^2 + \varepsilon_2^2)} \tag{8.2}$$

where Q is the volume fraction of particles and ε_1 and ε_2 are the real and imaginary parts of the complex dielectric constant $\varepsilon^*=\varepsilon_1-i\varepsilon_2$ of the particles. If the radii of the metal nanoparticles decrease below the mean free path of electrons in them, the plasma absorption band broadens. This results in reduction of effective optical conductivity in the particle which translates into an increase in the effective ε_2 of the particles. Hence $(\varepsilon_1+2n^2)^2 << \varepsilon_2^2$.

The final equation thus becomes

$$\alpha = \frac{18\pi Q n^3}{\lambda \varepsilon_2} \tag{8.3}$$

Equation 8.3 shows that the SPA depends not only on the particle size but also the refractive index of the matrix. Thus, synthesis of metal nanoparticles has gained considerable attention and popularity because of their unique properties and due to their potential applications. These nanoparticles have a wide variety of unique spectroscopic, electronic and chemical properties that arise from their small sizes and high surface/volume ratio. Thus, the preparation of

nanometer and monodisperse sized particles is one of the most important challenges and is an endless endeavor [226-238]. Nanoparticles have found their applications in catalysis, sensors, drug delivery, optoelectronics and magnetic devices [238-240]. Size, shape, and surface topology of particles also influence the properties. Hence, control over shape, surface topology, and aspect ratio plays a crucial role. In literature, several methods that include templating [231, 234], photolysis or radiolysis [230, 234-235], seeding [233, 236], electro-chemistry [235, 238], and ionic reduction [239-241] are reported. Still new methods are being explored by Researchers around the globe. Nanoparticles also exhibit new optical properties, which are observed neither in molecules nor in bulk metals [242-244]. One particular example is the presence of a strong absorption band in the visible region. This arises due to the surface-plasmon-oscillation modes of conduction electrons that are coupled through the surface to external electromagnetic fields [245-246]. Because of this plasmon band, the optical properties of copper, silver and gold nanoparticles have received considerable attention. It has been shown that color of noble metal nanoparticles depends on both size and shape of the particles, as well as the refractive index of the surrounding medium [230-246].

So far, many methods have been used to prepare nanostructured materials from the liquid phase and thus the solvent plays an important role in the process of reaction. Since different preparation methods lead to silver nanoparticles with different sizes and shapes, the fabrication technique has great influence on the properties of nanoparticles. Numerous physical and chemical methods have been employed in the preparation of nanoparticles. Silver nanoparticles are synthesized by using many methods such as chemical, sonochemical, radiolysis reduction and laser ablation [247-248]. Laser ablation in vacuum or a background gas was extensively used for fabrication of various nanopowders in gas phase [249]. Compared with the ablation in vacuum; formation of nanoparticles by pulsed laser ablation of targets in liquid environments has been less often studied. Recently, laser ablation in solution has become a promising method for the preparation of metal and metal oxide nanoparticles, and some network structures [250-251]. Preparation of nanoparticles by laser ablation in a liquid environment needs no vacuum equipment. One of the advantages of laser ablation in comparison with chemical methods is a lesser requirement of surfactant for capping of colloidal particles resulting in pure nanoparticles.

The purity of nanostructured materials is valuable for numerous fundamental and practical applications. In addition, by laser ablation, nanoparticles can be produced in arbitrary solution, which is suitable for nanocomposite fabrication and/or dispersion of nanoparticles in a polymeric matrix. Due to the importance of size control in nanoparticles preparation studies, the effects of laser ablation conditions are necessary for the future developments of this technique. Theoretical studies and computer simulations for modeling ablation mechanisms and cluster formation were only done for some materials in vacuum or low-pressure ambient gas [252]. Experimental studies on the effects of ablation mechanisms and parameters are very important for controlling the size and shape of nanoparticles. Many parameters influence ablation, nucleation, growth, and aggregation mechanisms.

Earlier our group has reported synthesis of silver nanoparticles for the first time in PVA free standing film which involves a sacrificial layer of polystyrene (PS) and biosynthesis of silver nanoparticles [253-256]. We reported formation of silver nanoparticles by heating the solid films containing $AgNO_3$ and PVA mixture in hot air oven. PVA acts simultaneously as the reducing agent and stabilizer for the nanoparticles and the matrix for homogenous distribution and immobilization [257]. In case of biosynthesis of silver nanoparticles, Moringa Oleifera leaf extract is used as reducing and stabilizing agent [244]. In this study we present a novel method to synthesize silver nanoparticles through laser irradiation.

8.2 Synthesis through Laser Irradiation

In literature, preparation of metal nanoparticles using metal ablation technique where target metal in solvent media is irradiated with lasers has been well documented [247-248]. However, in this chapter we report synthesis of silver nanoparticles in polymer PVA matrix in thin films and solutions by irradiating with nano, pico and femto second lasers (ns, ps, fs lasers). Polymers are good for stabilizers and alcohols are good for reducing agents. Since PVA is a polymer and contains OH group (alcohol), we prepared silver nanoparticles in PVA matrix. Earlier, our group thermally treated silver nitrate doped PVA thin films to synthesize silver nanoparticles in PVA matrix. However, thermal treatment usually takes long time. In this chapter a novel and

preparation of silver nanoparticles is reported by treating the solutions and thin films containing both silver nitrate and PVA with different lasers. Thus laser sources can be used as heat sources for the preparation of silver nanoparticles.

Three different concentration mixture solutions of $AgNO_3$ and PVA were prepared in our experiments. Each concentration consists of different ratios of silver nitrate with water (Solution A) and PVA with water (Solution B). Solutions A and B were magnetically stirred for complete miscibility for 8 hours before they are mixed and stirred again. Solution B was heated for a minimum period of 20 minutes while stirring to dissolve PVA polymer completely in water. Concentration 1 (C1) consists of 180 mg of $AgNO_3$ in 36 ml of water and 12.96 gms of PVA in 180 ml of water. Concentration 2 (C2) consists of 180 mg of $AgNO_3$ with 36 ml of water and 4.32 gms of PVA with 180 ml of water. Concentration 3 (C3) consists of 360 mg of $AgNO_3$ with 36 ml of water and 4.32 gms of PVA with 180 ml of water. C1 and C2 concentrations were prepared to see the effect of the density of the medium on the formation of Ag nanoparticles. Laser systems used for irradiation experiments are Nd: YAG ns laser delivering 1064 and 532 nm wavelengths, 6 ns pulses with 10 Hz repetition rate, Nd: YAG ps laser delivering 532 nm wavelength, 30 ps pulse width with 10 Hz repetition rate, and Ti: Sapphire fs laser delivering 800 nm wavelength, 100 fs pulses with 1 KHz repetition rate.

(a) Ns laser Irradiation

Solutions prepared with C2 concentration are irradiated with Nd: YAG ns lasers. Yellow color was observed after 10 to 15 minutes of irradiation which confirmed the formation of silver nanoparticles. UV-Visible spectra were recorded for the solutions irradiated at different energies and exposure times. Figure 1 (a) shows absorption spectra collected for different irradiation doses with same exposure time (30 minutes) and different exposure times with same energy in ns laser experiments. Blue shift of Plasmon peak was observed clearly with irradiation dose and exposure time. As irradiation dose/time is increased, it results in smaller size nanoparticles and thus lead to blue shift. Also in order to study the stability of silver nanoparticles, we recorded absorption spectra on different days.

Figure 1 (b) shows the absorption spectra recorded for silver nanoparticles in solution with C2 concentration, irradiated at 135 mJ Nd: YAG ns laser on different days. Peak positions are 404, 410, 411, and 416 nm respectively on different days. That is almost peak shift of 14 nm for 24 days which is very small and hence the prepared particles showed stability over several weeks of time. This shows that PVA acts as a very good stabilizer. Also, we noticed full width half maximum (FWHM) increased with period of time. This is due to the formation of larger size particles due to agglomeration which already resulted in peak shift. Figure 1 (c) shows the image of prepared nanoparticles in solution form at 17, 40, 70, and 135 mJ for half an hour irradiation. As irradiation dose is increased color of solutions turned to be more yellowish with higher irradiation dose. Higher irradiation dose means more thermal energy being deposited into the system which in turn increases the yield of silver nanoparticles.

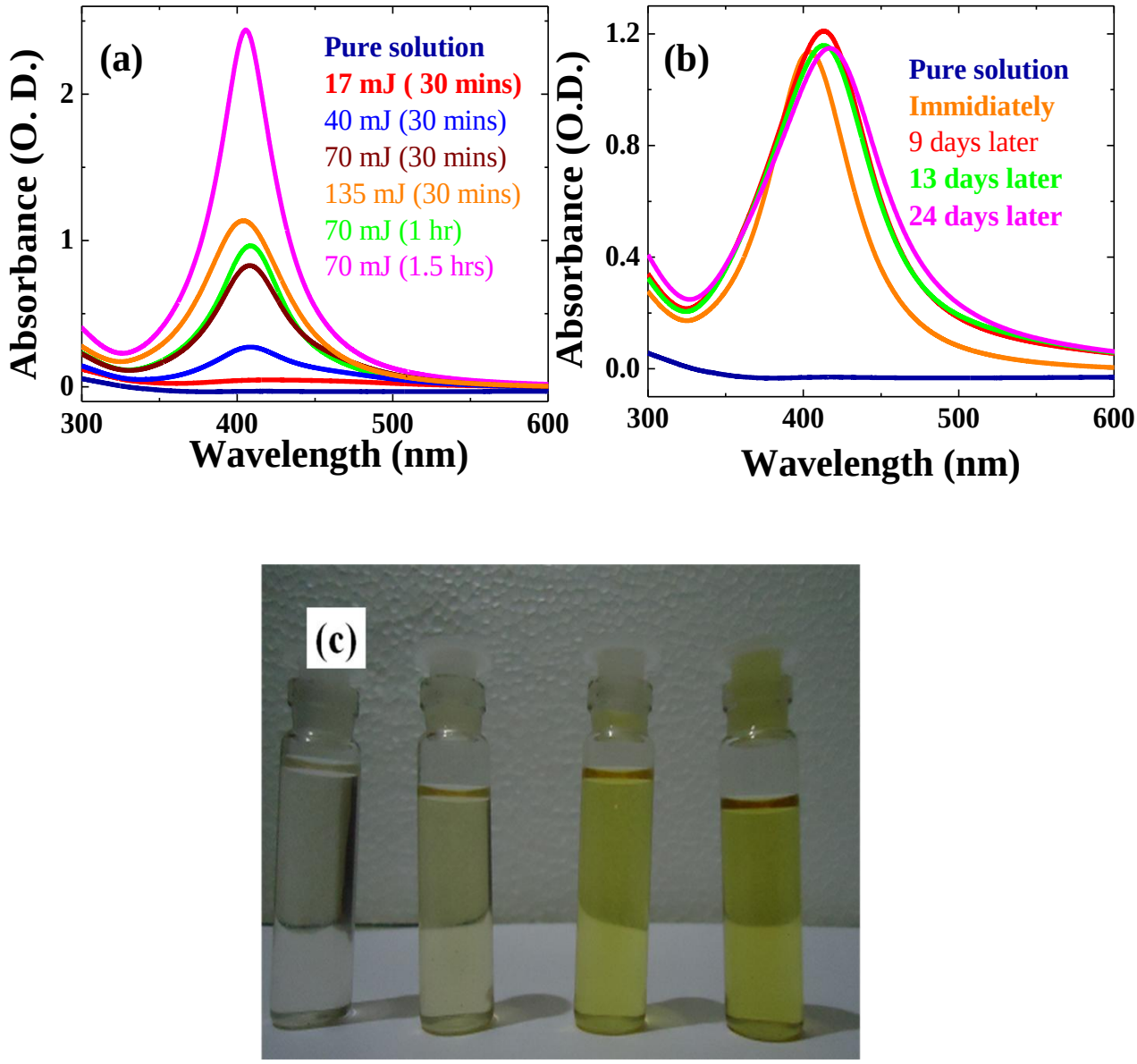

Figure 1. (a) Absorption spectra recorded for silver nanoparticles in solution for concentration C2 with nanosecond laser. (b) Absorption spectra recorded for silver nanoparticles in solution with C2 concentration, irradiated at 135 mJ Nd: YAG ns laser on different days. (c) Color formation in solutions after irradiated for 30 minutes at different energies with Nd: YAG ns laser. The energies are 17, 40, 70, and 135 mJ.

(b) Ps laser Irradiation

Similar investigations are carried out to ps laser irradiation experiments .Four different irradiation energies 3, 6, 12, 17 mJ are used each for 30 minutes and 17 mJ with one hour. Figure 2 shows the absorption spectra of the solutions. The investigations carried out with ps laser exactly match with ns laser results. When we compare 17 mJ irradiation dose for 30 minutes with ps laser with that of similar irradiation dose with that of ns laser, a blue shift was observed with shorter pulses indicating that total time duration of the pulse also plays a role in the size and shape of the nanoparticle formation.

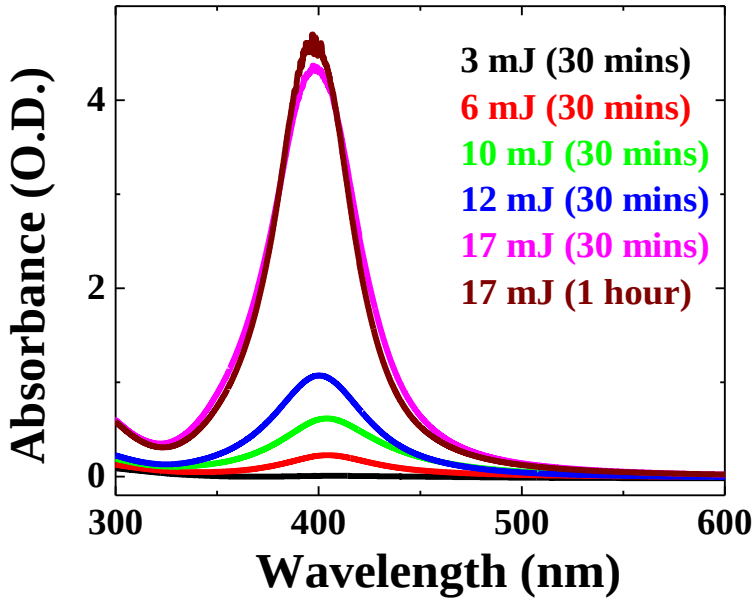

Figure 2. Absorption spectra recorded for ps laser irradiated solutions with concentration 2 (C2)

(c) Fs laser Irradiation

Similar experiments are carried out with fs laser also. We could not observe any color change with fs laser (800 nm) irradiation experiments when exposed directly without focusing. However, nanoparticles started forming when the fs laser irradiation was focused (focal length of the lens = 10 cms) in to the solution. The light intensity at the focus is of the order of 10^{15} Wcm^{-2} which is high enough for multiphoton absorption and ionization to set in and we conclude that the two and/or multiphoton absorption of IR photons is responsible for the formation of silver

nanoparticles [258-260]. Figure 3 (a) shows the absorption spectra recorded for fs laser irradiation experiments for solutions with concentration C2. Figure 3 (b) shows absorption spectra recorded on different days for fs irradiation experiments and peak is again red shifted indicating the agglomeration of particles as earlier.

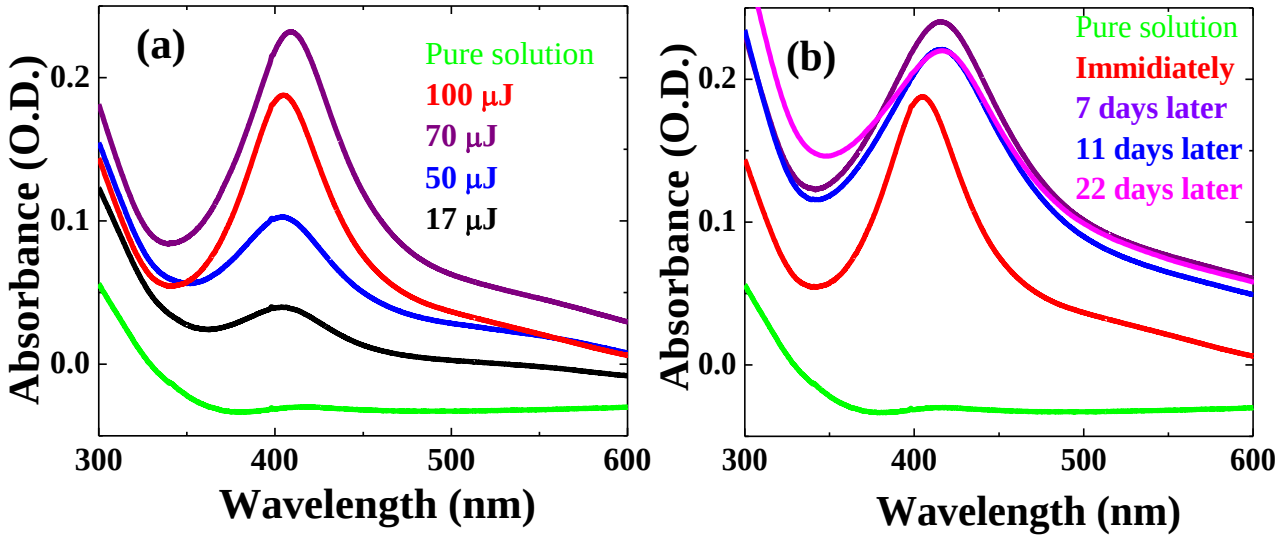

Figure 3. (a) fs laser irradiated solutions for 30 minutes, and (b) fs laser irradiated solution prepared with C2 concentration at 100 μJ, for 30 minutes.

(d) Irradiation experiments in thin films and solutions with third harmonic of Nd: YAG

We carried out similar investigations in case of thin films also as it is a solid polymer matrix and can be applied for several nonlinear applications. In case of solution, as particles will be always in Brownian motion, the whole solution appears yellow after several laser shots. This process also takes more time. In case of solids like thin films as molecular motions are almost not existing, only the region under illumination turns yellow from transparent. Thin films are made from C1 and C3 concentrations by placing 2 to 3 drops of mixed $AgNO_3$ and PVA solution on glass slides and drying them overnight. These films are irradiated with Nd: YAG ns laser second harmonic at 532 nm wavelength. Irradiation of these films also showed color change to yellow

from transparent. Absorption spectra recorded revealed a Plasmon peak around 400 nm which confirmed the formation of silver nanoparticles. Figure 4(a) shows the absorption peaks in thin film made out of C3 concentration while 4 (b) shows the same for C1 concentration. These films are also irradiated for 30 minutes.

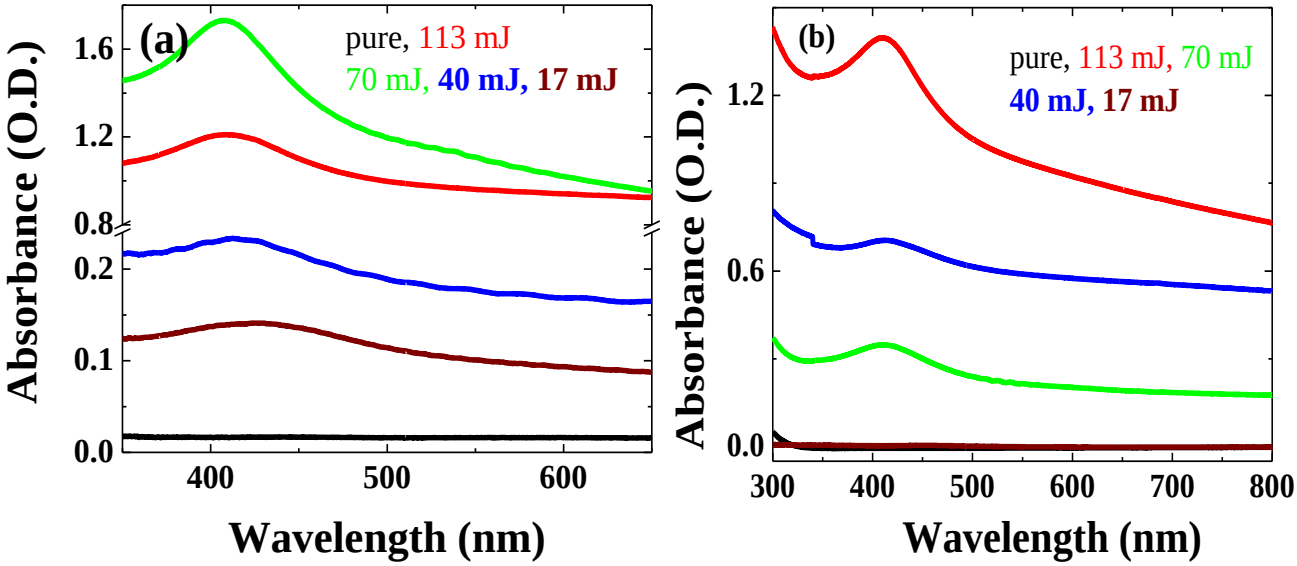

Figure 4. Absorption spectra of silver nanoparticles formed in thin films prepared with concentrations (a) C3 and (b) C1 using 532 nm

Absorption spectra recorded are fitted to a Lorentzian function to estimate peak position and full width half maximum (FWHM). The sizes of silver nanoparticles are estimated using the relation (8.4)

$$R=V_f\lambda_P^2/\ 2\pi C\Delta\lambda \qquad (8.4)$$

Where R is the particle size, V_f is the Fermi velocity of electrons in bulk metal (Silver: 1.38×10^8 cm/s), λ_P is the characteristic wavelength at which surface Plasmon resonance occurs, $\Delta\lambda$ is the FWHM, and C is the velocity of light in vacuum [258-259]. Results thus obtained are tabulated in table (1). Also, results obtained in case of solutions are shown in table (2) for comparison.

Table 1. Irradiation experiments in solution and thin films of C1 and C3.

S. No.	Experiment	Details of energy and exposure time	Peak (λ_p) (nm)	FWHM ($\Delta\lambda$) (nm)	Radius (R) (nm)
1	Thin films made from C3 concentration and irradiated with ns laser, irradiated for 30 minutes	17 mJ	421	146	~1
2		40 mJ	408	181	~1
3		70 mJ	402	112	1.06
4		113 mJ	407	107	1.14
5	Thin films made from C1 concentration and irradiated with ns laser irradiated for 30 minutes	17 mJ	526	56	3.64
6		40 mJ	411	110	~1
7		70 mJ	407	144	~1
8		113 mJ	404	179	~1
9	Solution made from C3 concentration and irradiated with ns laser irradiated for 30 minutes	17 mJ	442	200	~1
10		40 mJ	417	75	1.711
11		70 mJ	407	57	2.1447
12		113 mJ	404	64	1.88
13	Solution made from C1 concentration and irradiated with ns laser irradiated for 30 minutes	17 mJ	440	176	~1
14		40 mJ	416	87	1.4680
15		70 mJ	405	53	2.2840
16		113 mJ	405	56	2.1616
17	1064 nm irradiation for thin films synthesized from C3	End region	412	91	1.4
18		Middle region	424	107	1
19	1064 nm irradiation for thin films synthesized from C1	End region	421	106	1.234
20		Middle region	412	76	1.648

Table 2. Details of silver nanoparticles sizes obtained with concentration C2.

S. No.	Experiment	Details of energy and exposure	Peak (λ_p) (nm)	FWHM ($\Delta\lambda$) (nm)	Radius (R) (nm)
1	Concentration 2 and Irradiated with ns laser (Blue shift with irradiation dose and exposure time is observed)	135 mJ, 30 minutes	404	66	1.8
2		70 mJ, 30 minutes	408	60	2.1
3		40 mJ, 30 minutes	411	72	1.7
4		17 mJ, 30 minutes	430	100	1.4
5		70 mJ, 1 hour	408	55	2.3
6		70 mJ, 1.5 hours	405	48	2.5
7	135 mJ, 30 minutes irradiation with ns laser (Red shift with different days is observed)	Immediately	404	66	1.8
8		9 days later	410	79	1.57
9		13 days later	411	81	1.54
10		24 days later	416	99	1.29
11	Concentration 2 with ps laser (Blue shift with irradiation dose is observed)	3 mJ, 30 minutes	490	51	3.47
12		6 mJ, 30 minutes	405	56	2.16
13		10 mJ, 30 minutes	405	64	1.89
14		12 mJ, 30 minutes	400	56	2.11
15		17 mJ, 30 minutes	398	51	2.3
16		17 mJ, 1 hour	398	43	2.72
17	Concentration 2 with fs laser irradiated for 30 minutes (red shift with irradiation dose)	17 μJ	400	93	1.27
18		50 μJ	401	78	1.52
19		70 μJ	409	67	1.84
20		100 μJ	405	65	1.86

C1 sample film did not observe any formation of color and thereby indicating that no surface plasmon peak has found when recorded with UV-Visible absorption spectrometer when irradiated with 17 mJ of ns laser. This is due to low concentration of Ag ions in the thin films prepared with solution C1 when compared with C2 and C3 concentrations. This confirms that the density Ag ions in the medium control the formation of nanoparticles. Table 1 show the results obtained in solutions of C1 and C3. Also C1 and C3 solutions are exposed to one hour with 3rd harmonic of Nd: YAG ns laser (355 nm), we could still observe the formation of nanoparticles. As irradiation dose is nearly 300 μJ, the yield was less. Figure 4 (a) shows the absorption spectra recorded for these solutions irradiated at 300 μJ energy with 355 nm radiation. They exhibited broad absorption spectra with a peak around 400 nm as shown in plot figure 5 (a) indicating polydispersity of nanoparticles in the solution. 355 nm excitation in particular shows the formation of large size nanoparticles ranging from 60 nm to 2 μm, which are not of spherical shape. However thin films prepared with C1 and C3 concentrations did not show any nanoparticles formation when irradiated with 300 μJ, 355 nm pulses, which possibly could be due to low energy of irradiation and the rigidity of the polymer in comparison to the solution.

In figure 5 (b), the absorption spectra recorded for thin films made with concentrations C1 and C3 are shown. The spectra in films are narrower and more towards the shorter wavelength than those in the solution irradiation. This again confirms that polymer rigidity might be playing a role. As shown in figure 5 (c), laser excitation of the films shows an interesting phenomenon that the edges of the irradiated region show stronger nanoparticle formation compared to the centre which has higher energy. It is interesting and quite likely that the thermal energy associated with the laser pulses at the centre might be diffusing Ag ions outwards. Table 1 (s. nos. 17 to 20) shows the details of absorption peak and FWHM. There is a peak shift observed in the absorption spectra collected from the middle portion of the irradiated region and the end portion.

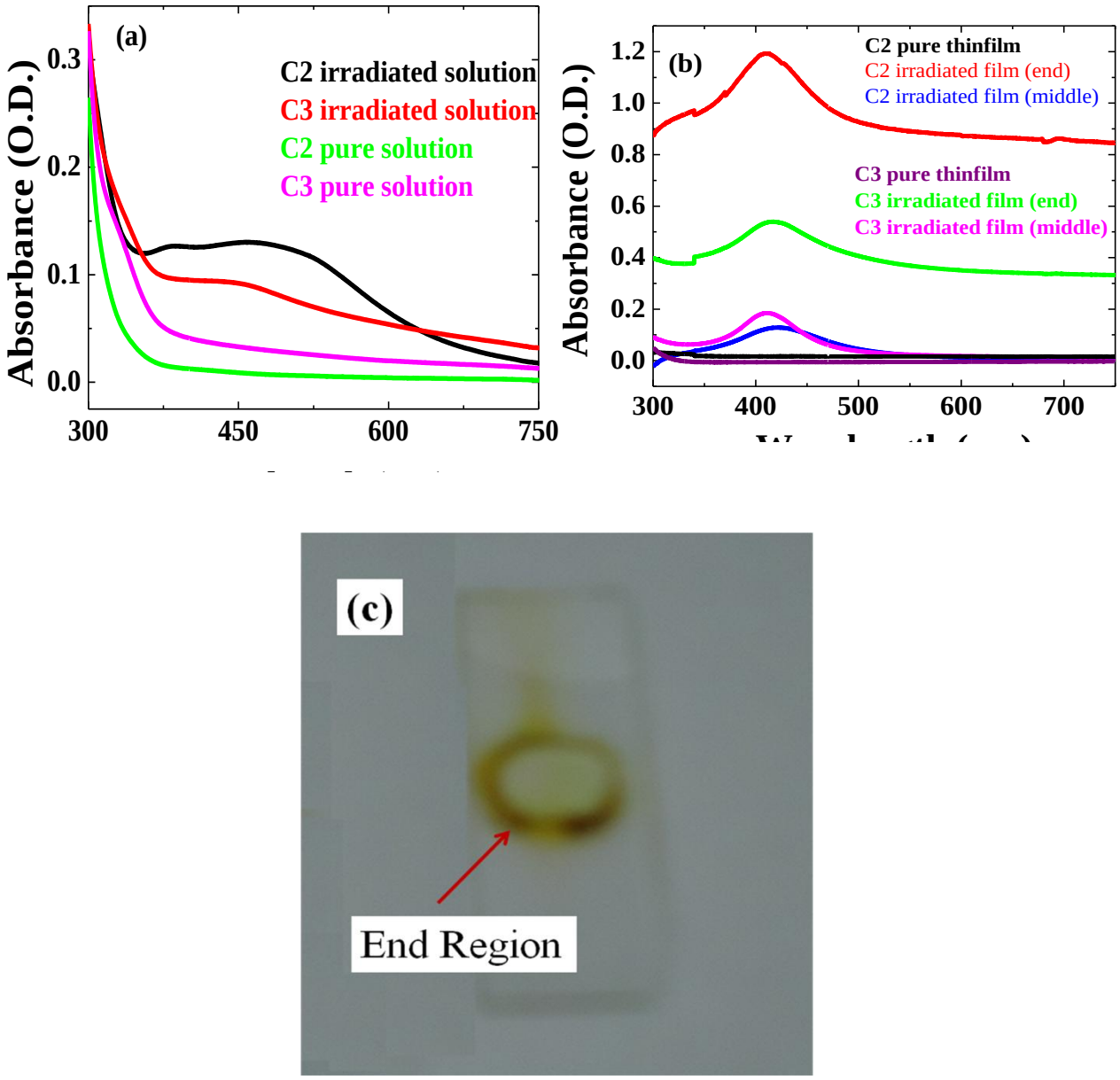

Figure 5. Absorption spectra of (a) C3 and C1 solutions irradiated with 355 nm laser at 260 μJ energy for 1 hour (b) thin films prepared with C3 and C1 concentrations irradiated with 1064 nm Nd: YAG ns laser. These films are exposed nearly an hour. (c) Irradiated thin film prepared with C1 concentration and exposed to 1064 nm Nd: YAG ns laser. Intense yellow color formation is observed at the edges of the modified region.

(e) TEM Analysis

In order to see the particle sizes, we carried out our particle analysis with TEM. One drop of silver nanoparticles solution is carefully placed on a copper TEM grid and evaporated for one hour so that the solvent is completely dried. We recorded the transmission electron microscope (TEM) images for nanoparticles prepared in solutions with concentrations C1 and C3 irradiated with different laser wavelengths. Figure 7 (a) shows the TEM image of silver nanoparticles with C1 concentration and 7 (b) shows with that of C3 concentration when irradiated with 70 mJ of 532 nm second harmonic Nd: YAG ns laser. We observed that the particle size varies from 2-100 nm. 355 nm laser irradiation in C3 led to the observation of nanoparticles with different shapes illustrated in figures 7 (c) and 7 (d). Inset of figure 7 (d) shows the color of irradiated solution with concentration C3 using 355 nm laser. The 355 nm irradiated solution turns in red color. TEM images showed silver nanoparticles with different shapes and sizes for this irradiated solution. We observed smaller size nanoparticles with 532 nm laser irradiation. Larger size nanoparticles with different shapes are observed with 355 nm laser irradiation as shown in figures 7 (c) and 7 (d). Figure 7 (d) shows the hexagonal shape of prepared silver nanoparticle with 355 nm laser irradiation. Thus, the laser parameters such as laser wavelength, energy and role of environment such as temperature etc cannot be ruled out in the preparation of silver nanoparticles.

Figure 8 (a) shows one silver nanoparticle of size 200 nm prepared with ns laser 532 nm wavelength in C3 concentration solution. Figure 8 (b) shows the electron diffraction pattern of the same nanoparticle. Figure 8 (b) indicates that the prepared silver nanoparticles have polycrystallanity with cubic symmetry.

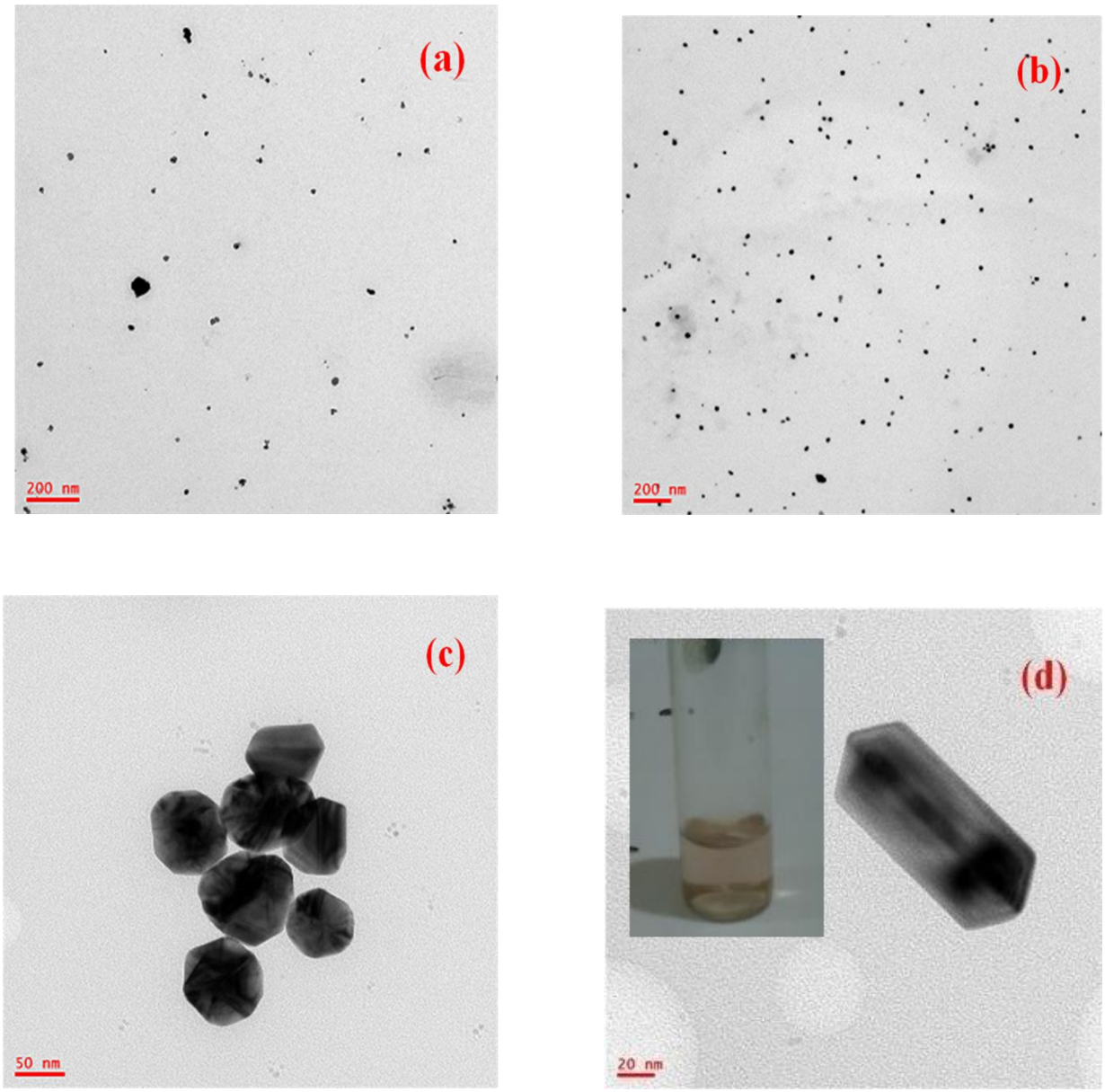

Figure 7. TEM image of silver nanoparticles obtained in (a) C1 solution irradiated with 70 mJ energy with 532 nm laser (b) C3 solution irradiated with 70 mJ energy with 532 nm laser (c) C3 solution with 355 nm laser irradiation. Different shapes are observed. (d) C3 solution with 355 nm laser irradiation. Hexagonal shape structure is observed. Inset of 7 (d) shows the irradiated solution turned into red in color.

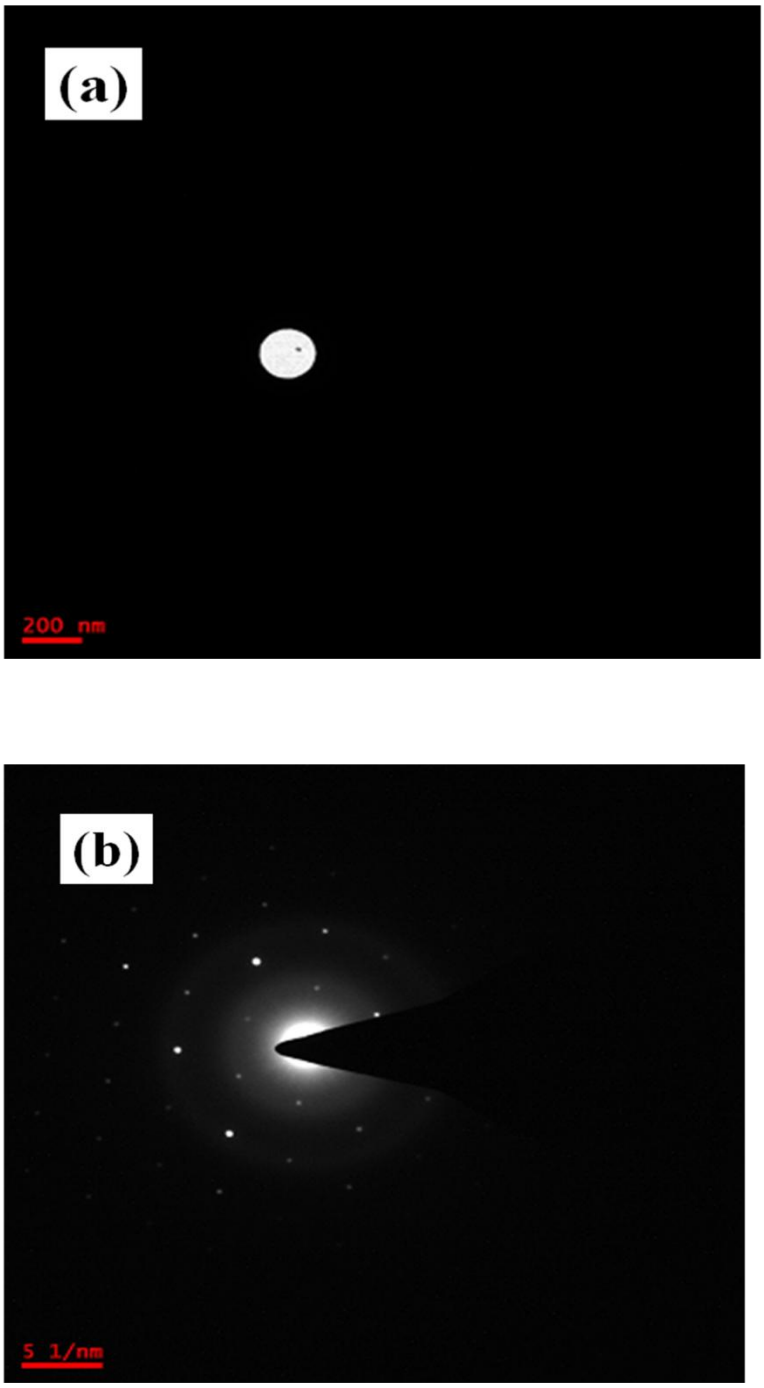

Figure 8. (a) TEM image of 200 nm sized silver nanoparticle obtained in C3 solution irradiated with 70 mJ energy with 532 nm laser (b) Electron diffraction pattern of single nanoparticle.

8.3 Femtosecond laser inscription of the structures

We have fabricated several microstructures on thin film containing silver nitrate and PVA using fs laser direct writing technique. In the modified regions, we observed silver nanoparticles. Figure 9 (a) shows the SEM image of fabricated structures using 40 X microscope objective with 1 mm/s speed. Figure 9 (b) shows the SEM image of silver nanoparticles within the structure fabricated at 100 µJ energy with 1 mm/s speed. Particles of sizes around 60-80 nm are observed. In order to confirm the silver nanoparticles formation due to fs laser inscription, we made a thin film of silver nitrate and PVA as follows. 360 mg of silver nitrate is mixed and stirred with 36 ml of water for two hours. 4.32 grams of PVA is mixed with 180 ml of water and stirred for a day with initial one hour of heating along with stirring.

These solutions are stirred till no precipitation is seen. These solutions are again mixed and stirred for an hour. Thin films are made by spin coating technique with 1000 rotations per minute for 15 minutes time. Thus prepared thin films are allowed to dry before fs laser experiments are carried out. We fabricated a grating on the surface at 80 µJ energy, 0.5 mm/s speed with 40 X microscope objective. Period is 60 µm. Figure 9 (c) shows the absorption spectra of freshly prepared thin film and fs laser inscribed grating film. There is no plasmon absorption band observed for freshly prepared and unirradiated film. But, when grating is fabricated we observed plasmon peak around 400 nm due to the formation of silver nanoparticles. This investigation opened the doors to the applications realized in plasmonics and Surface Enhanced Raman Scattering (SERS).

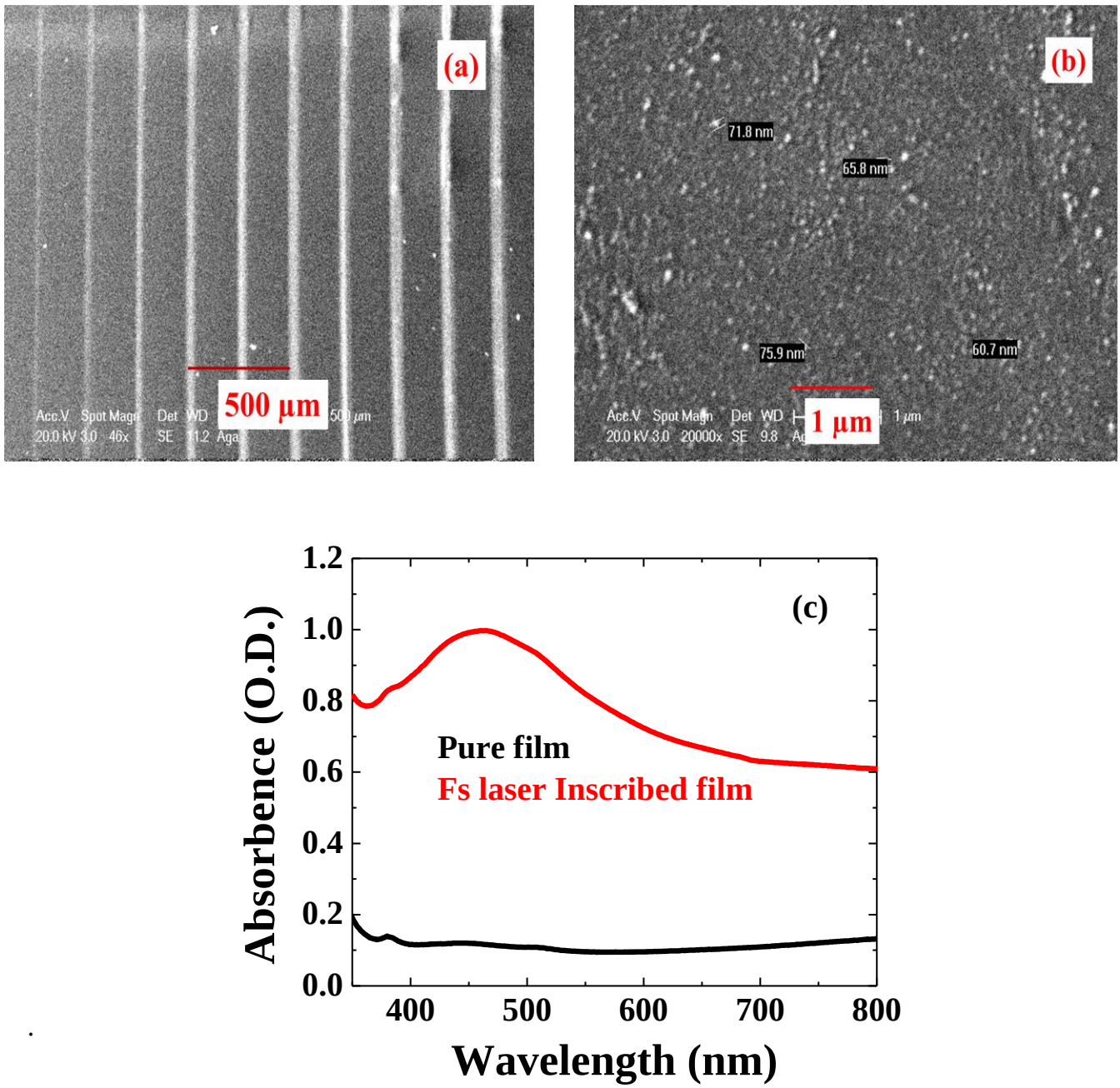

Figure 9. (a) SEM image of microstructures fabricated on PVA thin film containing silver nitrate at different energies. Energies from right to left are 100 µJ-10 µJ in steps of 10 µJ. (b) SEM image of a single microstructure fabricated at 100 µJ energy with 1 mm/s speed. (c) Absorption spectra of pure and irradiated film.

8.4 Nonlinear optical properties

In this section, we demonstrate and present some of the nonlinear optical properties of the silver nanoparticles prepared in solutions prepared and explained in earlier sections. Let us assume a spatial and temporal Gaussian profile for laser pulses. We derive the general equation for open aperture (OA) normalized energy transmittance as follows.Two photon absorption (TPA) process involves a transition from ground state (1) of a material to a higher-lying state (2) by the simultaneous absorption of two photons via an intermediate virtual state, as schematically shown in figure 10 (a). Then, the attenuation of the incident light is described by

$$\frac{dI}{dz} = -\beta I^2 \tag{8.5}$$

where β is the two-photon absorption coefficient.Three photon or multi photon absorption processes involve a transition from the ground state to a higher-lying state by the simultaneous absorption of three or more number photons via multiple numbers of virtual states as shown in figure 10 (b). In this case, the attenuation of the incident light is described by

$$\frac{dI}{dz} = -\alpha_n I^n \tag{8.6}$$

where α_n is the multiphoton absorption coefficient.

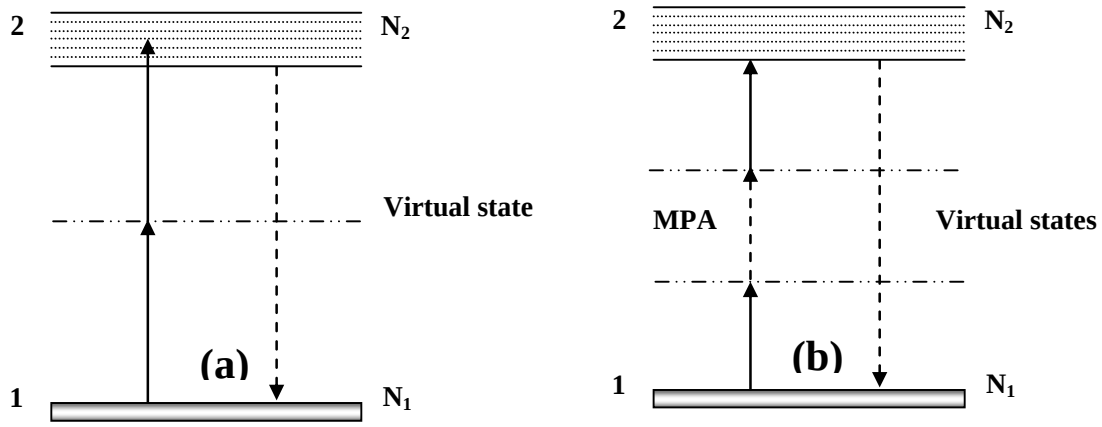

Figure 10. Schematic energy level diagram for (a)Two-photon absorption (TPA); (b)Multi-photon absorption (MPA).

By taking the equation and integrating, we get

$$\frac{dI(z)}{dz} = -\alpha_n I^n(z)$$

$$\int_{I_{in}}^{I_{out}} \frac{1}{I^n(z)} dI(z) = -\alpha_n \int_0^L dz$$

$$-\alpha_n L = \left[\frac{I^{-n+1}}{-n+1}\right]_{I_{in}}^{I_{out}} \Rightarrow \alpha_n L = \frac{1}{n-1}\left[\frac{1}{I_{in}^{n-1}} - \frac{1}{I_{out}^{n-1}}\right]$$

$$\alpha_n L = \frac{1}{(n-1)I_{in}^{n-1}}\left[1 - \frac{1}{T^{n-1}}\right], \text{where } T = \frac{I_{out}}{I_{in}} \quad T^{n-1} = \frac{1}{1+\alpha_n L(n-1)I_{in}^{n-1}}$$

$$T = \frac{1}{\left[1+\alpha_n L(n-1)I_{in}^{n-1}\right]^{\frac{1}{n-1}}}$$

$$\frac{I_{in}}{\omega_0^2} = \frac{I_{00}}{\omega_Z^2}, \quad \text{where } I_{in} = \frac{I_{00}}{1+\frac{Z^2}{Z_0^2}} \text{ and } \omega_Z^2 = \omega_0^2\left(1+\frac{Z^2}{Z_0^2}\right)$$

$$T = \frac{1}{\left[1+(n-1)\alpha_n L\left(I_{00}/\left(1+(Z/Z_0)^2\right)\right)^{n-1}\right]^{1/n-1}}$$

$$\Rightarrow T_{OA(nPA)} = \frac{1}{\left[1+(n-1)\alpha_n L\left(I_{00}/\left(1+(Z/Z_0)^2\right)\right)^{n-1}\right]^{1/n-1}} \tag{8.7}$$

where α_n is the effective MPA coefficient (n = 2 for 2PA; n = 3 for 3PA, and so on)

$$T_{OA(3PA)} = \frac{1}{\left[1+2\alpha_3 L_{eff}^{'}\left(I_{00}/\left(1+\left(\frac{z}{z_0}\right)^2\right)\right)^2\right]^{\frac{1}{2}}} \qquad T_{OA(4PA)} = \frac{1}{\left[1+3\alpha_{4n} L_{eff}^{''}\left(I_{00}/\left(1+\left(\frac{z}{z_0}\right)^2\right)\right)^3\right]^{\frac{1}{3}}}$$

I_{00} is the peak intensity (at Z=0), I_{in} is intensity at sample position (if Z- is the distance from focal point I_{in} (I_Z) is the intensity at that point), $Z_0 = \pi\omega_0^2/\lambda$ is Rayleigh range, ω_0 is the beam waist at the focal point (Z=0), dz is small slice of the sample, I_{in} is input intensity and I_{out} is output intensity of the sample.

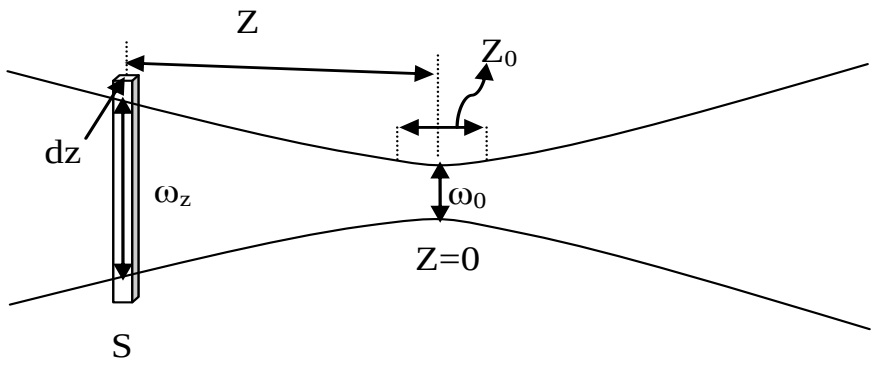

Figure 11. Schematic diagram of focused laser beam.

By retaining only the 2PA term and ignoring all other terms, we have an analytical expression for OA Z-scan for merely two-photon absorbers. Similarly retaining the 3PA term and ignoring the other terms provides us an analytical expression for OA scans for only three-photon absorbers.

$$T_{OA(2PA)} = \frac{1}{1+\alpha_2 L_{eff}\left(I_{00}/\left(1+\left(z/z_0\right)^2\right)\right)} \tag{8.8}$$

$$T_{OA(nPA)} = \frac{1}{\left[1+(n-1)\alpha_n L\left(I_{00}/\left(1+\left(\frac{z}{z_0}\right)^2\right)\right)^{n-1}\right]^{\frac{1}{n-1}}} \qquad T_{OA(3PA)} = \frac{1}{1+2\alpha_3 L_{eff}^{'}\left(I_{00}/\left(1+\left(z/z_0\right)^2\right)\right)^{1/2}}$$

(8.9)

The effective path lengths in the sample of length L for 2PA, 3PA are given as

$$L_{eff} = \frac{1- e^{-\alpha_0 L}}{\alpha_0} \quad L'_{eff} = \frac{1- e^{-2\alpha_0 L}}{2\alpha_0} \tag{8.10}$$

By expanding $T_{OA\,(2PA)}$ into series terms we obtain the following relation [261-261].

$$T_{OA(2PA)} = 1 - \left[\frac{\alpha_2 I_0 L_{eff}}{2^{\frac{3}{2}}\left[1+\frac{Z^2}{Z_0^2}\right]}\right] \tag{8.11}$$

We recorded normalized transmittance using Z-scan technique in order to test the Ag nanoparticles grown by laser irradiation possess the nonlinear optical properties as the ones synthesized through other techniques. We used a frequency doubled, Q-switched Nd: YAG (Spectra Physics, INDI 40) laser, delivering 6 ns laser pluses at 532 nm and a repetition rate of 10 Hz. In a Z-scan experimental set up, a laser beam with a transverse Gaussian profile is focused with a lens. The sample in a 1 mm thick cell is then translated along the propagation direction of the focused beam. At the focal point, the sample experiences maximum intensity, which will gradually decrease in either direction from the focus. The thickness of the sample is chosen such that it is smaller than the Rayleigh range of the focused beam, which was nearly 4.3 mm. Apertures are introduced in the path for beam shaping and calibrated neutral density filters were used to vary the laser intensity. The data is then recorded by scanning the cell across the focus and collecting the data through a SRS boxcar averager (model SR250), the output of which is given to a personal computer through an analog-to-digital (ADC) card. Figure 12 (a) shows the normalized transmittance curves collected using Z scan open aperture technique for C3 concentration solution recorded at different intensities. For comparison purpose, we have plotted (figure 12 (b) with the absorbance in arbitrary units, in normalizing both the curves) freshly prepared (red), and the preserved sample (black). If we compare the absorption spectra of the freshly prepared and the one with a long period of shelf time (figure 12 (b)), we see a broadening of the absorption spectrum and the peak shifts towards longer wavelength from 407 nm to 420 nm. This is due to an increase in the size of the particle.

The nonlinear absorption coefficient (α_2) is obtained by fitting the nonlinear transmission expression of an open aperture Z scan using the following relation which was already explained. Figure 12 (a) also shows the theoretical fit using the above equations for the best fit at input intensity of 0.143 GW/cm^2. The nonlinear absorption coefficient (α_2) was found to be 140 cm/GW. The experimental data presented include an error of ±5% arising from the errors in estimation of the beam waist at focus, and the neutral density filter calibration to estimate the input power. Our earlier work on biosynthesis of silver nanoparticles has α_2 ~2.72×10^2 cm/GW [244]. The lower value observed is mainly due to the smaller particle size, while the biosynthesis yielded larger size particles. The larger size particle's surface plasma moves towards the excitation wavelength of 532 nm.

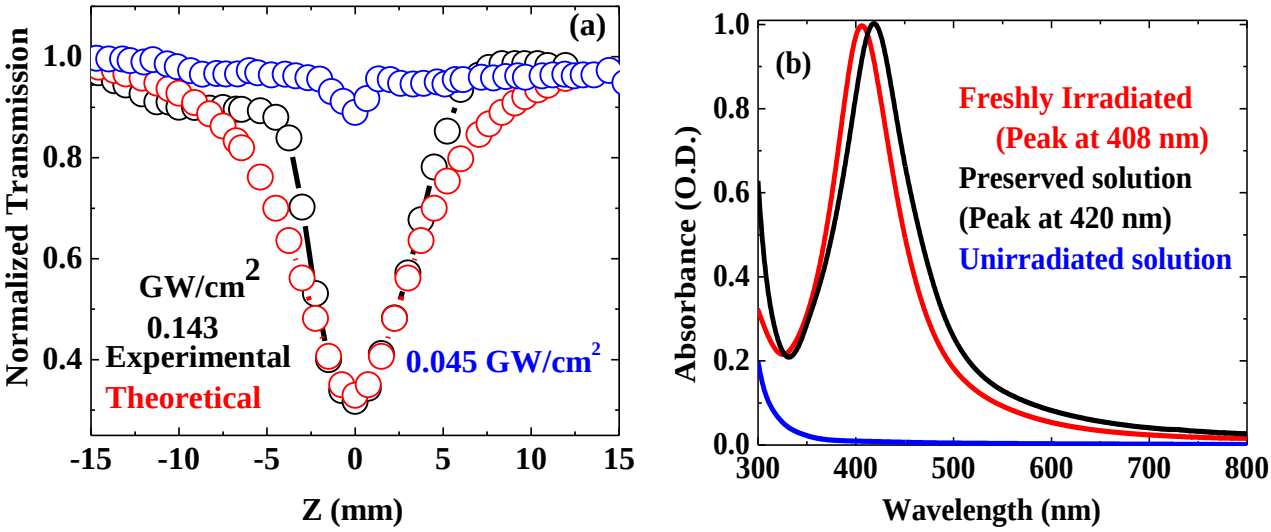

Figure 12. (a) Normalized transmittance Z scan open aperture curves for silver nanoparticles in solution prepared with concentration C3 (b) Normalized absorption spectra of freshly prepared silver nanoparticles and stored silver nanoparticles prepared with concentration C3.

8.5 Conclusions

In this chapter, a brief survey of literature is given on the synthesis of silver nanoparticles. Our earlier works on silver nanoparticles is also briefly mentioned. A novel method to synthesize silver nanoparticles through laser irradiation of silver precursor $AgNO_3$ in PVA polymer matrix is presented. The preparation of silver nanoparticles and results obtained by irradiating the mixture of silver nitrate ($AgNO_3$) and PVA solution with nano, pico and femtosecond lasers are discussed. Formation of silver nanoparticles is confirmed through the observation of plasmon peak around 400 nm using UV-Visible absorption spectrometer. The results obtained in the preparation of silver nanoparticles in liquid phase are extended to thin films also using laser irradiation technique. Femtosecond laser inscription of microstructures is also presented and these regions showed the formation of silver nanoparticles within the microstructure. Linear and nonlinear optical properties are studies using UV-Visible absorption spectroscopy and Z scan technique. The nonlinear absorption coefficient (α_2) is estimated as 140 cm/GW at an input intensity of 0.143 GW/cm^2.

Chapter 9

9.1 Summary of Results

In this thesis, we presented the laser irradiation effects on different polymers and crystals. Four polymers Poly Methyl Meth Acrylate (PMMA), Poly Di Methyl Siloxane (PDMS), Poly Styrene (PS), and Poly Vinyl Alcohol (PVA) are used in the study. Results obtained on lithium niobate crystal are presented. First part of the thesis is devoted to femtosecond (fs) laser direct writing in polymers and crystals. The second part of the thesis contains silver nanoparticles synthesis using nano, pico and femto second (ns, ps, fs) laser irradiations in solution and thin films containing silver nitrate and PVA mixture.

The high intensities of the fs laser pulses and their low pulse widths make fs laser micro machining a superior technique compared with nanosecond (ns) and continuous wave lasers. Two regimes of intensities leading to refractive index change modification at lower intensities (photo chemical model) and void formation (photo thermal model) at higher intensities are presented. Intermediate region explained by formation of void surrounded by refractive index change modification (Photo physical model) is carried out to fabricate microstructures, and gratings. Diffraction gratings are fabricated with different writing parameters in these materials. These polymers are transparent to visible as their band gap (4-6 eV) is more than the energy of 800 nm wavelength (1.55 eV) photon. The modification occurred through 800 nm wavelength photons are due to multi photon ionization. The modification even in case of lithium niobate crystal shows multi photon ionization as it is also transparent to visible light and band gap is more than 1.55 eV energy. Keldysh parameter which demarcates different ionization schemes such as tunneling, intermediate and avalanche ionizations showed tunneling ionization being the dominant mechanism for the investigated polymers and lithium niobate crystal.

Features size is observed to be increasing with no. of scans, energy, and more exposure (low scanning speed) in all polymers and crystal. Highest diffraction efficiencies of 34% in PMMA and 10% each in PDMS, and PS respectively are achieved. Refractive index change is estimated from first order diffraction efficiencies and found to be 10^{-3}. Heat treatment given to the diffraction gratings in order to enhance the diffraction efficiency has not yielded in any improvement as the gratings fabricated are of void type. Also different complex structure such as

curved shapes, Y couplers, and micro fluidic channels are fabricated and demonstrated in the thesis.

For the first time, emission from the fs laser modified regions is observed in case of all polymers. Formation of optical centers in fs irradiated polymers is shown to be main reason for the observed emission. The transitions within the functional groups (aldehyde, ketone etc) such as $n \rightarrow \pi^*$, $\pi \rightarrow \pi^*$ led to the observed emission. Some of the emission peaks are found to be matching with Raman peaks of polymers which are presented in the thesis. The emission peak is found to be changing with excitation wavelength in all the investigated polymers. Site selective photo excitation and red edge effect (REE) are described in this context. Also, the formation of different optical centers cannot be ignored along with REE. Unique excitation spectrum at different monitoring wavelengths is presented. Formation of micro explosions are observed instead of straight line structures at low energies (typically ~nJ) and at higher scanning speeds (more than 3 mm/s) which can be attributed to no overlapping of pulses (high scanning speed) and low thermal wave propagation (low pulse energy). Applications of these luminescent micro craters to memory based devices are demonstrated by treating each luminescent micro crater as bit 1. Life time of the emission is measured in case of fs irradiated PS and found to be nearly ns.

Formation of paramagnetic type of free radicals such as peroxide and alkoxy radicals is observed in the fs laser irradiated PMMA, PDMS, and PS which are confirmed through Electron Spin Resonance (ESR) spectrometer. Fs irradiated PMMA, and PS showed life time of these free radicals nearly a day. Fs irradiated PDMS showed existence of free radicals even after six months. Change in the life time of these free radicals is attributed to different host environments of the polymer. Elemental analysis is carried out to the modified regions using Energy Dispersive X-ray Absorption Spectroscopy (EDXAS) and Field Emission Scanning Electron Microscope (FESEM). Change in weight percentage is observed in case of fs laser modified regions compared with pristine regions. The change in weight percentage is attributed to the distribution of different elements in the polymer chain and formation different optical and paramagnetic centers on fs laser irradiation. Lithium Niobate crystal has not shown any formation of optical centers but however, pure lithium niobate crystal (unirradiated) has shown ESR signal as lithium niobate contains O_3 group and could be possibly due to peroxide type of

free radical. As polymers are anisotropic due to lack of symmetry they showed ESR signals in all orientations unlike lithium niobate crystal which has symmetry.

Confocal micro-Raman studies are carried out to study the effect of fs laser pulses on Raman modes in both polymers and lithium niobate crystal. Broadening and suppression of modes are observed in case of structures fabricated at higher energies as it results in void formation. This broadening is due to the formation of defects in polymers. Also, broadening and suppression of Raman modes is found to be more prominent in the middle regions of the structure compared with end regions. Raman mapping is performed across the structure and observed the changes to be in accordance with the incident Gaussian pulse. These results are investigated and reported in both polymers and lithium niobate crystal.

Silver nanoparticles in solution and thin films are synthesized using silver nitrate and PVA mixture at different concentrations and different laser irradiations of ns, ps, and fs lasers. This is a novel technique as it is faster compared with thermal treatment given to the same solutions and thin films and also formation of the nanoparticles is instantaneous in this method. Detailed studies are carried out by varying pulse width, wavelength, exposure time, and energy of the laser and the results are presented. Formation of nanoparticles is confirmed through color change from transparent to yellow. Irradiated solutions and thin films at different concentrations showed plasmon peak in the absorption spectra. Formation of different sized nanoparticles at different energies with peak shift is observed. Transmission electron microscope (TEM) results confirmed the formation of nanoparticles with size of the particles varying from 2 to 200 nm. Formations of silver nanoparticles with hexagonal and different shapes were observed in particular with 355 nm laser irradiation. Influence of wavelength, pulse width, exposure time, and energy in the synthesis of silver nanoparticles is highlighted. Electron diffraction patten of a single nanoparticle in TEM showed polycrystallinity with cubic nature for the silver nanoparticles prepared. Fs laser fabrication of microstructures showed the formation of silver nanoparticles in the microstructure. Nonlinear optical properties of these nanoparticles are studied. The nonlinear absorption coefficient (α_2) achieved is 140 cm/GW.

9.2 Future Scope

Fabrication of waveguides, Y couplers are interesting to study in both polymers and crystals for applications involved in waveguides. Grating couplers which can couple light found its applications in integrated optics and reports on the fabrication of the diffraction couplers are sparse in the literature. As array of microdots is reported in the thesis, it would be interesting to carry out the fabrication and characterize the polymers by fabricating three dimensional photonic crystals. Synthesis of photonic crystals through chemical routes only is reported and literature is abundant. Fs laser direct writing of photonic crystals is superior compared to chemical routes as it is faster and atmospheric conditions (environment) has little or no role to play.

By synchronizing the three dimensional stage, laser pulses and other electronic equipment, one can control laser pulses whenever digital information comes. This leads to array to micro modifications which fluoresce in case of polymers. Thus, one can store the digital information (data) in these polymers and it can be read with read beam as these modifications fluoresce. Investigations of the origins of emission are carried out at room temperature only in the present thesis. It would be interesting to carry out investigations at low temperatures. At room temperature, we could not observe multiple ESR signals for different polymers.

Only the synthesis of silver nanoparticles is reported in the thesis. It can be carried out to other metal nanoparticles such as gold, aluminum etc. Synthesis of properties of alloy nanoparticles will be more interesting. Only open aperture normalized transmittance of Z scan which gives nonlinear absorption coefficient is reported in the thesis. Comparison of the nonlinear optical properties of silver, gold, and alloy of silver and gold will be interesting to know the better nonlinear optical material. Several reports available in literature show applications involved in Surface Enhanced Raman Scattering (SERS). Since direct illumination of laser onto the solutions and thin films lead to nanoparticles formation, it would be an interesting experiment to use the excitation laser for Raman as an irradiation source to record Raman and observe simultaneously enhancement of Raman modes. Femtosecond laser inscription of structures on silver nitrate and PVA film showed nanoparticles in the microstructure. It would be fascinating to carry out experiments on plasmonics.

1. T. H. Maiman, “Stimulated optical radiation in ruby,” Nature, Vol. 187, No. 4736, 493-494, 1960.
2. P. A. Franken, G. Weinreich, C. W. Peters, and A. E. Hill, “Generation of optical harmonics,” Physical Review Letters, Vol. 7, No. 4, 118-119,1961.
3. K. Itoh, W. Watanabe, S. Nolte, and C. B. Schaffer, “Ultrafast Processes for Bulk Modification of Transparent Materials,” MRS Bulletin, Vol. 31, 620-625, 2006.
4. X. Liu, D. Du, G. Mourou, “Laser Ablation and Micromachining with Ultrashort Laser Pulses,”IEEE Quantum Electronics 38, 1706-1716, 1997.
5. C. Momma, S. Nolte, G. Kamlage, F Von Alvensleben, A Tunnermann, “Beam delivery of femtosecond laser radiation by diffractive optical elements,”Applied Physics A 67, 517-520, 1998.
6. R. Haight, A. Wagner, P. Longo, and D. Lim, "High resolution material ablation and deposition with femtosecond lasers and applications to photomask repair," Journal of Modern Optics **51**, 2781-2796, 2004.
7. G. Kamlage, T. Bauer, A. Ostendorf, and B. N. Chichkov, "Deep drilling of metals by femtosecond laser pulses," Applied Physics A-Materials Science & Processing **77**, 307-310, 2003.
8. P. P. Pronko, S. K. Dutta, J. Squier, J. V. Rudd, D. Du, and G. Mourou, "Machining of Submicron Holes Using a Femtosecond Laser at 800-Nm," Optics Communications **114**, 106-110 (1995).
9. B. N. Chichkov, F. Korte, J. Koch, S. Nolte, and A. Ostendorf, "Femtosecond laser ablation and nanostructuring," *Proc. SPIE Vol. 4760 High Power Laser Ablation IV (*SPIE, Bellingham, WA, 2002), pp. 19-24, 2002.
10. R. Haight, D. Hayden, P. Longo, T. Neary, and A. Wagner, "MARS: Femtosecond laser mask advanced repair system in manufacturing," Journal of Vacuum Science & Technology B **17**, 3137-3143, 1999.
11. S. Taccheo, G. Della Valle, R. Osellame, G. Cerullo, N. Chiodo, P. Laporta, O. Svelto, A. Killi, U. Morgner, M. Lederer, and D. Kopf, "Er : Yb-doped waveguide laser fabricated by femtosecond laser pulses," Optics Letters **29**, 2626-2628, 2004.

12. C. Florea, and K. A. Winick, "Fabrication and characterization of photonic devices directly written in glass using femtosecond laser pulses," Journal of Lightwave Technology **21**, 246-253, 2003.
13. K. Minoshima, A. M. Kowalevicz, E. P. Ippen, and J. G. Fujimoto, "Fabrication of coupled mode photonic devices in glass by nonlinear femtosecond laser materials processing," Optics Express **10**, 645-652, 2002.
14. A. M. Streltsov, and N. F. Borrelli, "Fabrication and analysis of a directional coupler written in glass by nanojoule femtosecond laser pulses," Optics Letters **26**, 42-43, 2001.
15. Y. Sikorski, A. A. Said, P. Bado, R. Maynard, C. Florea, and K. A. Winick, "Optical waveguide amplifier in Nd-doped glass written with near-IR femtosecond laser pulses," Electronics Letters **36**, 226-227, 2000.
16. M. Kamata, M. Obara, R. R. Gattass, L. R. Cerami, and E. Mazur, "Optical vibration sensor fabricated by femtosecond laser micromachining," Applied Physics Letters **87,** 051106, 2005.
17. K. M. Davis, K. Miura, N. Sugimoto, and K. Hirao, "Writing Waveguides in Glass with a Femtosecond Laser," Optics Letters **21**, 1729-1731, 1996.
18. W. Watanabe, S. Sowa, T. Tamaki, K. Itoh, J. Nishii "Three-Dimensional Waveguides Fabricated in Poly(methyl methacrylate) by a Femtosecond Laser," Jap. J. Appl. Phys., Part 2, **45**, L675-L767, 2006.
19. A. Zoubir, C. Lopez, M. Richardson, and K. Richardson, "Femtosecond laser fabrication of tubular waveguides in poly(methyl methacrylate)," Opt. Lett. **29(16),** 1840-1842 2004.
20. S. Sowa, T. Tamaki, K. Itoh, J. Nishii, W. Watanabe, "Three-dimensional waveguides fabricated in poly(methyl methacrylate) by a femtosecond laser," Jap. J. Appl. Phys., Part 2: Letters **45(29-32)**, L765-L767,2006.
21. K. Wang, D. Klimov, Z. Kolber, **"**Waveguide fabrication in PMMA using a modified cavity femtosecond oscillator," Proc. SPIE **6766**, 67660Q, 2007.
22. K. Ohta, M. Kamata, M. Obara, N. Sawanobori, "Optical waveguide fabrication in new glasses and PMMA with temporally tailored ultrashort laser," Proc. SPIE **5340**, 172, 2004.
23. W. Watanabe, S. Sowa, T. Tamaki, K. Itoh, J. Nishii "Three-Dimensional Waveguides Fabricated in Poly(methyl methacrylate) by a Femtosecond Laser," Jap. J. Appl. Phys., Part 2, **45**, L675-L767, 2006.

24. A. Zoubir, C. Lopez, M. Richardson, and K. Richardson, "Femtosecond laser fabrication of tubular waveguides in poly (methyl methacrylate)," Opt. Lett. **29(16),** 1840-1842, 2004.

25. S. Sowa, T. Tamaki, K. Itoh, J. Nishii, W. Watanabe, "Three-dimensional waveguides fabricated in poly(methyl methacrylate) by a femtosecond laser," Jap. J. Appl. Phys., Part 2: Letters **45**(29-32), L765-L767, 2006.

26. K. Wang, D. Klimov, Z. Kolber, **"**Waveguide fabrication in PMMA using a modified cavity femtosecond oscillator," Proc. SPIE **6766**, 67660Q, 2007.

27. K. Ohta, M. Kamata, M. Obara, N. Sawanobori, "Optical waveguide fabrication in new glasses and PMMA with temporally tailored ultrashort laser," Proc. SPIE **5340**, 172, 2004.

28. H. Becker, C. Gärtner, "Polymer microfabrication technologies for microfluidic systems," Analytical and Bioanalytical Chemistry, **390(1)**, 89-111, 2008.

29. Y. Xia, J.A. Rogers, K.E. Paul, G.M. Whitesides, "Unconventional Methods for Fabricating and Patterning Nanostructures," Chem. Rev. **99(7)**, 1823-1848, 1999.

30. B.D. Gates, Q. Xu, M. Stewart, D. Ryan, C.G. Willson, G.M. Whitesides, "New approaches to nanofabrication: Molding, printing, and other techniques," Chem. Rev. **105(4)**, 1171-1196, 2005.

31. R.R. Gattass, and E. Mazur, "Femtosecond laser micromachining in transparent materials," Nat. Phot. **2**, 219-225, 2008.

32. S. Juodkazis, V. Mizeikis, H. Misawa, "Three-dimensional Microfabrication of materials by femtosecond lasers for photonics applications," J. Appl. Phys. **106,** 051101, 2009.

33. S. Nolte, M. Will, J. Burghoff, and A. Tuennermann, "Femtosecond waveguide writing: a new avenue to three-dimensional integrated optics," Appl. Phys. A **77**, 109-111, 2003.

34. S. Juodkazis, V. Mizeikis, Shigeki Matsuo, Kosei Ueno, and Hiroaki Misawa, "Three-dimensional micro- and nano-structuring of materials by tightly focused laser radiation," Bull. Chem. Soc. Jpn., **81(4)**, 411–448, 2008.

35. M. Ams, G.D. Marshall, P. Dekker, M. Dubov, V.K. Mezentsev, I. Bennion, M.J. Withford, "Investigation of ultrafast laser–photonic material interactions: challenges for directly written glass photonics," IEEE J. Sel. Top. Quant. Electron., **14(5)**, 1370-1381, 2008.

36. J. Qiu, K. Miura, K. Hirao, "Femtosecond laser-induced microfeatures in glasses and their applications," Journal of Non-Crystalline Solids, **354,** 1100–1111, 2008.

37. G. Della Valle, R Osellame, and P. Laporta, "Micromachining of photonic devices by femtosecond laser pulses," J. Opt. A: Pure Appl. Opt. **11,** 013001, 2009.

38. E.N. Glezer, M. Milosavljevic, L. Huang, R.J. Finlay, T.H. Her, J.P. Callan, and E. Mazur, "Three-dimensional optical storage inside transparent materials," Opt. Lett. **21**(24), 2023-2025, 1996.

39. B.H. Cumpston, S.P. Ananthavel, S. Barlow, D.L. Dyer, J.E. Ehrlich, L.L. Erskine, A. A. Heikal, S.M. Kuebler, I. Y. S. Lee, D. McCord-Maughon, J. Q. Qin, H. Rockel, M. Rumi, X.L. Wu, S.R. Marder, J.W. Perry, "Two-photon polymerization initiators for three dimensional optical data storage and microfabrication," Nature **398**, 51-54, 1999.

40. Z. Nie, H. Lee, H. Yoo, Y. Lee, Y. Kim, K.-S. Lim, M. Lee, "Multilayered optical bit memory with a high signal-to-noise ratio in fluorescent polymethylmethacrylate," Appl. Phys. Lett. **94,** 111912, 2009.

41. H. Tang, H. Jiu, B. Jiang, J. Cai, H. Xing, Q. Zhang, W. Huang, A. Xia, "Three-dimensional optical storage recording by microexplosion in a doped PMMA polymer," Proc. of SPIE, **5643**, 258-263, 2005.

42. D.F. Farson, H.W. Choi, C. Lu, L.J. Lee, "Femtosecond laser bulk micromachining of microfluidic channels in poly (methyl methacrylate)," J. Laser Appl. **18(3)**, 210-215, 2006.

43. M. Haiducu, M. Rahbar, I.G. Foulds, R.W. Johnstone, D. Sameoto, M. Parameswaran, "Deep-UV patterning of commercial grade PMMA for low-cost, large-scale microfluidics," J. Micromech. Microeng. **18**, 115029-115035, 2008.

44. Y.V. White, M. Parrish, X. Li, L.M. Davis, and W. Hofmeister, "Femtosecond micro- and nano-machining of materials for microfluidic applications," Proc. SPIE **7039**, 70390J-1-70390J-10, 2008.

45. D. Gómez, I. Goenaga, I. Lizuain, M. Ozaita, "Femtosecond laser ablation for microfluidics," Opt. Eng. **44**, 051105, 2005.

46. D. Day, M. Gu, "Microchannel fabrication in PMMA based on localized heating by nanojoule high repetition rate femtosecond pulses," Opt. Exp. **13(16)**, 5939-5946 (2005).

47. C.G. Khan Malek, "Laser processing for bio-microfluidics applications (part II)," Anal. Bioanal. Chem., **385**, 1362–1369, 2006.

48. C. Monat, P. Domachuk, B.J. Eggleton, "Integrated optofluidics: a new river of light," Nat. Photonics, **1,** 106-114, 2007.

49. J. H. Si, J. R. Qiu, J. F. Zhai, Y. Q. Shen, and K. Hirao, "Photoinduced permanent gratings inside bulk azodye-doped polymers by the coherent field of a femtosecond laser," Appl. Phys. Lett. **80**, 359-361, 2002.
50. L. Ding, D. Jani, J. Linhardt, J.F. Künzler, S. Pawar, G. Labenski, T. Smith, and W.H. Knox, "Large enhancement of femtosecond laser micromachining speed in dye-doped hydrogel polymers," Opt. Exp. **16(26)**, 21914-21921, 2008.
51. L. Ding, R. I. Blackwell, J. F. Kunzler, and W. H. Knox, "Femtosecond laser micromachining of waveguides in silicone-based hydrogel polymers," Appl. Opt. **47(17)**, 3100-3108, 2008.
52. J. Si, Z. Meng, S. Kanehira, J. Qiu, B. Hua, K. Hirao, "Multiphoton-induced periodic microstructures inside bulk azodye-doped polymers by multibeam laser interference," Chem. Phys. Lett. **399**, 276-279, 2004.
53. J.H. Si, J. R. Qiu, J. F. Zhai, Y. Q. Shen, K. Hirao, "Photoinduced permanent gratings inside bulk azodye-doped polymers by the coherent field of a femtosecond laser," Appl. Phys. Lett. **80(3)**, 359-361, 2002.
54. T.N. Kim, K. Campbell, A. Groisman, D. Kleinfeld, C.B. Schaffer, "Femtosecond laser-drilled capillary integrated into a microfluidic device," Appl. Phys. Lett. **86**, 201106, 2005.
55. S. Demming, A. Llobera, R. Wilke, S. Büttgenbach, "Single and multiple internal reflection poly (dimethylsiloxane) absorbance-based biosensors," Sensors and Actuators, B: Chemical **139(1)**, 166-173, 2009.
56. S.K. Sia, G.M. Whitesides, "Microfluidic devices fabricated in poly(dimethylsiloxane) for biological studies," Electrophoresis, **24(21)**, 3563-3576, 2003.
57. C.R. Mendonca, L.R. Cerami, T. Shih, R.W. Tilghman, T. Baldacchini, and E. Mazur, "Femtosecond laser waveguide micromachining of PMMA films with azoaromatic chromophores," Opt. Exp. **16(1)**, 200-206, 2008.
58. G. Zhou, M. J. Ventura, M. R. Vanner, and M. Gu, "Use of ultrafast-laser-driven microexplosion for fabricating three-dimensional void-based diamond-lattice photonic crystals in a solid polymer material," Opt. Lett. **29**, 2240-2242, 2004.
59. M. Straub, M. Gu, "Near-infrared photonic crystals with higher-order bandgaps generated by two-photon photopolymerization," Opt. Lett. **27**, 1824- 1826, 2002.

60. P. Maker, R. Terhune, and C. Savage, "Proceedings of the Third International Conference on Quantum Electronics," P. Grivet, and N. Bloembergen, eds. (Columbia Unversity Press, 1964), p. 15559, 1964.

61. M. Hercher, "Laser-Induced Damage in Transparent Media," Journal of the Optical Society of America **54**, 563, 1964.

62. E. N. Glezer, M. Milosavljevic, L. Huang, R. J. Finlay, T. H. Her, J. P. Callan, and E. Mazur, "Three-dimensional optical storage inside transparent materials," Optics Letters **21**, 2023-2025, 1996.

63. A. Zoubir, C. Lopez, M. Richardson, and K. Richardson, "Femtosecond laser fabrication of tubular waveguides in poly (methyl methacrylate)," Optics Letters **29**, 1840-1842 2004.

64. H.Misawa,S.Juodkazis,"3D Laser Microfabrication principles and applications,"WILEY-VCH Verlag GmbH Co. KGaA, 2006.

65. E. G. Gamaly, A. V. Rode, B. Luther-Davies, and V. T. Tikhonchuk, Phys. of Plasmas, 9, 949-957, 2002.

66. B. E. A. saleh, M. C. Teich, Fundamentals of Photonics, (John Wiley&Sons, NY, 1991) 81-107, 1991.

67. Robert W. Boyd, "Nonlinear Optics," 3rd edition, Academic Press.

68. N. W. Ashcroft, N. D. Mermin, Solid State Physics (Holt Rinehart and Winston, New York, 1976).

69. C. B. Schaffer, A. Brodeur, and E. Mazur,"Laser-induced breakdown and damage in bulk transparent materials using tightly-focused femtosecond laser pulses," Measurement Science and Technology **12**, 1784 -1794, 2001.

70. L. V. Keldysh, Soviet Physics JETP **20**, 1307, 1965.

71. B. C. Stuart, M. D. Feit, S. Herman, A. M. Rubenchik, B. W. Shore, and M. D.Perry, "Nanosecond-to-Femtosecond Laser-Induced Breakdown in Dielectrics,"Physical Review B-Condensed Matter **53**, 1749-1761, 1996.

72. B. Rethfeld," Free-electron generation in laser-irradiated dielectrics,"Phys. Rev. B, Vol. 73, 035101 (6 Pp), 2006.

73. B. Rethfeld, "Unified Model for the Free-Electron Avalanche in Laser-Irradiated Dielectrics," Phys. Rev. Lett. Vol. 92, No. 18, 187401 (4 Pp).

74. R. Loren, Cerami, Eric Mazur, Stefan Nolte and Chris B. Schaffer, "Femtosecond laser micromachining,", in Ultrafast Optics, Ed. Rick Trebino and Jeff Squier (Trafford Publishing, Victoria, Canada, 2007).

75. C. B. Schaffer, J. F. Garcia, E. Mazur, Bulk heating of transparent materials using a high-repetition rate femtosecond laser, Appl. Phys. A **76**, 351-354, (2003.

76. A. Zakery, Y. Ruan, A. V. Rode, M. Samoc, and B. Luther-Davies, Low-loss waveguides in ultra-fast deposited As_2S_3 chalcogenide films, JOSA B, **20**, 1-9, 2003.

77. S. I. Anisimov, Kapeliov.Bl, and T. L. Perelman, "Electron-Emission from Surface of Metals Induced by Ultrashort Laser Pulses," Zhurnal Eksperimentalnoi I Teoreticheskoi Fiziki **66**, 776-781, 1974.

78. M. Agranat, A. Benditskii, G. Gandel'man, P. Kondratenko, B. Makshantsev, G. Rukman, and B. Stepanov, "Inertialess metal glow produced by picosecond pulses," Soviet Physics JETP **52**, 27 – 31, 1980.

79. M. Agranat, S. I. Anisimov, S. Ashitkov, B. Makshantsev, and I. Ovchinnikova,"Thermal radiation emitted by metals due to disturbance of an equilibrium between electrons and the lattice," Soviet Physics Solid State **29**, 1875-1880, 1987.

80. P. B. Corkum, F. Brunel, N. K. Sherman, and T. Srinivasanrao, "Thermal Response of Metals to Ultrashort-Pulse Laser Excitation," Physical Review Letters **61**, 2886-2889, 1988.

81. B. N. Chichkov, C. Momma, S. Nolte, F. vonAlvensleben, and A. Tunnermann, "Femtosecond, picosecond and nanosecond laser ablation of solids," Applied Physics A-Materials Science & Processing **63**, 109-115, 1996.

82. J. Konig, S. Nolte, and A. Tunnermann, "Plasma evolution during metal ablation with ultrashort laser pulses," Optics Express **13**, 10597-10607, 2005.

83. M. Weikert, and F. Dausinger, "Surface structuring," in *Femtosecond Technology for Technical and Medical Applications,* ed. F. Dausinger, F. Lichtner, and H. Lubatschowski (Springer-Verlag, Berlin 2004), pp. 117-129.

84. C. Florea, and K. A. Winick, "Fabrication and characterization of photonic devices directly written in glass using femtosecond laser pulses," Journal of Lightwave Technology **21**, 246-253, 2003.

85. K. Miura, J. R. Qiu, H. Inouye, T. Mitsuyu, and K. Hirao, "Photowritten optical waveguides in various glasses with ultrashort pulse laser," Applied Physics Letters **71**, 3329-3331, 1997.

86. J. W. Chan, T. R. Huser, S. Risbud, and D. M. Krol, "Structural changes in fused silica after exposure to focused femtosecond laser pulses," Optics Letters **26**, 1726 -1728, 2001.

87. J. W. Chan, T. R. Huser, S. H. Risbud, J. S. Hayden, and D. M. Krol, "Waveguide fabrication in phosphate glasses using femtosecond laser pulses," Applied Physics Letters **82**, 2371-2373, 2003.

88. J. W. Chan, T. R. Huser, S. H. Risbud, and D. M. Krol, "Modification of the fused silica glass network associated with waveguide fabrication using femtosecond laser pulses," Applied Physics A-Materials Science & Processing **76**, 367-372, 2003.

89. R. Bruckner, "Properties and structure of vitreous silica. I," Journal of Non-Crystalline Solids **5**, 123-175, 1970.

90. R. Bruckner, "Properties and structure of vitreous silica. II," Journal of Non-Crystalline Solids **5**, 177-216, 1971.

91. D. Homoelle, S. Wielandy, A. L. Gaeta, N. F. Borrelli, and C. Smith, "Infrared photosensitivity in silica glasses exposed to femtosecond laser pulses," Optics Letters **24**, 1311-1313, 1999.

92. M. Will, S. Nolte, B. N. Chichkov, and A. Tunnermann, "Optical properties of waveguides fabricated in fused silica by femtosecond laser pulses," Applied Optics **41**, 4360-4364, 2002.

93. K. M. Davis, K. Miura, N. Sugimoto, and K. Hirao, "Writing Waveguides in Glass with a Femtosecond Laser," Optics Letters **21**, 1729-1731, 1996.

94. Y. Shimotsuma, P. G. Kazansky, Q. Jiarong, and K. Hirao, "Self-organized nanogratings in glass irradiated by ultrashort light pulses," Physical Review Letters **91**, 247405, 2003.

95. L. Sudrie, M. Franco, B. Prade, and A. Mysyrewicz, "Writing of permanent birefringent microlayers in bulk fused silica with femtosecond laser pulses," Optics Communications **171**, 279-284, 1999.

96. L. Sudrie, M. Franco, B. Prade, and A. Mysyrowicz, "Study of damage in fused silica induced by ultra-short IR laser pulses," Optics Communications **191**, 333-339, 2001.

97. E. N. Glezer, and E. Mazur, "Ultrafast-laser driven micro-explosions in transparent materials," Applied Physics Letters **71**, 882-884, 1997.

98. J. R. Qiu, K. Miura, and K. Hirao, "Three-dimensional optical memory using glasses as a recording medium through a multi-photon absorption process," Japanese Journal of Applied Physics Part 1-Regular Papers Short Notes & Review Papers **37**, 2263-2266, 1998.

99. T. Gorelik, M. Will, S. Nolte, A. Tuennermann, and U. Glatzel, "Transmission electron microscopy studies of femtosecond laser induced modifications in quartz," Applied Physics A-Materials Science & Processing **76**, 309-311, 2003.
100. C. B. Schaffer, A. O. Jamison, and E. Mazur, "Morphology of femtosecond laser induced structural changes in bulk transparent materials," Applied Physics Letters **84**, 1441-1443, 2004.
101. J. W. Chan, T. R. Huser, S. H. Risbud, and D. M. Krol, "Modification of the fused silica glass network associated with waveguide fabrication using femtosecond laser pulses," Applied Physics A-Materials Science & Processing **76**, 367-372, 2003.
102. V. R. Bhardwaj, E. Simova, P. B. Corkum, D. M. Rayner, C. Hnatovsky, R. S. Taylor, B. Schreder, M. Kluge, and J. Zimmer, "Femtosecond laser-induced refractive index modification in multicomponent glasses," Journal of Applied Physics **97**, 83102, 2005.
103. Claude Rulliere, "Femtosecond Laser Pulses-Principles and Experiments," 2nd edition, Springer publications
104. P. G. Kryukov, "Ultrashort-Pulse lasers, "Quantum Electronics **31**(2), 95-119, 2001.
105. V. N. Lugovoi and A. A. Manenkov, "On the Self-Focusing of Femtosecond Laser Pulses in Air: Comments,"Laser Physics, Vol. 15, No. 9, 1269–1275, 2005.
106. Spectra-Physics Inc. operation manuals for *Mai-Tai*^{TM} and *Spitfire*^{TM}.
107. J-C. Diels, and W. Rudolf, *Ultrafast laser pulse phenomenon*, 2nd Ed. Academic Press, Elsevier (2006).
108. ESP 300 Motion Controller/Driver Manual
109. John Wertz, James R. Bolton, "Electron Spin Resonance elementary theory and practical applications," McGraw-Hill Book company.
110. Raymond S. Alger, "Electron Paramagnetic Resonance: Techniques and applications," John Wiley & Sons, Inc.
111. L. Reimer H. Kohl, '*Transmission Electron Microscopy Physics of Image Formation*', **5th** Ed, Springer, New York, 10013, USA (2008).
112. Z. L. Wang, Transmission Electron Microscopy of Shape-Controlled Nanocrystals and Their Assemblies, *J. Phys. Chem. B,* **104,** 1153-1175, 2000.

113. A. Baum, P. J. Scully, W. Perrie, D. Jones, R. Issac, and D. A. Jaroszynski, “Pulse-duration dependency of femtosecond laser refractive index modification in poly(methyl methacrylate),”Opt. Lett. 33, 651-653, 2008.

114. L. Singh, K.S. Samra, J. Rad. Phys. Chem. 77, 252, 2008.

115. R. D. Mathad, H. G. Harish Kumar, B. Sannakki, S. Ganesh, K. S.S. Sarma, M. V. Badiger, “High energy electron irradiation effects on polystyrene films”, Radiation Effects & Defects in Solids 164 (10), 656–664, 2009.

116. W.A. Jabbar, N.F. Habubi, and S.S. Chiad, Journal of the Arkansas Academy of Science, Vol. 64, 101-105, 2010.

117. Andrew J. Lovinger; Don D. Davis, Frederic C. Schilling, Frank J. Padden, Jr., and Frank A. Bovey, John M. Zeiglert, Solid-state Structure and Phase Transitions of Poly (dimethylsilylene), Macromolecules, 24, 132-139, 1991.

118. Hung, et. al., *"Further Analytical Study of Hybrid Rocket Combustion"*, NASI-10210, 1972.

119. Karabeyoglu, et. al., "Transient Combustion in Hybrid Rockets," AIAA 95-2691, 1995.

120. Wooldridge, et. at., "Internal Ballistic Considerations in Hybrid Rocket Design," J. Spacecraft, Feb. 1967 and http://hybridsnow.tripod.com/PMMA-thermo.html.

121. Akhan Tleoubaev, Andrzej Brzezinski, “Thermal Diffusivity and Volumetric Specific Heat Measurements Using Heat Flow Meter Instruments for Thermal Conductivity 29 / Thermal Expansion 17 Conference, Laser Comp, Inc., 20 Spring Street, Saugus, Massachusetts 01906 USA (9 pages).

122. E. G. Gamaly, S. Juodkazis, K. Nishimura, H. Misawa, B. luther-Davies, L. Hallo, P. Nicolai, V. T. Tikhonchuk, “Laser-matter interaction in the bulk of a transparent solid: Confined microexplosion and void formation”Phys. Rev. B 73, 214101, 2006.

123. A. C. Tien, S. Backus, H. kapteyn, M. Murnane, and G. Mourou, “Short-Pulse Laser Damage in Transparent Materials as a Function of Pulse Duration”Phys. Rev. Lett. 82, 3883-3886, 1999.

124. N. Sanner, O. Uteza, B. Chimier, M. Sentis, P. Lassonde, F. Legare, and J. C. Kieffer, “Toward determinism in surface damaging of dielectrics using few-cycle laser pulses” Appl. Phys. Lett. 96, 071111, 2010.

125. S. M. Eaton, H. Zhang, M. L. Ng, J. Li, W.-J. Chen, S. Ho, P. R. Herman, "Transition from thermal diffusion to heat accumulation in high repetition rate femtosecond laser writing of buried optical waveguides," Opt. Exp. 16, 9443-9458, 2008.

126. H. Zhang, S. M. Eaton, P. R. Herman, "Low-loss Type II waveguide writing in fused silica with single picosecond laser pulses,"Opt. Exp. 14, 4826-4834, 2006.

127. C. Wochnowski, Y. Cheng, K. Meteva, K. Sugioka, K. Midorikawa, S. Metev, J. Opt. A: Pure Appl. Opt. 7, 493-501, 2005.

128. K. L. N. Deepak, D. Narayana Rao, S. Venugopal Rao, "Fabrication and optical characterization of microstructures in poly(methylmethacrylate) and poly(dimethylsiloxane) using femtosecond pulses for photonic and microfluidic applications," Appl. Opt. 49, 2475-2489, 2010.

129. K. L. N. Deepak, S. Venugopal Rao, D. Narayana Rao, "Femtosecond laser-fabricated microstructures in bulk poly(methylmethacrylate) and poly(dimethylsiloxane) at 800 nm towards lab-on-a-chip applications," Pramana- J. Phys. 75, 1221-1232, 2010.

130. K. L. N. Deepak, R. Kuladeep, S. Venugopal Rao, D. Narayana Rao, "Luminescent microstructures in bulk and thin films of PMMA, PDMS, PVA,and PS fabricated using femtosecond direct writing technique," Chem. Phys. Lett. 503, 57-60, 2011.

131. K. L. N. Deepak, R. Kuladeep, D. Narayana Rao, "Emission properties of femtosecond (fs) laser fabricated microstructures in Polystyrene (PS)," Opt. Commun. 284, 3070-3073, 2011.

132. K. L. N. Deepak, R. Kuladeep, V. Praveen Kumar, S. Venugopal Rao, D. Narayana Rao, "Spectroscopic investigations of femtosecond laser irradiated polystyrene and fabrication of microstructures"Opt. Commun.3074-3078,2011.

133. Z. Nie, H. Lee, H. Yoo, Y. Lee, Y. Kim, K. S. Lim, M. Lee, "Multilayered optical bit memory with a high signal-to-noise ratio in fluorescent polymethylmethacrylate,"Appl. Phys. Lett. 94, 111912, 2009.

134. Z. Nie, K. S. Lim, H. Lee, M. Lee, T. Kabayashi, "Femtosecond laser induced photoluminescence in poly (methyl methacrylate) and three-dimensional optical storage," J. Lumin.131, 266-270, 2011.

135. Z. G. Nie, K. S. Lim, W. Y. Jang, H. Y. Lee, M. K. Lee, T. Kabayashi, "Multilayered optical bit storage in $Sm(DBM)_3$Phen-doped poly(methyl methacrylate) read out by fluorescence and reflection modes ,"J. Phys. D: Appl. Phys. 43, 485101, 2010.

136. S.-H. Cho, W.-S. Chang, K.-R. Kim, J.W. Hong, "Femtosecond laser embedded grating micromachining of flexible PDMS plates," Opt. Commun. **282**, 1317-1321, 2009.

137. A. Baum, P.J. Scully, M. Basanta, C.L.P. Thomas, P.R. Fielden, N.J. Goddard, W. Perrie, P.R. Chalker, "Photochemistry of refractive index structures in poly (methyl methacrylate) by femtosecond laser irradiation," Opt. Lett. **32(2),** 190-192, 2007.

138. A. Baum, P.J. Scully, W. Perrie, D. Jones, R. Issac, and D.A. Jaroszynski, "Pulse-duration dependency of femtosecond laser refractive index modification in poly (methyl methacrylate)," Opt. Lett. **33(7),** 651-653, 2008.

139. C. Wochnowski, Y. Cheng, K. Meteva, K. Sugioka, K. Midorikawa, S. Metev, "Femtosecond-laser induced formation of grating structures in planar polymer substrates," J. Opt. A: Pure Appl. Opt. **7**, 493-501, 2005.

140. P J Scully, D Jones and D A Jaroszynski, "Femtosecond laser irradiation of polymethylmethacrylate for refractive index gratings,"J. Opt. A: Pure Appl. Opt. 5, S92-S96, 2003.

141. S. Hirono, M. Kasuya, K. Matsuda, Y. Ozeki, K. Itoh, H. Mochizuki, W. Watanabe, "Increasing diffraction efficiency by heating phase gratings formed by femtosecond laser irradiation in poly(methyl methacrylate) ,"Appl. Phys. Lett. 94, 241122 (3pp), 2009.

142. T. Lippert, Thomas Dickinson, "Chemical and spectroscopic aspects of polymer ablation: Special features and novel directions," J. Chem. Rev.103, 453-485, 2003.

143. N. Bityurin, B. S. Lukyanchunk, M. H. Hong, T. C. Chong, Chem. Rev., 103, 519-552, 2003.

144. Lippert, T. *Plasma Process. Polym.* **2**, 525-546, 2005.

145. Srinivasan, R.; Braren, B.; Casey, K. B. "Ultraviolet laser ablation and decomposition of organic materials," Pure Appl. Chem., Vol.**62**, No.8, 1581-1584, 1990.

146. Patrick, F. C.; Manish Prasad.; Barabara, J. G. *Accounts of Chemical research*, **41(8)**, 915-924, 2008.

147. Zoubir, A.; Lopez, C.; Richardson, M.; Richardson, K., "Femtosecond laser fabrication of tubular waveguides in poly(methyl methacrylate)," Opt. Lett.,Vol. 29, 1840-1842, 2004**.**

148. Wochonowiski, C.; Cheng, Y.; Meteva, K.; Sugioka, K.; Midorikawa, K.; Metev, S. *J.*, "Femtosecond-laser induced formation of grating structures in planar polymer substates,"Opt. A, Vol.7, 493-501, 2005**.**

149. Sowa, S.; Watanabe, W.; Tamaki, T.; Nishii, N.; Itoh, K. *Opt. Express* **2006**, 14, 291-297.

150. Della Valle, G.; Osellame, R.; Laporta, P. *J. Opt. A: Pure Appl. Opt.* **2009,** 11, 013001-013018.

151. Bityurin, N.; Malyshev, A.; Lukyan Chuk, B.; Anisimov, S.; Bauerle, D. *Proc. of SPIE* **1996**, 2802, 103-112.

152. M. Watanabe, S. Juodkazis, H. B. Sun, S. Matsuo,H. Misawa, Phys. Rev. B 60 (1999) 9959.

153. T. Kudrius, G. Slekys, S. Juodkazis, J. Phys. D: Appl. Phys. 43 (2010) 145501.

154. R. N. Nurmukhametov, L. V. Volkova, S. P. Kabanov, J. Appl. Spectr. 73, 55-60, 2006.

155. K. L. N. Deepak, S. Venugopal Rao, D. Narayana Rao," Effects of thermal treatment on femtosecond laser fabricated diffraction gratings in polystyrene," Appl. Surf. Sci. 257, 9299-9305, 2011.

156. K. L.N. Deepak, R. Kuladeep, S. Venugopal Rao, D.Narayana Rao, "Studies on defect formation in femtosecond laser-irradiated PMMA and PDMS," Radiation effects and defects in solids [In press].

157. Panke, D., and Wunderlich, W. J. Appl. Polym. Sci. Appl. Polym. Symp. 1979, **35**, 321.

158. Ershov, Y. A., Kuzina, S. I. and Neiman M. B. "The mechanism of light-induced ageng of light stabilisation of polymers,"Russ. Chem. Rev., Vol.38 (2), 147-163,1969.

159. Mayo, F.R. and Miller, A. A., J. Am. Chem. Soc.,"The oxidation of unsaturated compounds.VII.The oxidation of methacrylic esters," Vol.80, No.10,2493-2496, 1958.

160. Barnes, C. E. J. Am.Chem. Soc., "mechanism of vinyl polemarization.I.role of oxygen," Vol.67, No.2, 217-220, 1945.

161. Barnes, C. E., Elofson, R. M. and Jones G. D., "Role of Oxygen in Vinyl Polymerization. II Isolation and Structure of the Peroxides of Vinyl Compounds," J. Am. Chem. Soc., 72, No.1, 210-215,1950.

162. B. Dickens, J. M. Martin, D. Waksman, Polymer, 1984, 25, 706-715.

163. G.B. Talapatra, D. Narayana Rao and P.N. Prasad, "spectal diffusion within the inhomogeneously broadened- n-π^* singlet-triplet transition of the orientationally disorder solid of 4-bromo-4-chlorobenzophenone," J. Phys. Chem. Vol.88,No.20, 4636-4640, 1984.

164. J. Xu, X.H. Huang, N.L. Zhou, J.S. Zhang, J.Ch. Bao, T.H. Lu, C. Li, Materials Letters 58 (2004) 1938– 1942.

165. Colin N. Banwell, Elaine M. McCash, Fundamentals of Molecular Spectroscopy, 4th edition, Tata McGraw-Hill publishing company limited.

166. Silverstein

167. K. J. Thomas, M. Sheeba, V P N Nampoori, C P G Vallabhan, and P Radhakrishnan "Raman spectra of polymethyl methacrylate optical fibres excited by a 532 nm diode pumped solid state laser" J. Opt. A: Pure Appl. Opt. 10 (2008) 055303 (5pp).

168. D. W. Mayo, F. A. Miller, R. W. Hannah, Course Notes on Interpretation of Infrared and Raman spectra, Wiley Interscience, 2003.

169. Sung Chul Bae, Hyunjung Lee, Zhiqun Lin, and Steve Granick, "Chemical Imaging in a Surface Forces Apparatus: Confocal Raman Spectroscopy of Confined Poly(dimethylsiloxane)", *Langmuir* 2005, *21,* 5685-5688

170. Y. Djaoued, S. Badilescu, S. Balaji, N. Seirafianpour, A.-R. Hajiaboli, R. Banan sadeghian, K. Braedley, R. Bruning, M. Kahrizi, Vo-Van Truong, Micro-Raman Spectroscopy Study of Colloidal Crystal Films of Polystyrene-Gold Composites, Appl. Spectr. 61(2007) 1202-1210.

171. Y. Badr, M. A. Mahmoud, "Enhancement of the Optical Properties of Poly Vinyl Alcohol by Doping with Silver Nanoparticles," Journal of Applied Polymer Science, Vol. 99, 3608–3614 (2006).

172. Galley W C and Purkey R M, Proc. Natl Acad. Sci. USA 1970;67, 1116-1121.

173. Rubinov A N and Tomin VI, Opt. Spektr. 1970;29;1082-1086.

174. Terenin AN. Photonics of Dye Molecules. Nauka:Leningrad, 1967.

175. Birks JB. Photophysics of Aromatic molecules. Wiley-Inter-science: London 1970.

176. Alexander P. Demchenko, "The red-edge effects: 30 years of exploration" Luminescence 2002;17: 19-42.

177. Al-Hassan KA and Rttig W, Free volume sensing fluorescent probes. Chem. Phys. Lett. 1997;268, 110-116.

178. 27.Al-Hassan KA and El-Bayoumi MA, Large edge-excitation red shift for a merocyanine dye in poly (vinyl alcohol) polymer matrix. J. Polymer Sci. B 1987, 25, 495-500.

179. Al-Hassan KA and Azumi T. The red edge effect as a tool for investigating the origin of the anomalous fluorescence band of 9,9'-bianthryl in rigid polar polymer matrices. Chem. Phys. Lett. 1988; 150, 344-348.

180. Bajorek A and Paczkowski J. "Influence of the attachment of chromophores to a polymer chain on their twisted intramolecular charge transfer in dilute solution" Macromolecules 1998; 31, 86-95.

181. Datta A, Das S, Mandal D, Pal SK and Bhattacharyya K. "Fluorescence monitoring of polyacrylamide hydrogel using 4-aminophthalimide" Langmuir 1997, 13, 6922-6926.

182. P. B. Ayscough, Electron Spin Resonance in Chemistry, Methuen, London, 1967.

183. D. J. T. Hill, J. H. O'Donnell, and P. J. Pomery, in Electron Spin Resonance, Royal Society of Chemistry Specialist Periodical Reports, Vol. 13A, Cambridge, 1992, Pp 202.

184. M. Velter-Stefanescu, O. G. Duliua, N. Preda, "On the relaxation mechanisms of soma radiation induced free radicals in polymers," J. Optoelectron. Advanced Mat. **7(2)**, 985–989 (2005).

185. H. Y. Kaptan and O. Guven, J. Appl. Poly. Sci. 64 (1997) 1291.

186. Vera-Maria Graubner, Rainer Jordan, Oskar Nuyken, Bernhard Schnyder, Thomas Lippert, Rudiger Kotz, Alexander Wokaun, "Photochemical modification of Cross-Linked Poly(dimethylsiloxane) by irradiation at 172 nm" Macromolecules 2004, 37, 5936-5943.

187. Vyso Komol. Soyed 8, 1418 (1966)

188. Marchal J., Valks, L., C. R. Acad. Sci. Paris. 272, 2045 (1971).

189. Ohnishi,S, Tanei, T., Nitta, I., J. Chem. Phys. 37, 2402, 1962.

190. K. K. Wong, ed. Proprties of Lithium Niobate (IEE, London, UK, 2002).

191. Airan Rodenas, Amir H. Nejadmalayeri, Daniel Jaque, and Peter Herman, "Confocal Raman mapping of optical waveguides in LiNbO3 fabricated by ultrafast high-repetition rate laser-writing," Opt. Exp. 16, 13979-13989.

192. E. Cantelar, J. A. Sanz Garcia,G. Lifante, F. Cusso, and P. L. Pernas, "Single polarized Tm3+ laser in Zn-diffused LiNbO3 channel waveguides,"Appl. Phys. Lett. 86, 161119 (2005)

193. L. Wang, K. M. Wang, F. Chen, X. L. Wng, L. L. Wang, H. Liu, and Q. M. Lu," Optical waveguide in stoichiometric lithium niobate formed by 500 keV promplantation," Optics express 15, 16880-16885 (2007).

194. P. Baldi, M. de Micheli, K. El Hadi, A. C. Cino, P. Aschieri, and D. B. Ostrowsky, "Proton exchanged waveguides in LiNbO3 and LiTaO3 for integrated lasers and nonlinear frequency converters, " Opt. Eng. 37, 1193-1202 (1998)

195. M. Hempstead, J. S. Wilkinson, and L. Reekie, " Waveguide lasers operating at 1084 nm in Neodymium-diffused lithium niobate," IEEE Photon. Technol. Lett. 4, 852-855 (1992).

196. P. D. Townsend, P. J. Chandler, and L. Zhang, Optical effects of Ion Implantation (Cambridge University Press, Cambridge, 1994).

197. W. M. Young, R. S. Feigelson, M.M. Fejer, M. J.F. Digonnet, H. J. Shaw, "Photorefractive damage resistant Zn-diffused waveguides in MgO:LiNbO3," Opt.Lett. 16, 995-997 (1991).

198. R. Regener, and W. Sohler, "Loss in low-finesse Ti:LiNbO3 optical waveguide resonators," Appl. Phys. B 36, 143-147 (1985).

199. Thomas, J., Heinrich, M., Zeil, P., Hilbert, V., Rademaker, K., Riedel, R., Ringleb, S., Dubs, C., Ruske, J.-P., Nolte, S., and Tu¨nnermann, T., "Laser direct writing: Enabling monolithic and hybrid integrated solutions on the lithium niobate platform," Phys Status Solidi A 208, 276-283, (2011).

200. Thomson, R. R., Campbell, S., Blewett, I. J., Kar, A. K. & Reid, D. T., "Optical waveguide fabrication in z-cut lithium niobate (LiNbO3) using femtosecond pulses in the low repetition rate regime," Appl Phys Lett 88, 111109 (2006).

201. Nejadmalayeri, A.H., Herman, P.R., "Ultrafast laser waveguide writing: lithium niobate and the role of circular polarization and picosecond pulse width," Opt. Lett. 31, 2987-2989 (2006).

202. A. H. Nejadmalayeri and P. R. Herman, "Rapid thermal annealing in high repetition rate ultra fast laser waveguide writing in lithium niobate, " Opt. Express 15, 10842-10854 (2007).

203. J. Burghoff, S. Nolte, and A. tunnermann, "Origins of wave guiding in femtosecond laser-structures LiNbO3,"Appl. Phys. A 89, 127-132 (2007).

204. J. Burghoff, H. Hartung, S. Nolte and A. Tunnermann, "Structural properties of femtosecond laser-induced modifications in LiNbO3," Appl. Phys. A 86, 165-170 (2007).

205. A. Rodenas, J. A. Sanz Garcia, D. Jaque, G. A. Torchia, C. Mendez, I. Arias, L. roso, and F. Agullo-Rueda, "Optical investigation of femtosecond laser induced micro stress in neodymium doped lithium niobate crystals," J. Appl. Phys. 100, 033521 (2006)

206. W. Yang, P. G. Kazansky, and Y. P. Svirko, "Non-reciprocal ultra fast laser writing," Nature Photon. 2, 99-104 (2008).

207. F. K. Christensen, M. Mullenborn, "Sub-band-gap laser micrpmachining of lithium niobate," Appl. Phys. Lett. 66 (21), 2772-2773 (1995).

208. C. Thierfelder, S. Sanna, Arno Schindlmayr, and M. G. Schmidt, "Do we know the bandgap of lithium niobate," Phys. status Solidi C 7, No. 2, 362-365 (2010).

209. H. Lao, H. Zhu, and X. Chen, "Surface Ablation of Congruent and Mg-Doped Lithium Niobate by Femtosecond Laser," ISSN 1054-660X, Laser Physics, 1-5 (2009).

210. N. V. Sidorov, M. N. Palatnikov, V. T. Gabrielyan, P. G. Chufyrev, and V. T. Kalinnikov, "Raman spectra and structural perfection of Normally Pure Lithium Niobate crystals," Inorganic Materials, Vol. 43, No. 1, 60-67, 2007.

211. V. Caciuc, A. V. Postnikov and G. Borstel, " Ab initio structure and zone-center phonons in LiNbO3," Physical review b 61 (13), 8806-8813, 2000.

212. S. M. Kostritskii, and P. Moretti, "Micro-Raman study of defect structure and phonon spectrum of He-ion implanted LiNbO3 waveguids, phys. Stat. Sol (c) 1, No. 11, 3126-3129 (2004).

213. Y. Zhang, L. Guilbert, P. Bourson, K. Polgar, and M. D. Fontana, " Characterization of short range heterogeneties in sub-congruent lithium niobate by micro-Raman spectroscopy," J. Phys. Cond. Matter. 18, 957-963 (2006).

214. F. Abdi, M. Aillerie, P. Bourson, M. D. Fontana, and k. Polgar, "Electro-optic properties in pure LiNbO3 crystals from the congruent to the stoichiometric composition," J. Appl. Phys. 84, 2251-2254 (1998).

215. A. Jayaraman, and A. A. Ballman, "Effect of pressure on the Raman modes in LiNbO3 and LiTaO3," J. Appl. Phys. 60, 1208-1212 (1986).

216. C. A. Merchant, J. S. Aitchison, S. GarciaBlanco, C. Hnatovsky, R. S. Taylor, F. Agullo Rueda, A. J. Kellok, and J. E. E. Baglin, "Direct observation of waveguide formation in KGd(WO4)2 by low dose H+ ion implantation," Appl. Phys. Lett. 89, 111116 (2006).

217. I. Savova, I. Savatinova, and E. Liarokapis, "Phase composition of z-cut protonated $LiNbO_3$:a Raman study,: Opt. mat. 16, 353-360 (2001).

218. C. Kittel, Introduction to solid state Physics, John Wiley and sons, New York (1996).

219. H. Raether, Surface Plasmons, Springer-Ver lag Tracts in Modern Physics, Springer-Verlag, New York, 111 (1998).

220. Kreibig U, Vollmer M, Optical properties of Metal clusters, Springer, Berlin (1995).

221. Kerker M, The scattering of Light and other electromagnetic radiation, Academic Press, New York 1969.

222. Bohren C F, Huffman D R, Absorption and scattering of Light by small particles, Wiley, New York (1983)

223. Papavassiliou G C, Prog. Solid. State Chem. 12, 185 (1979)

224. Faraday M, Philos. Trans. 147,145, 1857.

225. Mott N F, Jones H, The theory and properties of metals and alloys, Oxford Press, Oxford, Pg. 105 (1936).

226. G. Schmid, Chem. Rev. 92, 1709 (1992).

227. L. N. Lewis, Chem. Rev. 93, 2693 (1993).

228. B. C. Gates, Chem. Rev. 95, 511 (1995).

229. J. H. Fendler, Chem. Mater. 8, 1616 (1996).

230. Zhou Y, Wang CY, Zhu YR et al (1999) A novel ultraviolet radiation technique for shape-controlled synthesis of gold nanoparticles at room temperature. Chem Mater 11:2310–2312.

231. Van der Zande BMI, Böhmer MR, Fokkink LGJ et al (2000) Colloidal dispersions of gold nanorods: synthesis and optical properties. Langmuir 16(2):451–458

232. Kim YJ, Johnson RC, Hupp JT (2001) Gold nanoparticle-based sensing of "spectroscopically silent" heavy metal ions. Nano Lett 1(4):165–167

233. Jana NR, Gearheart L, Murphy CJ (2001) Wet chemical synthesis of high aspect ratio cylindrical gold nanorods. J Phys Chem B 105(19):4065–4067.

234. Kamat PV (2002) Photophysical, photichemical and photocatalytic aspects of metal nanoparticles. J Phys Chem B 106(32): 7729 – 7744.

235. Kim F, Song JH, Yang P (2002) Photochemical synthesis of gold nanorods. J Am Chem Soc 124:14316–14317.

236. Nikoobakht B, El-Sayed MA (2003) Preparation and growth mechanism of gold nanorods (NRs) using seed-mediated growth method. Chem Mater 15:1957–1962.

237. Daniel MC, Astruc D (2004) Gold nanoparticles: assembly, supramolecular chemistry, `quantum-size-related properties, and applications towards biology, catalysis and nanotechnology. Chem Rev 104(1):293–346.

238. Yu YY, Chang SS, Lee CL et al (1997) Goldnanorods: Electrochemical synthesis and optical properties. J Phys Chem B 101(34):6661–1664.

239. Chen W, Zhao J, Lee JY et al (2004) Phtochromism of diarylethene-capped gold nanoparticles. Chem Lett 33(4): 456 –457

240. Sung KM, Mosley DW, Peelle BR et al (2004) Synthesis of monofunctionalized gold nanoparticles by Fmoc solid-phase reactions. J Am Chem Soc 126:5064–5065

241. Hiramatsu H, Osterloh FE (2004) A simple large scale synthesis of nearly monodisperse gold and silver nanoparticles with adjustable sizes and with exchangeable surfactants. Chem Mater 16(13):2509–2511.

242. S. Underwood and P. Mulvaney, Langmuir 10, 3427 (1994).

243. M. J. Hostetler, C. J. Zhong, B. K. H. Yen, J. Anderegg, S. M. Gross, N. D. Evans, M. Porter and R. W. Murray, J. Am. Chem. Soc. 120, 9396 (1998).

244. R. Sathyavathi, M. Bala Murali Krishna and D. Narayana Rao, J. Nanosci. Nanotechnol. 11, 2031 (2011).

245. A. Henglein, Chem. Rev. 89, 1861 (1989).

246. P. Mulvaney, Langmuir 12, 788 (1996).

247. R.A. Salkar, P. Jeevanahdam, S.T. Aruna, Y. Koltypin and A. Gedanken, J. Mater. Chem. 9, 1333 (1999).

248. A. Henglein, J. Phys. Chem. B 104, 6683 (2000).

249. A. Bogaerts, Z. Chen, R. Gijbels and A. Vertes, Spectrochem. Acta B 85, 1867 (2003).

250. G.X. Chen, M.H. Hong, B. Lan, Z.B. Wang, Y.F. Lu and T.C. Chong, Appl. Surf. Sci. 228, 169 (2004).

251. Z. Pasati, G. Peto, Z.E. Horvath and A. Karacs, Appl. Surf. Sci. 168, 114 (2000).

252. A. Bogaerts, Z. Chen, R. Gijbels and A. Vertes, Spectrochem. Acta B 85, 1867 (2003).

253. S. Porel, N. Venkatram, D. Narayana Rao and T. P. Radhakrishnan, J. Appl. Phys. 102, 033107 (2007).

254. S. Porel, N. Venkatram, D. Narayana Rao and T. P. Radhakrishnan, J. Nanosci. Nanotech. 7, 1887 (2007).

255. S. Philip Anthony, S. Porel, D. Narayana Rao and T. P. Radhakrishnan, Pramana – Journal of Physics (Special Issue on Nanoscience and Technology) 65, 871 (2005).

256. S. Porel, S. Singh, S. Sree Harsha, D. N. Rao and T. P. Radhakrishnan, Chem. Mater. (Communication) 17, 9 (2005).

257. Longenberger and G. Mills, J. Phys. Chem. 99, 475 (1995).

258. H. Zeng, J. Qiu, X. Jiang, C. Zhu and F. Gan, J. Phys. Condens. Matter. 16, 2901, 2004.

259. J. Shin, K. Jang, K. S. Lim, I. B. Sohn, Y. C. Noh and J. Lee, Appl Phys A 93, 923, 2008.

260. K. L. N. Deepak, R. Kuladeep, K. Shadak Alee, D. Narayana Rao, Journal of Nanoscience and Nanotechnology [In Press].

261. M. Sheik-Bahae, A. A. Said, T. Wei, D. J. Hagan and E. W. Van Stryland, " Sensitive Measurement of Optical NonlinearitiesUsing a Single Beam "IEEE J. Quantum Electron. 26,760-769, 1990.

262. X. Gu, Q. Huang, S. Q. Tan, M. Wang, W. Ji, "Z-scan analytical theories for characterizing multiphoton absorbers,"Appl. Phys B, 95,375-381, 2009.

About the author

K. L. N. Deepak, son of K. Krishna Rao and K. Manjuvani, was born in Srikakulam, of Andhra Pradesh, India, in July 1982. He received his primary and secondary school education near vizag district, AP state. He then completed his intermediate education from A. M. A. L. College, Anakapalli in Vizag district, A. P. state. After the completion of his Intermediate, he joined for B.Sc. Hons and M.Sc. (Physics) at Sri Sathya Sai Institute of Higher Learning (Sri Sathya Sai University), Prasanthi Nilayam campus. He registered for Ph. D. program in August 2006 under the guidance of Prof. D. Narayana Rao, School of Physics, University of Hyderabad, Hyderabad. He is the winner of "Young Scientist" award instituted by Dr. K. V. Rao Scientific Society in the year 2010 under the category of Physics. He also got best poster award for his work during National Laser Symposium (NLS) 09 conference conducted at BARC, Mumbai during Jan 13th-16th, 2010.

Experimental expertise:

- Femtosecond Supercontinuum generation in nonlinear crystals and transparent media
- Femtosecond and nanosecond Z-scan technique to measure the nonlinear optical properties of thin films and liquids.
- Femtosecond time resolved box-car degenerate four-wave mixing to look into the nonlinear optical properties of materials.
- Pulse width measurement of the fs laser using the intensity autocorrelation correlation techniques.
- Nanosecond degenerate four-wave mixing in backward geometry
- Femtosecond laser direct writing in glasses, nonlinear crystals for micro-optical devices and direct writing of channel waveguides.
- Preparation of nanoparticles and their characterization

Instruments: Handling Expertise / Operated:

- 100 fs Ti:Sapphire laser system (Mai Tai oscillator + Spitfire regenerative amplifier + OPA)
- High power Nd: YAG Lasers (6 ns, 10Hz)

- He-Ne Lasers
- Raman shifter (H_2 gas)
- Confocal Microscope
- Atomic force microscope (AFM)
- Nano positioner
- UV-Vis-NIR absorption spectrometers (Varian-Cary 5000), Fluoremeters (Fluoromax-3)
- 200 MHz Digital Oscilloscope (Tektronix)
- Lock-in Amplifiers (SRS 830, Princeton Applied Research)
- Boxcar Averager and Integrator (SRS-250)
- Stepper Motor Controller
- Spectrometers (Jobin Yvon, Ocean Optics USB2000), CCD cameras
- Power Meters (Scientech and Ophir)
- High power optics
- Confocal micro-Raman spectrometer
- Scanning electron microscope
- Transmission electron microscope

Awards during the course of Ph.D.:

1. Winner of **Young scientist Award** in Physics for the year 2010, instituted by Dr. K. V. Rao Scientific society.
2. Best poster award during NLS 09 conference conducted at BARC, Mumbai during Jan 13^{th}-16^{th} 2010.

List of Publications

Journal publications:

1. "Fabrication and Optical Characterization of microstructures in PMMA and PDMS using femtosecond pulses for photonic and micro fluidic applications". **K.L.N. Deepak**, D. Narayana Rao, S. Venugopal Rao, Applied Optics **49**, 13, 2475 (2009).
2. "Femtosecond laser-fabricated microstructures in bulk poly(methylmethacrylate) and poly(dimethylsiloxane) at 800 nm towards lab-on-a-chip applications," **K. L. N. Deepak,** S. Venugopal Rao, D. Narayana Rao, Pramana 75 (6), 1221-1232 (2010).
3. "Luminescent microstructures in bulk and thin films of PMMA, PDMS, PVA, and PS fabricated using femtosecond direct writing technique" **K. L. N. Deepak**, R. Kuladeep, S. Venugopal Rao, D. Narayana Rao, Chemical Physics Letters **503**, 57-60 (2011).
4. "Emission properties of femtosecond (fs) laser fabricated microstructures in Polystyrene (PS)" **K. L. N. Deepak**, R. Kuladeep, D. Narayana Rao, Optics Communications **284**, 3070-3073 (2011).
5. "Spectroscopic investigations of femtosecond laser irradiated Polystyrene and fabrication of microstructures" **K. L. N. Deepak**, R. Kuladeep, V. Praveen Kumar, S. Venugopal Rao, D. Narayana Rao, Optics Communications **284**, 3074-3078 (2011).
6. "Studies on Defect Formation in Femtosecond Laser Irradiated PMMA and PDMS" **K. L. N. Deepak**, R. Kuladeep, S. Venugopal Rao, D. Narayana Rao, Radiation Effects and Defects in Solids [Accepted].
7. "Effect of heat treatment to efficient buried diffraction gratings in Polystyrene" **K. L. N. Deepak**, S. Venugopal Rao, D. Narayana Rao, Applied Surface Science **257**, 9299-9305(2011).
8. "Synthesis of silver nanoparticles in poly (vinyl alcohol) matrix in solution and thin films through laser irradiation" **K. L. N. Deepak**, R. Kuladeep, S. Alee, D. Narayana Rao, Journal of Nanoscience and Nanotechnology [Accepted].
9. "Depolarization properties of the femtosecond supercontinuum generated in condensed media". R. Sai Santosh Kumar, **K. L. N. Deepak**, and D. Narayana Rao, Phys. Rev. A **78**, 043818 (2008) (Virtual Journal of ultrafast science, Vol. 7, Issue 11, November 2008).

10. "Control of the polarization properties of supercontinuum generation in a noncentrosymmetric crystal". R. Sai Santosh Kumar, **K. L. N. Deepak**, D. Narayana Rao, Opt. Lett. **33,** 1198 (2008).

Conference Papers (International and national):

1. "Supercontinuum Generation in quadratic media with controllable polarization properties", R. Sai Santosh Kumar, **K. L. N. Deepak**, N. Venkatram, D. Narayana Rao, , *5th Asian Conference on Ultrafast Phenomena (ACUP 2008),* 6 - 9 January 2008, Singapore. **[Invited talk].**

2. "Femtosecond laser direct writing of Microstructures in POLY (METHYL METHACRYLATE)", **K. L.N. Deepak**, S. Venugopal Rao, R. Sai Santosh Kumar, D. Narayana Rao, *International Conference on Fiber Optics and Photonics-08*, IIT Delhi, India, Dec 15^{th}-17^{th} 2008 **[Oral Presentation]**.

3. "Synthesis of Silica nanoparticles and its photonic crystal", **K. L. N. Deepak**, S.N. B. Bhaktha, A. Chiappini, M. Ferrari, D. Narayana Rao, *International Conference on Fiber Optics and Photonics-08*, IIT Delhi, India, Dec 15^{th}-17^{th} 2008 **[Poster Presentation]**.

4. "Direct Writing of Microstructures in Bulk Poly (Mehtyl MethAcrylate) using Femtosecond Pulses" ,**K.L.N. Deepak**, S. Venugopal Rao, R. Sai Santosh Kumar, D. Narayana Rao, *Eighth DAE-BRNS National Laser Symposium (NLS-08)*, LASTEC, Delhi, India, Jan 7^{th}-10^{th} 2009 **[Poster Presentation]**.

5. "Microstructures and Diffraction Gratings in Poly(Dimethyl Siloxane) fabricated using femtosecond pulses", **K.L.N. Deepak**, S. Venugopal Rao, R.Sai Santosh Kumar, D. Narayana Rao, *International Conference on Optics & Photonics(ICOP-2009)*, CSIO, Chandigarh, India, Oct. 30^{th}- Nov. 1^{st} 2009. **[Poster Presentation]**.

6. "Femtosecond Laser Written Microstructures in PDMS and PMMA for Photonic Applications" , **K. L. N. Deepak** ,D. Narayana Rao, , S. Venugopal Rao, *28^{th} International Congress on Applications of Lasers & Electro optics (ICALEO 2009)*, Orlando, Florida, USA, Nov. 2^{nd}-5^{th} 2009. **[Poster Presentation]**.

7. "Femtosecond Laser Fabrication and Optical Studies of Microstructures in PMMA and PDMS" , **K.L.N. Deepak**, S. Venugopal Rao, D. Narayana Rao, *2009 Frontiers in Optics*

(FiO)/Laser Science XXV (LS)/Fall OSA Optics & Photonics Congress, San Jose, California, USA - October 11-15, 2009. **[Poster Presentation]**.

8. "Femtosecond laser processing of polymers for photonic and Micro fluidic applications". **K.L.N. Deepak**, S. Venugopal Rao, D. Narayana Rao, Second International Conference on Polymer Processing and Characterization (ICPPC 2010):, Kottayam, Kerala, India, Jan 15th-17th, 2010. **[Oral Presentation].**

9. "Electron spin resonance (ESR), laser confocal, and micro-Raman studies of the femtosecond laser modified regions in Poly (Methyl Methacrylate) (PMMA) and Poly (Dimethyl Siloxane) (PDMS)". **K.L.N. Deepak,** D. Narayana Rao, S. Venugopal Rao, National Laser Symposium -09, BARC, Mumbai, India, Jan 13th- 16th, 2010. **[Poster Presentation + Best Poster Award].**

10. "Physics of femtosecond laser direct writing and modified regions in polymers Poly (Methyl Methacrylate) and Poly (Dimethyl Siloxane)", **K. L. N. Deepak,** D. Narayana Rao, S. Venugopal Rao, India Singapore Joint Physics Symposium 2010 ISJPS 2010), University of Hyderabad, Hyderabad, India, February 19th-21st, 2010. **[Poster Presentation].**

11. "Laser Direct Writing of Photonic Devices in x-cut Lithium Niobate using Sub-100 Femtosecond Pulses" S. Venugopal Rao, T. Shuvan Prashant, **K.L.N. Deepak,** G. Manoj Kumar,S.P. Tewari,and D. Narayana Rao , International Conference on Photonics at IIT Guwahati, December 11th -15th , 2010. **[Poster Presentation].**

12. "Spectroscopic Characterizations of the femtosecond laser modified regions in bulk and thin films of Poly Methyl Methacrylate (PMMA), Poly Dimethyl Siloxane (PDMS), Polystyrene (PS), and Poly Vinyl Alcohol (PVA)" **K. L. N. Deepak**, S. Venugopal Rao, R. Kuladeep, V. Praveen Kumar, D. Narayana Rao, , International Conference on Photonics at IIT Guwahati, December 11th -15th , 2010. **[Poster Presentation].**

13. "Femtosecond laser (fs) fabricated microstructures in bulk and thin films of Poly Methyl Methacrylate (PMMA), Poly Dimethyl Siloxane (PDMS), Poly Vinyl Alcohol (PVA) and Polystyrene (PS)", **K. L. N. Deepak**, S. Venugopal Rao, D. Narayana Rao, National Laser Symposium conducted at RRCAT, Indore , December 1st-4th, 2010. **[Poster Presentation].**

14. "Femtosecond laser fabrication of microchannels in bulk and thin films of Polystyrene", **K. L. N. Deepak,** S. Venugopal Rao, V. Praveen Kumar, R. Kuladeep, D. Narayana Rao,

National Laser Symposium conducted at RRCAT, Indore , India, December 1st-4th, 2010. **[Poster Presentation].**

15. "Micro fabrication in bulk and thin films of PMMA, PDMS, PS, and PVA and their spectroscopic characterizations towards Lab on a chip device applications", **K. L. N. Deepak**, S. Venugopal Rao, D. Narayana Rao, Lab-on-a-chip European Congress is going to be held at Hamburg, Germany, 30th June-1st July, 2011. **[Accepted for poster presentation].**

16. "Femtosecond Laser Direct Writing And Spectroscopic Characterization Of Microstructures, Craters, And Gratings In Bulk/Thin Films Of Polystyrene", **K. L. N. Deepak**, S. Venugopal Rao, D. Narayana Rao, Optics 11 conference, Calicut, India, May 23rd-25th, 2011. **[Poster Presentation].**

17. "Femtosecond laser micro fabrication in polymers towards memory devices and micro fluidic applications", **K. L. N. Deepak**, S. Venugopal Rao, D. Narayana Rao, SPIE Laser Damage symposium 2011 is going to be held at Boulder, Colorado, USA, 18th-21st, Sep. 2011.